Università degli Studi di Ferrara

DOTTORATO DI RICERCA IN SCIENZE DELL' INGEGNERIA

CICLO XXXI

COORDINATORE Prof Stefano Trillo

Modeling approaches for gas turbine deterioration analysis

Settore Scientifico Disciplinare ING-IND/08

Dottorando
Nicola Casari

Tutore
Prof. Michele Pinelli

Anni 2016/2018

This page was intentionally left blank.

This page was intentionally left blank.

This page was intentionally left blank.

Abstract

Gas turbines are a popular source of power for aerospace and land-based applications. Nevertheless the importance of particle ingestion and its implication is an often underestimated problem which can lead to the variation of geometry of aerodynamic surfaces, entailing performance degradation and, possibly, a reduction in engine life. The presence of sand and other type of particles can cause erosion or deposition in both the compressor and turbine sections. This problem can occur for land based turbines operating in harsh environment, where the problem can be mitigated (but not eliminated) by installing filtration systems. For what concern the aerospace field, filtration systems cannot be used. Volcanic eruptions and sand dust storms can send particulate to aircraft cruising altitudes. Also, aircraft operating in remote locations or at low altitude can be subjected to particle ingestion, especially in desert environments.

A thorough analysis of the deterioration mechanisms of gas turbines, and of their modelling, including erosion, deposit formation and deposit evolution over time has not been presented in the literature so far. In this work, the modelling of all such mechanisms has been performed for both the hot and the cold section. In all the presented approaches, the blade contamination process analysis is based on the Computational Fluid Dynamics (CFD) study, with a Eulerian-Lagrangian approach. The stochastic particle tracking for the trajectory computation has been employed. With this approach, both the transient and the steady state tracking can be performed, and both the methods will be employed: the choice of the time treatment will be made by comparing the time scale of the deposition/erosion phenomena to the time scale of the performance degradation.

The boundary variation as a consequence of the particle impact has been implemented, either with a mesh morphing approach or innovative techniques that are proposed to include the particle impact consequences on the flow field. The displacement of the boundary, or the variation of some of its characteristics (e.g. roughness), represents the most important effect of the deposit/erosion and, therefore, particular care should be taken when dealing with it.

From this work, some important information regarding the areas which are affected the most by the particles ingestion can be retrieved and the techniques that can be employed for the evaluation of the effects of the particle-wall interaction are explained. Indeed, Thanks to the model here proposed, a preliminary methodology for the robust design under fouling conditions is proposed.

Eventually a non-dimensional analysis of the behaviour of particles upon impact is proposed, suggesting that a universal map for the classification of the consequences of the impingement can be outlined. Such map is proposed as a tool for the detection of the effect of the impact. Eventually, starting from the considerations and the models

developed, a design-for-fouling oriented optimization is proposed.

Sommario

Nonostante le turbine a gas siano una comune fonte di energia sia per applicazioni stazionarie che per il campo aeronautico, l'effetto della presenza di particolato nell'aria processata è un aspetto che è stato spesso sottostimato nella letteratura. Le particelle presenti nell'aria possono risultare, a seguito dell'impatto con le superfici bagnate dal flusso, in una variazione di geometria e comportare una riduzione delle performance o piuttosto della vita utile della macchina. Sabbia o, in generale, altri tipi di contaminant possono causare erosione o deposizione sia nelle sezioni fredde (compressore) che calde (turbina) della macchina.

Questo problema si verifica tipicamente per turbine a gas stazionarie che lavorano in ambienti ostili, aventi alta concentrazione di particolato nell'aria: in tali casi, il problema può essere solo mitigato, ma non completamente evitato, dall'installazione di sistemi di filtrazione all'aspirazione della macchina. Tali filtri non vengono invece utilizzati in caso di turbomacchine per la propulsione aeronautica. Perciò, a seguito di tempeste di sabbia o eruzioni vulcaniche, possono essere presenti particelle all'altezza di crociera. In alternativa, il decollo, l'atterragio o il volo a bassa quota in località remote possono rappresentare un'ulteriore rischio per l'ingestione di particelle.

Un'analisi completa di tutti gli aspetti del deterioramento delle turbine a gas e della loro modellazione numerica, tenendo in considerazione erosione, formazione del deposito ed evoluzione del deposito nel tempo non è ancora stata presentata in letteratura. In questo lavoro viene presentata la modellazione di tutti questi meccanismi, di entrambe le sezioni della macchina. In particolare, per tutti i fenomeni analizzati, il processo di contaminazione delle pale è basato sullo studio numerico tramite CFD (Computational Fluid Dynamics), con un approccio Euleriano-Lagrangiano. La traiettoria delle particelle è calcolata considerando il contributo stocastico derivante dalla turbolenza del moto. Con tale approccio possono essere considerati sia il tracciamento transitorio che quello stazionario: entrambi i metodi saranno utilizzati e la scelta dell'uno piuttosto che dell'altro verrà giustificata in base al tempo caratteristico del fenomeno che si sta considerando. Infatti la decisione sarà basata sul confronto del tempo caratteristico del fenomeno di erosione/deposizione con quello relativo alla rapidità con cui si manifesta il degrado delle prestazioni a livello di macchina.

La modifica delle condizioni al contorno del dominio e, in particolare, delle pareti interessate dall'impatto di particelle costituisce il passaggio fondamentale per rappresentare il loro effetto. L'implementazione presentata in questo lavoro è stata ottenuta mediante due diversi approcci: mesh mobili (moving mesh) e una serie di tecniche innovative che verranno prersentate nel seguito.

Da questo lavoro possono essere ottenute alcune informazioni importanti riguardo le

aree che sono maggiormente affette dalla presenza di particelle. Inoltre alcune tecniche che possono essere usate per la valutazione dell'effetto dell'interazione parete-particella vengono illustrate. Infine viene presentata un'analisi non-dimensionale del comportamento della particella all'impatto, suggerendo come può essere realizzata una mappa universale per la classificazione delle conseguenze di tale impatto. Dalle considerazioni e dai modelli sviluppati, viene infine proposta una metodologia preliminare per la progettazione della pala in condizioni di presenza di particelle.

Contents

List of Tables

List of Figures

Introduction

The presence of particulate in the air represent a real hazard for gas turbines either for aero-propulsion or power-generation. They can affect the machine operation in several ways, ranging from the lowering of performances, to the shortening of the time between overhauls up to bring about abrupt shutdown. The seriousness of the effect depends on several factors such as the nature of the particulate that is ingested, its amount and the engine operating conditions.

The source of contaminants can be either natural (e.g. sand storms, volcanic eruptions, oceans) or related to the human activities (e.g. transports, industrial plants, heating). To each of these sources corresponds a size distribution of the particulate with a different chemical composition and a different effect on the machine operation. It is worthy to remark that even a small concentration of particulate in the air, of the order of few PPMs, reflects in a very high amount of foulant ingested. For instance, an high thrust turbofan engine can process a mass flow rate of approximately 500 kg/s, resulting in rates of ingestion of solid contaminant up to the order of 1 $kg_{particles}$/s.

The importance of this problem is well known among operators and manufacturers. Focusing on the industrial turbomachinery, the particulate ingestion problem can be mitigated by the installation of filters: highly effective filtration systems are very efficient in removing particles larger than about 1 μm to 2 μm. This means that compressor erosion is not a problem frequently found in industrial gas turbines. However, depending on the type of filtration system used, smaller particles can enter the engine. These particles are too small to cause erosion issues, but they are likely to cause compressor fouling. Extensive research has been pushed forward by the oil & gas community in order to find the most suitable filtration system with respect to each different installation conditions (offshore rather than land-based). The particles carried by the airflow are known to affect heavily the compressor section rather than the hot parts. Nonetheless, other sources of contaminants can be associated with the fuel, for example when turbines are operated with syngas. Over the last years, energy and climate change policies associated with the continuous increase in natural gas costs pushed governments to invest in renewable energy and alternative fuels. Although synfuels are cleaned and filtered before entering the turbine combustor, impurities are not completely removed. Therefore, the high temperature reached in the turbine nozzle can lead to the deposition of contaminants onto internal surfaces, entailing hot parts degradation.

In the aerospace fields, solid particles can enter the power stream of jet engines for different reasons. Particles can be ingested during take-off or landing in harsh environments, or during cruise at altitude through volcanic dust clouds or sand storms. In this case, there is no filtration system that can be used for engines. Both the compressor and

the HPT sections suffer of this problem, though in a different fashion. The compressor deterioration due to particles is related both to erosion and fouling, while for the hot section, deposition is the main issue, in relation with the high TET. The time scale of the two sections degradation is different: if compressor suffers of a relatively slow degradation of performance over time, the hot section deposition is able to demand energy shut down in a few minutes of exposure. This especially applies when the particulate is composed by volcanic ash.

To date, no satisfying prediction model for a safe-to-fly concentration has been developed and therefore the authority (CAA - UK Civil Aviation Authority) has fixed a precautional threshold of 2 $\mathrm{mg}_{ash}/\mathrm{m}^3_{air}$. If the concentration of ash in the air exceeds this limit, no flight is allowed in the relative airspace. The seriousness of this threat is highlighted by the disruption brought to air travel by volcanic events in recent years.

Rationale

This work aims to investigate the degradation of gas turbine performances as a consequence of particle ingestion. Since particle impact may have various consequences and the effects it has on the flow field is closely related to the section of the machine in which such event occurs, multiple techniques have been developed. Each of these techniques has been implemented or entirely developed to have the most reliable representation of such phenomena. This thesis is therefore structured according to the three main consequences of the particle impact, namely:

- Deposit formation
- Blade erosion
- Deposit evolution over time

For each of the categories, the cold and the hot sections will be investigated separately, highlighting the peculiarities. Besides, the techniques that have been employed or developed *ad hoc* will be accurately described, pointing out the pros and the cons of their application.

Thanks to the models developed during the degradation analysis, two applications have been investigated.

Firstly, a preliminary method for the robust design of the blades in fouling conditions has been tested. The pressure side of a vane has been modified to verify the effect of the curvature on the performance in "clean" and "contaminated" environment conditions.

Secondly, a non dimensional analysis has been carried out, with the aim of unifying the different behaviour investigated for each of the sections, generalizing the impact consequences by means of a map. By analyzing the experimental data available in the literature, each different regime is identified and collected in a predictive tool. This map is proposed as a reference for giving an *a priori* idea of the regime to which the impacting conditions under investigation belong.

As the reader might have noticed, no corrosion-related issues has been mentioned. This work indeed does not include any specific study regarding the deterioration of the substrate due to chemical interaction with the particles/carrier flow. This remark represents a limitation of the current thesis.

This page was intentionally left blank.

Thesis outline

This work provides the background for the papers, details the numerical setup and summarizes the results. The different degradation mechanism forms the framework of the thesis.

Chapter 1 Is a general introduction to the problem, including an overview on the sources of particulate in the air and the degradation effects related.

Chapter 2 Gives the numerical background and explain the methods used for the particle tracking methods. The geometries analyzed throughout the following chapters will be disclosed here, and an overview of the software used is given.

Chapter 3 Studies the deposition formation, both for the hot and the cold section. The numerical models and the computational technique employed for the analyses will be described.

Chapter 4 Analyzes the evolution of the deposit over time, its detachment or toughening due to the local flow conditions

Chapter 5 Is related to the study of the erosion on compressor and turbine blades.

Chapter 6 Proposes a first application in the track of the results of the previous analyses: the first steps in formalizing a robust design under fouling conditions.

Chapter 7 Summarizes the findings and proposes some perspectives: a non-dimensional map that classifies the behaviour of the particles upon impact.

Appendix I Is the technical design of the numerical test bench employed for the cold section analyses.

Appendix II Reports the schematic and describes the test bench developed at the university of Ferrara.

This page was intentionally left blank.

Originality and Contributions by Others

The originality of this work resides in the thoroughness of the analysis carried out. All the aspects of the particle ingestion problem (deposition, erosion, deposit evolution over time) have been analyzed and gathered together. Multidisciplinary tools have been employed for the definition of the mathematical models where not available or not commonly used by the community. Moreover, during the development of this work, other numerical tools that might be of help for the community have been conceived. The numerical study has been supported and placed side by side with experimental data available in the literature. Finally, such experimental data are gathered and collected in a map, that is of help in the identification of the impact behaviour regime. For proving the effectiveness of the proposed methods, a first design-for-fouling concept has been developed.

This work takes its origin from the "Fouling in turbomachinery" research topic carried out at the University of Ferrara, but benefits from the visiting period and advice from prof. di Mare and prof. Montomoli. Indeed the experience of the Ferrara turbomachinery group (historically related to compressors) has been of great inspiration and has been extended with novel numerical techniques. Besides, the analysis has been broadened to the hot section of the machine, in the desire of achieving an overall view of the gas turbine deterioration due to particle injection.

Lastly, the non-dimensional analysis of the chapter 7 is due to the work of Dr. Suman and Dr. Fabbri: their contribution has been of paramount importance in the development of the impact behaviour map and on the considerations about the material properties.

This page was intentionally left blank.

Chapter 1

Problem Statement

This chapter reports a global overview of performance degradation due to particle presence in the flow field processed by the machine. The several aspects of the blade contamination mechanism are analyzed, starting with a broad overview of the source of particulate and showing how these particles affect the gas turbine operations.

1.1 Particulate source

1.1.1 Air contamination

Air is dispersed with contaminants that may be solid, liquid, or gaseous. Such materials typically result from both natural and human processes, as suggested by Smith (2012). Volcanic and other geothermal eruptions, soil or sand transported by wind, gases released from vegetation, pollen, spores, and sea spray particles are just some examples of natural sources. Human related pollutants can be related to a variety of combustion and industrial activities. Although the two sources are equally important in terms of amount of particulate production, the spatial scale related to the dispersion and the re-entry is quite different. Man-made contaminants have a rather local impact Lyons and Pease (1973), whereas nature-related particles tend to have a global-scale dispersion. The relevance of the phenomenon is such that several models for the prediction of particle dispersion and deposition have been developed. For example Zender et al. (2003), developed a model for predicting the annual mean mobilization and deposition tendencies. Their results, reported in Fig. 1.1, stress the global impact of natural sourced contaminants, showing the effectiveness of the transport from the sources (Fig. 1.1 (a)) to the downind areas (Fig. 1.1 (b)). It is also interesting to note the more localized effect of dry deposition ((Fig. 1.1 (c)) if compared to wet one 1.1 (d), that involves the spreading of the particles

to larger distances.

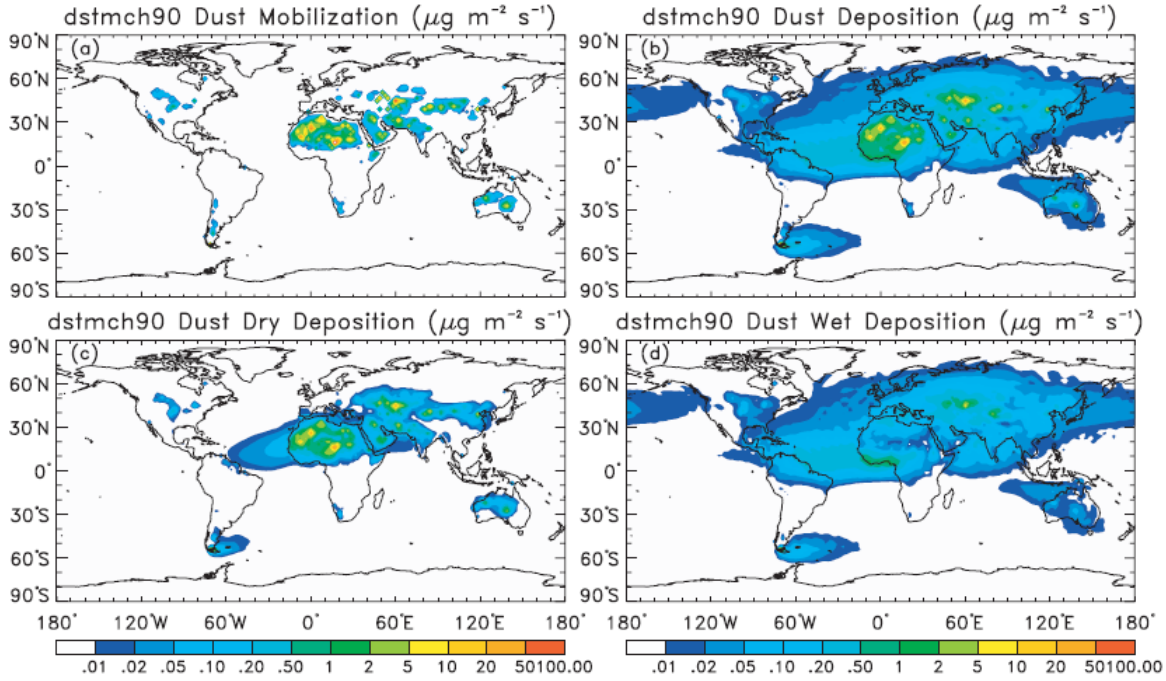

Figure 1.1: Predicted annual mean dust source and sink fluxes in $\mu g/m^2\ s^{-1}$ for (a) mobilization, (b) total deposition, (c) dry deposition, (d) wet deposition. Scale is logarithmic. From Zender et al. (2003)

Natural-derived particles are dispersed in the environment according to three different main mechanisms, as suggested by Wilcox et al. (2010): suspension, saltation and creep. Suspension describes the process where particles are carried by the wind. Saltation is when the particles move forward on the ground through a series of leaps and jumps. Creep is when the particle will travel across the ground during heavy winds. These contaminants are not lifted into the air but move through rolling or sliding action. The occurrence of one mechanism rather than the other, and the effectiveness of such transportation is closely dependent on the particle size. Larger and heavier particles will travel for short distances before falling on earth, while smaller particles will have a lower can remain suspended in the air for days at a time.

Among the others, particular attention should be devoted to volcanic ashes. Explosive volcanic eruptions are responsible for the production of particulate matter that, along with other aerosol droplets, is carried upwards as a consequence of buoyancy and then dispersed by winds, as reported by Sparks et al. (1997). As suggested by Casadevall (1992), volcanic ash can spread over large distances away from the source, disrupting air traffic, hazarding airports, as in Guffanti et al. (2009), even altering atmospheric composition according to Myhre et al. (2013). Figure 1.1 represents the dust deposition at the ground and it is therefore useful for gathering information on the particulate load an industrial gas turbine will be exposed to during the operation. When it comes to evaluate the effects of the volcanic ash on the flight traffic, different models should be employed.

As proposed by Marti et al. (2017), each volcanic eruption can be considered as a source in a precise location on the earth. Therefore, the time-dependent evolution of the originated cloud can be predicted, by considering the weather conditions. For example, Figure 1.2 reports the mass loading distribution evolution obtained for the 2011 Caulle eruption. Models like NMMB-MONARCH-ASH, see Marti et al. (2017) can predict the cloud spreading on the global scale suggesting which routes are going to be affected by the eruption itself.

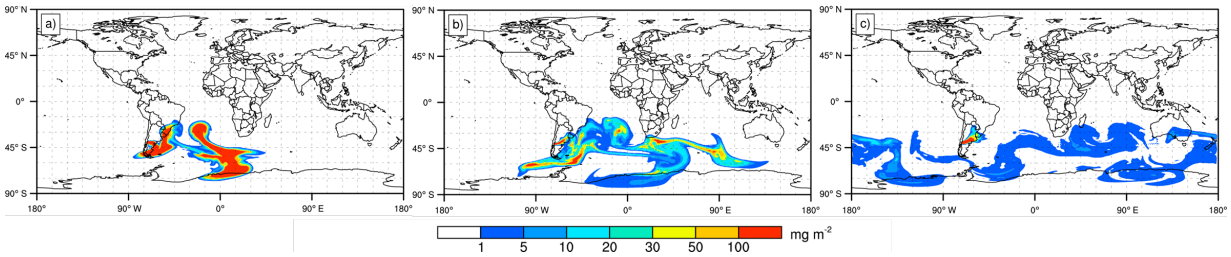

Figure 1.2: NMMB-MONARCH-ASH total column concentration (mass loading; mg m^{-2}) from global simulation for the 2011 Caulle eruption. Results for (a) 8 June at 09:00 UTC, (b) 10 June at 04:00 UTC, and (c) 14 June at 06:00 UTC.. From Marti et al. (2017)

Some extra information that might be useful in case of volcanic eruptions regards the prediction of the same cloud reported in Fig. 1.2, but according to the altitude level. For example, the model used by Marti et al. (2017) can be used for this type of analyses. Figure 1.3 reports the time evolution for two specific flight levels. Flight levels is defined as a vertical altitude at standard pressure, nominally expressed in hundreds of feet as reported in SID (2009). Reliable prediction models for the particle dispersion are therefore of paramount importance for the decision of whether allowing flight or not in a certain airspace area. In Figure 1.3 is labelled in red the area in which no flight should be allowed: according to the CAA (UK Civil Aviation Authority), the threshold of 2 mg_{ash}/m^3_{air} is the limit above which no flight for any reasons is allowed.

Besides natural causes, an important source of contaminant is related to man-related activities. This particulate is generally related to the combustion occurrences, such as transportation, plumes, domestic heating, and has an highly variable seasonal trend. Specifically, winter has typically higher concentrations of man-made particulate. Furthermore, contaminants are very different in material, shape, dimension and source. In Lü et al. (2012) there are detailed SEM pictures that report the shape of typical aerosols dispersed in the Shanghai urban summer atmosphere, showing very different shapes. On the top of that, a detailed chemical analysis of the contaminants is reported. The results, focused on the Shanghai urban area, shows the particle size distribution is dominated by a fine particle (from 0.1 μ m to 2.5 μ m) constituted by soot aggregates and fly ashes. The size-segregated distribution is reported in Fig. 1.4.

Localized sources can have an high impact on the local distribution of particle dispersed in the air. In the same fashion as volcanic ash may represent a very high concentrated area the is superimposed to the local distribution, plumes or industrial emissions in general can

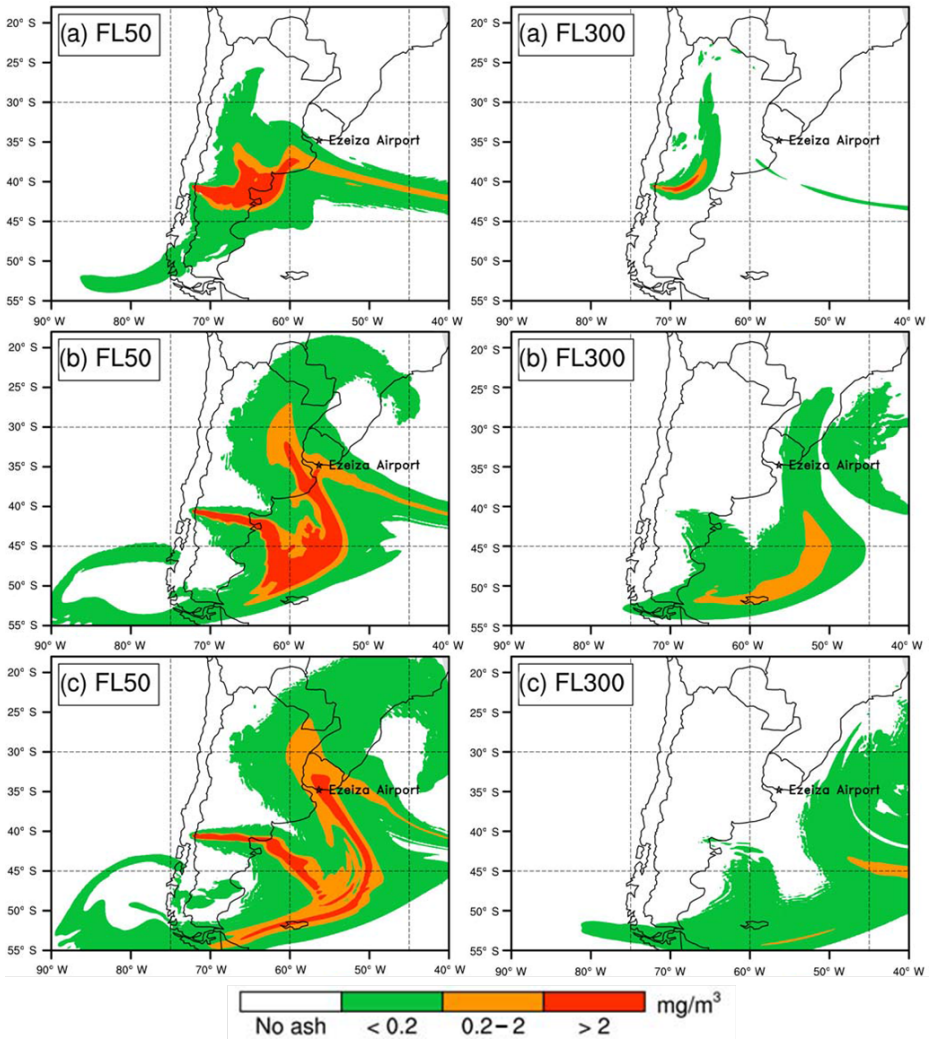

Figure 1.3: NMMB-MONARCH-ASH flight level ash concentrations (mass loading; mgm^{-3}) for the 2011 Caulle eruption before and after closure of the Buenos Aires (Ezeiza) airport and air space. Results for FL50 (left panels) and FL300 (right panels) for (a) 6 June at 11:00 UTC, (b) 7 June at 04:00UTC, and (c) 7 June at 12:00 UTC. Safe ash concentration thresholds are shown (red contours illustrate "no flying" zones). From Marti et al. (2017)

perturb the background concentration of particulate. Taiwo et al. (2014) Have studied the variation in the particle mass average concentration as a consequence of the presence of industrial activities. The study takes into account two neighbouring areas including the effect of the wind to consider the downwind dispersion of the particulate. Figure 1.5 show the increase in all the investigated particle size due to the presence of the plants.

1.1.2 Fuel Contamination

Energy and climate change policies associated with the continuous increase in natural gas costs pushed governments to invest in renewable energy and alternative fuels. In this perspective, the idea to convert gas turbines from natural gas to syngas from biomass

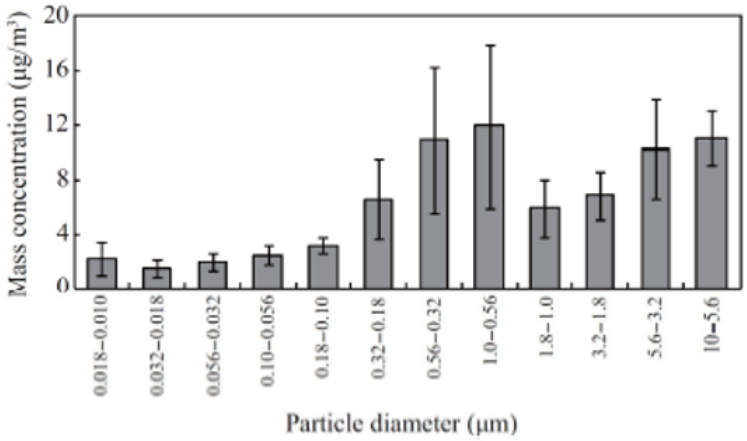

Figure 1.4: Mass concentrations of size-segregated particles collected in the Shanghai atmosphere. From Lü et al. (2012)

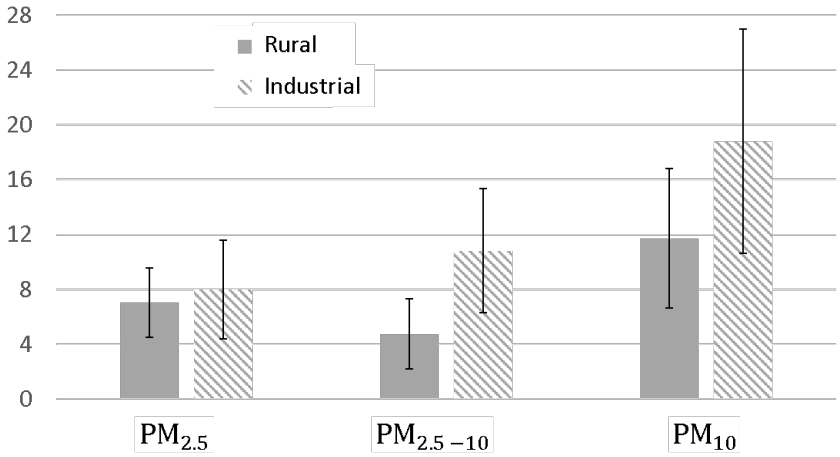

Figure 1.5: Average mass concentration in $\mu g m^{-3}$ in two sites to show the effect of the industrial activity. The error bars represent the standard deviation. From Taiwo et al. (2014)

gasification could be a suitable choice (Morini and Venturini 2012).

Biogas is a valid alternative to natural gas because of its low costs, high availability and low environmental impact. Biofuel is produced with the anaerobic digestion of plant and animal wastes and then burnt in gas turbine combustor. Although synfuels are cleaned and filtered before entering the turbine combustor, impurities are not completely removed. Therefore, the high temperature reached in the turbine nozzle can lead to the deposition of contaminants onto internal surfaces. In 1.1 the Lower Heating Value (LHV) of the synfuels and the fly-ash characterization are listed. The ash content is the part of the volatile matter of the fuel that does not contribute to the combustion. At the same time, the ash content represents the major contribution to the fouling issue. The chosen fuels are wood poplar, cow manure, rice hulls, and tropical hardwood. In particular, the fuel ash content, its chemical composition, and its relative softening temperature are reported. The chemical composition is referred to the weight fraction of silicon dioxide

SiO_2, aluminum trioxide Al_2O_3, iron trioxide Fe_2O_3, calcium oxide CaO, magnesium oxide MgO, sodium oxide Na_2O and potassium oxide K_2O. These data are obtained from the Phyllis 2 database ECN. The composition refers to the ash generated by the combustion of the related fuel and is referred to the dry condition. These oxides do not cover the entire composition for each fuel, but these individual oxides are thought to be most important in characterizing their physical behavior.

It is well known in the literature that the filtering efficiency in IGCC (Integrated Gasification Combined Cycles) allows for some fouling in the hot stages Holt and Alpert (2001). Therefore, the data from Tab. 1.1 are of paramount importance in order to gather information on the nature of the particulate that is actually injected into the turbine. The amount of particles effectively blocked by the filter is closely dependent on the technology of filter employed. Further details regarding the concentration of particles actually injected are reported in the next sections.

Table 1.1: Lower heating values (LHV) of the fuels and fly-ash material characterization (material composition in terms of weight fraction, ash content refers to dry conditions).

	LHV	Tsoft	Ash	Oxides (wt%)							
	[kJ/kg]	[K]	[%]	Na_2O	K_2O	CaO	MgO	SiO_2	Al_2O_3	TiO_2	Fe_2O_3
Wood Poplar	18190	1565	1.22	10	24.2	47.3	11.6	9.2	3.3	-	0
Cow Manure	16930	1516	8.89	5.9	9.4	32.1	9.8	19.8	1.51	-	0.9
Rice Hulls	12270	1673	23.4	0.1	1.2	0.2	0.2	95.6	2	-	0.1
Tropical Hard Wood	17250	1953	11.5	0.6	33.6	0.4	5.2	1.6	0.8	-	0.4

1.2 Land Based Gas turbines

Gas turbines operate by processing a very high amount of air, of the order of millions of cubic meters per hour. Considering a concentration of particulate of 10 $\mu g_{part}/m^3$, it is easy to derive that particles are ingested at a rate of tens of kilograms per hour. This load of particulate justifies the employment of filtering systems that are placed with the aim of cleaning the air processed by the machine. The selection of the proper intake filtration system is a complicate process that should account both for the characteristics of the environment in which the machine works, and the increase pressure drop compared to the increasing in filter efficiency, as reported by Wilcox et al. (2011). Such systems are responsible for cleaning as much as possible the air ingested by the machine.

1.2.1 Intake Filters

Without filters particles having a range from 0 up to more than 1000 μm, depending on the location, could easily reach the inlet of the compressor and could impact against

aerodynamic surfaces. The consequences of such impacts depends on the particle size, with larger particles that tend to cause erosion of the aerodynamic surfaces and the smaller ones that have higer probability to stick causing deposition. Both the phenomena will be treated in detail in the next sections. In order to avoid such issues to occur, the air-cleaning systems are typically composed composed of several stages, in what is commonly described as Staged Filtration (see Wilcox et al. (2011)): no universal filter exists that is able to remove the entire particulate matter from the air. The first stage is always a "prefilter", to remove erosive particles, rain, and snow and generally all the particles that are bigger than 10 μm. Such filter is generally an inertial separator. The second stage is usually represented by a low to medium-performance filter (effective for on finer-sized particles) or a coalescer to remove liquids. The third stage is often an high-performance filter able to remove the smallest particles. The exact sequence and the layout of the filter is highly influenced by the site conditions.

The filter technologies that are commonly employed for intakes of power generation power plants are summarized in Fig. 1.6. Sieving aims to block particles by reducing the space between the filter fibers making it smaller to particle diameter. Particles is therefore stuck between two fibers, as reported in Fig. 1.6a). Larger particles have a higher tendency to deflect from flow stream due to their inertia, making them to impact against the filter fiber Fig. 1.6d). Figure 1.6c) is relative to the diffusion mechanism, effective for the smallest particles typically less than 0.5 μm in size, exploiting the turbulent fluctuations. Smaller particles follow such fluctuations away from the main stream. This can lead to impact with the fibers and particles are captured. The last mechanism typically exploited is interception, that consists in following the flow until they touch a fiber in the filter media and be trapped and held, see Fig. 1.6c). This is likely to occur for medium sized particles that are too small to deflect from the streamline thanks to inertia but too large to diffuse.

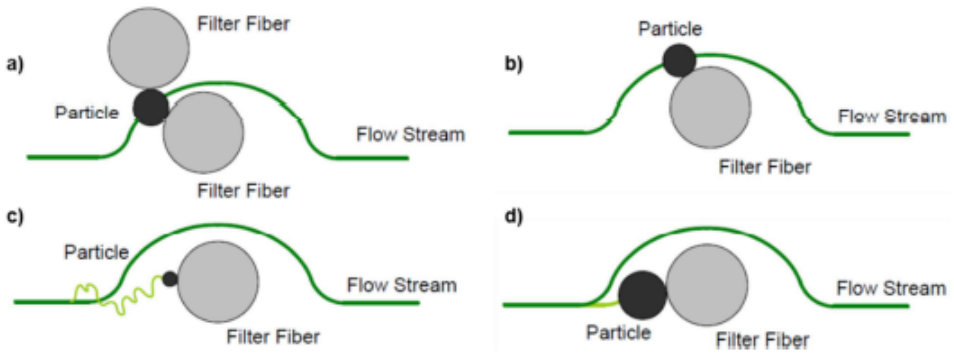

Figure 1.6: Filtration mechanism: a) sieving, b) interception, c) diffusion, d) inertial impaction. From Wilcox et al. (2011)

The last mechanism, not reported in Fig. 1.6 is related to the electrostatic charge. The mechanism is based on the attraction of particles to a charged filter. Filters always lose their electrostatic charge over time because particles are captured on their surface

occupy charged sites neutralizing their charge.

Filtration mechanisms, as suggested above, are always employed together to have the most effective cleaning as possible. The outcome of such procedure is commonly referred to as filtration efficiency, η_f. Such parameter is defined as the ratio between captured particle mass with respect to the entering particle mass. Different filters have different filtering efficiency whit respect to the particle size. This remark is reported quantitatively in Fig. 1.7, where the superposition of the effects is carried out to evaluate the total efficiency of the stages. It can be noticed that the total efficiency of the stages is high above 1 μm and below 0.01. In between there is a range of diameter in which a considerable amount of particulate can easily make its way through the filters and reach the inlet of the machine. Unfortunately, as it will be better explained in the following, such range of particles is the one that is most likely to cause fouling.

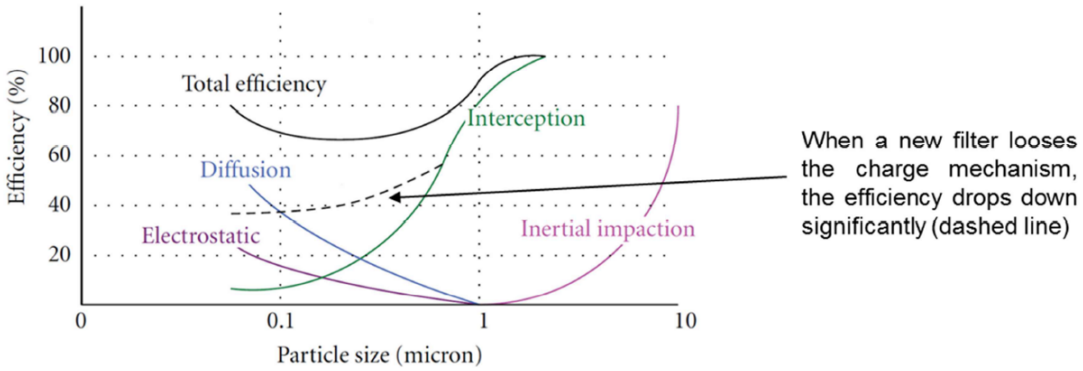

Figure 1.7: Combination of filtration mechanism to obtain filter efficiency at various particle sizes. From Wilcox et al. (2011)

1.2.2 Syngas Filters

In the previous paragraphs, the mechanisms at the basis of the air filtration have been presented. In the analysis carried out, no effect of the temperature has been accounted for. Nonetheless, each of the filter that has been realized for implementing the technologies described in Fig. 1.6 has a different behaviour at high temperature. High temperature filtration is required in case of syngas-powered machines, to avoid the ash that is inevitably produced with the syngas to reach the combustor section.

The filters that are commonly employed in this piece of syngas-cleaning apparatus are cyclones, candle filters, granular bed filters or electrostatic precipitators. As suggested by Villot et al. (2012), cyclones are effective only with particles that are bigger than 5 μm. At high temperatures the viscosity of the gas increases and therefore inertial separation effect is reduced, causing loss of efficiency. The cons of this technology are related to the ineffectiveness with smaller sizes: in the biomass gasification field, cyclones are usually

coupled with ceramic candle filters de Jong et al. (2003) or sintered metals filters Hofmann et al. (2008) to increase their efficiency with smaller particles.

Candle filters are arrays of ceramic, candle-shaped elements, with good filtration efficiency, near 100% for temperatures up to 800°C de Jong et al. (2003); Hofmann et al. (2008). The drawback of this technology is its fragility. A typical approach for filter cleaning is the counter-current of clean gas: hot gas must be used to avoid cracks due to thermal shocks. Cracks can also appear as a consequences of explosions inside candles due to the simultaneous presence of dust and flammable gas (Sharma et al. 2008). Lastly, residual particle deposit forms on the filter surface and leads to irreversible fouling, as reported by Hofmann et al. (2008). To increase the reliability of such filters, metal filters have started to be used. The alloy used in the candles can be operated at temperatures up to 1000°C, even if temperatures commonly seen in biomass plants are below 700°C (Sharma et al. 2008). The problem of filter fouling still remains, but deposit can be completely removed by a backwash filter with sulfuric acid, as reported in Ghidossi et al. (2009).

Granular bed filters is another option that is usually employed as an alternative to candle filters: they can be easily adapted for high temperature and pressure, by choosing the proper type of grain (Villot et al. 2012). Generally, the granular materials that allows the operation at high temperature are made of ceramic such as alumina or mullite. Regarding on the filtration efficiency of these devices, an expected value of 99% is reported for diameters greater than 4 μm and 93% for smaller particles (Sharma et al. 2008).

Electrostatic precipitators (ESP) are composed of two electrodes electrically charged. Particles present in the gas are charged and tend to drift toward the earthed electrode where they are neutralized Nair et al. (2003). Particles are collected by a rapping system of the collecting electrode. Few data are available in the literature regarding the use of this kind of filter to clean gases at high temperature and pressure. Recently, tests have been conducted on tar removal present in the syngas at high temperatures (up to 500°C), see for example Nair et al. (2003); Tamon et al. (1998). Pulsed corona discharges tests have shown a removal of about the 60% of the total tar contained in syngas. Besides, ESP converts heavy tars into lighter tars. High temperature and pressure operating ESP have been tested by Rinard et al. (1987); Tassicker (1986): temperatures up to 1000°C and pressures up to 3.5 MPa have been reached. Temperature increases reduce the efficiency of the ESP, whereas pressure increase has positive effect on its efficiency. The overall efficiency is between 95 and 100% for the smallest particles. An interesting feature is that the pressure drop across the filter is constant as the operating time increase, since there is no clogging of the apparatus.

1.2.3 Deterioration in land based gas turbines

As reported in section 1.2.1 and 1.2.2, the installation of filtering systems does not prevent a considerable share of the particles carried by the air or the fuel to enter the gas turbines.

A particle laden airflow has an higher tendency to cause compressor fouling, as suggested by Suman et al. (2017). A fouled axial compressor has deteriorated aerodynamic qualities, which causes the decrease in the air mass flow, in the efficiency and in the surge margin. A reduced mass flow through the turbine, as a consequence of the reduced mass flow processed by the compressor, entails a reduced pressure ratio of the compressor itself. All in all, an increase in the heat rate and a reduction of the specific output are the major drawbacks of compressor fouling.

As reported by Nicholson (1990) and Schurovsky and Levikin (1986) the axial compressor fouling increases during the first 1,000 operation hours. During this period of time, the gas turbine unit output and efficiency losses decrease exponentially and they will tend to stabilize after 1,000 - 2,000 operation hours. Several are the degradation mechanisms that affect compressor operation: Diakunchak (1992) listed the engine, and particularly the compressor, deterioration according to these different categories:

- permanent performance degradation, which is not recoverable after overhaul and the refurbishment of all clearances, replacement of damaged parts;
- performance degradation non-recoverable with cleaning/washing operations, but recoverable after overhaul;
- performance degradation recoverable with cleaning/washing operations.

All gas turbine experience performance losses over time caused by many different factors such as erosion of blade surfaces due to particle ingestion, fouling due to airborne pollution or oil vapors, blocking of cooling holes and labyrinth seals, and foreign object damage. From the list above, deterioration is generally referred to as either recoverable by routine maintenance actions or non-recoverable except by replacement of degraded engine components.

The mechanisms that concur in degrading the performances of compressors and, more generally, of gas turbines can be grouped in corrosion, erosion and fouling. Corrosion and erosion tend to be classified as non-recoverable with cleaning/washing operations while fouling is usually recoverable after on-line or off-line washing. From the work of Diakunchak (1992), unrecoverable deterioration is usually less than 1%, increasing if heavy fuels or synfuels are employed., as reported in Fig. 1.8.

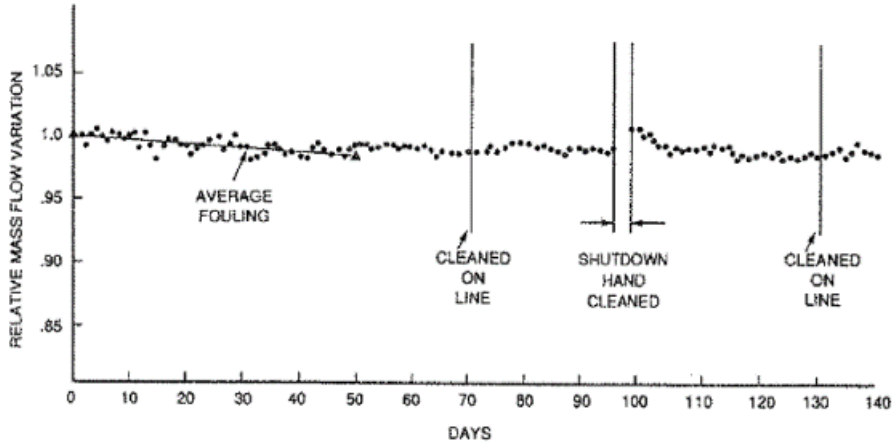

Figure 1.8: Relative mass flow variation with time. From Diakunchak (1992)

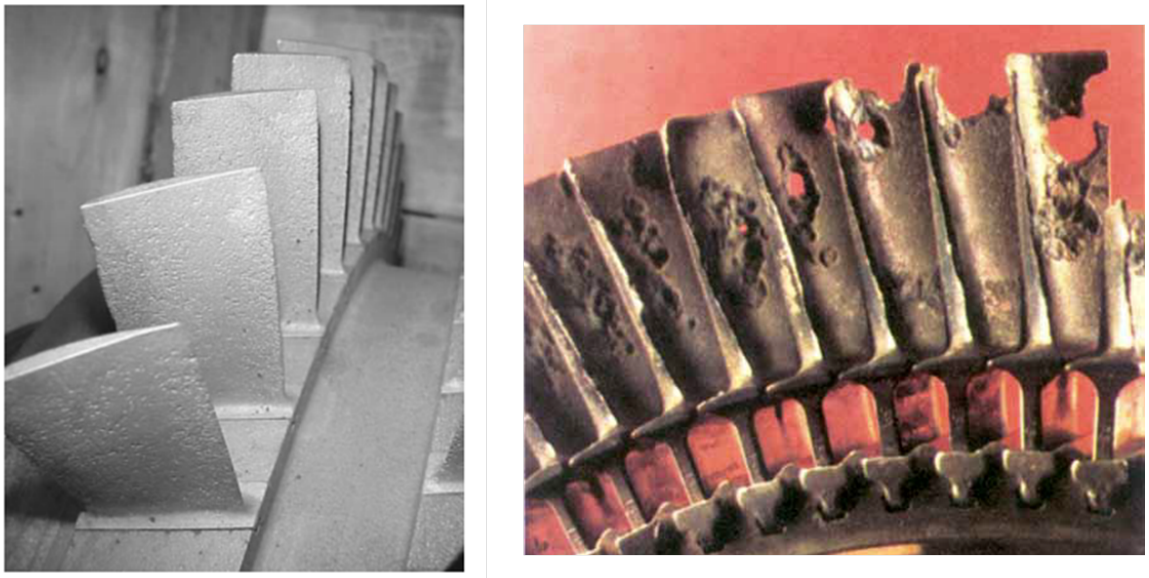

Figure 1.9: Cold-corrosion pitting on 403 Stainless Stell rotor blades (left, from Linden et al. 2001) And hot corrosion on turbine blades (right, from Wing and McGill 1981)

Corrosion

This work considers both the effects of erosion and deposition, but does not take into account corrosion. This phenomenon, that will be briefly described here, is defined as the loss of material from the surfaces of the flow path due to chemical reactions related to aggressive deposits (e.g. salts, mineral acids or reactive gases). It is commonly divided in "cold corrosion", if it takes place in the compressor, and is due to wet deposits of salts, acid and aggressive gases such as chlorine and sulfides. Hot corrosion is related to the hot section, thus if the components affected belong to the combustor or the turbine. It is known to be due to the presence of salts (e.g. sodium and potassium), mineral acids or reactive gases (e.g. hydrogen sulfide or sulfur oxides).

Due to the importance of the issue, several strategies for tackling the problem have

been developed over the years. Specifically, cold corrosion could be eliminated by coating the compressor airfoil. Hot corrosion requires the interaction of the metal surface with another chemical substance at elevated temperatures. To avoid such problem, nickel-based coatings are employed (Sidhu et al. 2006).

Erosion

As suggested by Grant and Tabakoff (1975); Hamed et al. (2006), erosion, defined as the abrasive removal of blade material by hard particles, is believed to be caused by particle than greater than 10 μm in diameter. These particles will rebound on the surface, removing a part of the substrate. Even if the amount of material removed per impact is very small, high particle loads and long operating hours, as turbomachinery usually present, eventually leads to changes in the geometry of the blade. This change in geometry causes deviations in the air flow path (changes in the inlet metal angle) and roughening of smooth surfaces. The problem usually manifests as pitting and cutting back of the leading edges and thinning of the trailing edges, see Fig. 1.10. This last aspect is particularly detrimental since it may result in blade failure even if this damage may be beneficial to performance (Diakunchak 1992). Besides, erosion has different effects on blades and vanes. Typically, eroded rotor blades have reduced solidity at the tip and vanes are affected the most near the root. Particularly in the rotor case, the erosive particles are centrifuged to the outer diameter of the compressor, increasing radial tip clearances or sealing gaps and results in higher leakage flows.

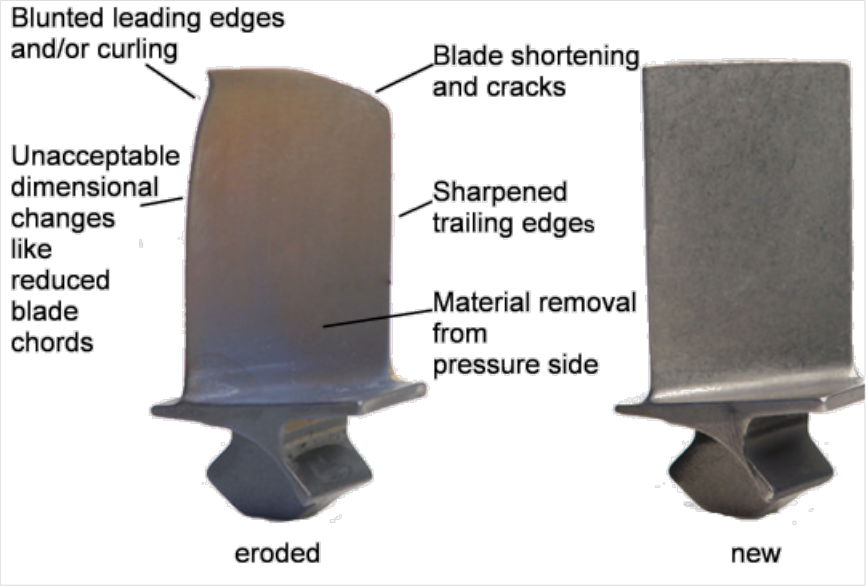

Figure 1.10: Comparison of eroded and new compressor blade. From Heutling et al. (2009)

The erosion problem in compressor has been studied numerically as well, for example Ghenaiet (2012) studied sand erosion issues on the first compression stage of a turbofan,

showing how different particle sizes have different impact location and stories in the machine. First numerical analyses of erosion problems are dated back to 1975, when Grant and Tabakoff (1975) presented a computational study using Monte Carlo methods on compressor vanes and blades, and validating data with experiments.

A review of the effects of the erosion and the consequent surface roughness has been pointed out by Bons (2010). He found interesting correlations between the roughness levels and the losses at different Reynolds number: at low Re, roughness can eliminate laminar separation bubbles (thus reducing loss) while at high Re (when the boundary layer is already turbulent), roughness can thicken the boundary layer to the point of separation (thus increasing loss). In the turbine, roughness has the added effect of augmenting convective heat transfer. While this is desirable in an internal turbine coolant channel, it is clearly undesirable on the external turbine surface.

As suggested above, cold erosion is not a primary issue in land based gas turbine, since filters can block the biggest particles preventing major erosion on the compressor side. Also in the hot section, the filtering systems described in 1.2.2 are able to block the vast majorities of the contaminants. The erosion issues related to land based gas turbines are mostly related to the power augmentation techniques by evaporative and overspray fogging. These power boost techniques can be of help in reducing the heat rate of the group and can give a power increase of up to 15 % depending on the environmental temperature (Chaker et al. 2001). The injection of water droplet is therefore a commonly employed technique, especially when the external temperature is high and thus the power output derating is non negligible.

The parameter that is of concern the most in this case is the droplet size. According to Bhargava et al. (2007), small differences in the size of droplets has major implications. The authors proposed two different scenario, considering droplets diameters of 20 and 30 μm, respectively. The larger particle size (30 microns) size droplets will have 3 to 4 times the mass and force of impact (and thus higher erosion potential). Besides, larger particles have 33% lower surface area/unit volume, lowering evaporation efficiency, a two times faster fall rate (higher water drain amount).

Fouling

Land based gas turbines are affected the most by compressor fouling, as reported in Fig. 1.11. Zaba (1980) analyzed the performance variation over time, showing the decrease in output power and efficiency. From Fig. 1.11 it can be distinguished recoverable fouling from not recoverable deterioration. It can be seen that, even after the washing events (for example points 3 to 4), the initial values of efficiency and power output are not achieved. The missing part is the non-recoverable erosion/corrosion that keeps increasing over time.

Nonetheless, it can be seen that the greatest share of the performance losses is due to fouling, that works up to ten times faster than the non-recoverable damage.

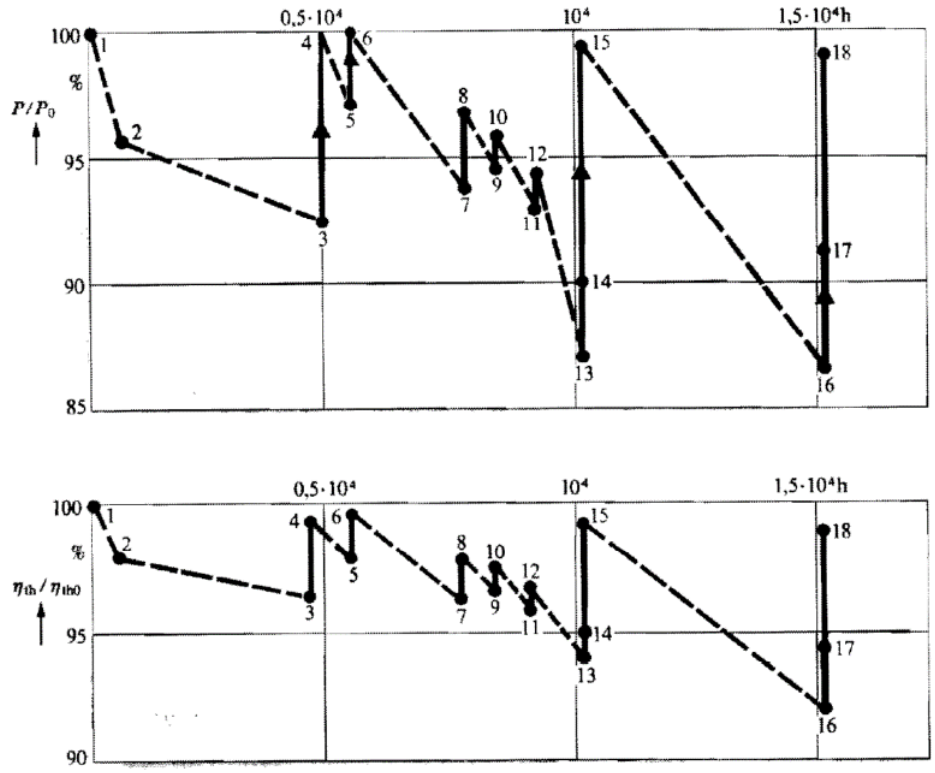

Figure 1.11: Variations in output and thermal efficiency as functions of lime when compressor is fouled, and recovery obtained by cleaning. From Zaba (1980)

Fouling consists of deposit and buildup of material on the flow path surface, as reported in Fig. 1.12 . Such deposits are likely to change the shape of airfoil, the airfoil inlet angle, increase surface roughness. This results in a reduction in compressor performance, in terms of reduced compressor discharge pressure, reduced compressor efficiency, increased compressor discharge temperature, reduced power output, increase of heat rate of the machine, slowing of shaft speed in multi-spool engines and onset of compressor stall or surge. Among the others, the variation of roughness especially in the leading edge area has a major impact on the surface performance.

Bammert and Woelk (1980) report that the rough blading causes shifting of the operating points to smaller suction volumes and narrowing of the characteristic field from the throttling line and rotating stall line. Interesting results on the effects of an increased roughness (and increased thickness) on the performance map of the blade can be retrieved from the work of Suder et al. (1995), and reported in Fig. 1.13. A rough coating has been applied in precise locations on the blade to understand the areas that are more sensitive to such issue. It can be seen that roughness increase on the suction side and on trailing edge is more detrimental with respect to the increased roughness on the pressure side. The entire coverage with rough coating is the worst in terms of performance degradation. The NASA rotor 37 have been used as a test case, comparing their own numerical simulations

Figure 1.12: Salt deposits on compressor blades, 18,000 hrs of operation. View on suction side. Fewer deposits near leading edge and in the hub region. From Kurz and Brun (2012)

with experimental results.

Similar results have been obtained by Gbadebo et al. (2004), by placing emery paper in precise locations on the blade as reported in Fig. 1.14 a-d. The roughness results in loss of total pressure, especially in the hub-corner region with a marked increase in the size of the separated region. Surface and flow visualization shows separation on the suction surface/hub corner for the baseline blade and for the roughened blade, 1.14. With roughness over the leading edge to peak-suction region, a larger 3D separation on the suction surface and hubwall arises. The separated region is likely to be the cause of the extra loss and deviation when compared with smooth blades.

When passing to the entire machine instead of a single cascade, the performance map variation can be seen in Fig. 1.15. Morini et al. (2010) reported the variation of compressor maps due to deterioration by using a stage-by-stage model. As can be noticed, fouling causes a shift of the pressure ratio curve toward a lower corrected mass flow rate value. The results of Morini et al. (2010) are confirmed by Diakunchak (1992), stating that typically about 70% to 85% of all gas turbine engine performance loss accumulated during operation can be related to compressor fouling.

The whole compressor analysis from the fouling standpoint reveals that not all the stages are subjected to the same amount of deposit. For example, Tarabrin et al. (1998) reports a 16 stages Nuovo Pignone MS5322 R(B) axial compressor operated for a long time without washing. Only the first 5 to 6 stages are subjected to fouling. Besides, blades report less deposit than vanes, probably due to the detachment effect related to the centrifugal forces.

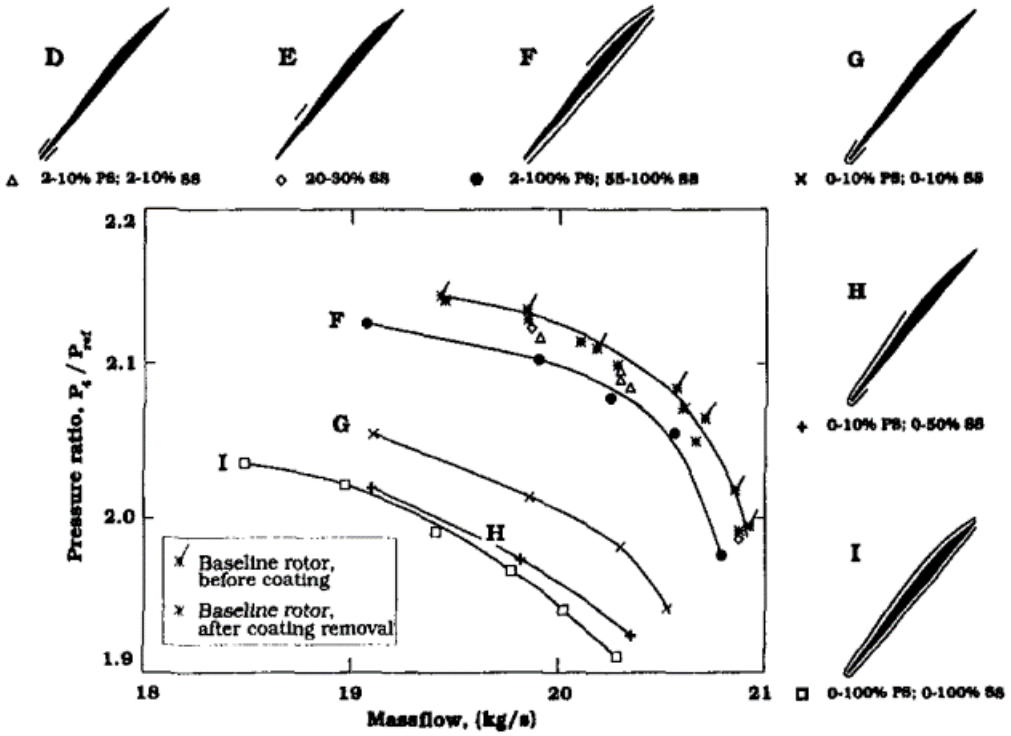

Figure 1.13: Pressure rise characteristics for the rough coatings at design speed. From Suder et al. (1995)

Few numerical investigations of single blades as well as multistage deposition issues have been reported in the literature. A numerical investigation of a single compressor blade has been performed by Suman et al. (2015), considering fouling on a transonic blade. More recently, the numerical simulation of an entire subsonic compressor has been performed by Aldi et al. (2018). In the same paper, the effect of the humidity on the sticking model employed is shown, as well as the effect on the tangential velocity. By considering these two effects, the numerical results show a good agreement with the experimental results available in the literature (Tarabrin et al. 1998). What numerical simulations have not been able to properly model yet is the relation between the amount of material stuck in a certain location and the performance of the machine itself. In other words, what is actually missing is a clear relation between deposit-induced local variations and their effect on the flow field.

As above mentioned, fouling is considered a recoverable degradation mechanism. Common procedure for recovering from fouling events is the washing of the compressor (e.g. Igie 2017; Suman 2015). Typically, water washing of the compressor can be conducted either online (while gas turbine is in operation) or offline. The first method is realized by injecting the cleaning solution into the compressor section while the engine is running in normal operation. In offline washing, the cleaning solution is injected after the machine is shut down and cooled, and it is running at sub-idle shaft speed. The advantage of the first method over the last is the absence of down-time periods. A review of the different method and cleaning solution is proposed by Mund and Pilidis (2006), showing how case

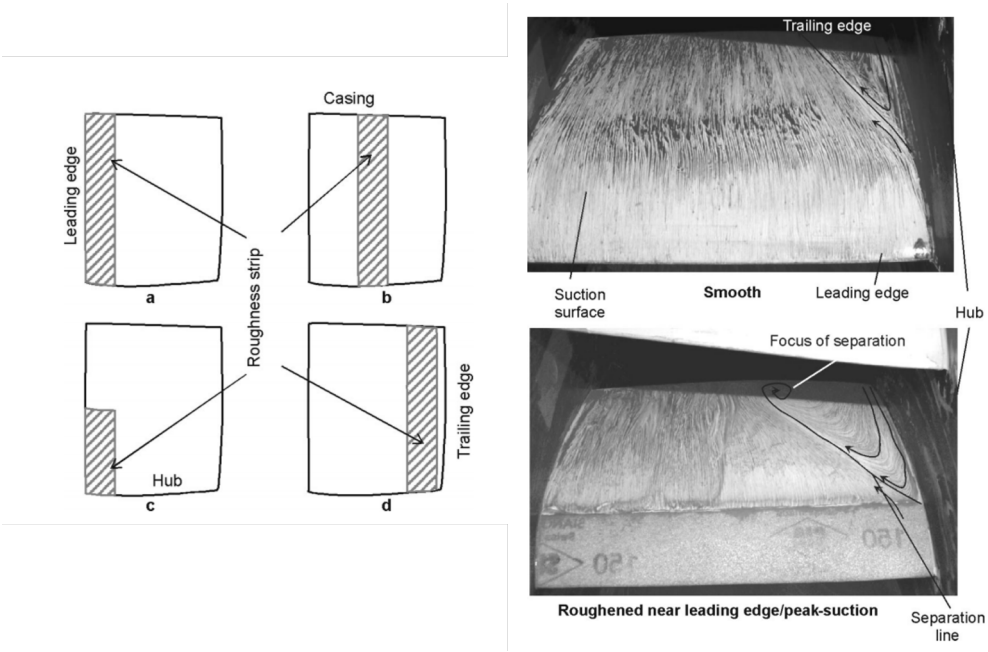

Figure 1.14: Schematic diagram of stator blade with roughness a) full strip (leading edge to peak-suction); b) full strip (midchord); c) 50% span from hub (leading edge to peak-suction); d) full strip (near trailing edge) and Suction surface flow visualization on smooth and roughened stator around leading edge/peak-suction at design point, Φ=0.51. From Gbadebo et al. (2004)

specific is the best set-up of the cleaning procedure. It must be remarked that the recover from fouling thanks to washing is very effective, as reported in Fig. 1.11: after offline washing the power output recover can be as high as the 10 %.

Numerical simulation of washing have been performed as well. For example, Mustafa et al. (2006) investigated water droplet (50 μm to 300 μm) flow pattern during on-line washing of an axial compressor. The range of droplet sizes used in their simulations is representative of the droplet dimensions used during online washing. The authors stress the importance of injecting a range of droplet size: the first few stages of an axial compressor, more prone to fouling than the last stages, should receive lower sized particles (to have less erosion issues), while bigger droplets, which are less likely to evaporate, should reach the back stages to perform cleaning of this area.

Hot section fouling effects in land based gas turbines are similar to the aero-engine applications. The reader is therefore referred to the section 1.3 for further details on this issue.

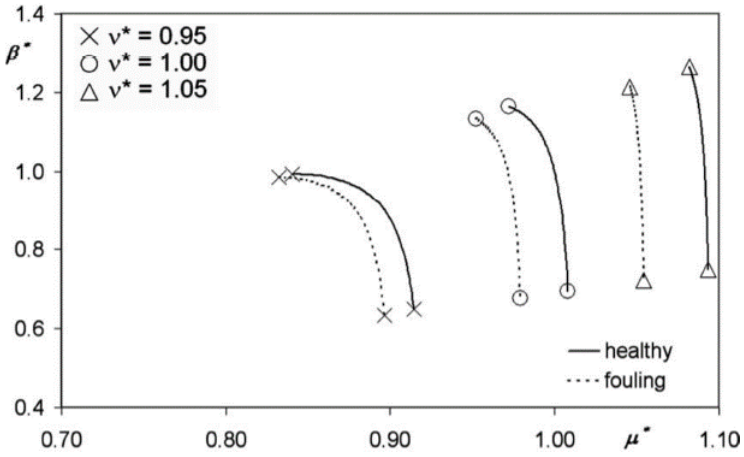

Figure 1.15: Effect of gradual fouling on all the stages: non-dimensional pressure ratio vs corrected mass flow rate. From Morini et al. (2010)

1.3 Aero-Engines

Aircraft following normal commercial routes and flight plans can fly through dust clouds for intervals of time ranging from few seconds to several minutes, as reported by Clarkson et al. (2016). During this time a large amount of particulate is ingested by the engines. Ash clouds can carry particulate with concentrations as high as 250 mg_{ash}/m^3_{air}. For a high thrust turbofan engine processing a mass flow rate of approximately 500 kg/s, the resulting rate of ingestion of solid contaminant can reach the order of 1 kg_{ash}/s. The presence of particles at cruising altitude or during take-off therefore poses a serious threat to the operation of aircraft engines. The seriousness of this threat is highlighted by the disruption brought to air travel by volcanic events in recent years Dunn (2012): Table 1.2 reports some of the most dramatic events of the last 40 years.

1.3.1 Degradation in aero-engines

The ingestion of particles inevitably brings about losses. Even if the size of the ingested particulate is such that the particles follow the streamlines and do not impinge against the blades, a certain amount of energy is lost due to the particles transport.

Both cold and hot section are affected by deposition. In this case, no filtering system is placed in front of the intake, and therefore the rate at which particle are ingested is higher than the land-based gas-turbines. On the other hand, the concentration of particulate, unless encounter with clouds, is typically lower at cruising altitude with respect to the ground. Another important fact to be accounted for is that most of the operating aircraft are powered by turbofan or turboprop engines. In these two cases, part of the air does not actually enter the core engine, but it contributes to the trust since it is processed by

Table 1.2: Notable Volcanic Ash/Aircraft Encounters. From Dunn (2012)

Year	Aircraft	Engine	Volcano
1980	Trans-America Lockheed L-382	Allison T56	Mt. St. Helens
1982	British Airways Boeing 747-200	R-R RB-211	Mt. Galgunggung
1982	Singapore Airlines Boeing 747-200	P/W JT9-D	Mt. Galgunggung
1985	Qantas Boeing 747-200	R-R RB-211	Mt. Soputan
1989	KLM Boeing 747-400	GE CF-6	Mt. Redoubt
1991	15 Separate encounters in two-week period	RB-211, CF-6, JT9-D	Mt. Pinatubo
2010	Airspace Closed	—	Eyjafjallajkull (ay-yah-fyah-lah-yer-kuhl)

the prop or by the fan. Therefore only a share of the particles that are dispersed in the captured streamtube are actually ingested into the core engine. Besides, the fan or the prop have a centrifugal effect on the particles, centrifuging the bigger ones towards the by-pass flow. The population of particles actually ingested is therefore different from the one that is present in front of the intake of the engine.

In this section particular focus will be put on the effects of particle ingestion on the hot part of the gas turbine, especially on the HPT. The effects on the compressor part are similar to what already reported for land-based machinery, with the difference that erosive particles can easily enter the intake, since no filter is placed.

Flights through volcanic ash are known to cause both erosion on the cold section and deposit on the hot section engine. For example, the encounter of the BA009 - Boeing 747 200 with the Mt. Galgunggung eruption in 1982 causes initially power loss from all four engines, while engine was flying at 37000 ft. Three engine out of four have been successfully restored when the ash cloud was left, around 12000 ft. As the engine restarted, the flight tried to climb again, but re-entered the cloud.

The inspection of the engine after the successful landing, has shown erosion of the compressor and deposition on the HPT, as reported in Fig. 1.16. It can be seen that deposition on the HPT is the most detrimental issue, leading to a reduction of the NPT throat of the 10 %. This evidence is in agreement with the analysis proposed by Dunn (2012) and summarized in Fig. 1.17. According to such analysis, conducted by injecting

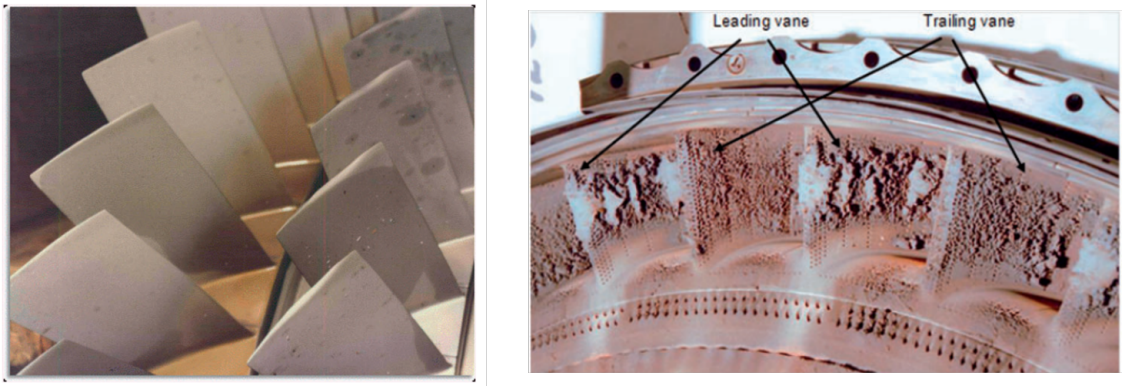

Figure 1.16: Damage analysis from flight BA009: LP compressor stage 1 & 2 blades (left) and HP NGVs from engine that could not be restarted after second ash encounter(right). From Clarkson et al. (2016)

volcanic ash into operating engines, the relative importance of the individual mechanisms depends upon TET value. If the TET is above 1283 K (that basically includes all the current operating engines, Kyprianidis 2011), the main damage mechanism is deposition of ash on the hot section components, mostly on the high-pressure turbine vanes.

Hot deposition happens since the particles following the core flow are heated through the combustor. If the Turbine Entry Temperature (TET) is sufficiently high, particles soften and can adhere to the surrounding solid surfaces. In general, the deposition of particles can change the shape of the vane in an uncontrolled way. Particles sticking on the first stage nozzle of the high pressure turbine result in an increase in aerofoil thickness and roughness. The deposits can also clog cooling holes, if present, leading to the rise of the blade surface temperature. In the most severe cases, as pointed out by Ogiriki et al. (2015), this leads to a reduction in life due to thermal stresses, local overheating and creep. The increased boundary layer displacement thickness - due to the increased roughness and uncontrolled change in shape - and the build-up of the deposit can cause a reduction in passage area and hence in the turbine capacity. This, in turn, can push the compression system beyond its stability limit, making the risk of surge highly likely. The prediction of deposition and rate, and of the deposit shape in the passages of high-pressure turbines is therefore a pressing and important problem.

The shut-down risk is unacceptable for allowing scheduled commercial flight to take place in case of an excessive ash concentration in the air. This remark is at the basis of the safe-to-fly chart proposed by Rolls-Royce and reported in Fig. 1.18. The two lines represent the mass flow of ash through an engine core for each ash concentration in the atmosphere for two different flows (45 kg/s and 22.5 kg/s, representative of large to medium civil turbofans at cruise). The mass flow of ash (y-axis) is the concentration of ash in the environment (the x-axis) times by the ratio of mass flow of air through the engine's core to the density of air. Therefore, given the power and altitude, all the ash concentrations of interest are on a diagonal line (as the blue and green lines). The events in the top-right region of the chart are representative of failures reported in the past,

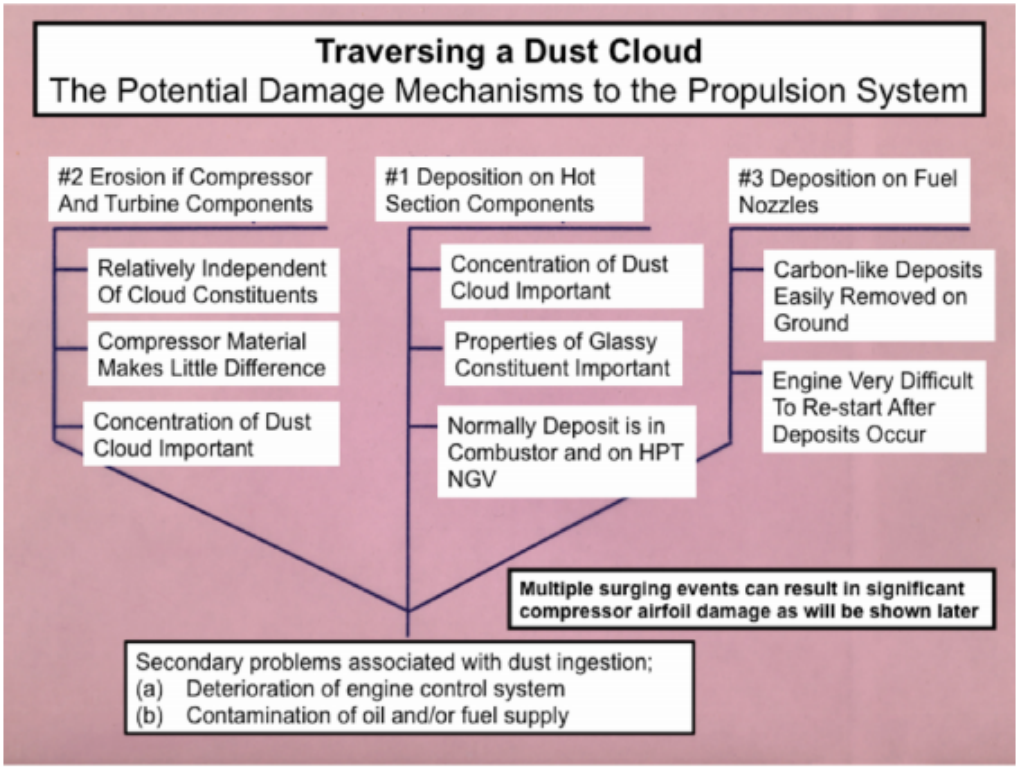

Figure 1.17: Potential damage mechanisms when traversing an ash cloud for an engine with TET in excess of $\sim$ 2310 ° R ($\sim$ 1283 K). From Dunn (2012)

either in test condition (Calspan tests, Dunn et al. 1994) or actually encounters (Tab. 1.2).

What is important to notice here is the different time scale of hot-section-deposition-related failure events, with respect to the loss of efficiency of the land-based units due to compressor fouling. The BA-009 event for example, reports a flight of about 7 minutes into the cloud, before loosing the 4 engines in a rapid succession. This remark should be considered when planning and designing numerical investigations of hot section deposition. The time scale of the performance variation is not completely "uncoupled" from the time scale of the particle deposition phenomenon.

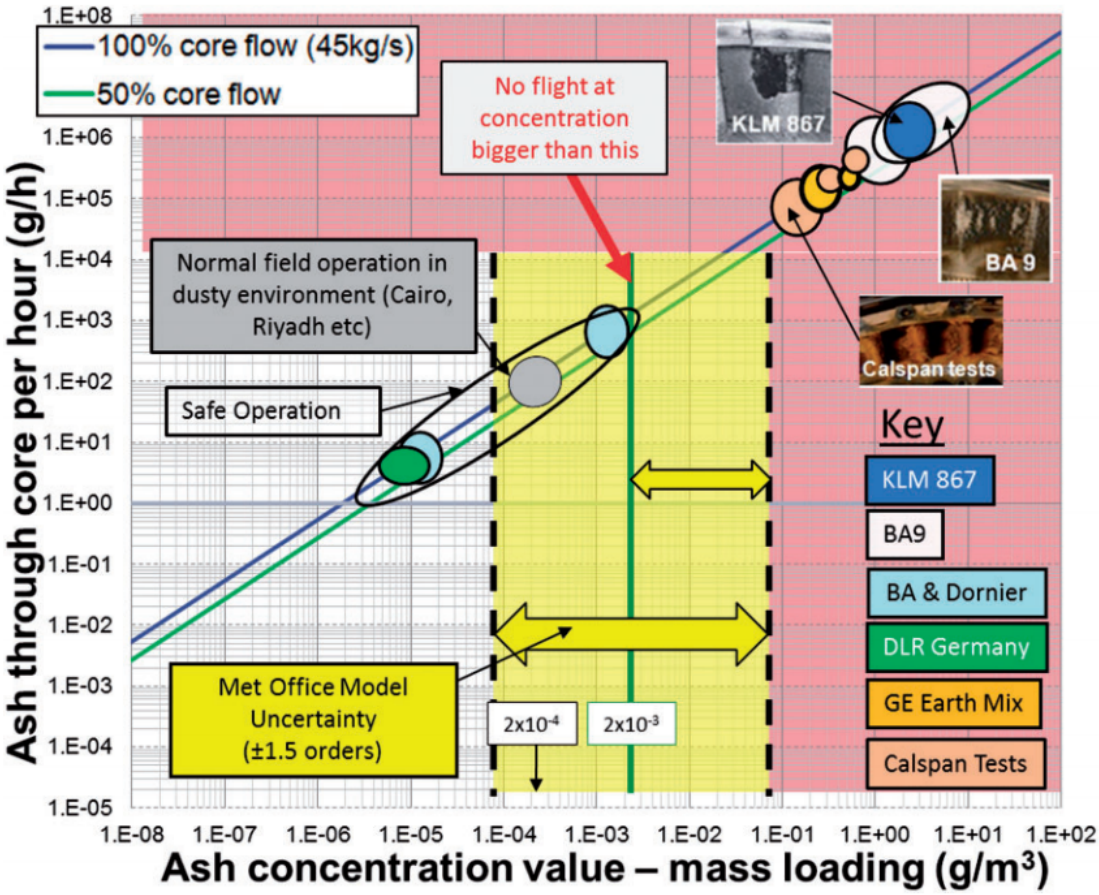

Figure 1.18: Safe-To-Fly Chart, Rolls-Royce. No flight should take place at the right of the green line (2 mg/m^3). Yellow-shaded area is the uncertainty level that affect current prediction models from MET Office. From Clarkson et al. (2016)

Chapter 2

Computational tools and numerical models

In this chapter the computational approaches that will be used in all the models will be described. Besides, the geometries employed in the different cases will be explained and experimental results for the flow field validation will be presented, where available.

2.1 Particle-laden fluids

Generally speaking, two different approaches can be used for the finite-volume based CFD simulation of multiphase flows and, specifically, particle laden flows. In both the cases, the carrier flow is solved by using a Eulerian approach and the difference regards the fashion the particulate is treated. It can be treated from a Eulerian or a Lagrangian standpoint.

The Eulerian-Eulerian approach treats both the gas and the particulate as a continuous. The motion governing equations are derived by considering a control volume fixed in the space and the contributions to the mass, momentum and energy conservation are evaluated for fluxes incoming and exiting from such volume, as described in Gidaspow (1994). This approach is particularly appreciated in terms of computational time and is often employed when highly concentrated flows are considered. Indeed the effects of the interactions (turbulence or particle-particle interactions) are easily accounted for. Nonetheless this method has not been employed in this work, since it is not suitable when detailed information regarding the impact parameters are required. Particularly, since the Eulerian approach requires an average over the cell volume the impact characteristic of the particles might be calculated erroneously. The contributions of incoming and rebounding particles can be considered at the same time, returning an velocity that is

actually wrong.

The Lagrangian formulation allows to calculate the path and motion of each particle. Indeed, the trajectory of the particle is a variable that is derived by solving its equation of motion. Particularly, a force balance is solved, and such forces are obtained from the separate resolution of the flow field, as explained in Ouellette et al. (2006), in terms of drag, lift, shear, diffusion, rotation and temperature gradient. This approach tends to be computational expensive as each of the particle must be tracked individually (even if the possibility of clustering is widely used to reduce the computational cost of this procedure, e.g. Corsini et al. 2014), requiring very high computational times for high particle loads. This approach is therefore largely used for diluted two-phase flows, where the particle-to-fluid volumetric ratio is small. It is particularly appreciated for the detailed physical description of the dispersed phase behaviour and especially when it comes to evaluate the particle-wall interaction.

The discrimination between dilute and dense suspension and between one-way and two-way coupling is related to the interaction the dispersed phase has with the turbulence. Referring to the work of Elghobashi (1991), the quantities that is of interest in such evaluation are here reported. The volumetric fraction of particles, $\Phi_p = N_p V_p / V$, where the subscript p label the particle-related properties, V is the volume (particle or particle and fluid) N is the number of particles; S is the distance between neighbouring particles and d is the particle diameter. Regarding the time scale involved in this problem, τ_p is the particle response time ($\tau = \rho\ d_p^2/18\ \mu_g$), τ_K is the Kolmogorov time scale and τ_e is the large eddy turnover time. The time scale dependency upon the volumetric fraction of particles is reported in Fig. 2.1.

Very low volumetric fractions ($\Phi < 10^{-6}$) identify the regime in which particles have a negligible effect on the turbulence, meaning the particle dispersion depends on the turbulent structures, but the *vice versa* does not hold. This regime is termed "one-way" coupling, meaning no effects of particles on turbulence are considered.

By increasing the volumetric loading ($10^{-6} < \Phi < 10^{-3}$), the turbulence is somehow affected by the presence of the particle and it is therefore called "two-way" coupling. An extra remark should be highlighted here: lowering τ_p (e.g. smaller diameter for the same particle material and fluid viscosity) increases the surface area of the particulate phase, and thus increases dissipation rate of turbulence energy. By increasing particles size, and therefore increasing particle Reynolds number $Re_p = (\mathbf{u} - \mathbf{u}_p) d_p / \nu$ to value greater than 400, vortex shedding behind particles takes place enhancing turbulence. The suspensions in these two regimes is usually referred as dilute. The third regime, with higher particle loading, is referred to as dense suspension, and the "four-way" coupling should be introduced: the particle-particle interaction should be considered as well (in addition to the former mechanisms).

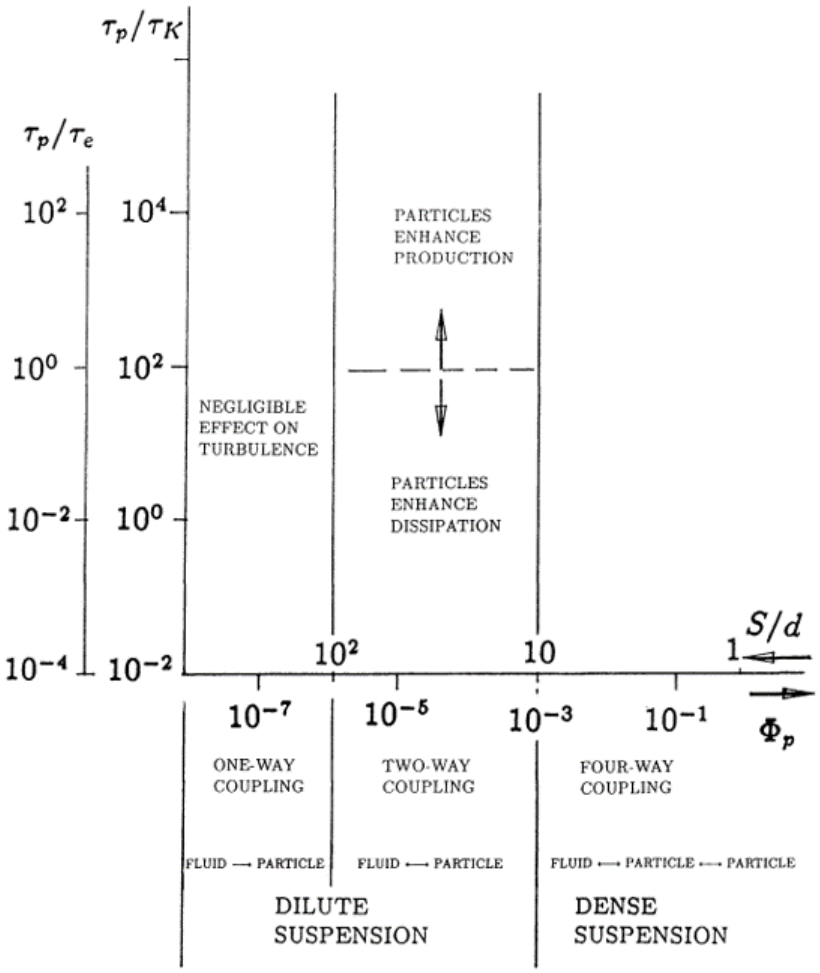

Figure 2.1: Map of flow regimes in particle-laden flows. From Elghobashi (1991)

Independently from the regime and the type of coupling, turbulent structures have a major effect on the particle trajectory. Notwithstanding, the common practice in turbulence modeling are RANS, that are known to model all the scales of the turbulence. Some techniques must therefore be included to account for the turbulent dispersion. More details on this feature will be provided in section 2.3

2.2 Lagrangian model

Throughout this work the Lagrangian, one-way model will be employed. Indeed, the volumetric concentration of the particles, even in the worst case scenario, is such that $\Phi \cong 10^{-7}$. Therefore, according to Fig. 2.1, the one-way coupling regime is sufficiently accurate for the simulation. As already mentioned, the Lagrangian model implies a force balance to be solved. Therefore, the Eulerian flow field is computed and then the Lagrangian balance is solved, using the solution of the carrier flow as an input. Depending on the fact that the simulation will be steady state or not, the flow field computation will be kept frozen during the particle tracking or will be updated every time step respectively.

The force balance to be solved is reported in Eqn. 2.1:

$$\frac{du_p}{dt} = F_D + \frac{g\left(\rho_p - \rho\right)}{\rho_p} + F_S + F_B \tag{2.1}$$

where u_p is the particle velocity, and therefore the left hand side is the inertial force per unit mass (particle acceleration). Regarding the right hand side, F_D is the drag force, the second term is the buoyancy, F_S is the Saffman Force and F_B is the Brownian force. These last two contributions are noticeable only whit very small particles and are generally neglected in this work. The buoyancy is neglected as well since no dependence on the orientation is allowed. Given these considerations, the most important among the forces involved in Eqn. 2.1 is the Drag forces.

Therefore, the choice of the proper formulation of the drag terms represents the most important step. The actual implementation is software-dependent and thus, since different software suites have been used throughout this work, the differences will be reported. The software used in this work are ANSYS-FLUENT, OpenFOAM and the code described in Carnevale et al. (2015) that has been updated with the particle tracking feature. In all the software, the same expression for the drag force is solved, and is reported in Eqn. (2.2):

$$F_D = 1\frac{18\mu}{\rho_p d_p^2}\frac{C_D Re_P}{24}(\mathbf{u} - \mathbf{u}_p) \tag{2.2}$$

where μ is the carrier flow viscosity, ρ_p is the particle density, C_D is the drag coefficient. The difference is in the calculation of the drag coefficient.

ANSYS-FLUENT calculates the drag term for spherical particles as reported in Eqn. (2.3)

$$C_D = a_1 + \frac{a_2}{Re_p} + \frac{a_3}{Re_p^2} \tag{2.3}$$

where the coefficients a_1, a_2 and a_3 are taken from Morsi and Alexander (1972). If the particle Mach number is greater than 0.4 and the Reynolds particle number is greater than 20, for the proper resolution of the particle motion the spherical drag law must be corrected by the proper high Mach number term provided by Clift et al. (2005). Sub-micrometric particle correlation is available as well, but is not used in this work.

In OpenFOAM, The term C_D of Eqn. (2.2) is not continuous, but is chosen according to the cases reported in Eqn. (2.4)

$$C_D = \begin{cases} 0.424 Re_p & \text{if } Re_p > 1000 \\ 24(1 + \frac{1}{6} Re_p^{2/3}) & \text{if } Re_p \leq 1000 \end{cases} \tag{2.4}$$

The code of Carnevale et al. (2015) has been updated with the capability of particle transport in either one-way or two-way coupling. Further details on this will be given in the section 3.2. Concerning the drag force, the C_D has been chosen as a function of the Re_P in agreement with the experimental data of Morsi and Alexander (1972).

2.3 Turbulence-particle interaction

The dispersion of particles in the fluid phase can be predicted using a stochastic tracking model. The time-averaged flow field determines the mean path of particles, while the instantaneous flow field governs each particle's turbulent dispersion from the mean trajectory. By computing the trajectory in this manner for a sufficient number of representative particles, the random effects of turbulence on the particle dispersion can be included.

One of the most used techniques to account for the turbulent dispersion, and applied in this work, is the Discrete Random Walk (DRW), was firstly proposed by Gosman and Ioannides (1983). Specifically, the velocity is perturbed with a vector in a random direction, where the random value is chosen with a Gaussian distribution. This means he DRW model assumes that the fluctuating velocities follow a Gaussian probability distribution, implying isotropic turbulence. This approach represents the standard in terms of turbulence-particle interaction in RANS.

The reliability of DRW in the prediction of the exact particle trajectory has been questioned by some authors, for example Forsyth et al. (2016). In their work, the authors highlight how the DRW tends to overestimate the actual deposition rate, as reported in Fig. 2.2. The particle non-dimensional deposition velocity is defined as reported in equation (2.5):

$$V_d^+ = \frac{1}{4} \frac{D}{L} \frac{u}{u^*} \left(\frac{C_{in}}{C_{out}} \right) \tag{2.5}$$

where D is the pipe diameter, L is the characteristic length, u* is the friction velocity, C_{in} and C_{out} are the incoming and outgoing concentration respectively. The particle relaxation time is the inverse of the drag force (see (2.2)). The authors propose the Continuous Random Walk model, Dehbi (2008): the flow is split in to isotropic and anisotropic at

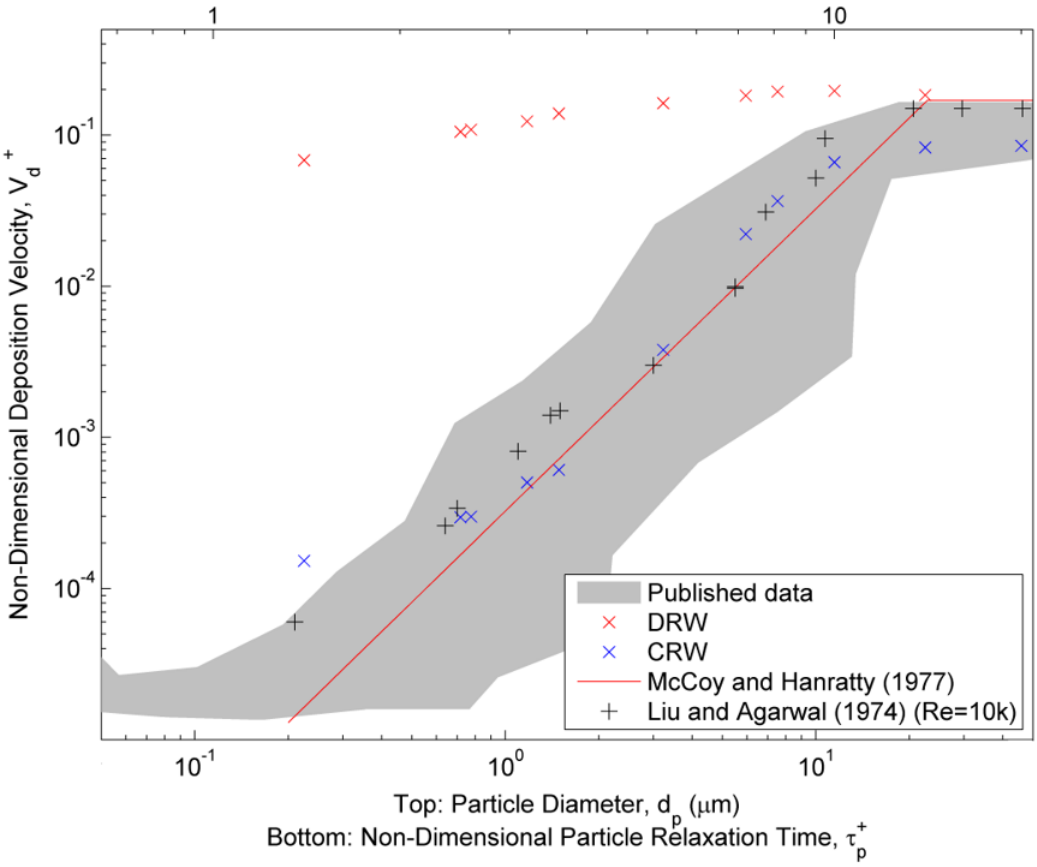

Figure 2.2: Non-dimensional deposition velocity V_d^+ against τ_p^+ for the CRW and DRW particle deposition model. Grey area shows extent of key published data. Data from Liu and Agarwal (1974) and From Forsyth et al. (2016)

y^+=100. In the bulk region, fluctuating velocities are calculated from turbulent kinetic energy, while at the boundary layer the anisoropic turbulence is accounted for by extracting statistics from DNS simulations.

From Fig. 2.2, it can be clearly seen that an higher deposition velocity is predicted as the DRW is used. The authors suggest the passage to CRW for diffusion dominated flows (lower non-dimensional relaxation time). The difference tends to be smaller as the inertial regime is approached (for $\tau_p^+ = 10^1$). In this work, the vast majority of the particles injected belong to the $\tau_p^+ \geq 10^0$ regime, thus slightly affected by such difference. No modification has been introduced to the DRW, since the error due to its application in the inertial regime is very small. However, this represents a limitation of the current analysis and efforts should be put in improving the modeling here presented.

Interestingly, Forsyth et al. (2016) reports how the passage from two equations k-ε turbulence model to complex RMS models have shown very little improvement in terms of deposition if DRW is applied. In this work, two-equations turbulence model (k-ε and SST k-ω) will be used.

2.4 Numerical domains

Four different numerical domains have been employed in this work, two of them for showing degradation problem in the cold section and two the hot part. In this section, such mathematical models will be described along with the boundary conditions and the numerical solutions obtained.

2.4.1 Cold section test case

Two different test cases have been used for the evaluation of the cold section degradation. The first geometry is a simple duct with bends, whereas the second is the NASA ROTOR 37 test case. In the following each of the models will be described.

Duct with a bend

The first test case is a rectangular sectioned duct presenting two bends, reported in Fig. 2.3. This shape has been chosen for being representative of the impact conditions of a subsonic compressor, but the simpler geometry helps in building the grid and testing the proposed models, keeping under control phenomena that might be hardly discernible in case of complex flow structures as in a compressor. Besides, the geometry has been realized keeping in mind the experimental validation (not yet carried out). The technical design is therefore reported in this work (see 7.11) and is currently under development at the University of Ferrara. The structured computational grid, chosen after a sensitivity analysis, is reported in Fig. 2.4.

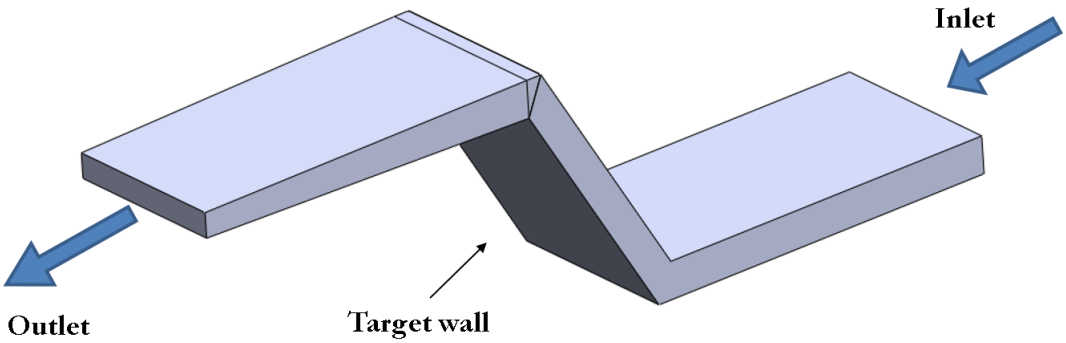

Figure 2.3: Numerical domain employed in this work.

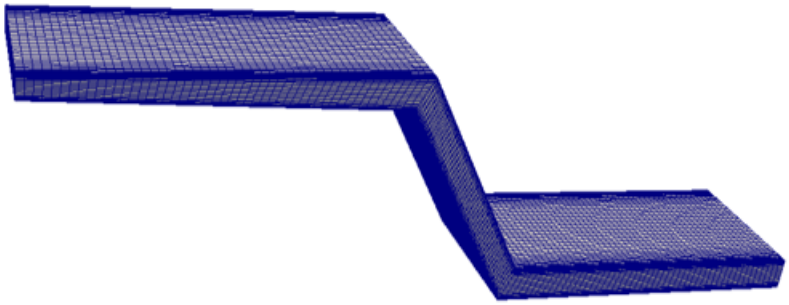

Figure 2.4: Computational grid used for the duct

In the evaluation of the different degradation processes, several flow conditions will be tested. Nonetheless, in several cases and for validation purposes, the boundary conditions reported in Tab. 2.1 are applied. The pressure jump across the nozzle has been imposed to reach an inlet Ma of 0.35. Under these conditions it is assumed that on the wall under investigation, that is the one labelled as target wall in Fig. 2.3, the flow conditions and the particle impact characteristics are not too different with respect to a real subsonic vane of an axial compressor, in order to show the capability and the applicability of the models that are presented in the next sections.

Under the boundary conditions reported in Tab. 2.1, In this figure, the dimensionless velocity (the local velocity divided by the inlet velocity) sampled along three different sections is depicted. The inlet velocity is 120 m/s due to the inlet Mach number chosen and the inlet conditions. The three measure lines are chosen to lie on the mid-width section (25 mm from both walls in Fig. 2.3. For all the three section in the x-axis the dimensionless distance from the upper wall is considered. For better understanding the trends in the three section, the flow field is reported in Fig. 2.6. It is well clear that the stagnation area due to the shape of the target wall causes the velocity to drop for the higher distances to the upper walls in section A. Consequently, a jet develops at smaller distance. Such high velocity stream is displaced towards the target wall after the bend. The separation downstream the bend close to the upper wall does not vanish along the straight section of the duct, and the flow remains detached in section B. The bend in the opposite direction at the very end of the target wall displaces the high speed stream towards the upper wall. The onset of the relative downstream separation can be identified

Table 2.1: Boundary conditions for the duct validation

	Quantity	Value
Inlet	p	171,197 Pa
	T	288 K
	Turbulence intensity	1 %
	Turbulence mixing length	0.00117 m
Wall	T	adiabatic
Outlet	p	101,325 Pa
Turbulence Model	k ω - SST	

by looking at the low velocity area in section C at a dimensionless distance around 0.95 in Fig. 2.5.

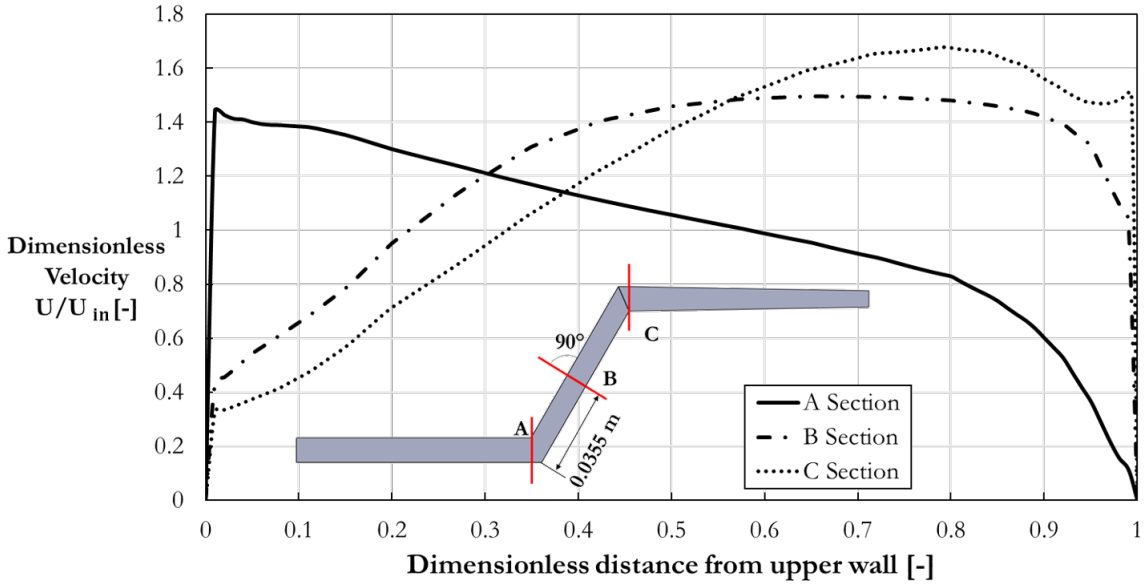

Figure 2.5: Dimensionless velocity profile as function of the distance from the upper wall

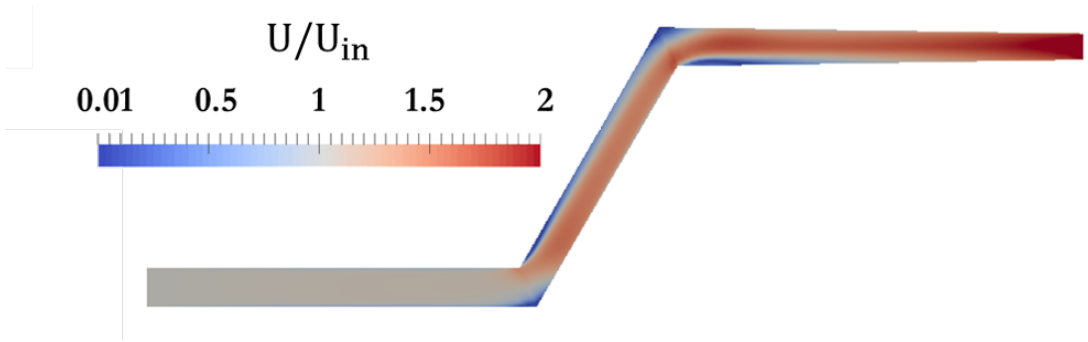

Figure 2.6: Computational grid used for the duct

This duct will be employed for proving the models proposed in the cases of deposit formation and deposit evolution over time in the cold section case.

NASA STAGE 37

This test case will be used for the erosion of the cold section. NASA stage 37 has been rebuilt starting from the report by Reid and Moore (1978), where the coordinates are reported. This stage is design for achieving peak efficiency of 0.840, at a mass flow rate of 20.74 kilograms per second. The pressure ratios resulting at the peak efficiency conditions were 2.00. The stage exhibits good stall margin (based on conditions at stall and peak efficiency) at 70 and 90 % of design speed. The computational grid that has been generated is composed of 3 different domains: inlet, rotor and stator, placing a mixing plane interface in between. The result of the meshing procedure is reported in 2.7.

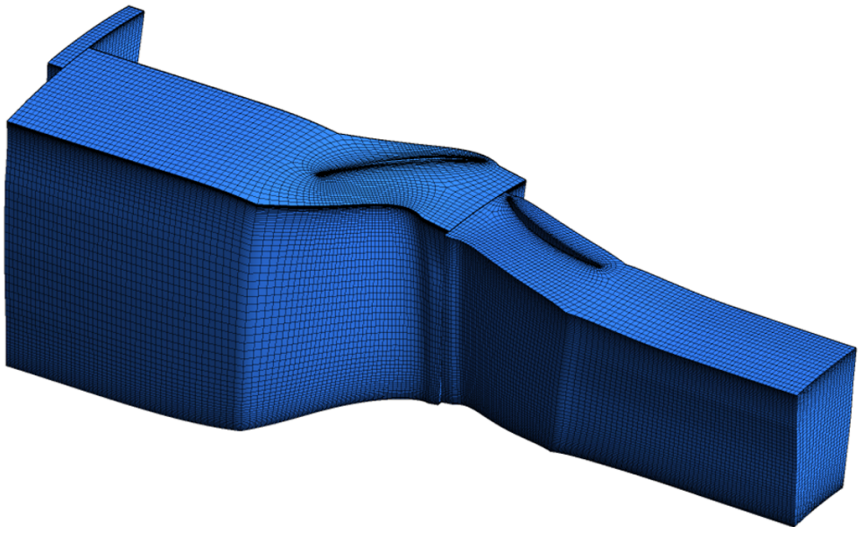

Figure 2.7: Computational grid of the NASA stage 37

The numerical analysis (carried out with ANSYS FLUENT 13.0) started with the reconstruction of the performance map of the stage, to validate the model and to give input to stage-stacking techniques as the one proposed in Fig. 1.15 by Morini et al. (2010). The performance map of the stage is reported in Fig. 2.8, calculated for 100% rotational speed (17188.7 rpm). Reasonable agreement has been found between numerical data and experiments, since the numerical curve is an offset of the experimental one

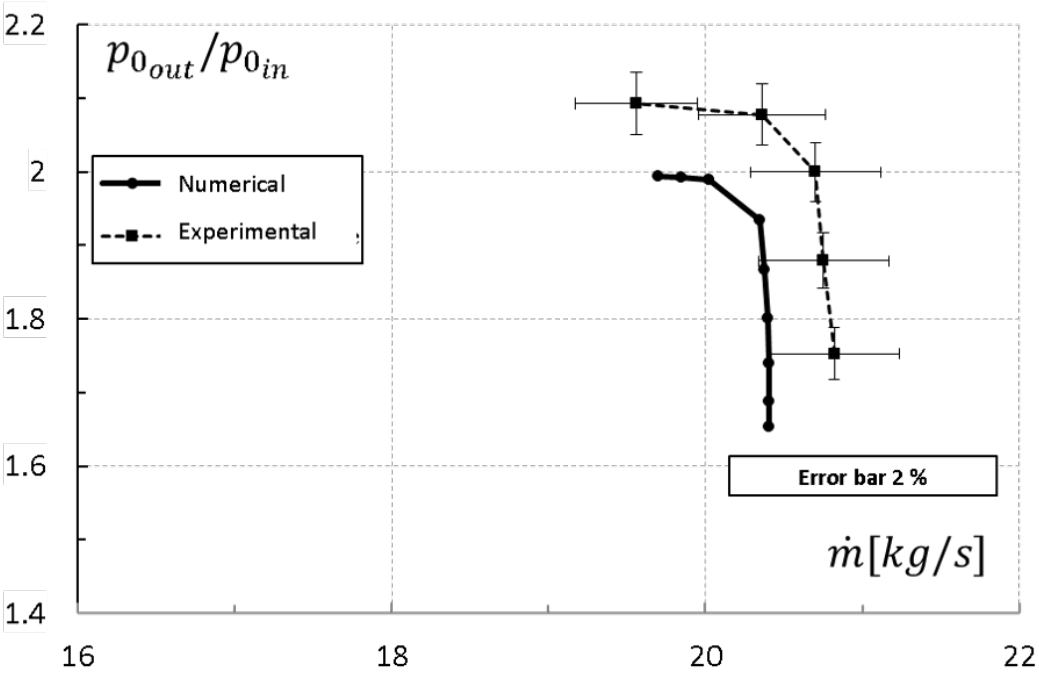

Figure 2.8: Comparison of numerical and experimental map for NASA stage 37

The flow analysis of the rotor has been therefore carried out at the best efficiency point, that is the central point of the map 2.8, characterized by an pressure coefficient $\Phi = 0.310$ and a flow coefficient $\Psi = 0.754$. For this point, the flow analyses have been performed at the best efficiency point and the consequent Mach contour at midspan is

reported in Fig. 2.9. Such point has been obtained imposing the boundary conditions reported in Tab. 2.2. It can be seen that the typical compressor cascade flow structures are correctly predicted from the simulation: the normal shock in front of the nose, the passage shock and the thickening of the boundary layer downwind.

Table 2.2: Boundary conditions for the NASA best efficiency point

	Quantity	Value
Inlet	p_0	0 Pa
	T_0	288.15 K
	Turbulence intensity	5 %
	Turbulence viscosity ratio	5
Wall	T	adiabatic
Outlet	p	50000 Pa
Turbulence Model	k ε - Standard Wall Functions	

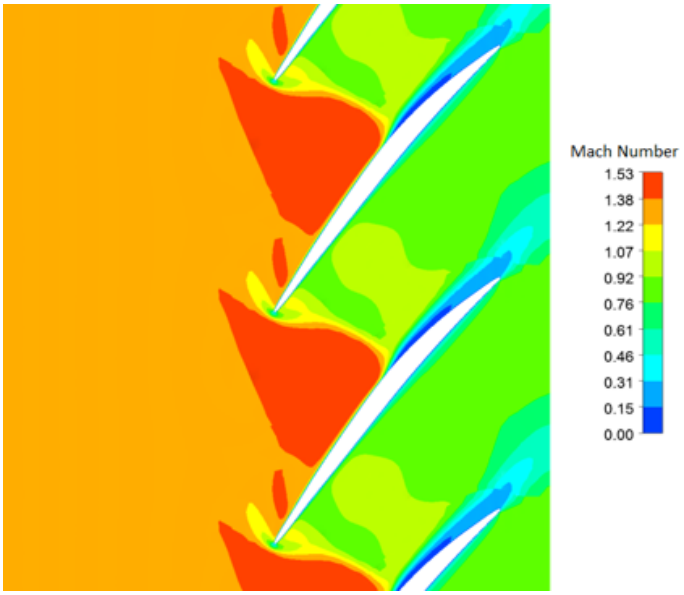

Figure 2.9: Blade-to-blade velocity field at the best efficiency point

2.4.2 Hot section test case

The test cases used for the hot section are the well-known LS-89 test case presented by Arts et al. (1990) and the GE - E^3 HPT nozzle(see Davis and Stearns 1985). The numerical analysis of the transonic HPT-vane (LS-89) has been investigated firstly by replicating the experiments of the tech report Arts et al. (1990), in order to validate the solver and the geometry. For the ash ingestion studies, the set of boundary conditions representative of flight at cruise is selected. The same procedure has been applied to the GE - E^3 HPT, but only subsonic conditions have been considered, given the fact that only the mean section is considered. From the design, such vane section is indeed conceived to work in subsonic conditions.

Table 2.3: Boundary conditions for the solver validation flow field

	Quantity	LS - 89
Inlet	p_0	149,350 Pa
	T_0	420 K
	Turbulence intensity	1 %
	Turbulence mixing length	0.0004 m
Wall	T	298 K
Outlet	Mis	1.02
	p	89,600 Pa

Throughout this work, only quasi-3D simulations of the vanes will be performed. Full 3D simulations are for sure an attractive options, but this work focuses more on the development of techniques and numerical tool that are useful to be tested first on 2D domains. The real geometry considering endwalls and cooling holes is an ongoing work carried on by the turbomachinery group at the University of Ferrara.

The structured multi-block numerical grid developed is reported in Fig. 2.10. The validation has been carried out using the boundary conditions for the flow field reported in Tab. 2.3. The comparison in terms of shock position is reported in Fig. 2.11.

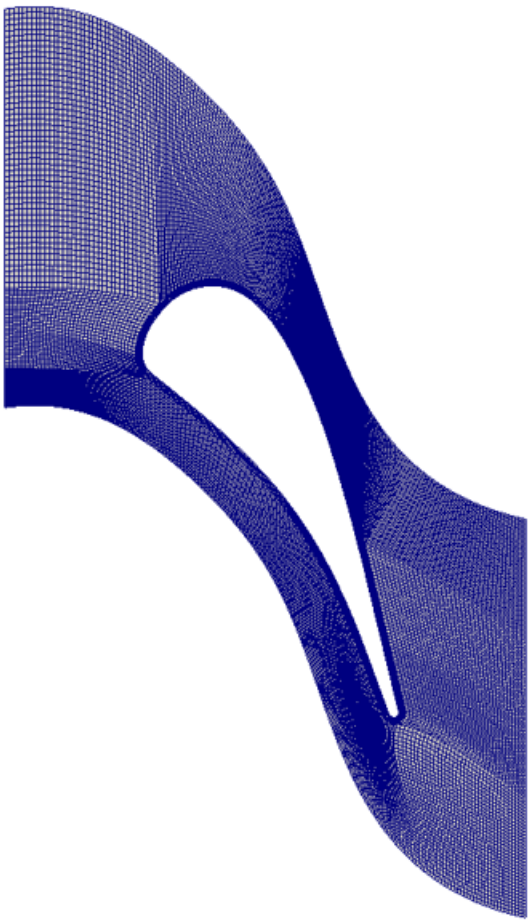

Figure 2.10: Numerical grid of the LS 89 HPT nozzle

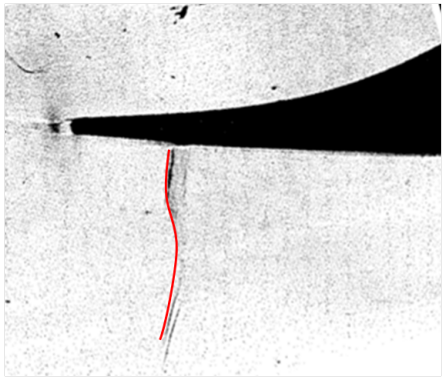

(a) Schlieren visualisation from Arts et al. (1990)

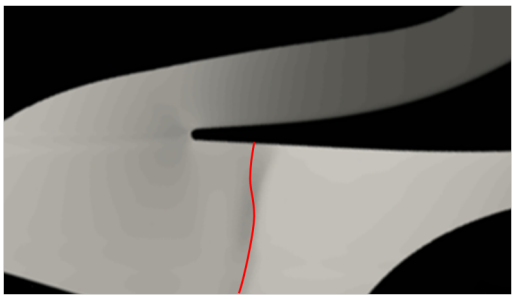

(b) Numerical results for validation

Figure 2.11: Schlieren visualisation from Arts et al. (1990) and results of the simulation

The boundary conditions reported in Tab. 2.3 have been used for validating the solver with the experimental data proposed by the author. When investigating each of the phenomenon, the boundary conditions will be updated according to the case under investigation. The table with the updated conditions will be reported in each section.

2.5 CFD suite

Different software have been used throughout this work, as disclosed in the section 2.2. For the NASA-STAGE simulation, the commercial package ANSYS-Fluent, version 13, has been chosen. Such software has automatic support for the Lagrangian particle tracking. The erosion model was tuned by imposing the coefficients that will be described in the 4.1.

For the analysis of the LS-89, in the deposit formation part (3.2), the CFD solver employed was Carnevale et al. (2015). Such code has been updated with the particle tracking procedure, that will be shortly described here:

For the implementation of the Lagrangian tracking, two grids have been used. The first one is the numerical domain, in which the tracking have been performed, is a rectangular domain. The elements are triangular and have the same areas. The second grid is the physical one and it is the one in which the carrier phase is computed. The second grid represents the projection of the first one onto the physical geometry of the vane through suitable functions, to obtain a C-type grid. The functions used are firstly a transfinite interpolation, to initialize the mesh. Then an elliptic smoothing based on a Laplace equation is introduced in the sistem of Eq. (2.6), as suggested by Thompson et al. (1998).

$$
\begin{aligned}
&\alpha x_{\xi\xi} - 2\beta x_{\xi\eta} + \gamma x_{\eta\eta} = 0 \\
&\alpha y_{\xi\xi} - 2\beta y_{\xi\eta} + \gamma y_{\eta\eta} = 0 \\
&\alpha = x_\eta^2 + y_\eta^2 \\
&\beta = x_\eta x_\xi + y_\eta y_\xi \\
&\gamma = x_\xi^2 + y_\xi^2
\end{aligned}
\tag{2.6}
$$

The relationships (2.6) describe a smooth distribution of computational coordinates (ξ, η) in physical space (x, y). The set of equations (2.6), derives from a Laplacian operator applied to the computational coordinates,as shown in Eq. (2.7). Since the unknowns are the coordinates in the (x,y) space, the set of equations that project the computational space into the physical one is the finite difference implementation of Eq. (2.6).

$$
\nabla^2 \eta = 0 \qquad\qquad \nabla^2 \xi = 0 \tag{2.7}
$$

The particle tracking is performed with the jump and walk algorithm by Mücke et al. (1996) and described here briefly. The search starts from the element where the particle is located before evaluating the movement (it can be seen as the initial condition from the tracking standpoint). Once the calculation of the new particle position is performed, three triangles are built using the final particle position and two of the three vertex of the element. The areas of these triangles is evaluated and divided by the area of the first element. The triangle with minimal area is used to identify the new element containing the destination of the particle. This kind of algorithm is very computationally efficient: with only three comparisons it can find the element containing the final position of the particle.

The solution of the discrete phase and the tracking of the particles are sequential: firstly the Lagrangian force balance is solved and then the tracking of the particle is performed, once the final position is known. This allows the code to evaluate whether the particle crosses the boundary of the domain.

For the modification of the boundaries as a consequence of the sticking, details of the implementation are reported in 3.2 part.

OpenFOAM

Regarding the computation of the duct, of the LS-89, in the erosion and long-time-exposure analyses, and for the GE-E^3 the open-source software suite OpenFOAM (Weller

et al. 1998) has been used. OpenFOAM (for "Open source Field Operation And Manipulation") is a C++ toolbox for the development of customized numerical solvers, and pre-/post-processing utilities for the solution of continuum mechanics problems, including computational fluid dynamics (CFD) based on the finite volume method (FVM). The code is released as free and open source software under the GNU General Public License.

This suite has been chosen in order to have the more possible flexibility. Most of the techniques presented largely rely on this flexibility modifying quantities that are difficult to be accessed otherwise.

The codes used in this work are the versions 3.0.1 and 1606+. In both cases, modifications have been included for both the flow field solver and the boundary conditions that are related to the particle-wall interaction.

The solvers *sonicFoam* and *rhoPimpleFoam* have been updated with the capability of particle tracking, that does not come with the standard installation of the software. *sonicFoam* is the transient solver for transonic/supersonic flows.

In *sonicFoam*, a non iterative method for handling the coupling of implicitly discretized time dependent fluid flow equations is utilized. The method, known as PISO (for pressure implicit with splitting of operators) Issa (1986) is based on the use of pressure and velocity as dependent variables and is applicable to both the incompressible and compressible versions of the transport equations. The main feature of the technique is the splitting of the solution process into a series of steps where operations on pressure are decoupled from those on velocity Marcantoni et al. (2012). *rhoPimpleFoam* is based on the same PISO algorithm of *sonicFoam*, but it suggested for applications where lower pressure jump are considered. In order to reach CFL greater than one, the SIMPLE algorithm (from Patankar 1980) is included. The PIMPLE (merged PISO and SIMPLE) algorithm is therefore employed.

The first solver (*sonicFoam*) has been used for the simulation of the turbine, and the second for the bend (*rhoPimpleFoam*). Besides, the dynamic mesh algorithm has been largely used for the morphing techniques, explained in the following . The particle sticking has been translated in a boundary condition on the blade surface and the algorithm takes care automatically of the spreading of the boundary displacement in the bulk of the domain. Fluxes are updated automatically according to the new metrics, see Jasak (2009).

This page was intentionally left blank.

Chapter 3

Deposit formation

This chapter deals with the fouling primary mechanism, that is deposit formation. The hot and the cold sections will be treated separately, and for each of them the models employed will be presented. Three different approaches will be shown, two for the compressor section and one for the hot part. The aim of this section is to identify the most suitable technique to account for particle deposition and, mostly, with the effect such deposition has on the flow field. Before the actual numerical modelling of the problems (cold and hot section), a brief introduction on the physics of each phenomenon will be given.

3.1 Cold deposition

The cold deposition will be evaluated on the bended duct reported in section 2.4.1. Two different approaches will be presented, both of them with the aim of relating the deposition of particles to a parameter that can actually affect the fluid flow in order to be able to estimate the losses. Particularly, what has been named Microscale-Deposition pattern and a porosity driven approach are presented here.

3.1.1 Physics and experimental evidence

Particles impinging onto the surface of a solid body can be reflected off the surface, stick to the surface or penetrate into the bulk. Often, the impact of a particle on a surface causes a deformation or destruction of both, the particle and the solid body. Only by understanding both the interactions and the mechanical response of the materials to these interactions can adhesion be understood.

The summary of all the possible consequences of particle-surface impact in cold condition is reported in Fig. 3.1. The map classifies the possible impact behaviour on the basis of particle velocity and particle diameter.

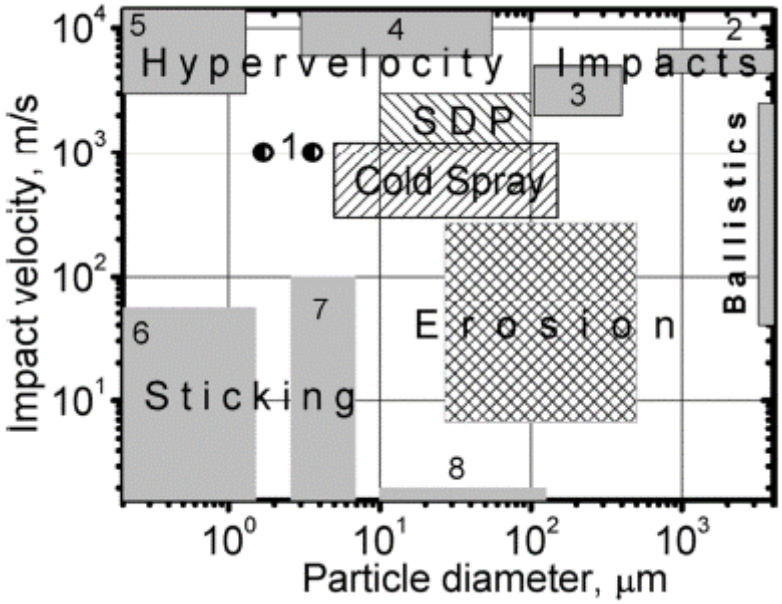

Figure 3.1: Particle impact on a solid surface: Influence of impact velocity and particle size on features of the interaction. Regions characteristic of certain impact phenomena are shown. From Klinkov et al. (2005)

The several regions can be therefore classified according to:

- *low-velocity impacts (1 to 100 m/s)*: in this region, smaller particle are known to stick to the surface, though such process is thought to be stochastic. Adhesion is governed by van der Waals, electrostatic forces and liquid bridging is known to play a fundamental role, Tomas (2007). Larger particles (1 mm) typically bounce on surfaces eroding them, or particle fragmentation may happen due to excessive stress inside the particle as a consequence of the impact.

- *ballistic impact and hypervelocity impact*: (500 to 3000 m/S): very high speed impact make solids to behave like liquids and locally, arising flow velocities are comparable to and can exceed the sound speed of the material.

- *cold spray*: moderate velocities and moderate particle size, combined with ductile materials, make the particles to deform and strong attach them to the surface. There is a minimum critical velocity for this to happen.

Several approaches have been developed in order to model the actual losses of energy upon impact and thus the sticking,rebound or erosion. Modeling has been developed starting from the analytical perspective Johnson et al. (1971), in line with the Hertz theory Hertz (1986). A more extensive review of the sticking models is reported in Suman

(2015), but what can be concluded is that most of the models and the results reported in literature do not provide a full understanding of the adhesion phenomena which is responsible for the fouling mechanism. The experimental approach is therefore one of the most employed method to obtain the sticking models and results available in the literature are the basis for the sticking model in cold sections employed in this work.

3.1.2 Microscale deposition pattern

Over last years, several methods have been developed in order to study the problem from the numerical standpoint. Examples of these techniques are the mesh morphing approach and the added-roughness-and-thickness method (Suder et al. 1995). In this section, an innovative procedure is proposed in order to evaluate the losses and the variation in the fluid flow due to the deposits. Particularly, an algorithm capable of determining the microscale deposition pattern has been developed. By using this methodology, a comprehensive analysis of the variation of the performance of the compressor over time can be carried out. The deposition severity and the subsequent roughness variation can be kept into account in a very detailed and precise fashion. Furthermore, this approach overcomes the difficulties that may arise by using a mesh morphing technique. The computational grid is not modified and thus its quality is retained, without re-meshing requirements, even for large deposits. The local roughness variation is accounted for without extra-effort.

The procedure developed, shown here in deposition problems, can be easily extended to erosion or even icing problems. The only parameter to be changed is the model that takes care of the particle-wall interaction, using an erosion rather than an icing law.

As above mentioned, the reduction in performance in folued compressors is due to the two main aspects deposition entails: variation of the roughness and variation in shape of aerodynamic surfaces. Surface roughness and its increase are critical for several structures of the flow field, e. g. the boundary layer separation, as pointed out by Bons (2010). Such parameter is usually quantified using the equivalent sand grain roughness k_s which is proved to increase if deposition occurs, see Bons (2010).

For what concerns the effects of thickness variation, the reader is referred to Suder et al. (1995), where an extensive analysis on this topic is carried out. The main conclusion from that work is that the effect of the thickness increase is smaller if compared to the effect of the increase in roughness.

In this work, the deposition problem is numerically investigated. Particularly, the focus is on the actual microscale deposition pattern, deriving from the particle ingestion and impingement on a surface. Very few contributions have been found in literature, with regards to the variation of the flow field as a consequence of particle ingestion. Most of

the studies report the variation of the flow field as a consequence of controlled and a-priori changes in the shape rather than roughness. Experimental works on this topic have been carried out by Suder et al. (1995) and Gbadebo et al. (2004).

Since the major effects of the deposition are related to the roughness increase, the aim of the work is to quantify such variation in terms of k_s. Indeed, the non-dimensional value $k_s^+ = k_s u_\tau / \nu$ was identified by Nikuradse (1933) in order to apply the roughness effect on the flow field. Particularly, if $k_s^+ > 70$, the regime can be described as fully rough and the loss coefficient is a function of k_s only, whereas for $5 < k_s^+ < 70$ both Re and k_s have an effect on the losses (transitionally rough regime). Computationally speaking, the law of the wall is still valid in case of a rough surface, but the constant B, from $u^+ = 1/\kappa^* ln y^+ + B$, is dependent on k_s^+.

For all these reasons, the equivalent sand grain roughness is of paramount importance for predicting the losses related to a rough surface. When dealing with gas turbines, various correlations have been employed to translate surface roughness parameters easily obtainable by measurments (R_a, R_q, or R_z) into k_s. The most used correlations are reported by Bons (2010). As underlined by the author, the wide variability of such correlations makes choosing the appropriate value for the application of interest a non-trivial step. The variation in the predicted value of k_s can be as much as a factor of 5 an increase in the displacement thickness, see for example Cadorin et al. (2010).

Few guidelines in this track can be found in the work of Goodhand et al. (2016). The authors try to overcome the uncertainty in the determination of the k_s, or of the ratio k_s/R_a, with a very careful experimental campaign. Depending on the morphology of the surface, peak-dominated rather than valley-dominated, mountainous rather than rolling hills, the effect of the same R_a on the flow field can be dramatically different. The shape of the boundary, in terms of roughness morphology, can be quantified by the average roughness R_a, the roughness slope R_{dq}, the root mean square roughness R_q and the skewness R_{sk}.

The roughness due to the particle deposition is therefore treated in the light of such remarks. A new technique is suggested here in order to quantify the roughness increase/variation due to the deposition. In particular the impact location is identified and the growth of the boundary, due to the particle impact in such position, is stored. The model proposed by Poppe et al. (2000), and successfully employed in estimating the particle adhesion on single blade or multistage compressor by Suman et al. (2015) and Aldi et al. (2017b), is used here. The outcome of such works has been proved to fit reasonably well with what actually happens in compressors by the work of Kurz et al. (2017). Nonetheless, it is important to note that the procedure proposed here is independent of the sticking model or the particle type and size.

In order to evaluate the effects of particle deposition on the flow field, the procedure

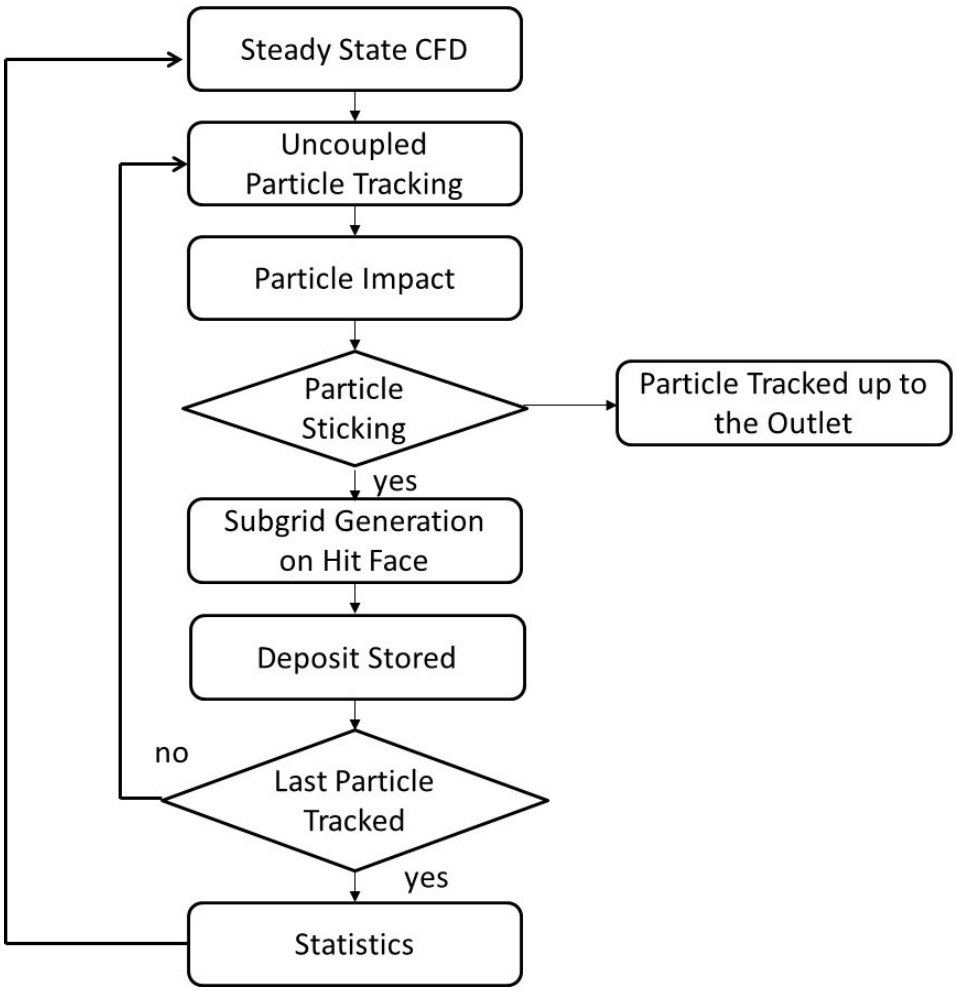

Figure 3.2: Outline of the procedure for the microscale deposition pattern detection

reported in Fig. 3.2 is implemented. As set out below, each of the following blocks will be described in detail. What it must be remarked it is that the particle tracking is uncoupled from the flow field solution. This is possible since the particle flow rate is low, allowing the use of the one way coupling approach. More comments on this are reported in the particle tracking-section below and in Suman et al. (2015).

In this section, the flow field is kept frozen and the particles are tracked on a fixed flow. Then, referring to Fig. 3.2, once the last trajectory has been computed, the CFD is run again after the modifications related to the computation of the statistics (more details on this below. This implies a stepwise variation of the flow field for every loop of Fig. 3.2.

CFD resolution of the flow field

The geometry employed in this work is reported in Fig. 2.3. This simple duct with a bend have been chosen in order to be easily reproducible in an experimental campaign. The boundary conditions are reported in Tab. 2.1, and they are representative of the first

stage vane of a heavy-duty gas turbine compressor, entailing an inlet $Ma = 0.35$.

The software used for this analysis is the open-source CFD toolkit OpenFOAM®-v1606+. The calculations have been carried out on a structured mesh of 120000 elements. The turbulence is accounted for in this work by using the k-ω SST model. The variant available in OpenFOAM is based on Menter et al. (2003). It is implemented as High-Re and therefore wall functions must be used for modeling the behaviour at the wall. Standard wall functions are used for such a scope. The roughness effect, in the software employed in this study, is introduced in the law of the wall for the turbulent kinematic viscosity ν_t. The wall function for the turbulent viscosity is calculated as Eq. (3.1)

$$\nu_t = \nu \left(\frac{y^+ k}{log\left(Ey^+\right)} - 1 \right) \tag{3.1}$$

where $y^+ = C_\mu^{0.25} y \sqrt{k}/\nu$ and k is the turbulent kinetic energy. Equation (3.1) holds both for rough and smooth walls, but the difference in the two cases is the definition of the term E. E is equal to the additive constant B in case of smooth wall (the hydraulically smooth regime is valid as long as k_s^+ is smaller than 2.25). In case of rough wall, E is given by Eq. (3.2)

$$E = {}^{B}\Big/\left[\frac{k_s^+ - 2.25}{87.75} + C_s k_s^+\right]^{sin[0.4258(log k_s^+ - 0.811)]} \tag{3.2}$$

where C_s is a roughness constant, it depends on the roughness type. It is usually assumed to be equal to 0.5, and such assumption is used in this work. The former equation is used for both transitionally rough and rough regime.

For what concerns the roughness of the target wall two different cases have been considered. In the first case the wall was considered hydraulically smooth, and thus with a $k_s = 0$. In this case, the particle deposition occurs on a perfectly clean and smooth surface, where no previous deposition has been imposed. In the second case, a roughness has been imposed. Specifically, an operated blade surface was scanned by means of an optical profilometer. Further details on this second case are reported in the sections below.

Particle tracking, impact and sticking

The size distribution, injected at the inlet of the domain, is chosen among the ones likely to cause deposition on the compressor inner walls in a real application: a population having a spherical shape with uniform diameter of 1 μm has been injected, with the same velocity of the flow. Then, the tracking algorithm computes the particle trajectory keeping into account the drag force only, with the formulation reported in section 2.2. The discrete

random walk model is employed in order to allow for the turbulent dispersion.

When an impact with the boundary region of interest takes place, the sticking decision has to be made. The sticking model, proposed by Poppe et al. (2000) and successfully employed in estimating the particle adhesion on single blade or multistage compressor by Suman et al. (2015) and Aldi et al. (2017b), is used here. The modification suggested by Aldi et al. (2017a) to account for the relative humidity in the air has not been introduced here.

The deposition model relies on the experimental sticking probability,S_p, trends reported in Poppe et al. (2000). Particularly, a correlation between the impact velocity v_n in the normal to the surface direction and S_p is defined. This correlation varies according to the particle diameter. In the present work, with a particle diameter equal to 1.00 μm the equation for a normal impact velocity lower than 4 m/s is reported in Eq. (3.3):

$$S_p = -0.112 v_n + 0.99 \tag{3.3}$$

and for higher impact velocity $(4 - 90)$ m/s the equation is Eq. (3.4)

$$S_p = -6\,10^{-5} v_n^2 - 6\,10^{-4} v_n + 0.545 \tag{3.4}$$

With this model, smaller particles have a wider range of normal impact velocity for which impact with the blade surface becomes (with a higher probability) a permanent adhesion.

The modification introduced to the sticking algorithm is the stochastic evaluation of the impact. Basically, in the analyses proposed by Suman et al. (2015) and by Aldi et al. (2017b), the stochastic content of the model was translated in a threshold: if the sticking probability of the particle S_p is above 0.5 the sticking happens, the particle is rejected otherwise. Contrarily, in this work a Metropolis-Hastings algorithm has been implemented. The sticking probability of the particle is compared with a randomly generated number belonging to the range [0,1]. If the threshold is greater than S_p the particle is rejected, otherwise it sticks.

Subgrid generation on the hit face

If the particle sticks, as decided by the algorithm in the section above, then such particle contributes to the variation of the boundary of the domain. The collection of the deposits on the boundary face is done by creating a 2D subgrid on the hit face.

Let's suppose the computational face reported in Fig. 3.3 is the one affected by the particle sticking. Since the grid is structured, and thus having quad elements as boundary,

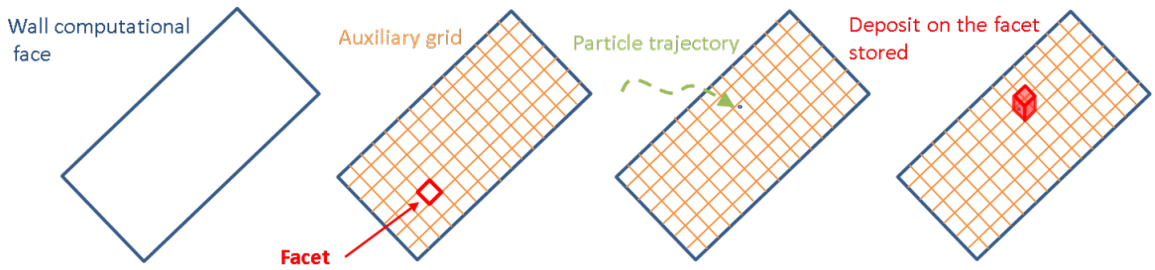

Figure 3.3: Procedure of subgrid generation on the hit face. From left to right, the wall boundary face to be hit by the particle is considered. Hence an auxiliary grid is built to increase the spatial resolution. In this way the computational face is divided into several facets. The facet hit can therefore be identified and the stuck particle is stored. The next particle hitting such boundary face will be piled over the previous one, accumulating the volume if the same facet is stricken, otherwise a new build-up on the new facet is built

it is relatively easy to build a 2D subgrid onto a quadrangular boundary face. This is done via the usual grid generation algorithms, e.g. via transfinite interpolation, by deciding the number of divisions in the two directions, streamwise and tangential, as reported in Fig. 3.3. The extension of this approach to unstructured grids, and espressly to grids having boundary faces that are different from quadrilateral, is beyond the aim of this work and it is considered to be the next step of this method.

The tracking algorithm locates the particle impact point inside one facet of the so-generated subgrid. The deposit in that facet is thus accumulated. In order to quantify the contribution to the final build-up given by the particle under analysis, a piling law must be assumed. In the current analysis, the height of the deposit on the impacted facet is updated by summing to the already-formed build-up the incoming particle diameter. This assumption is therefore representative of perfect particles piling. In this scenario, the void fraction of the simple cubic packing assumed is $\epsilon = 0.476$. The described procedure is repeated until the entire amount of particle is tracked. The schematic of the final boundary face, with the deposits accumulated on the facets, is reported in Fig. 3.4.

Statistics

The deposition pattern, after the procedure described in the previous paragraphs, is very detailed and, depending on the fineness of the subgrid realised on the face, it can reach the micrometric scale. Such amount of information can be used to compute statistics, with particular regards to the roughness quantities.

In such a scenario, both the 3D roughness parameters, see for example Mainsah et al. (2013), as well as the most used 2D parameters can be computed. This means that one can easily derive the "S" quantities (commonly related to 3D set of parameters) and the "R" quantities (usually referred to the 2D statistics) for each of the faces. To the

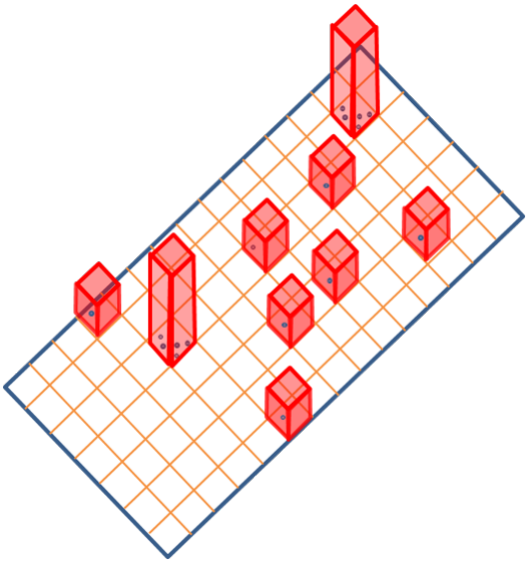

Figure 3.4: Schematic of the surface for the roughness evaluation. The profile to be analyzed is the surface given by the maximum between the base (smooth or rough) and the deposition peaks for each facet.

authors' knowledge, very few studies (if none at all) have been carried out for relating the S-type parameter to the k_s coefficient, used in the numerical analyses. Commonly, the "R" quantities are used when one has to deal with roughness. In this work, these quantities are used for the evaluation of the deposit impact on the flow field.

Nonetheless being a detailed pattern of deposition available, the way the 2D parameters are derived should be discussed. Since the 2D parameters must be evaluated along the flow direction, and a single value per face must be calculated, average operations should be realized. For what concerns the centerline average roughness R_a, Eq. (3.5) is used. It can be easily verified that the result, if averaged over the grid rows, is exactly the same with respect to the average amplitude of the surface S_a, reported in Eq. (3.6) from Mainsah et al. (2013).

$$R_a = \frac{1}{l_x} \int_0^{l_x} |z\left(x\right) - \mu| dx \tag{3.5}$$

$$S_a = \frac{1}{l_x l_y} \int_0^{l_x} \int_0^{l_y} |z\left(x, y\right) - \mu| dx dy \tag{3.6}$$

where l_x and l_y are the face sizes in the x and y direction, μ is the mean value given by (in the 3D case) :

$$\mu = \frac{1}{l_x l_y} \int_0^{l_x} \int_0^{l_y} z\left(x, y\right) dx dy \tag{3.7}$$

Indeed being R_a, S_a and μ linear, the result is the same if the mean is calculated along each row of the boundary sub-grid and by averaging these values or by calculating S_a.

The interchangeability of the parameter is not ensured if one considers the higher order moments of the distribution, since the linear hypothesis does not hold any longer. In this case, the 2D parameters are obtained by calculating such values row-wise (where rows are aligned in accordance with the stream-wise direction) and then averaging those values. The quantities of interests are the root mean square roughness R_q:

$$R_{q,i} = \left(\frac{1}{l_x, i} \int_0^{l_{x,i}} \left(z\left(x\right) - \mu \right)^2 dx \right)^{\frac{1}{2}} \tag{3.8}$$

and the skewness R_{ski}, which can be interpreted as a measure of the departure of the surface from symmetry.

$$R_{sk,i} = \frac{1}{l_{x,i} R_{qi}^3} \int_0^{l_x,i} \left(z\left(x\right) - \mu \right)^3 dx \tag{3.9}$$

The kurtosis of the profile, the measure of the sharpness of the peaks, is not used, since the work of Goodhand et al. (2016) does not relate the value of k_s to this quantity. The sharpness of the profile, or the fatness of the tails of the distribution, can be regarded as a fashion for defining the slope shape. Among the others, a way for defining kurtosis is that positive value of kurtosis are related to "heavy-tailed" distributions, see for example Taleb (2007). The first derivative variation of the profile slope is therefore related to this parameter and it is expected to have a major influence on the k_s. Unfortunately, no experimental correlations have been found in the literature, so this quantity has not been taken into account.

In order to find the parameter representative of the roughness profile slope within the face, the ASME B46.1 relation has been employed. Particularly, the RMS slope of the profile measured along the $i - th$ subgrid row is evaluated through:

$$R_{dq,i} = \sqrt{\frac{1}{M} \sum_0^{M-1} \Delta_j^2} \tag{3.10}$$

where the filter Δ_j is calculated using a 5^{th} order Savitzky–Golay filter

$$\Delta_j = \frac{1}{60\delta x} \left(z_{j+3} - 9z_{j+2} + 45z_{j+1} - 45z_{j-1} + 9z_{j-2} - z_{j-3} \right) \tag{3.11}$$

And δx is the row-wise face size. Consequently, the final values are obtained by

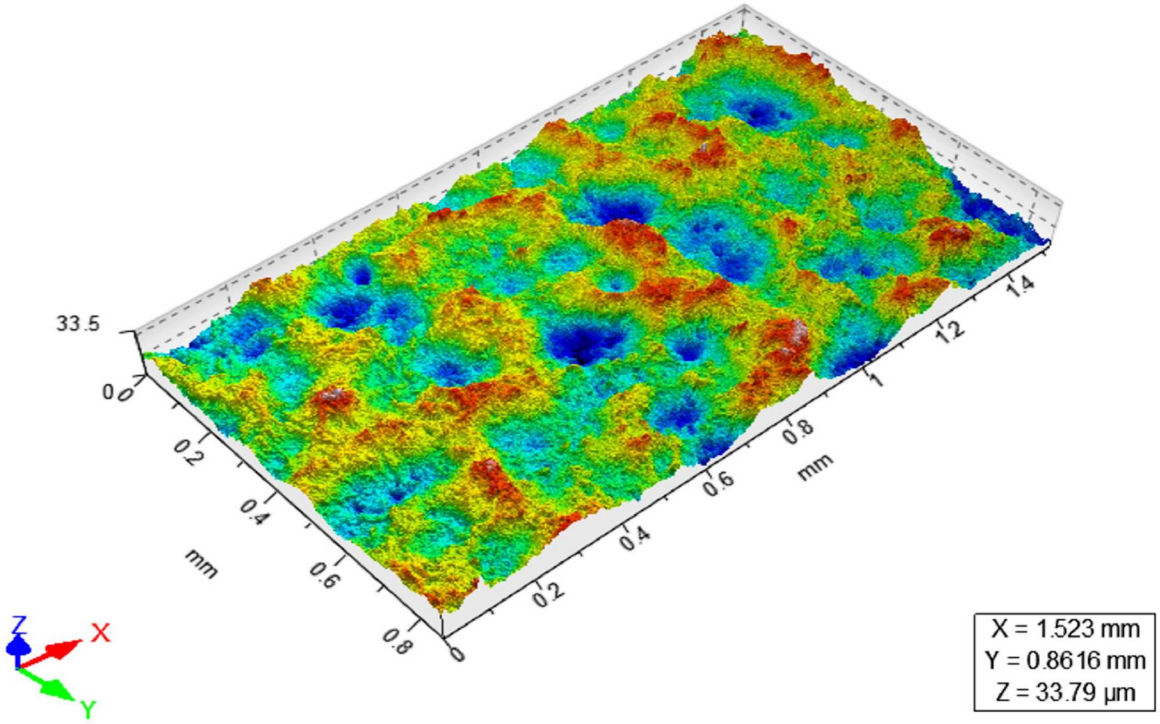

Figure 3.5: Profilometer scan of an operated compressor blade

averaging among the rows the reported in Eqs. (3.8), (3.9) and (3.10)

When applied to a discrete case, integrals must be converted in summations. Furthermore, being the deposit height uniform inside the facet, the former equations are averaged over the facet area. For example, the mean value takes the form of Eq. (3.12):

$$\mu = \frac{1}{MN} \sum_{0}^{M-1} \sum_{0}^{N-1} z\left(m,n\right) \frac{A_{ij}}{A_f} \tag{3.12}$$

A_{ij} is the area of the $ij-th$ facet of the boundary face f. M and N are the total number of face divisions (i.e. number of facets) in the x and y directions respectively.

Wall roughness value

A second set of simulations has been carried out considering a rough target wall (while the first CFD run with nominally "clean" surfaces). In order to have the more realistic profile as possible, an operated compressor blade has been scanned with an optical profilometer (Talysurf CCI - Taylor Hobson). The scanned surface is reported in Fig. 3.5.

From that scanning, the profile reported in Fig. 3.6 can be extracted. Having such profile, R_a, R_{sk} and the slope R_{dq} can be evaluated with the relations reported in paragraph *Statistics*,and thus k_s can be derived.

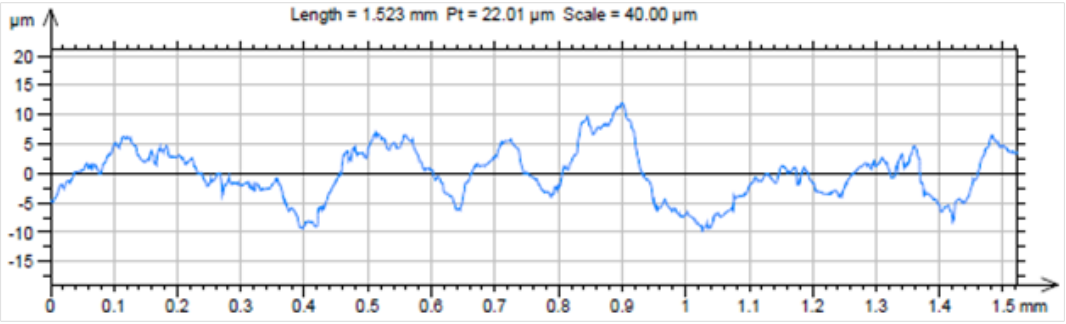

Figure 3.6: Roughness profile of the compressor blade in Fig. 3.5

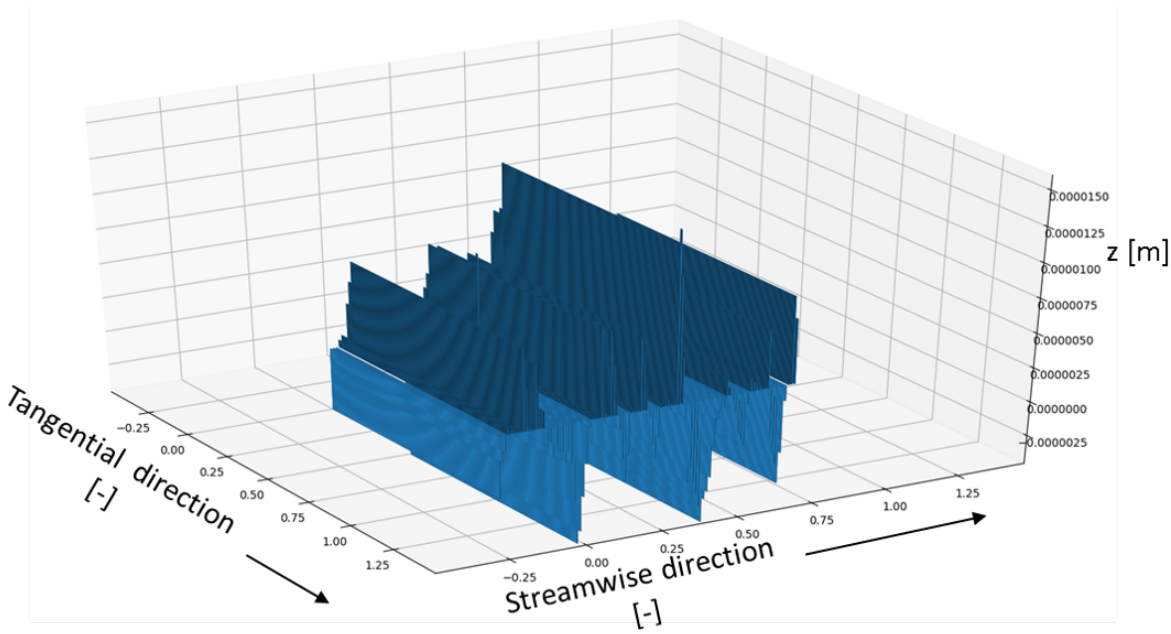

Figure 3.7: Roughness profile considered during the computation with rough walls. The profile reported in Fig. 3.6, has been extruded in the tangential direction and imposed on each one of the boundary faces hit by particles. The roughness profile can be regarded as the deposit at the time the particle stick to the boundary face. This means the particle just arrive will be piled above this surface.

When the wall has an imposed roughness, the procedure of Fig. 3.2 must be slightly modified. It is indeed required the generation of the roughness pattern when the particle deposits on the surface. In other words, when the particle hits the facet, it may fill a valley or deposit over a peak depending on the wall morphology in that area. To get this information, the peak-valley distribution must be created when that face is hit: the profile reported in Fig. 3.6 is sampled and the corresponding sampled height is associated with the facet. An example of this implementation is reported in Fig. 3.7. The curve resulting by sampling the profile in Fig. 3.6 has been extruded in the tangential direction.

Loop closure and influence of deposit on the flow field

Once statistics are computed, the characteristic of each boundary face is available. At this stage, the faces affected by deposit will have k_s value modified according to the law proposed by Goodhand et al. (2016), and here reported for simplicity (see Fig. 3.8 and Fig. 3.9). In Fig. 3.8, the variation in the equivalent sand grain roughness due to the average slope is reported. The effect of the distribution skewness can be retrieved by the law proposed in Fig. 3.9.

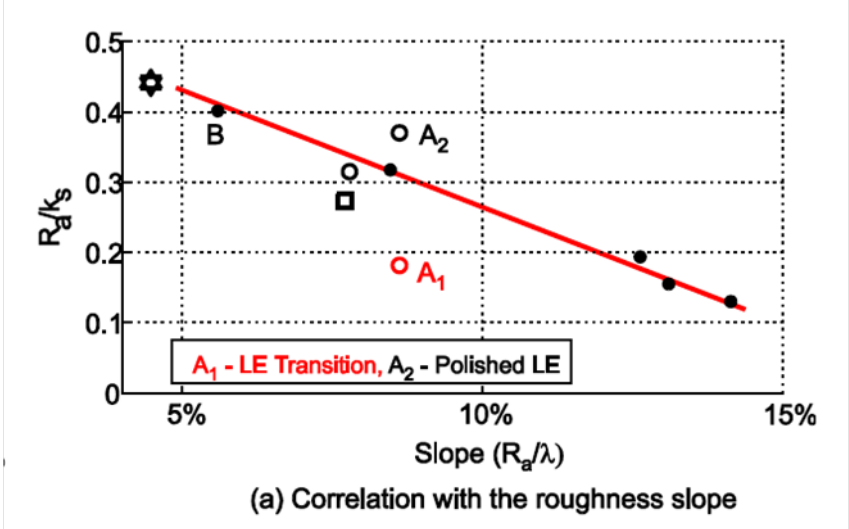

Figure 3.8: R_a/k_s as a function of the roughness slope. From Goodhand et al. (2016)

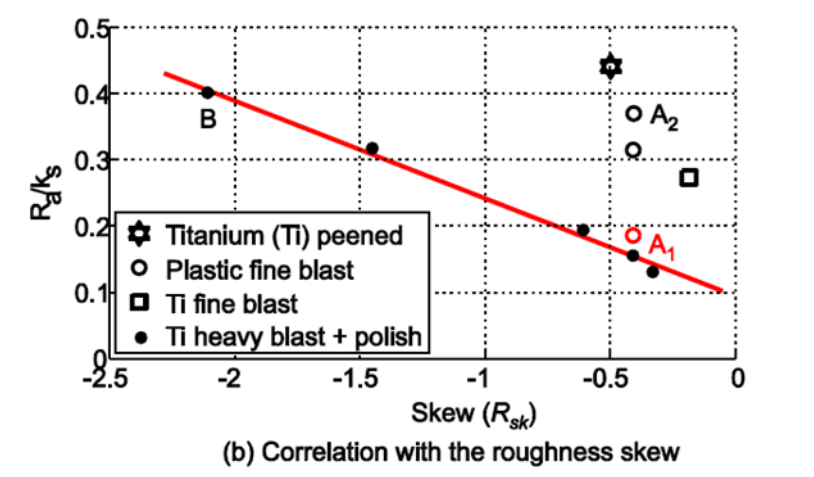

Figure 3.9: R_a/k_s as a function of the roughness skewness. From Goodhand et al. (2016)

Such a result is used in the set-up of the boundary condition for the next run. The algorithm developed modifies the k_s value in the turbulence boundary conditions. In the software used, this variation reflects on the modification of log-law and thus on the turbulent viscosity wall function. Especially, the value of E in Eq. (3.1) is modified updating k_s^+ in Eq. (3.2). As suggested by Cadorin et al. (2010), extra care must be taken when one has to deal with the imposition of the k_s for the wall function. Specifically, the nondimensional $k_s^+ = k_s u_\tau/\nu$ should be always smaller than the y^+. The unphysical

behaviour, deriving by choosing an equivalent sand grain larger than the distance from the wall of the first grid point, would make the results unacceptable. Thus, for the grid employed in this work, the simulation is valid as long as $k_s \leq 70\mu$m.

The new field can therefore be computed with the changes due to such a remark. It must be said that, theoretically, two different values of R_a/k_s can be derived by using the law reported in Fig. 3.8 or Fig. 3.9. The differences among the two different approaches are reported in the next paragraphs.

Effects of deposition on the flow field

The deposits on a boundary face reporting deposition appears as in Fig. 3.10. In Fig. 3.10, the base is made of the computational grid used for resolving the flow field. The novelty of this work lies in the subdivision of such face in facets. In Fig. 3.10, ten of these subdivisions are reported, and the final area of the facet can reach the micrometric size. This increase in the resolution of the wall deposition pattern is what allows the statistics computation and a better representation of the roughness effect on the flow field. The histograms are the piled particles that have deposited on each of the facets. This represents the "surface roughness" function.

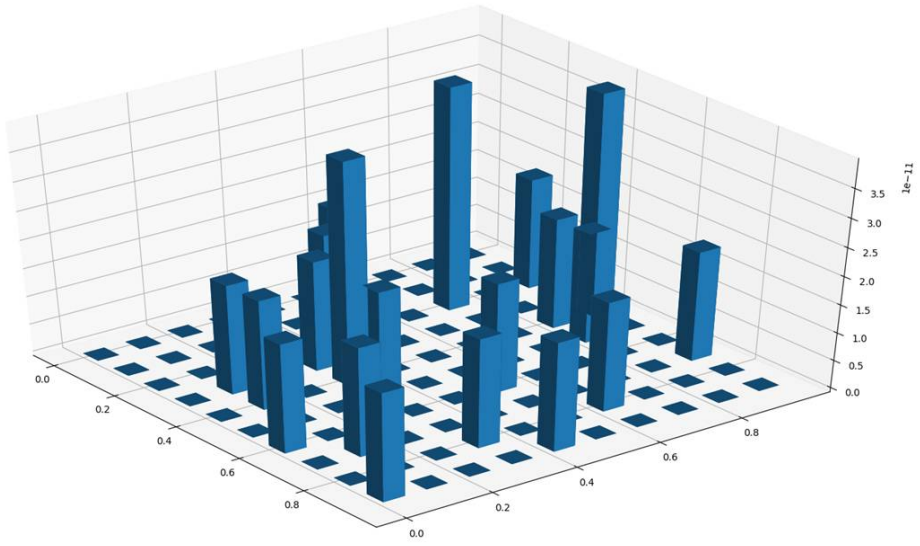

Figure 3.10: Histogram representing the deposits on the facets

From such a pattern of deposits the quantities reported in the paragraph *Statistics* can be easily computed. For determining the values to plug in as boundary conditions, the laws proposed by Goodhand et al. (2016) in Fig. 3.8 and 3.9 are used, and particularly, the Eqs. (3.13) and (3.14) are implemented.

Table 3.1: Variation of roughness parameter and mass flow rate after deposition has occurred. Roughness parameter variation are mean values.

	Skewness Effect		Average Slope Effect	
	ΔR_{sk}	$\Delta\dot{m}$	ΔR_{dq}	$\Delta\dot{m}$
Smooth wall	NA	NA	+ 15 %	- 2 %
Rough wall	+ 1	-1%	+ 4 %	- 1 %

$$R_a/k_s = -3.36(R_{dq}) + 0.6 \tag{3.13}$$

$$R_a/k_s = -0.15R_{sk} + 0.091 \tag{3.14}$$

Spherical particles have been injected in order to reach a total amount of 2 grams, of which less than the 10 % sticks to the target. Table 3.1 reports the outcome of the tests on the duct.

Smooth target

In the case of clean target, deposition occurs on a surface where the initial deposit height is null everywhere. An example of smooth boundary face recording deposition is reported in Fig. 3.10: it can be seen that the profile is strongly peak dominated. This entails a positive skewness of the distribution, according to the definition proposed in Eq. (3.9). It is required a long exposure period in order to have a negatively-skewed profile. The issue related with positive values of skewness is the fact that the results proposed by Goodhand et al. (2016) and reported in Fig. 3.9 are valid only for negative values of skewness. The extrapolation to positive values of the law returns negative k_s that is obviously unphysical and cannot be accepted. As a consequence, in this case only the effect of the slope variation is reported.

The deposition pattern on the target wall is reported in Fig. 3.11. The majority of the target area is not affected at all by deposition: in the corresponding faces, no roughness has been added and the profile remains smooth. Under these circumstances, only the effect of the slope has been considered, as above explained.

The k_s on the target wall varies from face to face. The average order of magnitude of k_s is of 10^{-7}. This value is related to the number of particles that deposits on each face. Such a value of the k_s is given by a slope R_d that varies in a range [0.5,1]%. The R_a on the faces affected by deposition is of the order of magnitude of 10^{-8}.

The reduction in mass flow rate due to deposition on compressor surfaces is a well known phenomenon. The flow rate coefficient reduction is indeed known to decrease as the

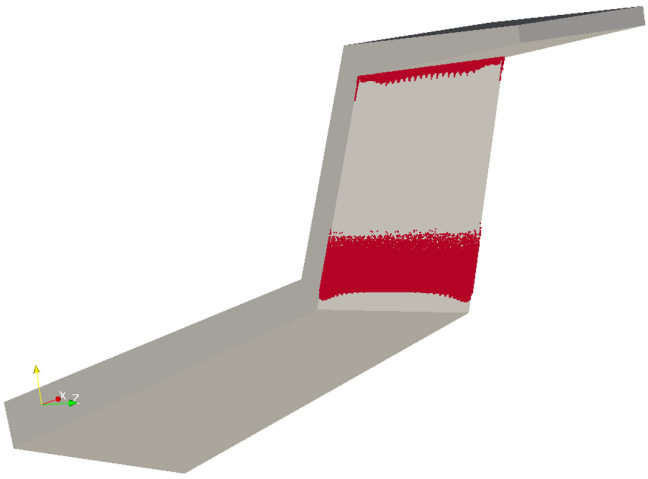

Figure 3.11: Deposition pattern on the target wall after the 2 grams of particulate has been tracked.

surfaces become more and more deteriorated, as found by Syverud (2007). Experimental analyses reporting the variation of the mass flow rate, as the roughness increases, are reported by Bammert and Woelk (1980). The Authors report a loss of flow rate of the 10% for an increase in the k_s/l from 0 to 10^{-3}, where l is the chord. The values found here are in good agreements with such remarks: the difference in the mass flow rate elaborated by the duct is of the 2%.

Rough target

The roughness parameters of the profile reported in Fig. 3.6 are: $Ra = 3.6\,\mu$m, $R_{sk} = -0.82$ and $R_{dq} = 0.11$. With these values, from Eqns. (3.13) and (3.14), k_s is computed. The two cases are slightly different, since the k_s computed with the skewness value is 13.9 μm, whereas the slope returns a value of 18.1 μm. In this case, both the skewness and slope variation effects have been analyzed. The resulting deposition pattern after the exposure to 2 10^{-3} kg of particles (equivalent to more than 1.5 10^6 particles tracked) is very similar to Fig. 3.11. This means that the tracking of the particles can be considered statistically independent from the turbulence standpoint.

For what concerns the skewness effect, the computation of the flow field and of the particle tracking is set-up with an equivalent sand grain roughness of $k_s = 13.9\mu$m, as above mentioned. Deposition happens in such a fashion that the profile is always more peak dominated, leading towards positive values of R_{sk}. By taking a look at Fig. 3.9, as R_{sk} increases the k_s increases (the ratio R_a/k_s decreases). Then, an higher values of the k_s is expected, and this is what actually occurs: the maximum k_s found is equal to 42.5 and in general is higher for all the faces affected by deposition, with respect to the ones that do not record particle sticking. The reduction in the flow rate is around the 1% when the skewness effect is considered.

The average slope roughness variation follows the same trend of the skewness, evolving from the 11 % to values around the 15 %. This sharp rise pushes the k_s values close to 40-50, that is roughly 20-30 times R_a, as one can see from Fig. 3.8. The reduction in the flow rate is very similar to the one reported for the skewness effect. For few faces the slope has been found to overcome the value of 20 %. In such cases, from Eq. (3.13) a negative value of the k_s would be predicted. The value of k_s has been bounded to 50 in that occurrences.

Final remarks

In this section, a novel technique for the numerical prediction of the roughness variation due to particle deposition has been proposed. The algorithm that has been employed here relies on the generation of a subgrid on the face hit by the particle. Deposits are accumulated in such facets providing a detailed evolution of the surface shape. Statistics can be computed and the fluid-dynamics parameters for the roughness computation. It is interesting to note that, by using the proposed approach, the fact of having a non-uniform sand grain roughness distribution over the compressor surface can be easily considered. The deposition pattern on the blade leads to R_a and consequently to k_s local changes: this method is proved to be suitable for taking into account such variations. This provides a powerful tool in the analyses of the effect of deposition on fluid flow, allowing for a local representation of the roughness variation.

A simple test case has been illustrated with the aim of showing the potential of the proposed technique. Both a smooth and a rough wall have been investigated, demonstrating that the technique is robust to the initial conditions of the target. In order to characterize the target wall roughness, the surface of real compressor blade has been measured.

The deposition has been found to heavily affect the flow field with differences up to the 2% in the flow rate with respect to the smooth wall.

The technique proposed here is therefore suitable for the variation of the k_s only when the boundary layer thickening is the responsible for the drag. No premature transition effect can be accounted for, as suggested by Goodhand et al. (2016)

3.1.3 Porosity driven approach

In this section, a different procedure is proposed in order to evaluate the losses and the variation in the fluid flow due to the deposits. Specifically, as the deposit grows, it is assumed it forms a porous medium attached to the wall. The porosity of this zone (related to the packing of the particles and to the amount of particles that sticks in to

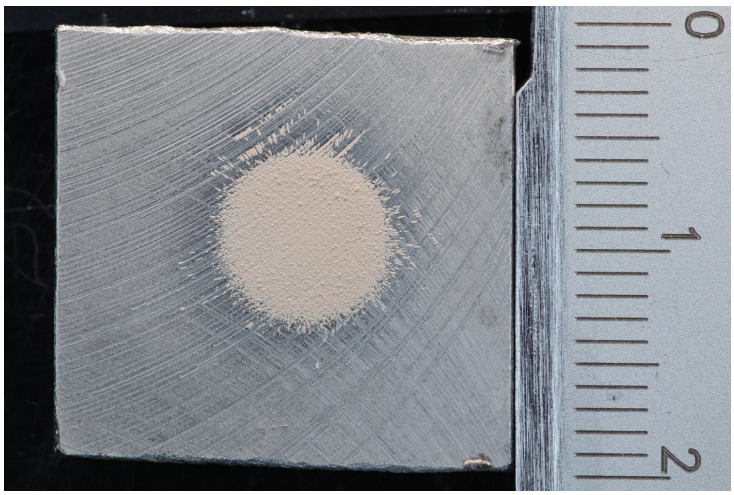

Figure 3.12: Particular of the target

a zone) is responsible for the deposition-induced losses. Different approaches to compute such losses are proposed and discussed. By using this methodology, the two main effects of fouling (variation in roughness and in shape of the airfoil) can be easily included in a comprehensive analysis of the variation of the performance of the compressor over time. Furthermore, this approach overcomes the difficulties that may arise by using a mesh morphing technique. The computational grid is not modified and thus its quality is retained, without remeshing requirements, even for large deposits.

The loss in performance, as already explained above, can be thought as related to two different effects of deposition: a macroscopic variation in shape or a microscopic variation in roughness Suder et al. (1995). Surface roughness and its increase are critical for several structures of the flow field, e. g. the boundary layer separation, as pointed out by many authors, e.g. Bons (2010); Goodhand et al. (2016). On the other hand, uncontrolled macroscopic variation in shape are well known to change the blade performance, causing an increase of the blockage and varying the aerodynamic load of the blade.

The approach proposed here tries to overcome the distinction above outlined, starting from the observation of actual deposits in compressor like conditions, obtained with a test bench specifically designed at the University of Ferrara (some detail in 7.11). Specifically, the macroscopic and microscopic scales are considered under a different standpoint.To better understand the line of reasoning proposed here, some experimental evidences are reported. These have been obtained by means of a test bench that has b, 1 mg of fine Arizona Road Dust was injected with a inlet velocity of approximately 40 m/s. Such stream (with a concentration of roughly 50 μg/m^3) has been directed in the normal to the surface direction against a flat stainless steel surface with controlled roughness. The resulting deposition, see Fig. 3.12 and 3.13 is very similar to the one that can be found in actual operated compressor, see for example Kurz and Brun (2001). The resulting deposition has been analyzed with a SEM and reported in Fig. 3.14.

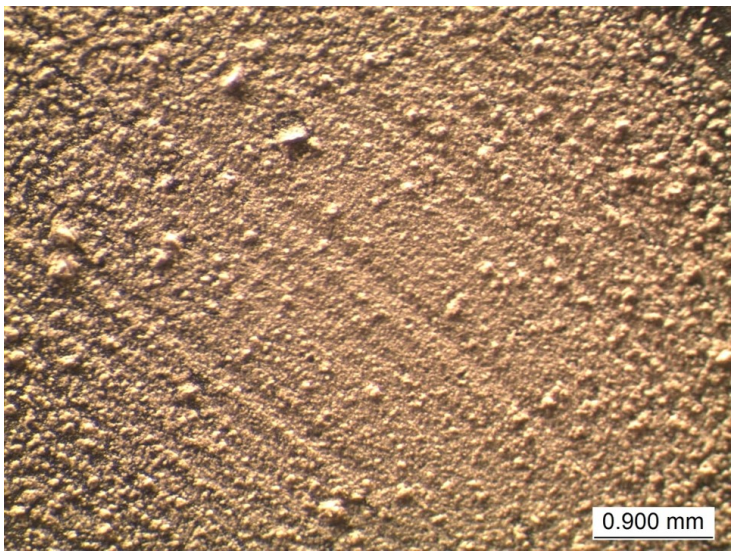

Figure 3.13: Stereo-Microscope close-up of the target

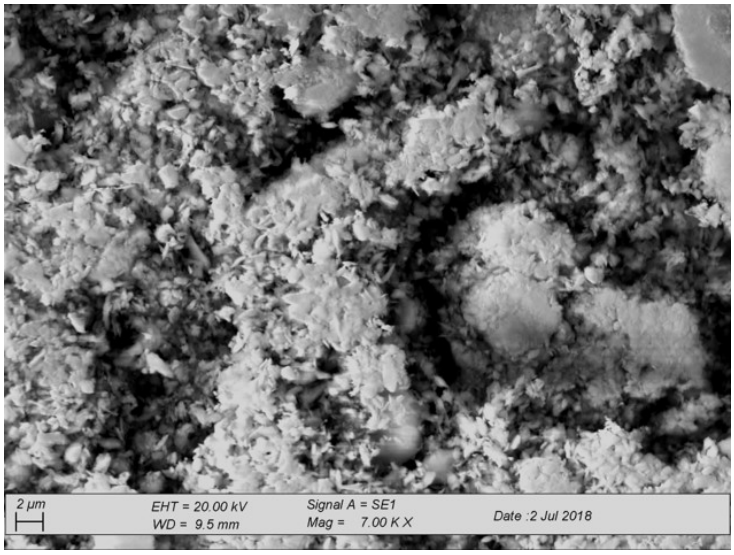

Figure 3.14: SEM image of the deposit on the target

The entire procedure is based on the one proposed by the authors in the section 3.1.2 but varies largely in the evaluation of the particle deposition effects (the statistic box in Fig. 3.2 is completely different).

The procedure reported in Fig. 3.2 is absolutely general and is thought as applicable to all the components of a turbomachinery (e.g. blades, annuli, ducts, combustor). The support for high fidelity simulations is intrinsic in the methodology itself, since the mesh quality is always retained. In this work the algorithm has been applied on a simple duct with a bend, as explained in section 2.4.1. The unidsturbed flow field has been obtained under the boundary conditions reported in Tab. 2.1. with a k-ω SST turbulence model.

Once the convergence of the numerical simulation of the flow field has been achieved, a steady-state particle tracking is performed on the frozen flow field. A population of spherical particles having an uniform diameter of 1 μm has been injected at the inlet

of the domain, with a random spatial distribution. The concentration of the particle considered for this study is 40 μg/m^3 which is a value representative of a relatively high-contaminated area Temime. It must be noticed that the duct is exposed directly to the concentration that is present in the air, as if there were no filtration systems placed at the intake. This would imply more detrimental results with respect to the actual conditions. In case a filtering system is employed, the filtering efficiency can be as high as 99.9999 % for smallest particles (see Perullo et al. (2015)).

The particle tracking follows the above mentioned lagrangian approach: the CFD solution of the flow field is employed to solve a force balance on the particles Zhang and Chen (2007).

Impact analysis and deposit storage

The novelty of this work resides on the fashion the sticking is treated and on how the consequences are evaluated, and this is the subject of the current section. When an impact takes place, the particle sticking probability S_p is calculated: the reader is referred to the section *Particle tracking, impact and sticking* for more details, since the same procedure has been employed here.

Particularly, a two level grid technique is employed, considering one grid for the flow field computation and a second, finer one for the particle sticking location. The term "subgrid" or "auxiliary grid" will be used when refferring to the finer grid generated on the computational boundary face on the wall. Such subgrid is generated when an incoming particle hitting the wall face is forced to stick there. Such auxiliary grid is therefore built to increase the spatial resolution for evaluating more accurately the deposit shape. In this way the computational face is divided into several facets. The subgrid is a structured quad grid realized with a transfinite interpolation algorithm Thompson et al. (1998). The facet hit can therefore be identified and the stuck particle is stored. The next particle hitting such boundary face will be piled over the previous one, accumulating the volume if the same facet is stricken, otherwise a new build-up on the new facet is built.

Porous medium coefficients and porosity of the deposit

Three different porous medium models are available in the software used for the numerical analysis: *DarcyForchheimer*, *fixedCoefficient* and *powerLaw*. All the three models work by adding a sink term in the momentum equation. In this work, the Darcy-Forchheimer model Nield et al. (2006) has been used. Such model represents the sink term of the momentum equation in case of inhomogeneous medium as in Eq. (3.15):

$$S_i = -\left(\mu D_{ij} + \frac{1}{2}\rho\,|u|\,F_{ij}\right) u_i \tag{3.15}$$

where S_i is the source term (negative since it is always a loss) of the $i-th$ component of the vector equation, D_{ij} and F_{ij} represent a 3 by 3 matrix with respectively the Darcy coefficients $[1/m^2]$ and the Forchheimer coefficients $[1/m]$.

The Darcy-Forchheimer model has been preferred to the others, since it is a more spread approach for the simulation of porous media. The values of the coefficients for packed particles are known and are typically given as a function of the particle mean diameter an the porosity Mukherjee et al. (2018). One relation that is commonly employed is the Carman-Kozeny relation (3.16), form McCabe et al. (1985):

$$K = \frac{d_p^2 \epsilon^3}{180(1-\epsilon)^2} \tag{3.16}$$

where K is the permeability of the medium, d_p is the particle diameter and ϵ is the porosity (the pore volume-bulk volume ratio). The Darcy coefficient is closely related to the permeability, since it can be calculated as its opposite: D=1/K. The particle size is uniform and equal to 1 μm and the porosity of packed spheres used here is ϵ= 0.476.

Darcy's flows are all the flows in which the inertial effect are not important, meaning a $\mathrm{Re}_d = |\mathbf{u}|d_p/\nu < 10$ Mukherjee et al. (2018). In the application tested in this work and, more generally, compressor like conditions imply Re_d that can be greater than such threshold. All these types of flow are known as non-Darcy flows, and thus the Forchheimer coefficient should be considered as well. Several correlations exist for the estimation of the Forchheimer coefficient, and in this work the Ergun equation is employed, see Eq. (3.17)

$$F = \frac{1.75}{d_p}\frac{1-\epsilon}{\epsilon} \tag{3.17}$$

where the constant 1.75 is purely empirical and is taken from Nemec and Levec (2005).

After the tracking of all the particles injected, for each of the boundary face that recorded particle sticking a distribution of deposit can be retrieved. Such distribution can therefore be used to gather information about the level of filling of the boundary cell. Two different approaches for the porosity evaluation has been considered at this stage.

Specifically, a local reference of frame aligned with the face edges can be built, and the distribution can be projected along one of the axis on the face of the boundary cell. As reported in Fig. 3.15, the deposit projection will cover only a part of the "normal-to-the-flow" area (assuming, for example, the flow aligned with the $\mathbf{C}_y$ direction). Considering

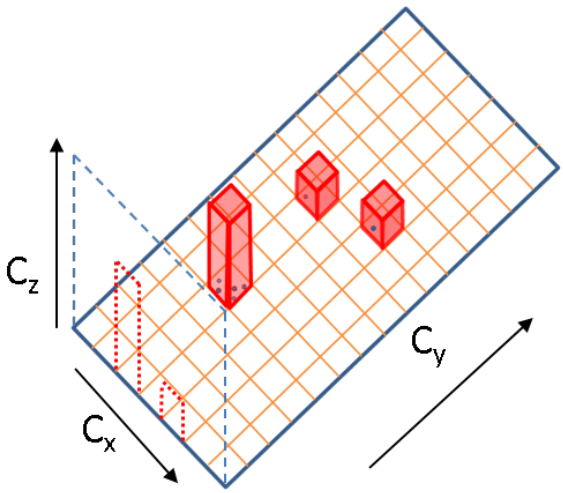

Figure 3.15: Projection of the porosity along the axis. In dashed blue one normal-to-the-wall face of the boundary cell, in dashed red the projection of the deposits

only such component of the porosity will entail the porosity coefficients matrices to be zero everywhere but in the second element of the diagonal (y-direction). Having the reference of the porosity oriented with the boundary face helps in considering only one element of the matrix, assuming anisotropic porosity of the medium. This is a simplistic assumption related to fluid-dynamics considerations, since the main flow is directed normal to the only direction where porosity is applied. Keeping into account other directions is considered a next step in this track.

The last step in order to have the coefficients properly set-up is to consider the quote of the frontal area (to the flow, so the area normal to $\mathbf{C}_y$) that is actually occupied by the porosity. As one can consider from the sketch reported in Fig. 3.15, only a share of the computational cell face is actually occupied from the projection of the porosity. This means that imposing the coefficient as they are calculated with eqns. (3.16) and (3.17) may overestimate the porosity of the cells, since the cell will be considered as completely full of deposits. By weighting the porosity on the part of area actually occupied by the deposit itself, the real porosity can be retrieved and that value can be imposed over the cell.

In order to evaluate different approaches to compute the porosity effects, two additional methods have been implemented. Firstly, instead of weighing the porosity by considering the fraction of frontal area occupied by the deposit, the volume of the cell will be considered. In other words, the percentage of cell volume which is actually filled up with deposit will be considered.

The last method that will be shown here considers the losses induced from the variation of the log-law related to the porosity. Indeed, one can imagine that porosity, besides creating blockage itself, affects the turbulent structures in a fashion that is similar to the surface roughness effects. This remark is formalized in the DNS analysis of a channel

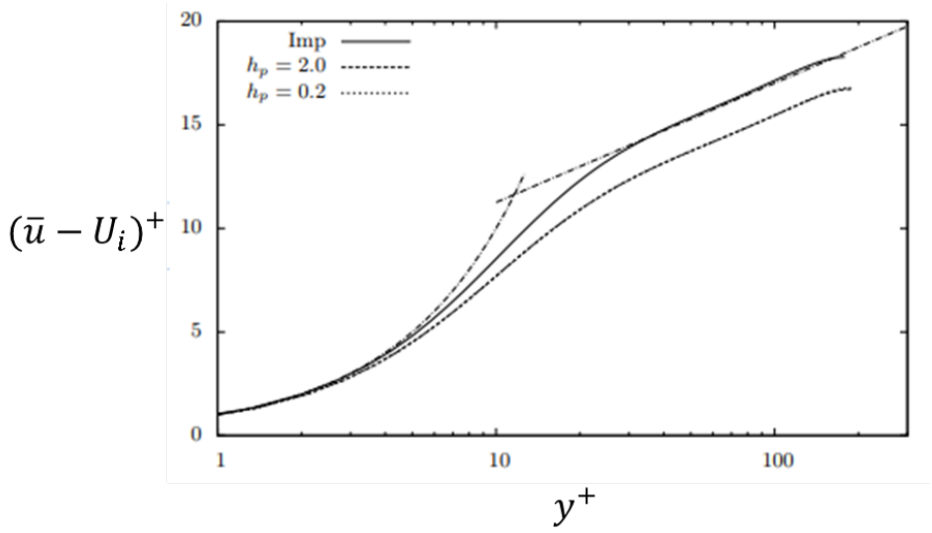

Figure 3.16: Effects of different porosity height on the turbulent structures. Solid line is for impermeable wall. Different height of porous layer have no effects on the log-law. From Rosti et al. (2015)

flow with a porous layer on the walls proposed by Rosti et al. (2015). In their work, the authors analyze the effect of the porosity on the non-dimensional velocity both in terms of porosity and height of the porous medium. Having a constant porosity value, in this case the focus was put on the influence of the porous layer height on the law of the wall. The results in Rosti et al. (2015) are reported in 3.16.

Figure 3.16 reports the variation of non-dimensional velocity difference (mean velocity minus the velocity of the flow at the porous layer interface). The porosity influences the law of the wall especially in the logarithmic region. In Rosti et al. (2015) it is reported that the log-law reported in Eq. (3.18), representing the solid line,

$$(\bar{u} - U_i)^+ = \frac{1}{\kappa} ln y^+ + B^+ \tag{3.18}$$

where $\bar{u}$ is the mean velocity, U_i is the velocity at the porous layer interface, κ is the von Karman constant equal to 0.41 and the constant B^+ is equal to 5.56, is still valid for the porous cases. Equation (3.18) still holds if the constant B^+ is assumed equal to 4. The form of the log law implemented into OpenFOAM is slightly different from the former expression and it is reported in Eq. (3.19)

$$\bar{u}^+ = \frac{1}{\kappa} ln E y^+ \tag{3.19}$$

The value E, in order to have the equality of the impermeable-wall log law of Eq. (3.18), is equal to 9.8. By combining the two different formulation of the log law, it is immediate to derive the value of E in terms of B^+, that is reported in Eq. (3.20).

$$E = e^{\kappa B^+} \tag{3.20}$$

The change in the value of E to match the new logarithmic profile of nondimensional velocity is 5.16, from Eq. (3.20) with B^+=4.

Two assumptions have been considered in this work, when applying the variation of log-law profile. In order to quantify the losses the boundary layer variation due to porosity induces, the velocity at the interface U_i has been assumed to be zero. Besides, no thickness of the porous layer has been accounted for in this case. The so-applied method is therefore insensitive to the actual amount of particulate deposited on the wall. On the boundary faces of the cells that are marked as porous, the modified form of the log-law is applied.

Effects of deposition on the flow field applying the porosity method

By applying the above listed boundary conditions (see Tab. 2.1) to the current problem, a resulting flow rate of 0.03 kg/s has been obtained. This will be the reference against which the effect of the deposits with the proposed model will be compared.

The cells that are affected by deposition, and are therefore marked as porous, are mostly grouped in the bottom area and the top of the target face. There is no deposition recorded for a considerable part of the target wall (in correspondence of the high velocity area). The cells that are affected by porosity are represented as solid boxes in 3.17. The pattern is symmetrical with respect to the mid-width of the target wall. Each of such cells is given a porosity via the Darcy and the Forchheimer coefficient, calculated as above.

With the current set-up, the average Re_d recorded is around 5. Such conditions is at the limit of the validity of the Darcy's flow regime. To avoid underestimating the porosity, the Forchheimer term is calculated as well. This term is multiplied by the velocity squared in Eq. (3.15), and so it becomes relevant only when the velocity is high.

With the models and the conditions described in this work, the amount of foulant ingested is representative of 15 hours of operation, where the concentration of 40 mg/m^3 is directly injected at the inlet of the domain. After such exposure time, the dust accumulated over the target wall according to the model of Poppe et al. (2000) is roughly the 10 % of the total mass injected. This is quite an high value if compared to common compressor applications Kurz and Brun (2012) considering a Stokes number of roughly 0.1. It must be remarked, though, that the streamline curvature of this case is quite high if compared to an axial compressor. With this configuration, the density of particle per face (boundary face of solid boxes in Fig. 3.17) is 1156.

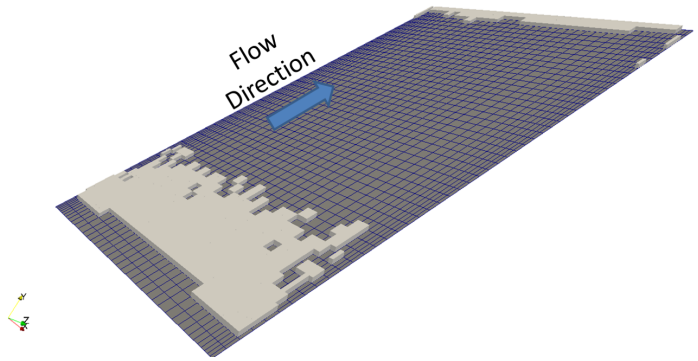

Figure 3.17: Pattern of the porous cells on the target faces. The solid boxes are the cells that are labelled as porous

Areal approach

The deposit is therefore converted to an index representative of the amount of the average frontal area occupied, as depicted in Fig. 3.15. The deposit projection represents around the 2.5% of the frontal face, with a maximum of 12%. Therefore the Darcy and the Forcheimmer coefficients obtained with Eq. (3.16) and (3.17) is to be multiplied by such coefficients. The Darcy coefficient as calculated from Eq. (3.16) is of the order of 10^{14}, and thus the 1% is around 10^{12}. The Forchheimer coefficient (Eq. (3.17)) is much lower being around 10^{6}.

By imposing such porosity, properly averaged, the flow field changes significantly. The velocity pattern on the cells that share a face with the target boundary is reported in Fig. 3.18, before and after the imposition of the porosity. The flow direction is upward. The undisturbed flow field (left hand side) shows the same pattern as described in the *Microscale deposition pattern* section, and reported in 2.6. Figure 3.18 right shows the relevance of the porosity induced by the deposits, making the flow-field pattern to be highly different from the undisturbed one. The low-velocity areas correspond to the deposits of Fig. 3.17. The stagnation area in the bottom of the target wall is enlarged due to deposit presence and becomes very irregular. The following high velocity area is highly affected by such irregular effects. The velocity returns to be uniform just before the end of the duct, where the next fouled region (the one close to the tip) affects the flow field disrupting the uniformity and inducing extra losses.

In terms of induced losses, the proposed algorithm reports a reduction of the mass flow rate of about the 5.5 %. Such losses are at least two times bigger with respect to the expected losses related to this case. Indeed, by considering the results from the previous approach, that are in agreement with some results in the literature, e.g. Bammert and Woelk (1980), show a reduction in the flow field that is slightly smaller. The order of magnitude of the reduction is around the 1 %. The algorithm as proposed predicts therefore high losses, for sure higher than the experimental values. In order to build an approach that is useful for actual compressor fouling calculation, the losses predicted

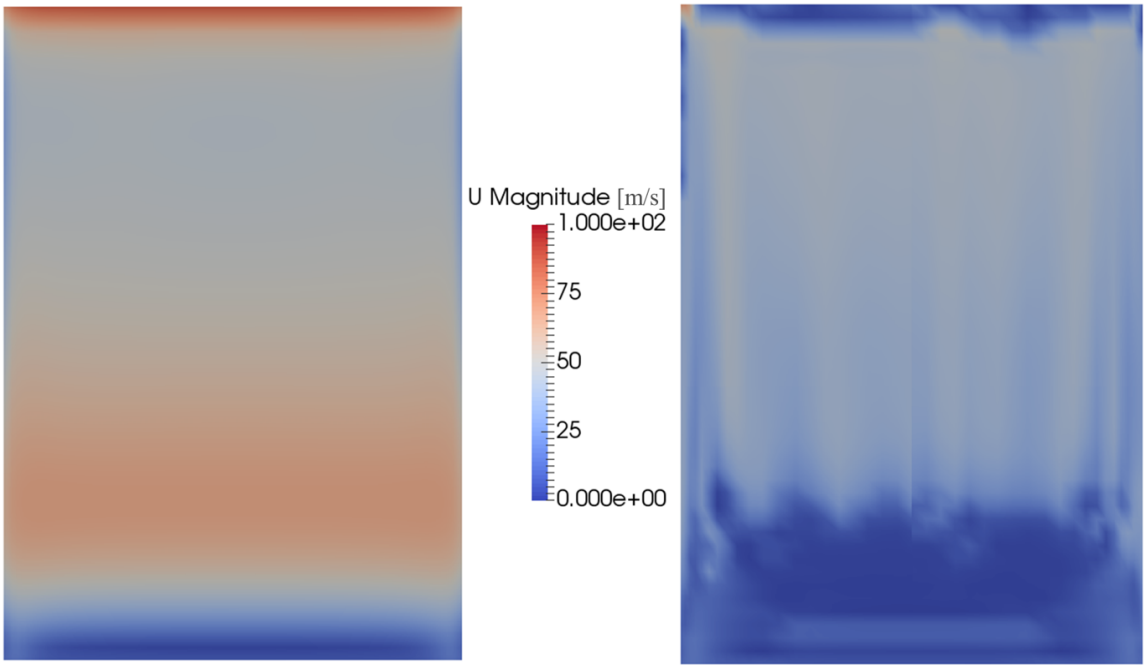

Figure 3.18: Pattern of velocity on the cells that share a face with the target boundary. Before deposition (left), and after porosity application.

should be lowered by extra considerations.

The projection of the deposit on the face normal to the flow as suggested in the previous paragraphs is an assumption that highly increases the actual amount of foulant deposited on the blade. Such operation would indeed "extrude" the maximum values of the deposits along the line to which it belongs. This procedure overestimates the overall deposit, since the maximum value is assigned to the entire line.

Volumetric Approach

A more accurate estimation would rely on the computation of the actual volume occupied by the deposits with respect to the volume of the cell under investigation. The degree of filling of the cell is the reduction factor to be applied to the porosity. From the same application reported above, the difference in the two cases have been computed.

By comparing the multiplication factor of the porosity (that are the degree of filling of the frontal area for the first case and the degree of filling of the cell for the second) some differences arise. Such multiplication factor is 100 to 2000 times smaller for the "volumetric" approach with respect to the "areal" one. This reflects directly on the value of the porosity coefficients D and F. The values of such coefficients is lowered from the order of magnitude of 10^{12} to $10^{9 \div 10}$. The volumetric filling reduces therefore the resistance of the porous medium to the flow, but it entails also the loss of some information. Indeed,

considering the projection on one face, the direction of the operation was relevant, with the volumetric approach it is not important. Therefore, the anisotropy that is conserved by the areal method is lost here.

The effects the volumetric approach entail are rather small if compared to the variation in the coefficients. Three order of magnitude in the reduction of porosity translates in just a 0.2 % in mass flow rate variation: the overall variation in the mass flow rate if compared to the clean case is about 5.3 %. The velocity pattern on the target wall is qualitatively similar to Fig. 3.18-right.

Log-Law Approach

Both the above-mentioned approaches are responsible for a generally high level of losses, meaning that a porosity coefficient averaged over the cell (area of a face or volume) is too detrimental with respect of the actual conditions. An higher porosity value, and thus a lower resistance for the flow should be probably employed for having more reliable estimation of the losses.

The different approach presented here does not make use of the Darcy and Forchheimer coefficients, but it rather consider just the effect of the porosity as worsening the boundary layer structures. The cells that are affected by deposition are applied the modified-coefficient log law. In the OpenFOAM implementation the way the log-law is treated influences the calculation of the turbulent viscosity ν_t. In this case the Spalding wall function Spalding (1961) up to the $\mathcal{O}(\kappa u^+)^3$ is used to model such feature, with the E coefficient changed to match the porous variation of the profile. This function is slightly different from Eq. 3.19, since it models all the regions (laminar, buffer and logarithmic) with a single equation. Nonetheless The application of the different coefficient E has effect only in the logarithmic area, since in the laminar sublayer, the equation collapses to $y^+ = u^+$ to be consistent.

By analyzing the effects of this last approach, the flow rate reduction for the same flow rate is of the order of 0.1 %, one order of magnitude less than the other two methods. This result seems to undershoot the losses with what is expected after the deposition. The presence of a small layer of porosity is therefore to be included, to account for the blockage and to the sink of momentum it introduces. Besides, the actual height of the deposit should be taken into account, since the variation of the log-law is universal in terms of difference between the average velocity and the velocity at the porous medium interface.

Final remarks

In this section three different methods for evaluating the losses related to cold fouling applications are presented. All the three methods are based on the assumption of treating the deposit as a porous medium, and from such perspective evaluating the losses. The porosity is implemented with the Darcy-Forchheimer law, that is useful to represent porous media independently from the Reynolds number.

The first method is based on the spacial subdivision of the boundary face in sub-facets by means of an auxiliary grid. The deposit is then stored in such facets and its projection on the face normal to the flow is the index of porosity of the cell. That index multiplies the actual porosity coefficients (Darcy and Forchheimer terms) in order to assign a porosity value to the cell that is representative of the actual level of filling of the cell.

The second approach is similar to the first, since the aim is finding an index for the correction of the porosity to account for the actual amount of deposits. This method corrects for the level of filling of the cell, considering the volume of the deposit with respect to the volume of the cell under analysis.

The last method does not consider the porosity index, but considers the porosity as it affects the boundary layer structures. In such a fashion, the porous cells are applied a boundary condition that uses a different log-law to account for the reduction in the non-dimensional velocity.

The application of the porosity coefficients as in the first two methods seems to lead to an overshoot of the losses. The order of magnitude of the coefficient for the porosity is still high even if reduced by a factor 10 (first method) to 1000 (second approach). A higher porosity (and thus a lower value for the Darcy and Forcheimmer coefficients) should be employed. On the other hand, the so-called log-law approach has shown to underestimates the actual effects of the deposition.

It is therefore advisable to use a lower porosity value, but including the effect of the variation of the boundary layer. The log-law should be changed, implementing such variation keeping into account the actual height of the deposit within the cell. Such remark represents a next step in this track, that would make the model ready to be applied in actual compressor fouling simulations.

3.2 Hot deposition

In this section, an innovative model for the estimation of the sticking probability is presented. The fouling effect is defined as function of particle velocity, temperature and size through an energy based approach. Expressing the energy involved in the impact through an Arrhenius' type equation a general formulation for the sticking coefficient is obtained. The method, named EBFOG (Energy Based FOulinG), is the first "energy" based model presented in the open literature that can account any common deposition effect in gas turbines.

Particle sticking on the first stage nozzle of the high pressure turbine causes several problems such as a growth of boundary layer thickness, decrement of the throat passage area and the clogging of coolant holes. These aspects can lead to the performance deterioration or, if the clogging of the cooling holes becomes severe, to a reduction of hot components life for thermal stresses, local overheating and creep Ogiriki et al. (2015). Furthermore a reduction in the passage area due both to a thicker boundary layers on the blades (due to the increased roughness) and to the build-up of foulant Kurz and Brun (2001),can lead to the reduction of the turbine capacity, especially near choking conditions.

3.2.1 Physics and experimental evidence

The understanding of the mechanism by which particles stick to the walls and the conditions which favourite or counter-act this process are of fundamental importance to predict the deposition rate. Indeed the first experimental studies to evaluate the extent of turbine deposition was carried out by Parker and Lee (1972). The deposit removal process is very time consuming and expensive: minimizing the deposition will reduce the time spent cleaning the engine and prolong the hardware's life. On the other hand the presence of the deposits must be avoided because it changes the roughness and the geometry of the walls. This aspect is very attractive in the perspective of introducing fuels derived from alternative sources Barker et al. (2013).

From the observation of several cases of deposition the influence of particle velocity, temperature and size has been identified, considering different experimental data in order to gain a better understanding of the fouling phenomenon. In particular sand deposition on a coupon at a prescribed approaching velocity Delimont et al. (2014) was considered, together with fly ash deposition on specimen varying gas temperature Crosby et al. (2007) and deposition efficiency in cold spray process varying the velocityDykhuizen and Smith (1998) and the temperature Legoux et al. (2007). Based on the observations made by Dunn (2012), the operating temperature investigated (i.e. 1800K) are well over the tem-

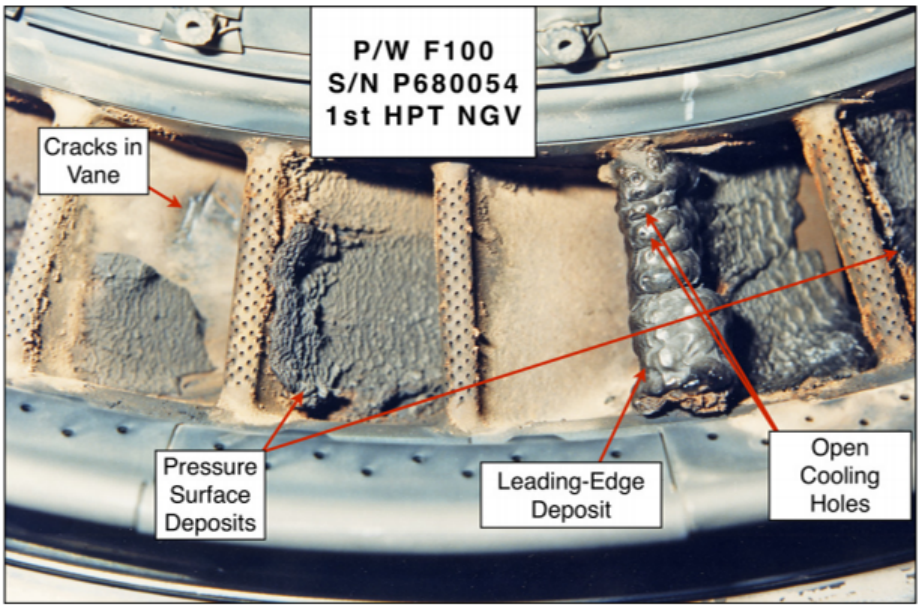

Figure 3.19: Deposits on high-pressure turbine vane leading edge for P/W F100. From Dunn (2012)

perature of 1283K. This temperature is referred to as a threshold TET (Turbine Entry Temperature) for the discrimination of the engine failure cause. Beneath this value, the main responsible of the engine damage is the compressor erosion. Over the threshold the first cause of failure is the deposition on hot section component: an HPT nozzle that underwent severe deposition issue is reported in Fig. 3.19.

The aim of this section is to provide a general model which can easily be implemented in every CFD code, to take into account the following contributions to fouling: particle, gas and wall temperature, particle size, particle velocity and particle composition. In order to do this the new model has been conceived as an energy based approach: as the energy involved in the impact increase, the sticking probability rises. The new approach shows good agreement with all the above mentioned cases. This model is based on an appropriate form of the Arrhenius equation which compares the energy of the particle/surface interaction (given by the sum of kinetic energy flux normal to the surface) with a threshold energy value (activation energy). If the impact involves an amount of energy greater than the activation energy the sticking process takes place.

Furthermore several application of this model to different kind of particle are presented. The final results of this paper are presented as a stability map for the engine (before the flame out) when the aircraft flies through a cloud of particles (such as volcanic ashes). The maximum flight time allowed depends on the density of the cloud and the accretion rate of the deposit.

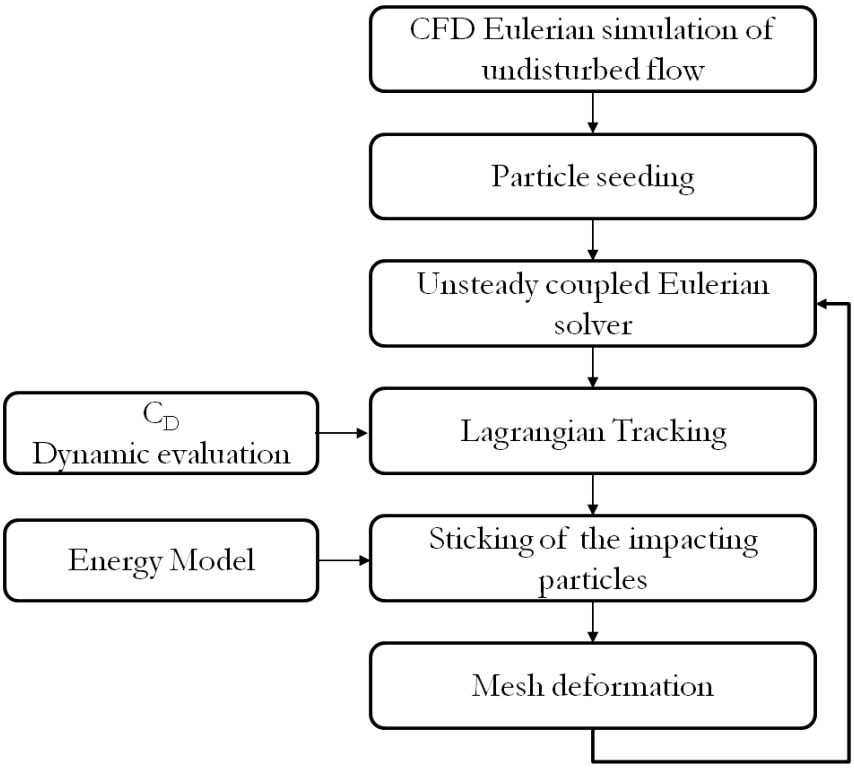

Figure 3.20: Computational procedure for the evaluation of deposition on hot section components

3.2.2 HPT deposition investigation

The procedure for the fouling effect evaluation on HPT nozzle performance follows the outline reported in Fig. 3.20. The model starts with a steady CFD solver that evaluates the flow field without the presence of a discrete phase. Once convergence is achieved, the particles are seeded. Thus two kinds of simulation has been carried on: a single way interaction (particle trajectory driven by the flow field) and a two-way interaction (particle affecting the flow field Elghobashi (1994)). The differences in the two approaches,explained in detail below, are very small, and therefore throughout this thesis, the one-way interaction model will be used.

From the flow velocity and the drag coefficient C_D of the particle (derived with the conditions suggested by Morsi and Alexander (1972)) a Lagrangian code evaluates the particles trajectory with a second order integration of the force.The particle tracking method is performed on a different grid using a jump and walk algorithm proposed by Mücke et al. (1996). The tracking implementation is fully parallel, as the CFD solver, and relies on message passing libraries (MPI).

When a particle hit the blade surface the energy based model evaluates the sticking probability. The proposed model is based on kinetic energy flux normal to the wall, temperature, particle size, and composition. If the particle sticks to the surface the geometry is automatically modified, re-meshed and the solver updates the flow field. The

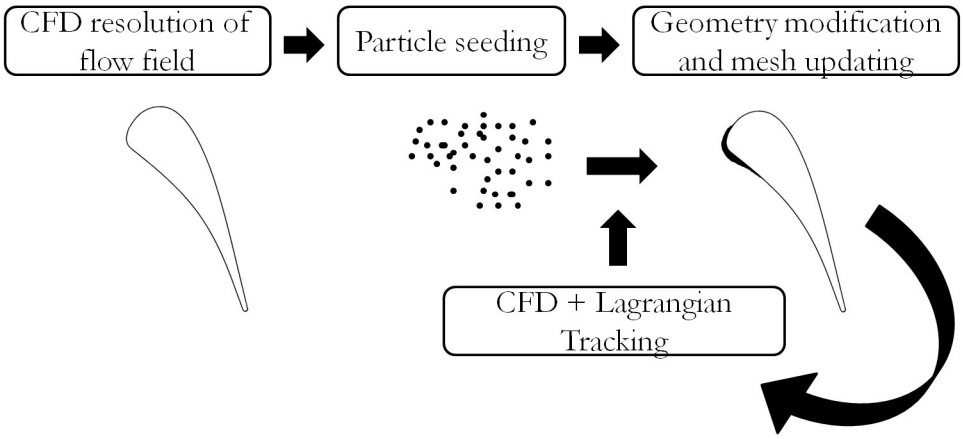

Figure 3.21: Sticking evaluation procedure

particles affect the flow field altering the boundary layer structure, shock intensity and roughness variation. It must be remarked that the effect of the roughness is not present in the simulations shown in this work because the mesh elements are bigger than the medium length scale that characterizes the roughness. In particular its change during the deposition process and the effect on the fluid flow has not been taken into account even if by using a denser mesh the solver will automatically model such effect.

The particle deposition in the first stage of a nozzle of an high pressure turbine, LS89 profile (see Arts et al. (1990)), has been investigated and simulated. In the following paragraphs the new approach towards deposition and fouling is explained, both in its physical outline and in its implementation: see Figure 3.21.

Once the undisturbed simulation reach the convergence, a specific distribution of particles is seeded. The particles seeding inside the computational domain has been done spreading a fixed amount of particles per each cell with a defined distribution of diameters. The particles distribution, size and concentration have been chosen following the suggestions of Taltavull et al. (2015) who defines thresholds for the particle dimension. The author has shown that even if the maximum size of particle ingested in an aircraft engine is about 100 μm, it is very unlikely that the bigger particles can arrive to the turbine: the size distribution reaching the turbine is very different from the one ingested at the intake. The causes for this change are basically two: the large particles are centrifuged towards the bypass air flow and part of those sent into the core are fragmented by the impact with compressor blades. The result of these interactions is that it is unlikely that particles larger than 30 μm can reach the turbine vanes.

The foulant agent used in this work is extracted from the Southern Iceland volcanic ash data, particularly it comes from the Laki volcano (exploded in 1784). Although slight difference in the composition and in the size have been reported Gislason et al. (2011), considering what found by Taltavull et al. (2015), the deposition deriving from this ash can be considered analogous to the case of the Eyjafjallajökull (the volcano which had

blocked the flights across the European skies in 2010). It is important to point out that the ash composition of the latter is poorer in iron and it is reasonable to expect a lower melting temperature, with an higher deposition rate.

The specific heat of the material found by Taltavull et al. (2015) is approximately 800 $J\ kg^{-1}\ K^{-1}$, while its density is roughly 3 $kg\ m^{-3}$. By following the distribution suggested by Taltavull et al. (2015) the particle size distribution is a uniform variable between 0.1 μm and 30 μm.

Quasi-Unsteady One/Two Way Coupling with Eulerian Solver

Depending on the particle concentration, the effect that the particles have on the fluid needs to be evaluated. In this article both the coupled and uncoupled method are used. The difference between the two approaches are reported below.

From the physical standpoint, the differences between the two methods lies in the correction of the conservation equations. In particular (since the variation of mass is not allowed in this article), the conservation equations for the flow field (3.21)

$$\frac{\partial}{\partial t}\begin{pmatrix}\rho\\ \rho\mathbf{U}\\ \rho e\end{pmatrix} = \begin{pmatrix}0\\ 0\\ 0\end{pmatrix} \tag{3.21}$$

must be modified and becomes:

$$\frac{\partial}{\partial t}\begin{pmatrix}\rho\\ \rho\mathbf{U}\\ \rho e\end{pmatrix} = \begin{pmatrix}0\\ \Sigma_i\mathbf{F}_{Di}\\ \Sigma_i H_i\end{pmatrix} \tag{3.22}$$

In the one way coupling, the particle has no effect on the fluid Elghobashi (1994) both in terms of momentum and energy transfer between the phases. Thus the problem of the computation of the flow and thermal fields can be solved in its classical form, Eq. (3.21).

In the two way coupling the transfer of energy and momentum from the discrete phase to the continuous one is computed. In this case the system of equations to be considered is the Eq. (3.22). The meaning of the terms on the right hand side of the Eq. (3.22) is the following:

- - The first term is the mass variation due to the particle-flow interaction. Since evaporation or condensation are not allowed in this treatise, this term is equal to zero.
- - The second one is linked to the momentum transferred from the flow to the particle or vice versa. It can be either positive (and tough the particle receive momentum from the fluid) or negative (the particle lose momentum in favor of the fluid). This happens for example in decelerating fluids or through shock waves. In general, this term is indicated with $\Sigma_i\mathbf{F}_{Di}$, where $\mathbf{F}_{Di}$ represents the drag force acting on the i-th particle contained in the cell.
- - The last term represent the transfer of energy between the two phases. This energy can be transferred in form of work done by the forces on the particles, and

though $\sum_i \mathbf{F}_i \cdot \mathbf{u}_{pi}$, where $\mathbf{u}_{pi}$ is the velocity of the i-th particle contained in the cell. Furthermore, a second kind of energy transfer may be present: the contact between particle and fluid allows the two phases to exchange heat. An additional term can be considered though: $\Sigma_i c_i \frac{\partial T_i}{\partial t}$. The last term of equations is $\Sigma_i H_i$, whit the meaning of Eqn. (3.23)

$$\Sigma_i H = \Sigma_i \mathbf{F}_i \cdot \mathbf{u}_{pi} + \Sigma_i c_i \frac{\partial T_i}{\partial t} \tag{3.23}$$

The treatise of the Lagrangian balance has already been discussed in the 2.2 section. In this work the drag coefficient C_D has been evaluated iteratively thanks to the correlations given by Morsi and Alexander (1972). The relation given by Morsi and Alexander (1972) for the evaluation of the drag coefficient is valid for perfectly spherical particles. As stated by Taltavull et al. (2015), the shape of the typical volcanic ash is far from being spherical. In this work, the assumption of considering an equivalent diameter for non-spherical particle has been introduced. A time buffer between the seeding of the particles and the sticking evaluation is required in order to let the particle reach their actual velocity. A test to evaluate the impact of particles in the free stream on shock structures has been carried out. With the concentration and particle sizes specified in this work a weak impact on shock structures is observed (without considering the deposition and subsequent geometrical variation). The actual tracking is described in section 2.5.

Sticking of impacting particles, EBFOG model

When a particle hit the blade surface the energy based model evaluates the sticking probability. The proposed model investigates the deposition process under a statistical mechanics perspective: during the impact the velocity and the temperature of the particle are involved. These features are the two sides of the same coin, being both a measure of the energy content, respectively thermal and kinetic. Starting from this idea it has been decided to consider the whole phenomenon from an energetic standpoint. The energy-based model is implemented through an Arrhenius-type equation. This equation in its general form, $k = Ae^{-\frac{E_{act}}{R_g T}}$, links the reaction rate to the temperature. In chemical reactions it considers that the higher the kinetic energy of two impacting particles, the higher the rate of the reaction.

This type of equations is used for the evaluation of the sticking process in heat exchangers. The initial rate of deposition (usually named crystallisation fouling) is driven by the concentration of the foulant agent. To foresee the accretion rate an Arrhenius type equation is used Reitzer (1964). In this article a similar equation is used to evaluate the deposition on the blades of an high pressure turbine. Basically, the denominator of the exponential is the specific thermal energy. So the equation can be read as a comparison between energies. Thus adding the velocity and the mass to the temperature

effect, a simple relation can be worked out and used to predict the sticking probability. Particularly, the effect of the dimension and the velocity is included in the kinetic energy. Hence its flux in the normal to the surface direction is added to the thermal energy at the exponential denominator. The exponential is the comparison between the activation energy and a reference energy for the case though.

$$S_p = Ae^{-\frac{E_{act}}{E_{case}}} \tag{3.24}$$

Where S_p is the sticking probability, E_{act} is the activation energy of the process and E_{case} is the reference energy for the case. This energy is comprehensive of both the kinetic and thermal terms. In particular, the temperature influences the activation energy of the process: the higher the temperature the lower the activation energy. This remark can be formalised expressing the exponential ratio in the following way:

$$\frac{E_{act}}{E_{case}} = \frac{C_1}{\frac{1}{2}m_p v_{p,n}^2 \left(1 + C_2 \frac{T}{T^*}\right)} \tag{3.25}$$

Where T^* is a certain temperature which cause the physical properties of the material to change. It is the softening temperature if the particle material is polycrystalline (e.g. ash, coal, sand) or the melting point if the material is a pure substance. In Eq. (3.25) the influence the temperature has on the activation energy is kept into account. In particular it is thought to affect the value of the constant C_1 through the Taylor expansion (3.26) truncated at the first order:

$$E_{act}(T) = \frac{C_1}{\left(1 + C_2 \frac{T}{T^*} + \cdots\right)} \tag{3.26}$$

The constant C_2 is a universal non-dimensional constant (it is the same for every materials) and it is equal to 3027: this value has been found through a multiparametric fitting procedure. In this way, thanks to a parametric fitting, the value of E and A can be extracted from the experimental data.Their value are thought to be dependent on the chemical composition of both wall and particle. Further studies are required to better understand the relation between these parameters and the conditions of the particle. In this sense this model can be considered a generalisation of the JKR model Johnson et al. (1971). The difficulties the usage of the analytical JKR model implies (prediction of the variation of the elastic properties of the material with the temperature, evaluation of the surface energy and effect of the impact) are overcome by EBFOG. By using the experimental data to obtain the model constants, it can be shown that the model is generally applicable. Eventually, to obtain the probability an incoming particle has to stick to the blade surface, the Eqn. 3.27 should be used.

$$S_p = Ae^{-\frac{C_1}{\frac{1}{2}m_p v_{p,n}^2\left(1+C_2\frac{T}{T^*}\right)}} \tag{3.27}$$

This is the fundamental assumption of the Energy Based Fouling model (EBFOG).

It must be remarked that the model to take into account the variation of composition of the blade surface during the deposition. In fact at the beginning of the simulation the blade is clean, but once a layer of deposit is formed, the material which covers the blade in the deposition area is the same of the incoming particles. For this reason the chemical interactions between the materials will be different in the two cases. The change in the activation energy of the process has not been taken into account, because few experimental data are available for the variation of the deposition rate with the exposure time but the proposed model can account this phenomenon.

Evidence of model validity based on literature

Several cases available in the literature have been investigated to prove the validity of the model. In the logarithmic graph of Figure 3.22 the linear trend of sticking probability with the reciprocal of the characteristic energy of the case is shown. The experimental data are taken from sand deposition on coupons at a prescribed approaching velocity Delimont et al. (2014), fly ash deposition on specimens varying gas temperature Crosby et al. (2007), deposition in cold spray coating processes Dykhuizen and Smith (1998) and coating in higher temperature processes Legoux et al. (2007).

Although the curves are representative of very different cases, the trend is similar. Adjusting the parameters in such a way that the curves becomes dimensionless and plotting the different cases in a logarithmic graph, all the cases of figure 3.23 collapse on a line.

If the groups of quantities which are related to the temperature (reduced temperature) are separated from the rest, in the Eq. 3.27, the graph represented in Figure 3.24 is obtained. A proof of the existence of a universal law for the energy variation with the reduced temperature is therefore achieved. By using Eq. (3.26) the same trend is shown. The depicted curve (where all the curves collapses) is the universal trend of the activation energy variation with the temperature. It is a rational function of the reduced temperature.

Boundary accretion

Particles deposition is a stochastic process which depends on the sticking probability. Particle energy is evaluated and, through the exponential comparison (3.24), the sticking probability corresponding to that energy value is estimated. To keep into account

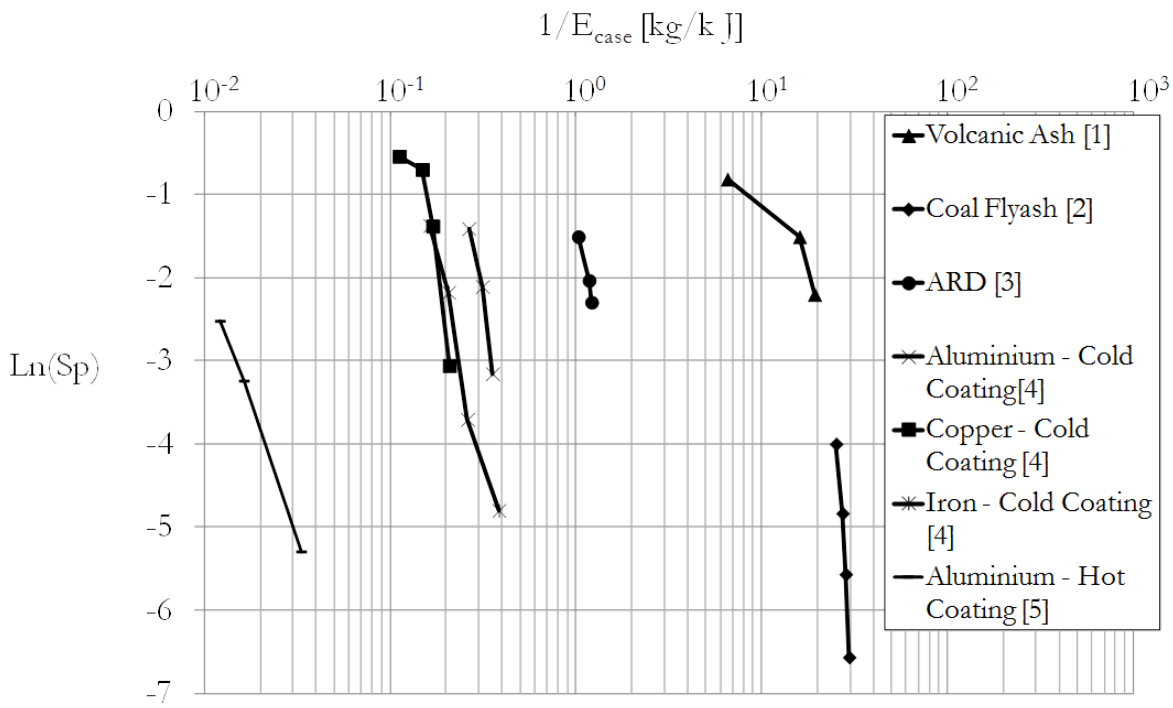

Figure 3.22: Comparison between different cases. References:1 Taltavull et al. (2015), 2 Crosby et al. (2007), 3 Delimont et al. (2014), 4 Dykhuizen and Smith (1998), 5 Legoux et al. (2007)

the contribution of each particle and to avoid problems such as the lowering of particle concentration, a Metropolis-Hasting algorithm is introduced.

The deposition of the particles on the surface determines the formation of deposits. It must be remarked that once a first layer of deposit is formed, the material of the surface changes. It is reasonable to expect a changing in the E_{act} and in the roughness of the wall in the deposition area. These aspects have not been considered in this work, mainly for lack of experimental data and mesh size. However a denser mesh can show a local increment in roughness, without altering the algorithm (even if in this case a full Navier Stokes solver needs to be used for the flow field evaluation). The accretion of the deposit has been built as normal displacement of the surface at the impact point.

Geometry modification as a result of the depostion

In this section the effects of the exposing a VKI - LS89 blade to the particle laden fluid are shown. Particularly two cases are analysed: the case of volcanic ash, as analysed by Taltavull et al. (2015), with composition specified in the previous paragraphs, and the case of sand Delimont et al. (2014) cloud. These two cases consider the impact of a volcanic or sand cloud during flight conditions. The difference on the shape of the deposition between these two cases and the effect on the performance are therefore pointed out.

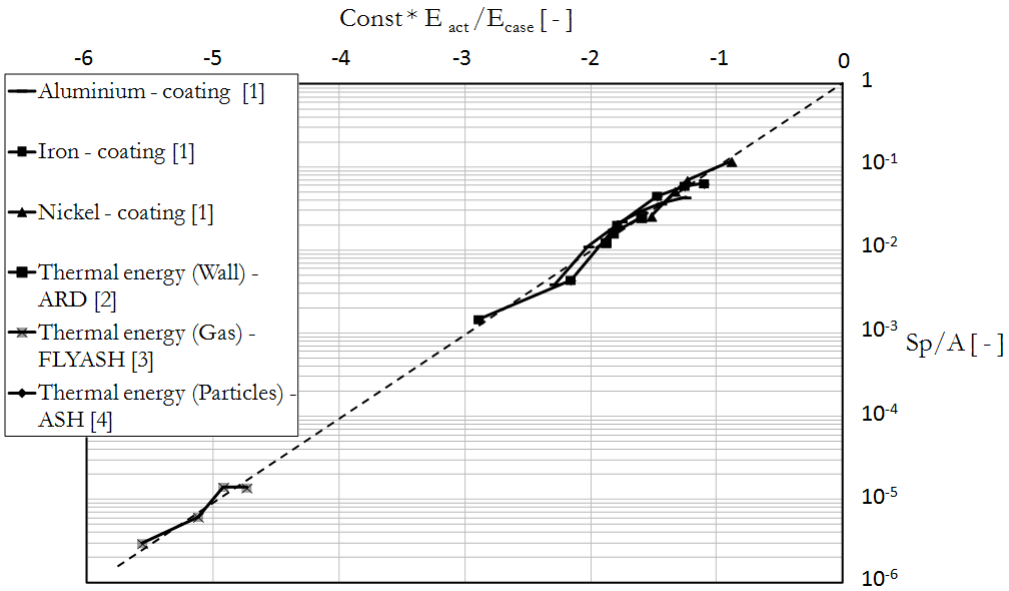

Figure 3.23: Comparison between different cases. References:1 Dykhuizen and Smith (1998), 2 Delimont et al. (2014), 3 Crosby et al. (2007), 4 Taltavull et al. (2015)

The results below are obtained using the boundary conditions provided by Arts et al. (1990), scaling the data to the corresponding typical values of a modern turbine. In this work the TET is assumed to be 1800 K and the static pressure at the inlet of the domain is assumed to be 10^6.

Quantitatively speaking the particles whose size is small (i.e. little or equal to 5 μm) tend to stick to the zone of the pressure side close to the trailing edge. This is because these particle have a small inertial effect and are able to follow quite entirely the fluid flow. The deflection from the streamlines happens only in the last part of the vane. The distribution of the deposit thickness along the blade (in normal to the surface direction) is shown in Figure 3.25. If the particle size is bigger (i.e. above 20 μm) the location of the impacts and of the deposition is shifted towards the leading edge. The variation of deposit thickness along the blade is reported in Figure 3.26.

From these graphs the variation of the throat area can be predicted. In this blade the throat area is very close to the trailing edge, being the duct simply convergent. The nominal minimum distance between two blades is $13.7mm$. The rate of variation of the throat area is evaluated for different concentration of the dispersed phase, for different particles material and for several ratio TET/T_{soft}. The results of these simulations are reported in Figure 3.27.

The y-axis in the previous graphs represent the rate of accretion of the build-up in the normal to the surface direction which corresponds to the throat section trace on the plane in this case. The unity of measurement is mm/s and though from this graph the reduction in the throat area can be derived.

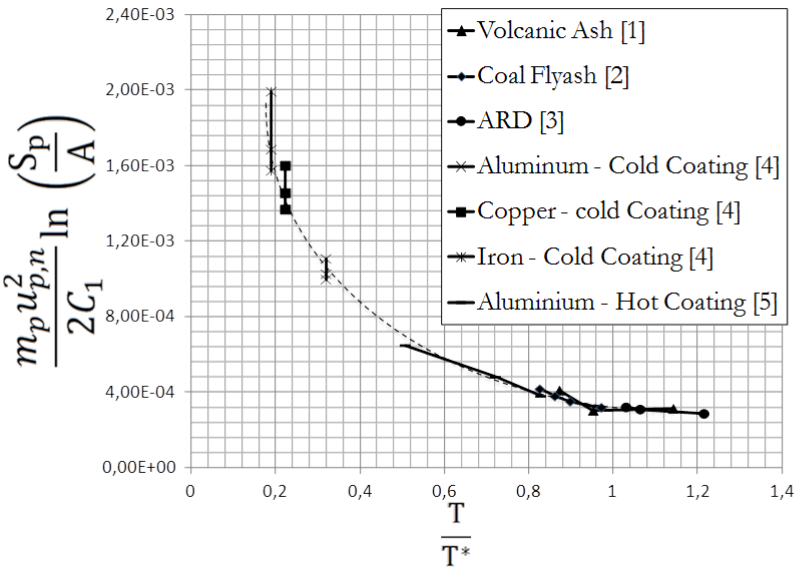

Figure 3.24: Universal law for the Activation energy variation with the temperature. References: 1 Taltavull et al. (2015), 2 Crosby et al. (2007), 3 Delimont et al. (2014), 4 Dykhuizen and Smith (1998), 5 Legoux et al. (2007)

Area Variation due to Fouling

The impact of area reduction on the jet engine performance is based on the fact that the flow processed by the compressor must be ingested by the turbine. So, in terms of non-dimensional mass-flow,

$$\frac{\dot{m}_1\sqrt{T_{01}}}{p_{01}} = \frac{\dot{m}_3\sqrt{T_{03}}}{p_{03}}\frac{p_{03}}{p_{01}}\sqrt{\frac{T_{01}}{T_{03}}}\frac{\dot{m}_1}{\dot{m}_3} \tag{3.28}$$

Where the subscript 1 stands for the inlet of high pressure compressor, 3 for the high pressure turbine section. The subscript 0 stands for the total value of the physical quantity. By assuming that the bleeds mass flow in the compressor are equal to the fuel mass flow ($\dot{m}_1 = \dot{m}_3$), the last term on the right hand side of the Eqn. (3.28) can be ignored.

A second assumption can be made: assuming that the cloud of foulant is encountered while the aircraft is flying at cruise velocity, the working point of the compressor is known and it is considered to be the design point. A common design assumption is that the design point lies on the line locus of the maximum efficiency points. This line is really close to the surge line, thus the risk of displacement of the working point beyond the surge line is not negligible in case of mass flow variation. In order to avoid this occurrence, a control system which prevent the point to cross the stall margin line (locus of the points whose distance from the surge line is equal to 2% of the adimensional flow) is always

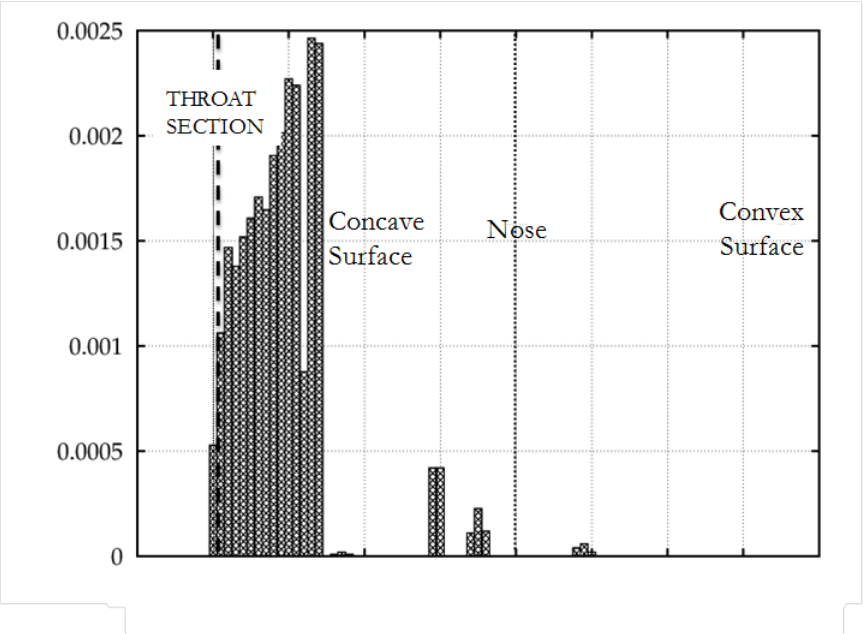

Figure 3.25: Thickness distribution on the LS89 VKI blade - particle size 1 μm at $T = 1800K$

present. In case the working point crosses the stall margin, the control system will reduce the load applied to the engine and the fuel flow to the engine. In the worst case scenario the engine will be switched off. This happens if the pressure ratio increases or the non-dimensional flow is reduced. Accordingly to its definition, this last quantity decreases only if $\dot{m}$ or T_0 decrease, or if p_0 increases.

The deposition of particles on the first stage HP nozzle can reduce the passage area of the vane. As a consequence, the capacity of the turbine will be reduced moving the compressor operating point towards the instability region (on the left of the surge line). If the reduction in the throat area increases, the compressor working point can cross the surge margin line. To avoid this risk, as suggested by Dunn (2012), the control system should reduce the TET to a value where the calcium impurity does not melt. The easiest way to do this is to retard the throttle to idle.

The amount of reduction in the passage area which causes the occurrence of such event depends on the specific engine, on the control system and on working parameters. Figure 3.27 shows the area variation in time as function of the concentration and the relative temperature. The area is reduced increasing the particles in the stream. Graphs obtained with the proposed model can for example be used to estimate how long an engine can flight in a volcanic cloud. Using the concentration of the cloud is possible to estimate the area change per unit of time. This reduces the mass flow of the engine by the same amount because the nozzle throat drives the engine mass flow. With this value is possible to estimate how many seconds/minutes the engine can flight before the compressor is too close to the stall region, using the compressor maps.

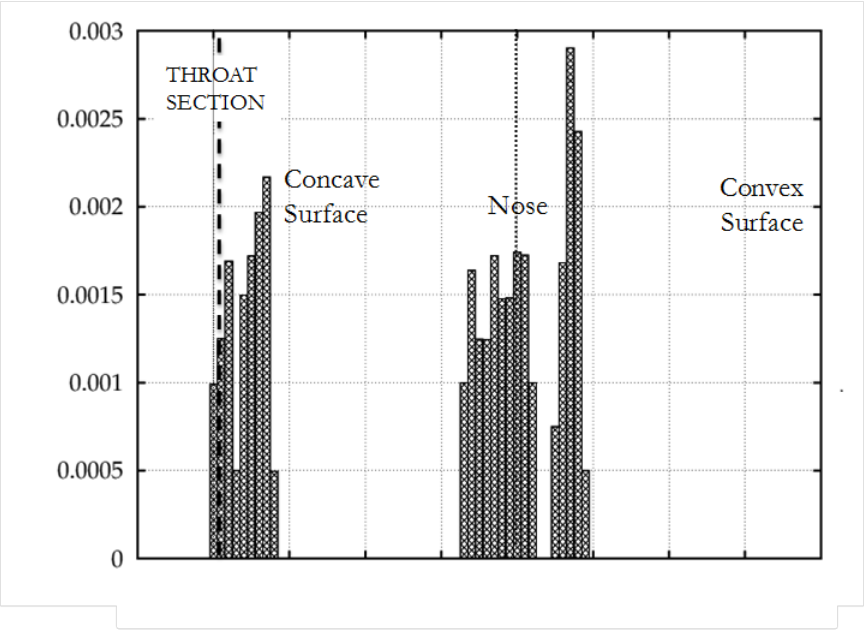

Figure 3.26: Thickness distribution on the LS89 VKI blade - particle size 25 μm at $T = 1800K$

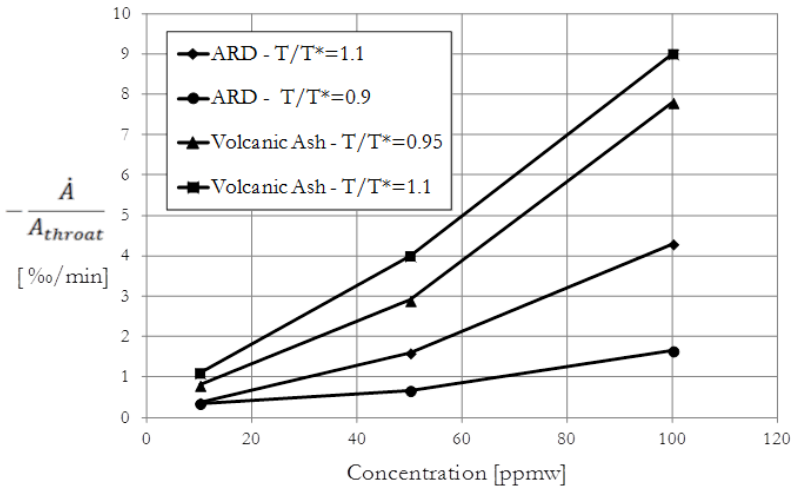

Figure 3.27: Area variation as function of the concentration and reduced temperature

Final remarks on hot section deposition

The present section reports shows the development of a fouling model that uses only the energy content of the particles, based on temperature and kinetic energy, to estimate the sticking probability. It is shown that the available data in the open literature verify the proposed law for the variation of the activation energy with the temperature. Though, whatever is the nature of fouling agent (volcanic ashes, sand etc), the sticking phenomenon is only connected to the energy content based on kinetic energy and thermal content, showing for the first time that a single model can characterize any common deposition phenomena in gas turbines, both in the compressor and in the turbine.

The model is implemented into a CFD solver and the well known LS89 test case

is modelled. A Lagrangian particle tracking is used and both the CFD solver and the tracking have a parallel implementation. In order to estimate the impact of flow field on particles and the influence of particles on flow structures, both a one way and a two way interaction model between the flow and the particles have been analysed and tested. For the final results a two way implementation is used.

For the LS89 simulation, an iterative approach is used to modify the geometry following the particle deposition. The deposition rate is used to evaluate the airfoil displacement and the geometry is modified accordingly. The mesh is altered and iteratively the flow field is updated by the CFD solver. The formulation is three dimensional and can be implemented in any CFD solver.

The impact of throat area reduction due to fouling it is also estimated. This is a crucial parameter in aircraft engines because it sets the mass flow of the engine and can push the axial compressor towards an unstable regime.

This page was intentionally left blank.

Chapter 4

Blade erosion

Erosion is a problem that mainly concerns aero-engines or, generally, aero-related applications. For instance, the operating life of helicopter engines operating in sandy areas is very short (from 50 to 250 hours) if compared to the same machine operated in a cleaner environment. Erosion in current commercial turbofan engines primarily attacks rotor blades, stator vanes, and outer shrouds in compressors. A study performed on commercial jet engines estimates that a minimum of 2 percent thrust specific fuel consumption loss is caused by the performance deterioration due to erosion, as shown by Tabakoff (1987).

The observed erosion mechanism can be described in terms of three distinct phases, which occur sequentially. In the initial phase, an impacting particle forms a crater, and material is extruded or displaced forming the crater. In the second phase the displaced metal is deformed by subsequent impacts: a lateral displacement of the material which can be accompanied by some ductile fracture in heavily strained regions. Finally, after a relatively few impacts, the displaced material becomes so severely strained that it is detached from the surface by ductile fracture, Levy et al. (1986). Alternatively, the micromachining model was proposed by Finnie (1972), where the erosion is due to removal of chips by sharp particles.

Analytical approaches for the erosion modeling are even more difficult to be achieved with respect to the sticking ones. Some models are available Das et al. (2006) but their validity has not been proven for gas turbine applications. Erosion models have typically coefficients that are tuned on the experimental results.

Examples of this category are the Finnie's model Finnie (1972) and the model by Tabakoff et al. (1990) that will be employed in the following.

4.1 Compressor Erosion

For the compressor erosion test case, the NASA stage 37 has been considered, as described in section 2.4.1. The steady state simulation has been performed under the boundary conditions reported in Tab. 2.2. Hydraulically smooth walls have been considered for this analysis. The validation of the simulation, the stage performance and the midspan rotor flow field are reported in section 2.4.1.

The Lagrangian phase has been tracked on the solved flow field with a steady-state approach. Specifically, sand ($\rho = 2560$ kg/m^3) has been injected at the inlet of the domain, seeding the parcels at the center of each of the domain faces. The shape of the injected particles is spherical.

This section is intended to be a sensitivity analysis to evaluate the effects of different parameters on the compressor stage. Specifically the numerical test that will be presented here focuses on the erosion level when a fixed particle flow rate analysis with different particle diameters are considered. Indeed, erosion is known to be caused by particles that have a larger diameter with respect to what is thought to be related to deposition issues, as reported in Ghenaiet (2012). Therefore the diameter investigated are 10 μm, 100 μm and 1000 μm.

The value of the particle flow rate to be injected is based on the study performed by Ghenaiet (2012), that considers the erosion of the first stage of the turbofan PW-JT8-D17 in taking-off conditions. Such conditions are reported in Tab. 4.1: the erosion tests here reported are carried out having as a reference the same particle-to-mass-flow-rate-ratio. The tested conditions for the analysis of the single blade, carried out considering fixed particulate mass flow rate, are summed up in Tab. 4.2.

The erosion model for the current analysis is the one provided by Ahlert, with the coefficients reported in Edwards et al. (2000). The erosion rate proposed by the model is based on Eq. (4.1):

Quantity	Value
rotating speed	8590 rpm
air mass flow rate	147 kg/s
number of blades	27
air mass flow per blade passage	5.444 kg/s
particle mass flow rate per blade passage	3.48 x $10^{-}3$ kg/s
particle to mass flow rates ratio	0.6395 x $10^{-}3$ kg/s

Table 4.1: Conditions for compressor erosion tested by Ghenaiet (2012)

Quantity	Value
Flow rate	20.309 kg/s
Rotor blade number	36
Mass flow rate per blade passage	0.564 kg/s
particle mass flow rate per blade passage	0.361 x $10^{-}3$ kg/s
particle injection velocity	171.3 m/s
particle density	2560 kg/m^3

Table 4.2: Injection conditions for the erosion test

Table 4.3: Ahlert constant for mild steel. From Edwards et al. (2000)

Constant in Eq. 4.1	Value
A	15.59·B-0.59·10-7 (B=Brinell Hardness)
α	$\pi/12$
a	-33.4
b	17.9
w	1.0
x	1.239
y	-0.1192
z	2.167
n	1.73

$$ER = AF_S F_\theta v^n \tag{4.1}$$

wehere A is a constant, F_S is the paticle shape factor (equal to: 1 for sand particles with sharp angles, 0.53 for semi-spherical particles; 0.2 for perfectly spherical particles), F_θ is a function of the impact angle θ, v is the particle speed relative to the wall and n is function of the particle speed. F_θ can be obtained according to the following relations, where θ is expressed in radians:

$$F_\theta = \begin{cases} b\theta + a\theta^2 & \text{if} \quad \theta \leq \alpha \\ xcos^2\theta sin(w\theta) + ysin^2\theta + z & \text{if} \quad \theta > \alpha \end{cases}$$

All the constant of Eq. 4.1, obtained on a purely empirical basis, are reported in Tab. 4.3.

4.1.1 Erosion pattern on the Rotor

Only the erosion pattern on the rotor will be investigated in this work. Different particle diameters reflect in different particle trajectories, and therefore in different erosion pattern. The impact of the particle size on their trajectory is reported in Fig. 4.1.

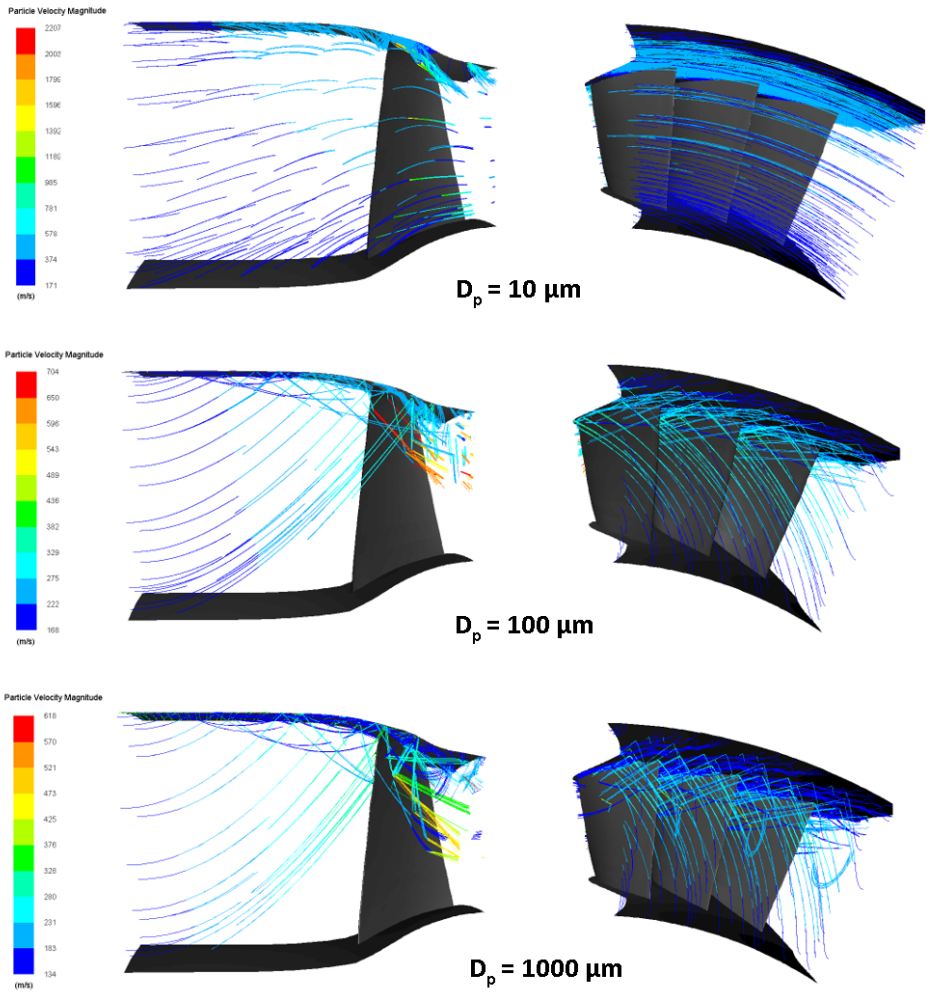

Figure 4.1: Particle trajectory in the rotor cascade, as a consequence of particle diameter.

It is well clear how particles that have smaller size tends to follow more closely the flow streamlines. This can be noticed especially comparing the trajectory of 10 μm particles with the one of 1000 μm: the centrifugal force has a major influence on the bigger particle, making them to deflect noticeably from streamlines. This remark is in line with the results available in literature, for example Tabakoff et al. (1990). Besides, smaller particle are heavily affected from tip leakage flows.

The difference in the trajectories reflect in a difference in the erosion rate on the shroud, as reported in Fig. 4.2.

The erosion pattern on the blade is reported in Fig. 4.4. All the particles size investigated impact against the leading edge of the blade contributing to the loss of material in this area. This result is in agreement with the experimental and numerical results found in literature. For example, Balan and Tabakoff (1984) report an experimental investigation on two dimensional compressor cascade. The results, summarized in Fig. 4.4, shows that the leading edge is flattened and the erosion is clearly visible both in pressure and suction side, the pressure surface of the airfoils is eroded with increase in surface roughness. The suction side surface remains unaffected except for the erosion that occurs in the

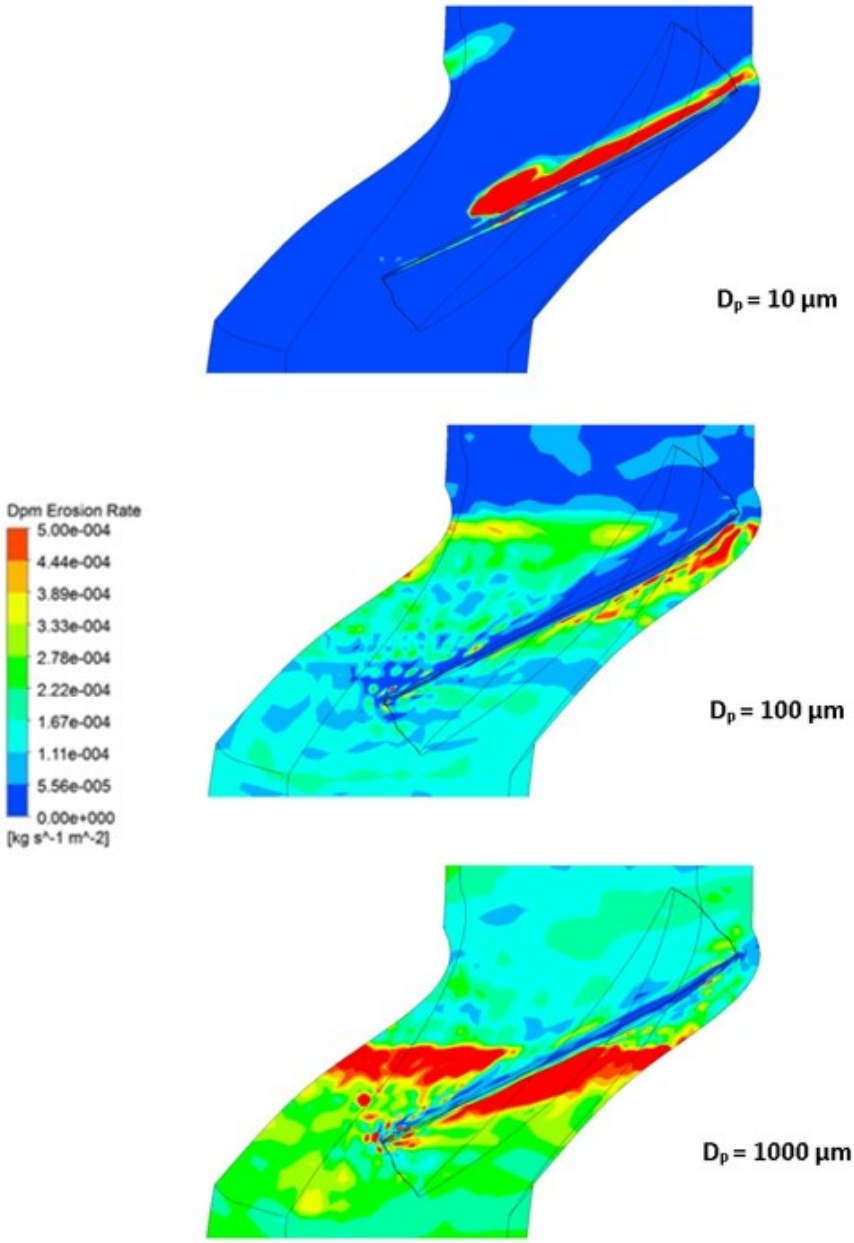

Figure 4.2: Erosion rate on the shroud for different particle diameter

leading edge and the increased surface roughness of a small region immediately following the leading edge.

Pressure and suction side erosion rate pattern are reported in Fig. 4.5 and 4.6. From such Figures it can be also seen the high values of erosion rate in the tip area: this is caused by particles that pass through the tip gap and thus, smallest particles are the main responsible.

Negligible erosion has been found in the hub region, due to the high centrifugal forces that tend to deflect particles toward the shroud.

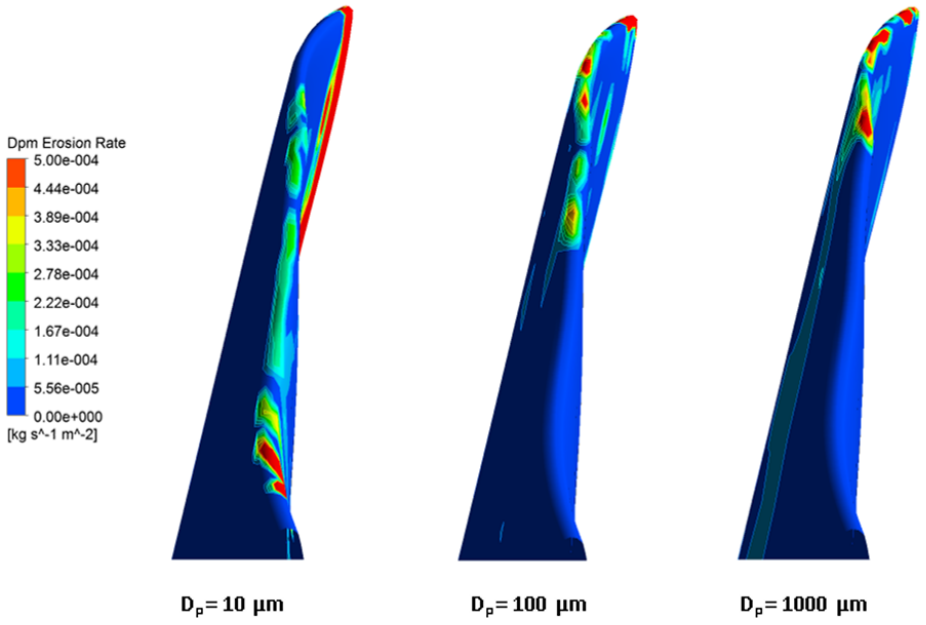

Figure 4.3: Erosion rate on the leading edge of the blade

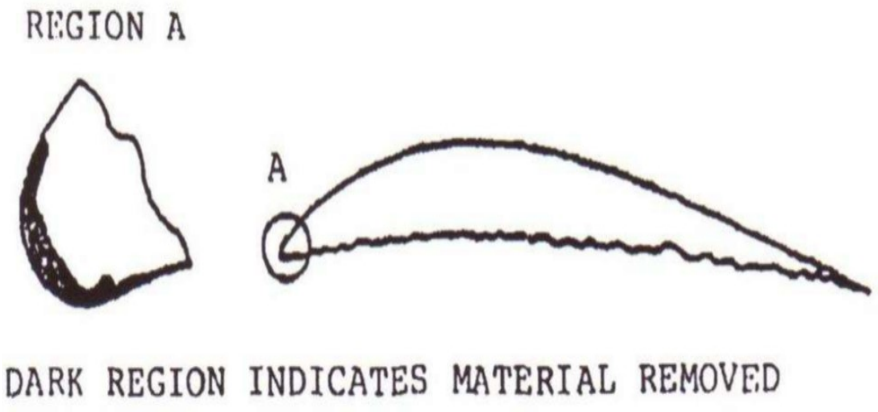

Figure 4.4: Erosion damages on compressor blade. From Balan and Tabakoff (1984)

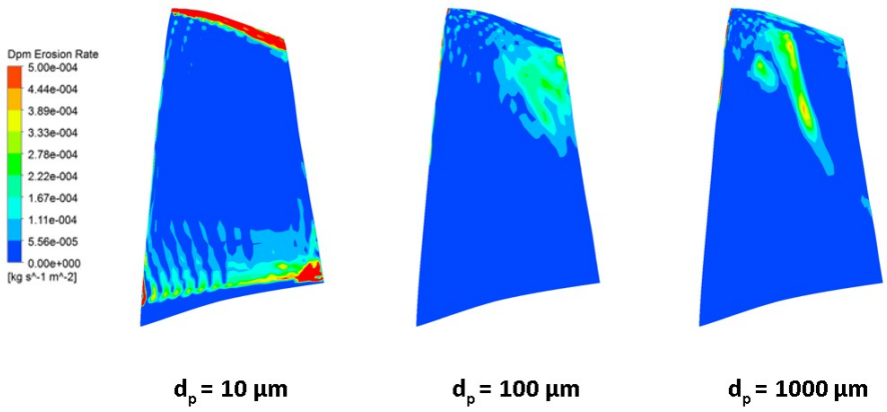

Figure 4.5: Erosion pattern on the pressure side

4.2 Turbine erosion

An impinging particle can stick or erode the metal which constitutes the blade. The deposition on the turbine blades is the main issue among the two and the clogging of cool-

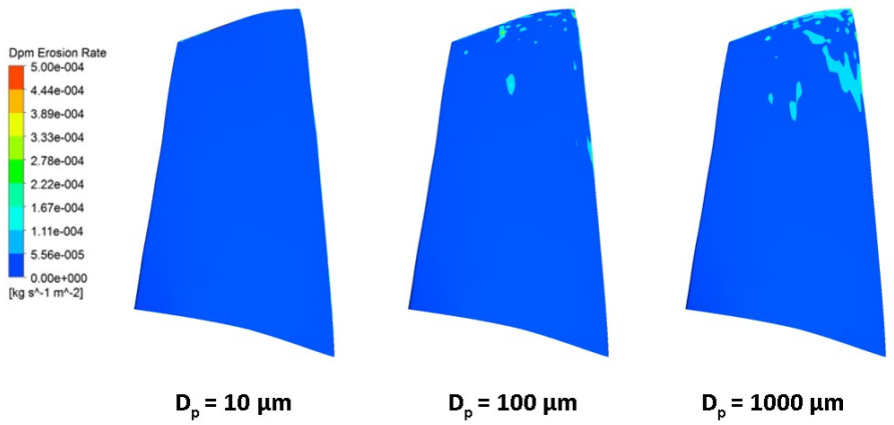

Figure 4.6: Erosion pattern on the suction side

ing holes can even speed up this process rising the blade surface temperature. Since the temperature affects the state of the particle and thus its stickiness, an higher temperature affects negatively the deposition problems.

In this section, the EBFOG model presented in 3.2 is coupled with the erosion, evaluated through the model proposed by Tabakoff. Geometry variation of blades subject to fouling are investigated by means of a moving mesh technique which accounts for the boundary displacement of the blade surface. The flow field, particle tracking and boundary accretion are obtained through an open-source CFD code (OpenFOAM® - 3.0.0).

Although in the former section only deposition issues on hot section components have been addressed, erosion is very dangerous as well, leading to the permanent loss of the material and to the irreparable change in the aerofoil. The main consequences of this problem are: increase in the tip clearances and blade surface roughness and changes in the blade shape, especially in the leading and trailing edges. The outcome of this process is the permanent deterioration in turbine performance and increased repair and maintenance costs. For more detailed explanations and analysis see, for example, Hamed and Kuhn (1995).

In this section the numerical study of the geometry variation of both transonic and subsonic vanes subject to fouling and erosion is investigated by means of a moving mesh technique which accounts for the boundary displacement of the blade surface.

The procedure to compute particles effect on the vane shape and thus on the turbomachinery performance follows the outline in Figure 3.21. Firstly, the CFD transient solver evaluates the flow field in the absence a solid phase. Once convergence is achieved, the flow is seeded with particles. These particles are tracked and the boundaries of the domain (blade) are updated. Then the undisturbed flow field is evaluated with the new geometry, in order to evaluate the differences in the performances.

When a particle hits the blade surface the EBFOG evaluates its sticking probability,

in the fashion described in 3.2. If the particle sticks to the surface, a mass balance is performed on the foulant deposit to determine its growth in thickness and the geometry is modified accordingly. The modification of the boundary it is hence done for every particle impact, thus the check for impacts is done for every time step. If no impact has occurred in the actual time step, the boundary is not changed. Blade is considered to be hydraulically smooth.

Particle deposition in the nozzle of the first stage of an high pressure turbine, has been investigated and simulated. The airfoils investigated are the VKI - LS89 profile (see Arts et al. 1990) and the GE - E^3 (see Davis and Stearns 1985).

Computational grid

The undisturbed flow field has been calculated using the opensource CFD software OpenFOAM ® v-3.0.0. The base mesh used for this work is a 2D mesh of the midspan profile. The mesh was realized used the utility *snappyHexMesh* provided with OpenFOAM®. The utility allows for the realisation of a hexahedra - dominated cut cell computational grid (further details can be found in Ingram et al. 2003). The quality of the grid obtained with this method is fairly high for the solver requirement. Two pitches have been considered in realizing of the GE - E^3 computational grid and three in the case of the LS-89. The meshes used can be found in Figure 4.7.

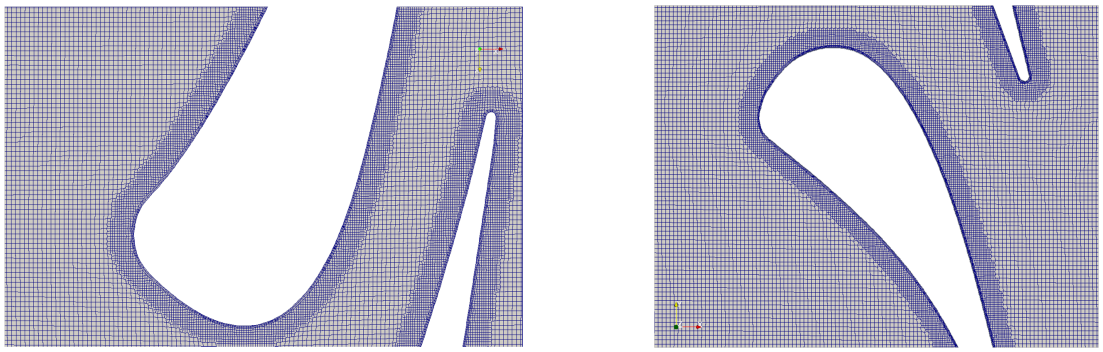

(a) Mesh for the GE-E^3 HPT vane (b) Mesh for the LS-89 VKI vane

Figure 4.7: 2D Meshes employed for the erosion prediction

Boundary conditions

The boundary conditions used for obtaining the flow field are reported in Table 4.4. The conditions for the E^3 have been taken from the design data reported in Thulin et al. (1982). The ones for the LS-89 are taken from Arts et al. (1990), but updated for realistic TET and pressure.

Once the convergence of the flow field is achieved particles are seeded at the inlet of the domain. The seeding follows the same in a random manner. The particles size

Table 4.4: Boundary conditions for the computation of the undisturbed flow field

	Quantity	LS - 89	GE - E^3
Inlet	p_0	1,493,500 Pa	1,324,600 Pa
	T_0	1700 K	1634 K
	Turbulence intensity	1 %	5 %
	Turbulence mixing length	0.0004 m	0.00174 m
Wall	T	1100 K	1100 K
Outlet	p	580,000 Pa	754,000 Pa

distribution was chosen according to the observation made by Taltavull et al. (2015): the maximum diameter injected is 30 μm. An uniform distribution has been chosen between the diameters of 1 μm and 30 μm.

Given the volumetric fraction related to the chosen concentration (i.e. 250 mg/m^3), the Eulerian-Lagrangian approach is used in this analysis, with the one-way approach. In this regime, the flow field affects (obviously) the particles movement, but not vice-versa.

The focus of this work is the direct effect of the ingestion of a volcanic ash on the shape of the HPT nozzle. For this reason it is assumed that the concentration of the cloud encountered by the aircraft passes entirely in the core flow.

Particle impact and mesh deformation

When a particle hits a surface, the EBFOG model evaluates its sticking probability. The kinetic energy of the particle, its surface and its composition are kept into account. Basically this model solves Eqn. 3.27, predicting the likelihood a particle has to stick to a surface. The sticking or the erosion capability of a particle depends on the value of this index: the decision is made using a Metropolis-Hastings algorithm. This procedure generates a pseudo random number belonging to range [0,1] to be compared with the value of S_p. This random number is the threshold: if S_p is greater than the threshold randomly generated the sticking process takes place. The displacement of the boundary has been implemented in such a way than particle mass is conserved. Whatever the impinging angle, the growth of the blade occurs always in the normal-to-the-surface direction.

If S_p is less than the randomly generated threshold the sticking process does not happen and the particle erodes the metal. Whatever the impinging angle, the erosion of the blade occurs always in the normal-to-the-surface direction. The amount of the displacement of the mesh face which has been hit by the particle is calculated according to the model proposed by Tabakoff et al. (1990). The ratio of the mass of eroded material to the mass of the impinging particle, ϵ, is predicted by Eqn. 4.2

$$\epsilon = K_1 \left\{ 1 + C_k \left[K_{12} sin \left(\frac{90}{\beta_0} \beta_1 \right) \right] \right\}^2 V_1^2 cos^2 \beta_1 \left[1 - R_t^2 \right] + K_3 \left(V_1 sin \beta_1 \right)^4 \tag{4.2}$$

Where, for fly ash particles impinging on steel (the coefficient used in this article), $K_1 = 1.505101 \times 10^{-6}$, $K_{12} = 0.296077$ and $K_3 = 5.0 \times 10^{-12}$. C_K is a parameter whose value depends on β_1 (impingement angle) and β_0 (angle of maximum erosion) as follows

$$C_k = \begin{cases} 1 & \text{if} \quad \beta_1 \leq 2\beta_0 \\ 0 & \text{if} \quad \beta_1 > 2\beta_0 \end{cases}$$

And $R_t = 1 - V_1 sin \beta_1$. The trajectories of the particles after the rebound if, erosion take place, are evaluated through the relations provided in by Tabakoff and Malak (1985). These empirical correlations are strongly material dependent and the equations for fly ash umpacting a 410 stainless steel have been implemented.

The effect of the deformed boundaries, due to erosion and deposition, is evaluated running the CFD simulations after the tracking of a certain amount of particles on the undisturbed flow field. The effect particles have on the walls is accounted for through the updating of the mesh. For quality requirement reasons, the movement of the boundaries is followed by a smoothing of the displacement on the internals point. The displacement of internal nodes is imposed solving a Laplace smoothing equation with constant diffusivity γ, as reported in eqn. 4.3.

$$\nabla \cdot (\gamma \nabla \dot{\mathbf{x}}) = 0 \quad in \ \mathcal{D} \tag{4.3}$$

Where $\dot{\mathbf{x}}$ is the mesh deformation velocity. The Laplace smoothing equation does not allow to take into account the coupling of the components of the motion vector due to rotation. This coupled motion can be handled by the pseudo-solid solver provided with the OpenFOAM®.

Deposition and Erosion analysis: effects

The CFD computation of the flow field has been carried out by using the *sonicFoam* solver of OpenFOAM ®. This solver is a pressure-based transient solver which uses a PISO method for handling the coupling of implicitly discretized time dependent equations. For a detailed description of the numerical scheme and its implementation the reader can refer to Marcantoni et al. (2012). In both cases the Crank-Nicolson method was used for

the time discretization. The boundary conditions used for the calculation are reported in Table 4.4.

The flow field resulting for the LS89 under the imposed boundary conditions is reported in Fig. 4.8a. Being the duct simply convergent, the throat section of the nozzle, labelled with the letter t, is at the very end of the vane. It is clearly visible that the flow is chocked. On the right hand side (Figure 4.8b), the isentropic Mach number distribution along the blade is plotted. The simulation of the ingestion has been run to simulate one physical second of ingestion time.

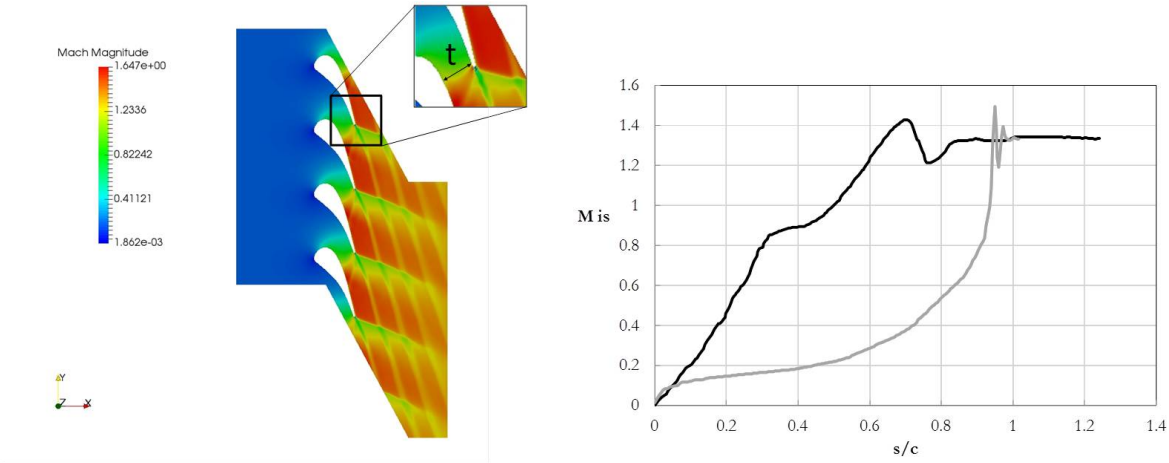

(a) Vane Mach when no ingestion occurs (b) Isentropic Mach along the clean LS 89 vane

Figure 4.8: Results for the flow field without particulate

Using the above mentioned models, the resulting deposition is located in the nearby of the leading and trailing edges (see Figure 4.9). In this figure the normal-to-the surface displacement along the blade is unwrapped. The negative displacement is index of deposition, whereas if the displacement is positive it is related to erosion. This result is remarkably similar to the one found by Webb (2011) investigating the fly ash deposition. This is the main consequence of the ingestion of the volcanic cloud together with an erosion of the pressure side (especially in the trailing edge region). From Figure 4.9, it is well clear that one of the area most prone to deposition is the throat section. It is well known, see for example Wenglarz and Fox (1990), the deposition in this section is the most significant, since it reduces the total mass flow through the turbine. Furthermore the aerofoil aerodynamic performance also is degraded most by deposit build-up on trailing edge regions. In this case both the effect occurs simultaneously. Although the effect on the following rotor blades aerodynamics has not been investigated in this article, a major drop in their performance is reasonably expected.

The linear average rate of accretion of the build-up over the first second of contaminated air ingestion can be derived from Figure 4.10. In Figure 4.10, the wall displacement (deposit/erosion) normalised with respect to the length of the vane (span) is reported. Being the case a 2-D analysis, the results are reported as a displacement (m_{disp}) per unit

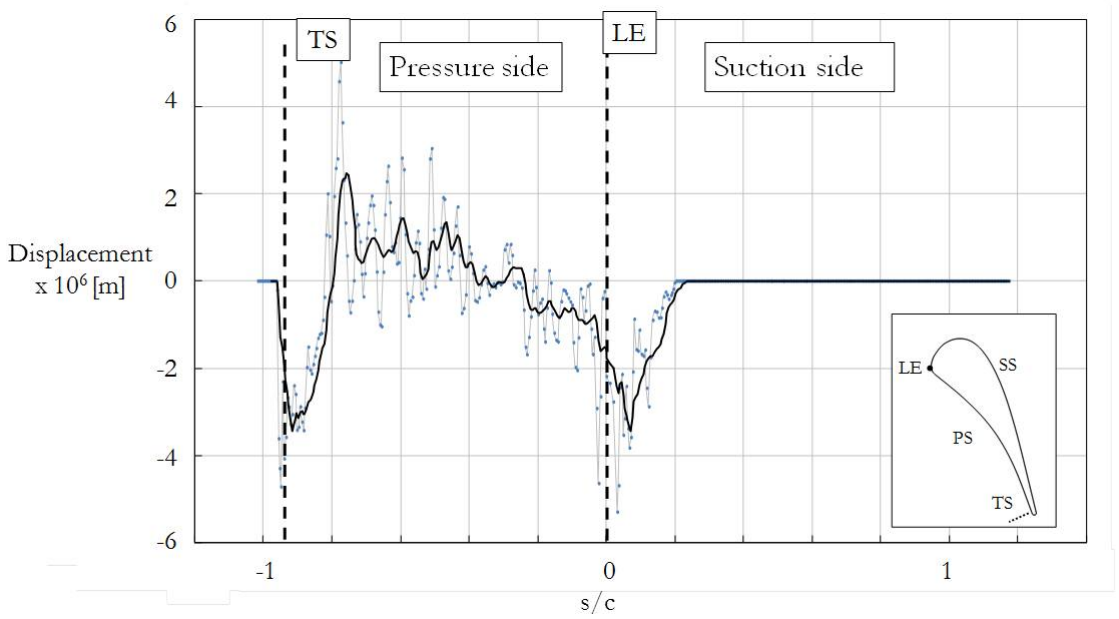

Figure 4.9: New blade profile after 1 s of exposure to 250 mg/m^3 contaminated air

length (m_{span}). The growth of the deposit follows a trend that is quite linear. A linear regression for this behaviour gives R^2=0.99. The linear assumption for the reduction of the 2-D throat section is therefore reasonable. For what concerns the erosion it can be seen that the rate of material ablation is rather constant (slope of the interpolating line). Here again the assumption of eroded material proportional with the time (in the 2D case, over the first second of ingestion) is acceptable (R^2 = 0.94). The rate of erosion and deposition are respectively 1.75x10^{-2} m_{disp} m_{span}^{-1} s^{-1} and 1.57x10^{-2} m_{disp} m_{span}^{-1} s^{-1}.

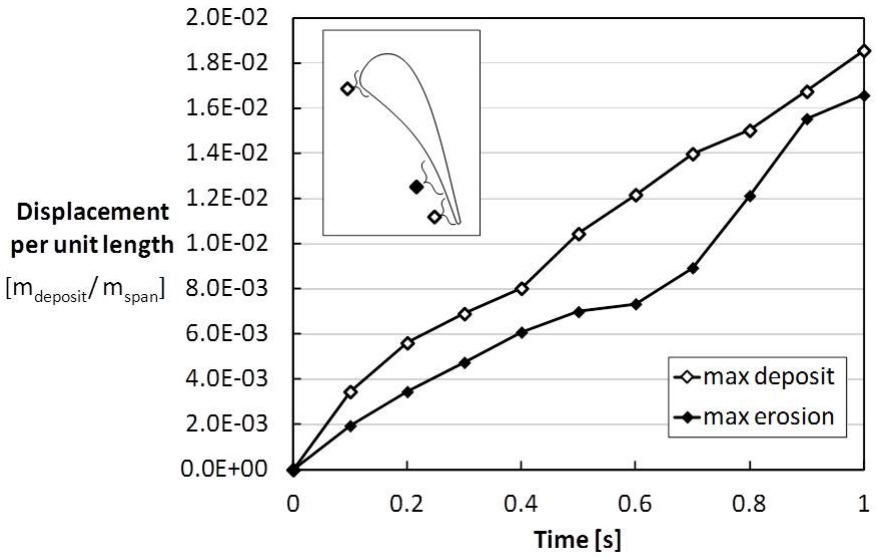

Figure 4.10: Linear displacement of the wall for the LS-89 vane over the first second of exposure to 250 mg/m^3 contaminated air

GE - E^3

The flow field resulting for the GE - E^3 under the imposed boundary conditions is reported in Figure 4.11a. The throat section of the nozzle, labelled with the letter t, is in the nearby of the end of the vane (the duct is convergent - divergent). In this case in the throat section the flow is subsonic and thus the duct is not in chocking conditions. On the right hand side (Figure 4.11b), the isentropic Mach number distribution along the blade is plotted. The simulation of the ingestion has been run to simulate one physical second of ingestion time.

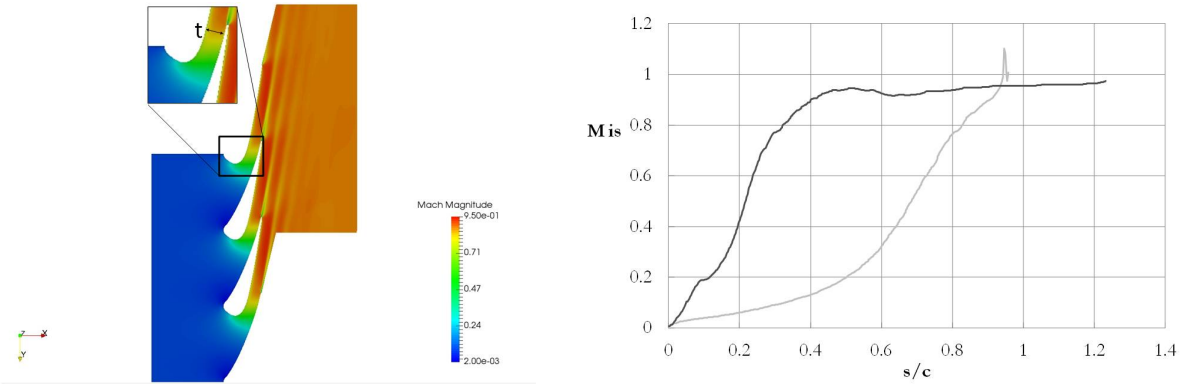

(a) Vane flow field when no ingestion occurs (b) Isentropic Mach along the clean EEE vane

Figure 4.11: Results for the flow field without particulate

The linear average rate of accretion of the build-up over the first second of contaminated air ingestion can be derived from Figure 4.12. In Figure 4.12, the wall displacement (deposit/erosion) normalised with respect to the length of the vane (span) is reported. Being the case a 2-D analysis, the results are reported as a displacement (m_{disp}) per unit length (m_{span}). The growth of the deposit follows a trend that is quite linear. A linear regression for this behaviour gives R^2=0.99. The linear assumption for the reduction of the 2-D throat section is therefore reasonable. For what concerns the erosion it can be seen that the rate of material ablation is rather constant (slope of the interpolating line). Here again the assumption of eroded material proportional with the time (in the 2D case, over the first second of ingestion) is acceptable (R^2=0.99). The rate of erosion and deposition are respectively 6x10^{-3} m_{disp} m_{span}^{-1} s^{-1} and 6.6x10^{-3} m_{disp} m_{span}^{-1} s^{-1}.

It can be seen form Figure 4.13 how the throat section is subject to deposition. In this figure the normal-to-the surface displacement along the blade is unwrapped. The convention on the sign is the same of Figure 4.9 (negative displacements mean deposition and positive ones stand for erosion). This result shows an average behaviour of deposition on the pressure side of the blade from the leading edge up to the throat section where the deposition has its peak. Moving downwards along the vane, a peak of erosion is detected and the trailing edge area seems not to be affected by the particle impingement. This overall behaviour is the same found by Webb et al. (2013) on the same geometry but with different test conditions. In that work, coal fly ash deposition is experimentally

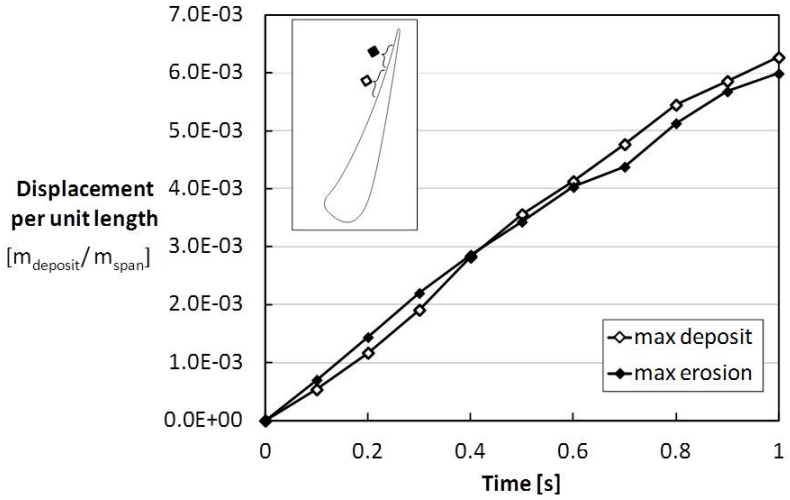

Figure 4.12: Linear displacement of the wall for the E3 vane over the first second of exposure to 250 mg/m^3 contaminated air

investigated and massive deposition is found up to the throat section. After that point no deposition is reported.

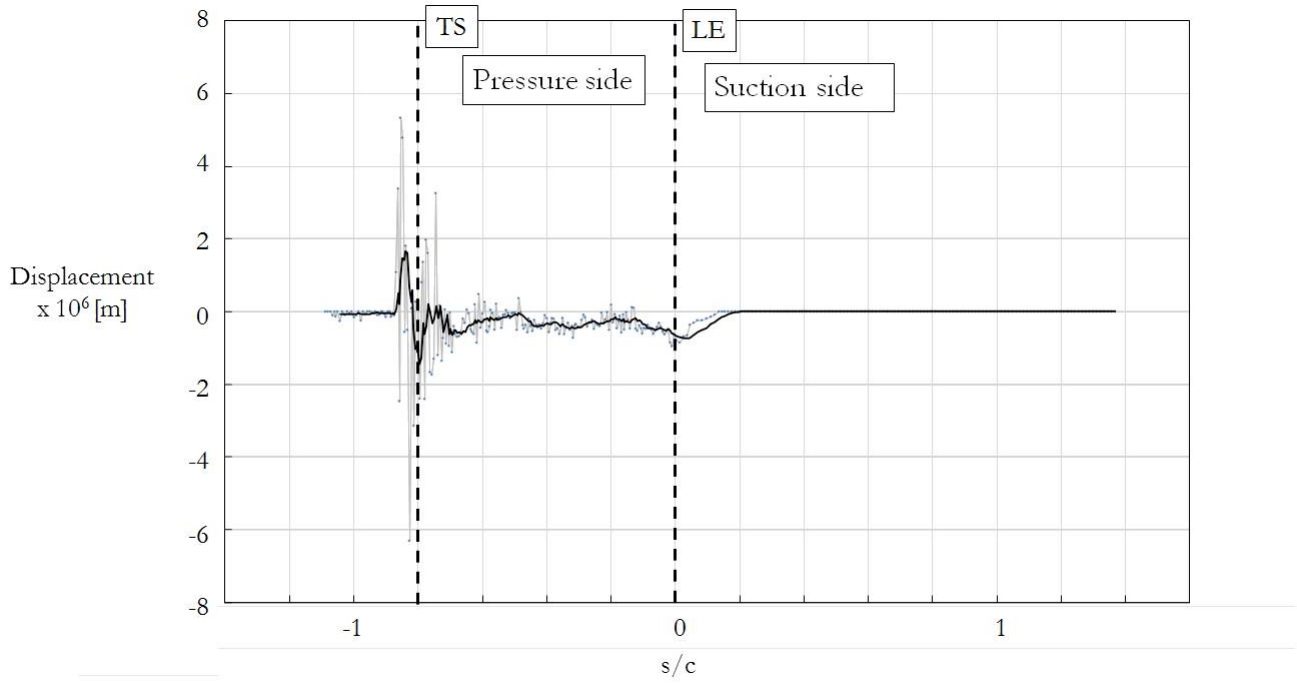

Figure 4.13: New blade profile after 1 s of exposure to 250 mg/m^3 contaminated air

Final Remarks

In this section the consequences of the ingestion of a volcanic ash cloud with a concentration of 250 mg m^{-3} on the nozzle of two modern high pressure turbine is investigated. The consequences of a flight through such a kind of cloud are both erosion and deposition, even if the deposition is the major effect. This trend appears in both cases of transonic

and subsonic vane, even if in the transonic case the prevailing of deposition is more accentuate. The absolute location of the deposit is different in the two cases: in the LS-89 vane the pressure side in the nearby of the trailing edge experiences the highest deposition rate whereas in the second case the trailing edge is eroded. In both cases the deposition has its peak in the throat section. This remark enforces the need of monitoring the evolution and the rate of accretion of the throat section.

This page was intentionally left blank.

Chapter 5

Exposure over time - effects on the deposit

In this chapter a detailed analysis of the deposit evolution over time is reported. The mechanisms that bring to deposit weakening and subsequent detachment or to its toughening, making it more difficult to be removed are discussed. The cold and the hot section will be treated separately, since they are subject to different phenomena that lead to completely different deposit behaviour.

5.1 Deposit evolution in compressors

Variations in the flow field can make the flow quantities close to the deposit to change, and it may happen that the conditions for the sticking do not hold any longer. If this is the case, the build-up detachment may happen. This occurrence can mitigate the fouling effects and may be exploited for keeping the performance of the compressor as high as possible over the operating period. In this section, the evaluation of the adhesion forces and the possible deposit detachment will be investigated. Particularly, the same forces that keep a gecko stuck to a surface are considered, as sketched in Fig. 5.1: the van der Waals forces (due to the proximity of the two bodies) and the Laplace force (due to the curvature of the liquid film related to the humidity). The so formulated model, named gecko-like for such a reason, is used for the numerical analyses of a deposition problem. Both the sticking and possible build-up detachment are considered. The results reported here can be regarded as an a-priori estimate of the forces to be kept into account when dealing with compressor fouling problems.

Besides deposition modeling, that has been the focus of the section 3.2, extra care should be taken when one evaluates the evolution of the deposit over time. In other words,

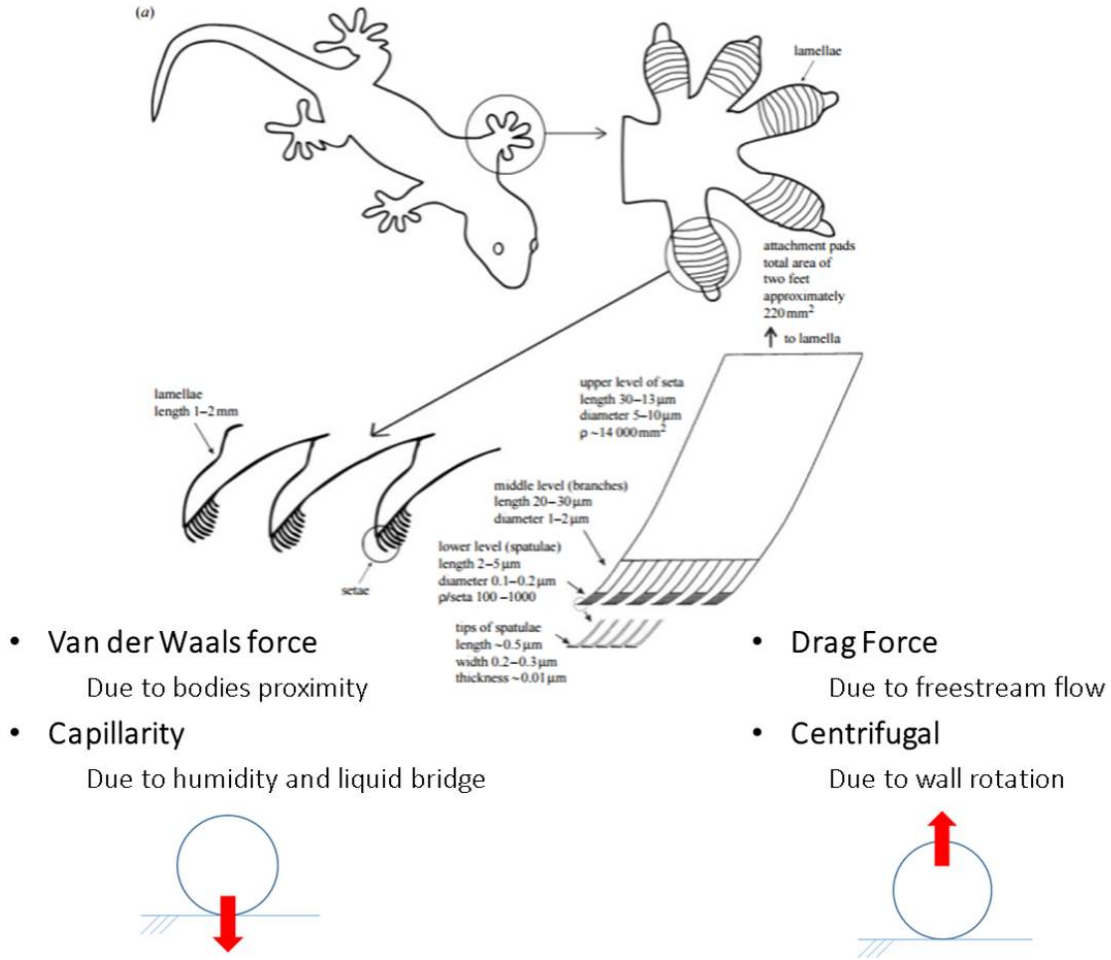

Figure 5.1: Gecko-Like model: the forces acting on a particle stuck on a surface are the same that keep a gecko stuck to a wall

the flow conditions may be suitable for the particle sticking (according to the model one is using), but at the same time the particle cannot hold on such surface: the drag force may be too strong or the flow conditions can change and detach the particle itself. On the top of that, the presence of humidity or, generally speaking, a third substance at the particle/surface interface is known to have a major effect on the sticking capabilities of a particle, as shown by Aldi et al. (2017a). This study is particularly focused on this aspect of the performance degradation. With the test bench described in Appendix 2, long lasting tests have been performed. Looking at Fig. 5.2 it is clear how the adhesion phenomenon is affected by the detachment process over the exposure time. This is the problem that is of concern in this section.

A simple test case, presented in section 2.4.1, is analysed under such light. The conditions for the particle sticking and the flow velocities are similar to those one can find in a subsonic compressor. Particular attention is drawn on the particle behaviour and particle-wall interaction: both the sticking and the deposit detachment is discussed and modelled. The variation of wall shape is kept into account accordingly by a moving mesh technique.

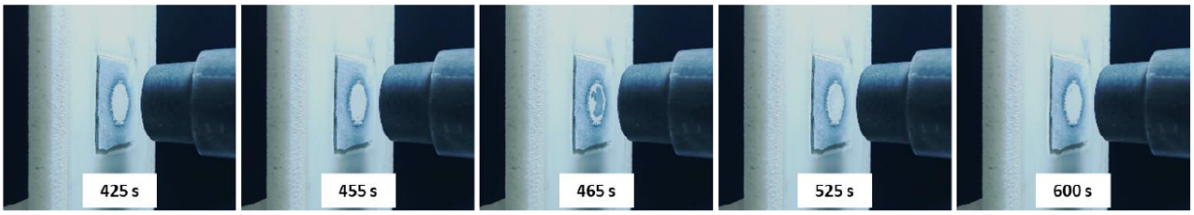

Figure 5.2: Frame analysis. Test condition: exposure time of 600 s, impact velocity of 22 m/s

In the following several sensitivity analyses will be carried out in order to outline the quantities and the conditions under which a stuck particle can detach from the surface. Varying the inflow conditions, the centrifugal force acting on the particle, the filling angle due to the liquid bridge and the nature of such bridge (humidity rather than a oily substance) the forces that should be considered when compressor fouling is analyzed are pointed out.

When an impact with the wall takes place, the sticking decision has to be made. The sticking model proposed by Poppe et al. (2000) and discussed in the section 3.1 is applied here.

Boundary displacement

If sticking happens, the geometry should be updated consequently. In the numerical approach implemented in this section the boundary displacement due to particle sticking is reported in Fig. 5.3.

A particle sticking to the blade reflects in a variation in the domain boundaries, causing the inflation of the surface inward the domain. Such a deformation have been implemented by the authors as a displacement of a node of the mesh on the blade. The node that is moved is the closest to the impact point, as shown in Fig.5.3. The amount of displacement is such that the particle mass is conserved. The final shape of the domain is a quadrilateral-based pyramid. The choice of moving to this approach, from the first implementation described in 3.2, is to have a more realistic representation of the actual deformation. Indeed in the "facial deformation" approach the spread of the deformation involves 9 faces in case of structured grid for every impact as can be seen in Fig. 5.4. This new

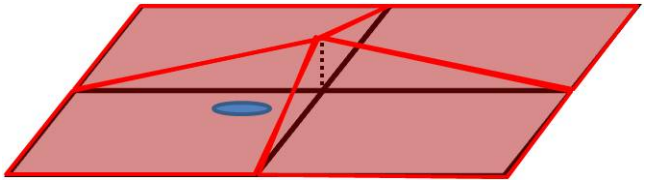

Figure 5.3: Boundary faces displacement due to particle sticking: nodal deformation

approach is the one that minimizes the "numerical spread" of the particle that is intrinsic in the dynamic mesh approach.

The algorithm proposed here is the following. Once a face is hit, the nearest mesh node is sought. Identified the point, the four boundary faces sharing the node are located and their center position is acquired. In this fashion, the control area that constitutes the base for the volume of the displacement is the area comprised within the quadrilateral which vertices are the centres of these faces, as reported in Fig. 5.5. The final shape of the boundary in the impact area is reported in Fig. 5.3. The amount of the displacement is such that the volume of the pyramid is the same of the stuck particle.

Detachment

The decision of whether the particle detaches or not is made after a force balance is carried out on the stuck particle. Particularly, the detaching forces acting on the particles are the centrifugal and the drag force. These forces have usually different directions but in first approximation they can be both applied to the center of gravity of the particle. Especially, the drag force is usually applied further from the surface with respect to the center of mass, see O'Neill (1968) for further details. Other effects, such as turbulent bursts, have not been kept into account since the work of Soltani and Ahmadi (1994) proved these are negligible.

For what concerns the forces that tend to keep the particle attached to the surface, the main forces are the van der Waals and the capillarity Berbner and Löffler (1994). The electrostatic force is always small (of at least one order of magnitude) and can therefore be neglected in the analysis.

The detachment of the particle from the surface is thought to be due either to the force in the normal to the surface direction and to the rolling detachment. The rolling detachment may happen due to the action of the detaching torque. This moment is defined as the one due to the action of the detaching forces on the liquid film edge, assumed as the momentum pole. Further details on this are given below.

In the following, all the forces acting on the stuck particles are listed and explained. It must be remarked that the particles that roll or slide along surfaces many times can

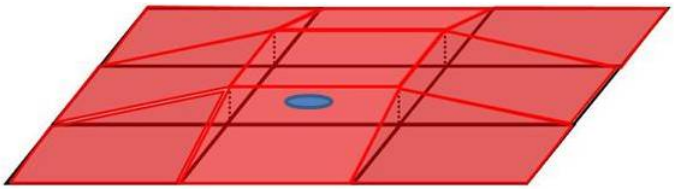

Figure 5.4: Boundary faces displacement due to particle sticking: facial deformation

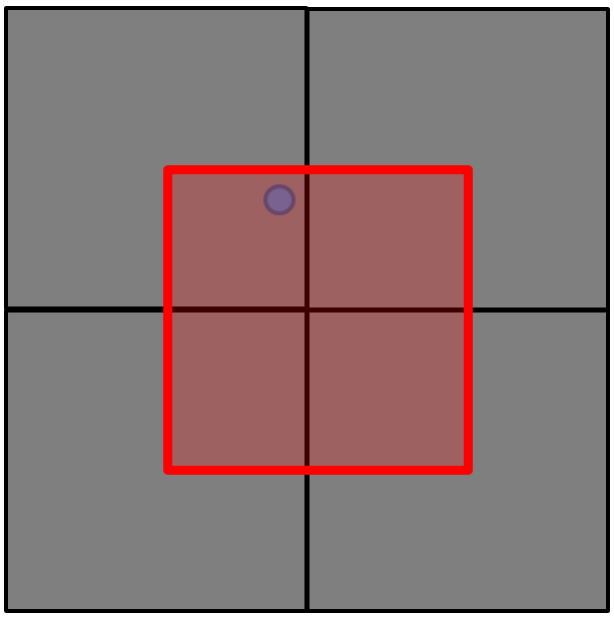

Figure 5.5: Control area for the displacement evaluation. In grey the boundary mesh used for the CFD. The impact point is depicted with the circle and in red the control face used for the deposit height evaluation

become highly charged, and particles containing large quantities of crystalline materials such as quartz can have a piezoelectric effect when deformed in an impact that would result in charge buildup. In this case such forces are neglected, as suggested by Soltani and Ahmadi (1994) as well as turbulent bursts.

Capillarity

The presence of humidity in the air results in a thin water film around the particle. Alternatively, this film may be composed of oily substances, depending on the environment the particle is. When the particle sticks to a surface the liquid film acts as an adhesive meniscus that fights the forces that tend to remove the particle from the surface. The total force through the bridge between sphere and the plate consists of three parts, as suggested by Orr et al. (1975): a surface-tension force (inside the meniscus), a capillary pressure force (transmitted by the water, but originates in meniscus curvature), and buoyancy in the wet segments of the sphere and plate. In this work the capillarity force is intended as composed by two contributions: the Laplace force and the surface tension force. The buoyancy is neglected since the effects of the gravity are very small (the volume of fluid enclosed in the liquid bridge is negligible).

The Laplace pressure arises when one solves the surface tension in the normal to a circumferential circle direction. If one considers a vapour bubble in a liquid, this must react to the force with an internal pressure in order not to collapse Israelachvili (2011). The same pressure is experienced by the meniscus between particle and surface. Thus the Laplace force is caused by the pressure difference across the interface of the curved

surface. An expression for this pressure was given by Orr et al. (1975). The basic idea of the relation is that the force is proportional to the pressure difference times the meniscus area. The formulation of the Laplace force proposed by Orr et al. (1975) is:

$$F_L = -\pi\kappa\gamma R^2 sin^2\Psi \tag{5.1}$$

Where κ represents the mean curvature of the meniscus, γ is the surface tension of the liquid of the meniscus, R is the particle radius and Ψ is the filling angle. The geometrical parameters are reported in Figure 5.6. For the calculation of the mean curvature and of the filling angle the procedure outlined in Kim and Bhushan (2008) can be employed.

The thermal equilibrium relation (i.e. Kelvin equation) gives the mean curvature of the meniscus as Israelachvili (2011):

$$\kappa = \frac{\Re\, T}{V\gamma} ln\left(\frac{p_v}{p_{v,0}}\right) \tag{5.2}$$

Where $\Re$ is the real gas constant, T is the temperature, p_v is the partial vapour pressure and $p_{v,0}$ is the saturation pressure of water at the temperature T. The ratio $p_v/p_{v,0}$ is the relative humidity. The derivation of the other geometrical quantities relies on the comparison of Eq. (5.2) with the relation proposed by Orr et al. (1975) that returns the mean curvature of meniscus between sphere and plane when the contact angles on sphere and plane are different. Theoretically, an iterative procedure should be set up in order to find the actual filling angle Ψ, as described in Orr et al. (1975). In the same article it is pointed out that if Ψ is less than 10° the procedure can be avoided and Eqn. (5.1) can be replaced by Eq. (5.3).

$$F_L = 2\pi\gamma R\left(\cos\theta_1 + \cos\theta_2\right) \tag{5.3}$$

The former assumption is equivalent to assume a circular shape for the meridional

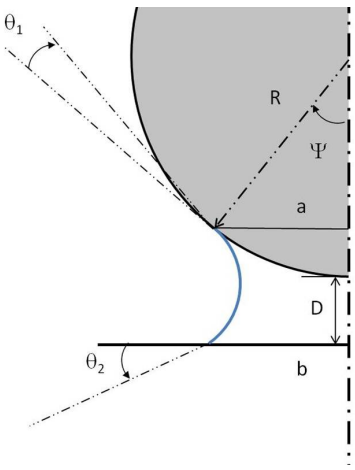

Figure 5.6: Schematic of the particle, meniscus and blade surface.

curvature of the meniscus and that the axial force on the particle is not dependent on the amount of liquid within the liquid bridge. This is the assumption employed here and it is justified by the fact that the radius of the particle is much larger than the curvature radius of the liquid bridge. Indeed, the radius provided by Eq. (5.2) is of the order of 10 nm, that is 10 to more than 100 times smaller than the particle radii investigated here. The values used in Eq. (5.3) are the contact angle for silicon and stainless steel. The value of the filling angle Ψ investigated in this work are 5° and 10°. In the case of water film, these value are representative of a rather dry environment and a humid environment respectively (with relative humidity close to 100 % in the second case).

Van der Waals

The London - Van der Waals force is a short range force that originates in the instantaneous dipole generated by the fluctuation of electron cloud around the nucleus of electrically neutral atoms. It decreases rapidly as the distance increase, but its value has entity similar to the liquid bridge when the particle is in "contact" with the surface Berbner and Löffler (1994).

At least two theories are available in the literature for the quantification of this force: the Hamaker and the Lifshitz theory Visser (1972). For both of them the formulation of the van der Waals force when the contact between the two solids is mediated by a liquid is given by, (according to Hamaker),

$$F_{VdW} = \frac{A\,2R}{12D^2} \tag{5.4}$$

where A is the Hamaker constant. The Lifshitz theory can be related to the former one by replacing A by $3/4\pi\,h\bar{\omega}$, where $h\bar{\omega}$ is the Lifshitz- van Der Waals constant which is dependent only on the material Visser (1972). For this reason in the following the term Van der Waals force will refer to the Hamaker theory without loss of generality. It is common practice to add subscript to the constant A in order to point out the elements in contact, so in this case it takes the form A_{123} where 1 refers to the sphere (particle), 2 to the surface (blade) and 3 to the liquid medium (water). The database for the A constant is often available only in the form A_{jj}, meaning the contact of spheres of the same materials. In order to obtain the constant representative of the case, the relation proposed by Viesser is used Visser (1972):

$$A_{123} = C_t\,(A_{12} + A_{33} - A_{13} - A_{33}) \tag{5.5}$$

where C_t depends on the medium material 3 and is equal to 1.6 for water, and the mixed terms A_{ij} should be evaluated using the geometric average

$$A_{ij} = \sqrt{A_{ii}A_{jj}} \tag{5.6}$$

As shown by Bowling Bowling (1988), van der Waals force can be much bigger if deformation of the particle happens. This deformation can be due to two different aspect of sticking: impact with the surface of high speed particles or deformation due to pressure in the contact point related to the attraction forces. In the following, the estimation of the deformation due to these two contributions will be carried out.

Ultrafine particles, that is the class to which particles that are likely to cause fouling belong (see ISO 12103-1:2016 2016), are generally hard. In particular, considering sand as a contaminant, from the work of Daphalapurkar et al. (2011) the mechanical properties of the for the deformation prediction can be estimated. Specifically, a Young modulus $E = 90$ GPa, and a yielding stress of $\sigma_{yeld} = 6.1$ GPa have been assumed. In order to estimate the actual contact radius, the energy dissipated upon impact must be somehow quantified. A reasonable way to compute this quantity is to carry out the balance among energy before the impact and energy involved in the impact itself, as suggested by Attané et al. (2007) or by Kleinhans et al. (2016) among the others. In such works, the energy content of the particle before the impact is computed and compared with the work dissipated in the deformation. In this study the same methodology is employed, considering as energy before the impact the kinetic energy and the surface energy. All the available energy is converted in deformation upon impact and in the surface energy of the "deformed" particle. The energy balance becomes

$$E_{kin,0} + E_{surf,0} = E_{def,1} + E_{surf,1} \tag{5.7}$$

where 0 represents the state before impact and 1 the "deformed" state of the stuck particle. Since large deformations are not expected, and particle is thought of retaining its nominal shape (a part for very small deformation in the contact area) the surface energy in 0 and 1 is basically the same and can therefore be dropped. The balance is therefore among kinetic energy and energy dissipated in the deformation process.

The kinetic energy considered in Eq. (5.7) is the kinetic energy in the normal to the surface direction. In this work, and generally in compressor fouling problems, the particle velocities in the normal to the surface direction hardly overcome 100-150 m/s. Specifically, in this study, impact velocities are always lower than 75-80 m/s. Assuming a normal impact velocity of 100 m/s and a density of 2500 kg/m, for a particle having a diameter of 1 μm, the kinetic energy is equal to $E_{kin,0} = 1/2\, mv^2 = 5 \cdot 10^{-12}$ J. In the final step of the sticking phase, labelled with 1 in Eq. (5.7), the particle has dissipated all the incoming kinetic energy in deformation mechanisms.

The maximum deformation has been guessed by considering the sand stress-strain curve. It is well known that the energy involved in deformation processes is the area under such curve. By assuming a linear law for the elastic region (e.g. an elastic perfectly plastic model), this area is actually a triangle if one remains below the yielding stress.

The strain-energy density, given by the kinetic energy divided by the particle volume, is equal to 12.5 MJ/m^3. The resulting stress is equal to 1.5 GPa, meaning the particle remains in the elastic regime, with a corresponding maximum strain of 0.0167. Under such conditions, when the elastic recover happens (e.g. when the impulsive action of the impact vanishes), no residual strain is left on the contact area. No extra correction term for the deformation must be applied to the van der Waals force due to impact.

For what concerns the second cause of the deformation, that is the attraction among two bodies in contact, an estimation of the pressure on the interface is given by Bowling Bowling (1988). Specifically, in the contact area it can be reached a force per unit area of the order of magnitude of 0.01 MPa. The stress is applied for as long as particle and surface remain in contact and so it is not required to overcome the yielding stress in order to have a deformed area of contact. Nonetheless, the amount of this stress is such that the corresponding strain is of the order of 10^{-9}. This would cause a very small deformation, meaning deformation effects of the van der Waals forces are negligible.

Drag

The drag force is usually quantified by the drag coefficient C_DMorsi and Alexander (1972), as explaned in 2.2. In the free stream flow, the formulation of the drag coefficient implemented has already been discussed. When the particle analysis is close to the wall some considerations must be done. Since the particles under investigation are small, the Reynolds number is small and thus the Stokes drag can be used Soltani and Ahmadi (1994): in this case $C_D = 24/Re_p$. Being in proximity of the wall, one may reasonably assume that the particle is within the laminar substrate O'Neill (1968) and thus the velocity component on the center of a spherical particle is given by Eq. (5.8)

$$u^+ = R^+ \quad \text{since} \quad u^+ = y^+ \tag{5.8}$$

where, for smooth surfaces,

$$u^+ = u/u_\tau \qquad y^+ = u_\tau y/\nu \tag{5.9}$$

u_τ is the friction velocity $u_\tau = \sqrt{\tau_{wall}/\rho}$ and τ_{wall} is the wall shear stress. ν is the kinematic viscosity of the fluid. Substituting Eq. (5.9) in Eq. (5.8), the fluid velocity at a distance from the wall equal to the particle radius is

$$u = \frac{u_\tau^2 R}{\nu} \tag{5.10}$$

Keeping this in mind, the drag force evaluated in the center of a particle stuck to the wall (i.e. $u_p = 0$)

$$F_D = C_D \frac{1}{2} \rho u_c^2 A_p \tag{5.11}$$

where $A_p = \pi R^2$ is the cross sectional area with respect to the flow direction. Assuming Stokes flow, substituting Eq. (5.10) in Eq. (5.11), the expression for the computation of the drag force near to the wall is:

$$F_D = \frac{3\pi}{2}\rho f R u_\tau^2 \tag{5.12}$$

and $f = 1.7$ is the correction factor proposed by O'Neill (1968) in order to account for the presence of the smooth wall.

A final remark on the calculation of the drag force regards the rarefaction effect. The small size of the particle force to keep into account the correction proposed, among the others, by Soltani and Ahmadi Soltani and Ahmadi (1994), that is evaluating the drag coefficient as $C_D = C_{D,Stokes}/Cu$, where Cu is the Cunningham factor. To calculate the Cunningham factor, Fuks (1989) proposed a dependence from the Knudsen number $Kn = \lambda/R$ where $\lambda = 2\mu/\rho\bar{c}$ (from Talbot et al. 1980) is the mean free path of the gas molecule. Eventually $\bar{c}$, the molecular mean speed, can be evaluated as $(\bar{c} = 8\Re T/\pi)^{1/2}$, as reported in Talbot et al. (1980). With these remarks Eqn. (5.12) becomes

$$F_D = \frac{3\pi}{2}\frac{\rho f R}{Cu}u_\tau^2 \tag{5.13}$$

That must be solved together with $Cu = 1 + Kn[1.257 + 0.4exp(-1.1/Kn)]$.

Centrifugal

The centrifugal force is, together with the drag, the main detachment force acting on a deposit. Its value is calculated using

$$F_C = m\omega^2 r \tag{5.14}$$

where r is the distance of the particle center from the rotational axis, and ω is the rotational velocity. In this study the radius of the machine is thought to be 0.3 m measured from the bottom of the inlet. This is representative of a small heavy-duty compressor.

The centrifugal forces in this work are applied only to the attached deposit and not on the fluid flow. In this sense its effect does not entail any flow curvature or variation. This is indeed a big approximation in terms of flow field and particle tracking behavior. The centrifugal effect is indeed known to have a major effect in the radial redistribution of particles. This effect is negligible for smaller particles, as reported by Aldi et al. (2017b), but its relevance increases as the particle diameter increases. In light of this, the deposition pattern found in this work is expected to be slightly different with what would actually happen in a real experiment. The centrifugal force will displace the majority of the impacts upward, toward the tip region (represented by the end of the target wall in

Fig. 2.3. The acceleration due to this force is related to the vertical direction and no effect on the axial one is expected. Since no criteria on the tangential viscosity is considered for the sticking, the impact velocity in the normal-to-the-surface direction is not thought to be affected in a dramatic way. In the same fashion, the centrifugal effect will be felt by the fluid itself. This will increase the upward velocity of the fluid along the target wall, contributing to increase the drag itself.

State this, the centrifugal effect on both particle and fluids are neglected here. This represents a shortcoming of the actual implementation. Although these forces should be actually considered and their effect may not be negligible, this work is an order-of-magnitude analysis of the particles attached to the surface. In light of these considerations, the centrifugal effects on the trajectories can be considered a next step of the modeling, without loss of generality for the results here presented.

Geometry modification and force balance

The assumption done for the balance evaluation is the following: the influence the deposit has on the flow is given by the sum of the effects of the particle, whereas the forces are evaluated on the single particle. In other words:

- The flow will consider as boundary the new displaced geometry (Fig. 5.3). With this new geometry the flow field is updated and relevant quantities, such as the wall shear stress, are calculated.

- The forces the flow exerts on the deposit are calculated considering a single spherical particle deposited. For instance the attaching or detaching torques are calculated with the same quantities (half of particle diameter and radius of the contact area).

For the force balance, the spatial distribution of the forces is reported in Figure 5.7.

The detachment happens either when, from the force balance in the normal to the surface direction, the prevailing force is the detachment one or, on the other hand, the detachment moment overcomes the attaching one. For what concerns the pole of the moment the assumption of rolling detachment Soltani and Ahmadi (1994) and of infinitely stiff meniscus have been done. This translates in a detachment point lying on the outer radius of the wetted area on the surface of the substrate. Such a wetted area is directly related to the value of Ψ.

The contributions to the attaching and detaching torque are therefore computed in the following fashion:

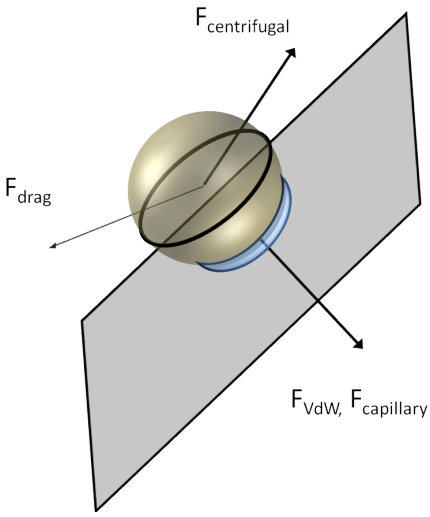

Figure 5.7: Spatial distribution of the forces acting on the stuck particle

- **Drag force** The drag force is thought to be applied in the center of gravity of the particle and, in this work, it is considered to be always parallel to the surface. Thus the drag torque arm is equal to the particle radius;

- **Centrifugal Force** The centrifugal force is always applied in the particle's center of gravity. The force is decomposed in the normal and tangential to the surface directions. As a consequence, the centrifugal force torque is proportional to the radius of the particle;

- **Capillary force** The capillary force is applied in the center of the meniscus bridge, and it is always considered to be normal to the surface. The arm is therefore always equal to the radius of the ring;

- **Van der Waals force** The van der Waals force is applied in the point where the meniscus bridge is thinner. In this work this is considered to be the center of the ring. Again the arm is equal to the radius of the meniscus.

The geometry modification for the boundary growth has been described in the *boundary displacement* section, and in particular in Fig. 5.3 and Fig. 5.5. In case of detachment the boundary is entirely deflated, recovering the starting position corresponding to the beginning of the simulation.

The deposition pattern corresponding to the inflow Ma = 0.3 is reported in Fig. 5.8. In this Figure, the target wall is reported and the flow direction is from left to right: the stagnation area is on the left hand side of the picture, and at the right there is the target "tip". For each of the tested diameter, replicating an inflow concentration of 20 μg/m^3, the stuck particles are reported. Particularly, the green points are representative of the 10 μm diameter particles, the red are for 5 μm and the black dots are the 1 μm ones. It can be seen that only the smallest particles cover the entire wall. Bigger particles have

higher inertia and thus they are more likely to impinge on the wall in the stagnation area on the left hand side. Contrarily, they are delayed in following the streamlines that moves smallest particle towards the tip region making them to stick there. This means that either big particles tend to stick to the bottom of the target wall or not to hit it at all. On the other hand, smaller particles tend to follow streamlines more closely. This justifies the fact that the entire wall is covered by particles. Nonetheless, higher density of deposited particles can be identified in the hub and tip areas. The deposition pattern for Mach number of 0.15 and 0.45 is qualitatively similar to the one reported in Fig. 5.8, except for the number of the deposited particles. This result may be used for qualitative validation of the results.

In light of extending this work to real compressor geometries, the left hand side of Fig. 5.8 can be related to the leading edge of a compressor blade, from the deposition standpoint. This remark is based on the presence of a stagnation area followed by a deviation in the fluid flow. Since the gravitational force in the particle tracking algorithm is neglected in this work, the direction of the bend (upward in this case) can be considered as a general deviation imposed to the flow. It must be said that the degree of deflection is quite high, and this implies more detrimental conditions with respect to real blades, entailing an higher amount of impacts.

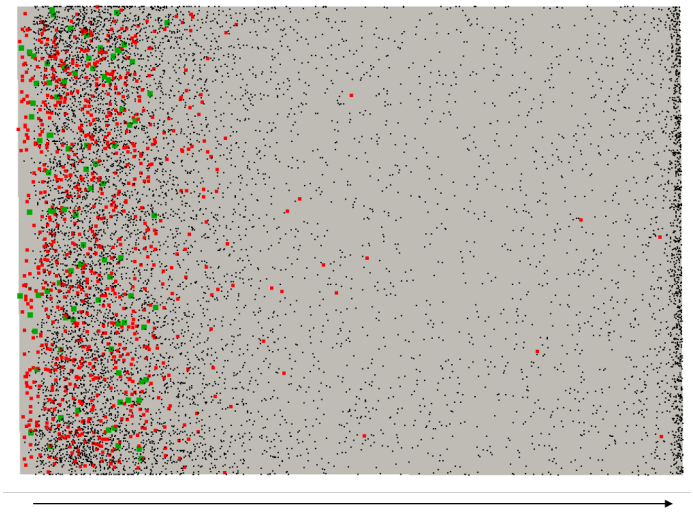

Figure 5.8: Deposition pattern on the target wall of particles for Ma=0.3. Green, red and black dots represents 10 μm diameter particles, 5 μm and 1 μm respectively. The black arrow represents the flow direction.

All the tested conditions are reported in Tab. 5.1. The values are derived as an average of the quantities under investigation over all the deposits recorded in such run. This is done in order to have a representative value of the case. This value gives an idea of which one of the forces considered here has actually a non-negligible effect on the deposit detachment. In this light, only some of the forces are worthy to be considered in a real compressor geometry simulation. Table 5.1 reports the average values of the forces on the deposit for three particle diameters (1, 5 and 10 μm) that are thought to be responsible of compressor fouling. Three different inflow conditions have been tested, varying the inlet

Table 5.1: Variation of forces on the particle according to particle diameter and inlet Mach number

2R	Ma_{in}	Centrifugal Force			Drag	Capillary force		VdW	Detach moment			Attach moment			
												Ψ_1		Ψ_2	
		ω_1	ω_2	ω_3		γ_1	γ_2		ω_1	ω_2	ω_3	γ_1	γ_2	γ_1	γ_2
	0.15				1e-10				8e-17	8e-17	1e-16				
1	0.3	1e-10	2e-10	3e-10	8e-10	1e-7	3e-7	5e-8	6e-16	1e-15	2e-15	4e-15	1e-14	1e-14	3e-14
	0.45				1e-9				9e-16	1e-15	2e-15				
	0.15				3e-9				7e-15	7e-15	1e-14				
5	0.3	1e-8	3e-8	5e-8	2e-8	5e-7	1e-6	2e-7	7e-14	8e-14	1e-13	1e-13	3e-13	3e-13	6e-13
	0.45				4e-8				1e-13	2e-13	2e-13				
	0.15				1e-8				7e-13	9e-13	1e-12				
10	0.3	1e-7	2e-7	4e-7	6e-8	1e-6	3e-6	5e-7	8e-13	1e-12	2e-12	7e-13	1e-12	1e-12	3e-12
	0.45				1e-7				1e-12	2e-12	3e-12				

Mach number (0.15, 0.3 and 0.45).

For each particle and inflow condition, three different rotational velocities on the particle (as above explained) have been tested: $\omega_1 = 655 rad/s$, $\omega_2 = 855 rad/s$ and $\omega_3 = 1000 rad/s$. Besides centrifugal forces, the surface tension of the material that constitutes the liquid bridge (simulating an oily substance, $\gamma_1 = 0.03 N/m$ rather than water, $\gamma_2 = 0.07 N/m$) and the filling angle ($\Psi_1 = 5°$ and $\Psi_2 = 10°$) are varied. These values cover a wide range of conditions that can occur during compressor operation. In the following it is worthy to keep in mind than detachment happens when the detaching moment overcomes the attaching moment. The other condition that may cause the detachment is due to the forces in the normal to the surface direction. This can only happen if the flow field is in the centrifugal force component in such direction is greater than the sum of the capillary and the Van der Waals force. This last occurrence never happens in the case investigated and thus it can be concluded that, generally speaking, the detachment of the particle from surfaces in compressors is mainly due to rolling detachment.

By analyzing carefully Tab. 5.1, it is interesting to note that the attaching moment clearly prevails only in case of 1 μm diameter particles, for almost all the tested condition. This is in agreement with what has been found by Kim and Bhushan (2008) or Berbner and Löffler (1994), showing that the importance of the adhesion forces is very strong for the smallest particles (in the nanometric ranges) and fades away as the diameter increase. Indeed both the Capillary and the Van der Waals forces depends on the diameter to the power one. The centrifugal effect on the other hand it is related to the particle volume. The drag weight prediction is not such straightforward since it is dependent both on the particle diameter, in Eq. (5.13), as well as on the wall shear. This is strictly dependent on the inflow condition and on the amount of the wall displacement. The displacement of the boundary is indeed important to evaluate possible extra-stresses deriving from the presence of an obstacle to the fluid flow.

Both the attaching and detaching moments are dependent on the filling angle: it is used in this work for determining the arm of the torque, being the capillarity independent on its value. Ψ is important in the evaluation of the sticking force only in case of submicrometric

particles, when the radius of curvature of the liquid bridge (see Fig. 5.6) is comparable with the particle one. In this case, as above stated, the particle radius is roughly 100 times bigger than the meniscus curvature. In such a scenario it is important to quantify the effect of the attaching arm, since the force is not dependent on Ψ, as suggested by Orr et al. (1975). Thus, assuming a filling angle for the detachment evaluation of 1 degree, lowers the attaching moment of one order of magnitude, if compared to $\Psi = 10°$. This can make the difference between neglecting the detachment effect and considering it since the two effects become comparable. This is particularly evident for example in the case of 5 μm particle, where in case of the higher rotational speed tested, entailing a detaching moment of 1e-13, the choice of $\Psi = 10°$ maintains the particle attached to the wall, whereas by choosing $\Psi = 5°$ the deposit tends to detach. The value of Ψ is related to the relative humidity of the air, as above mentioned. A more precise determination of the meniscus radius would involve the procedure proposed by Orr et al. (1975), and it considered a next step of this work. Thus, as the proceeds towards the latest stage of the compressor, it dries and thus its relative humidity decreases, as shown by Aldi et al. (2018).

As a consequences particle are more prone to detach in the first stages, due to the higher value of the relative humidity and thus a bigger value of the liquid bridge radius. The bigger sizes are, in all the situations tested, more prone to be detached. The centrifugal force itself is of the same order of magnitude of the Van der Waals forces. In all the case tested the capillary force is the double to ten times the Van der Waals forces, depending on the surface tension chosen. This is in agreement with the literature, for example with Berbner and Löffler (1994).

As an example, the variation of the detaching moment for different rotational velocities as the particle diameter increases is reported in Fig. 5.9. Such a graph is representative of a $Ma_{in} = 0.45$ The dashed line represents the attaching moment computed with γ_1 and Ψ_1. The points above such dashed line are related to particle detachment, whereas below such a line the detaching forces are smaller than the sticking ones. It can be seen that for the smaller rotational velocities the detachment is only possible for the particles that have an high inertia (for sure bigger than 7 μm). If one wants to detach the smallest particles, the rotational velocities must be dramatically increased. This is in agreement with what has been found, among the others, by Syverud et al. (2005) and Tarabrin et al. (1998): both the rotor and the stator experience deposition. The particles on the rotor are only partially centrifuged off the surfaces, according to the authors. Figure 5.9 seems to confirm such a remark.

A concluding remark regards the trend of the detaching moment along the target wall. In Fig. 5.10 , the detaching moment variation for one of the case tested is reported. Particularly the case having 2R = 1 μm, Ma_{in}=0.15, ω=655 rad/s, γ_2 and Ψ_1 has been chosen. It can be seen that two average operations must be carried out. For every location

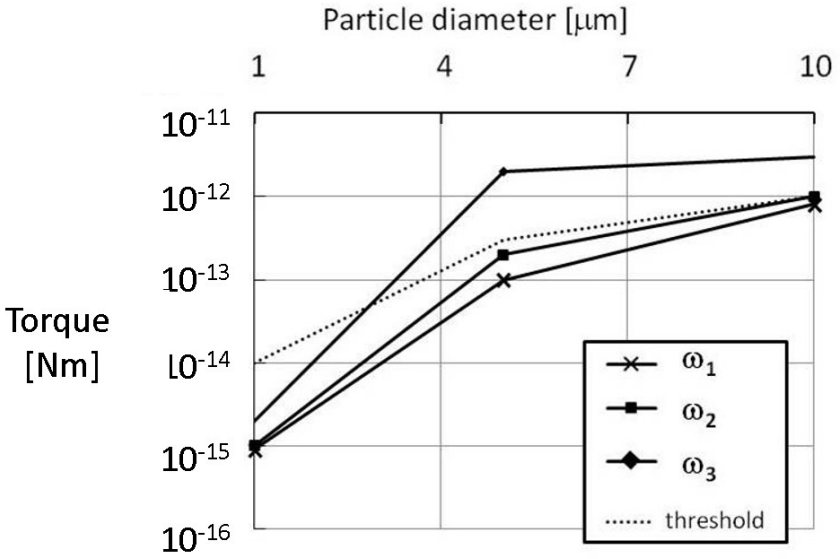

Figure 5.9: Detaching moment variation - Ma_{in}=0.45. Sticking moment (dashed line) computed with γ_1 and Ψ_1

along the chord (x/c) of the target wall, several particles deposits, and this translates in having multiple values of the detaching torque. This is related to the algorithm chosen for the boundary displacement, that collects along the grid lines the build-up (the deformation is translated in grid-points motion). So the multiple detaching moment value for each location are related to the different particles that are deposited tangential-wise.

The trendline of the distribution reported in Fig. 5.10 returns a very low value of the detaching moment for the smallest x/c. Here, the recirculation bubble due to the presence of a stagnation area lowers the drag effect, and the small distance from the rotational axis causes the centrifugal force not to be so effective. The drag effect returns to be noticeably as the flow reattaches to the target wall downstream the bubble, causing the detaching moment to rise. The lowering of the drag force after x/c = 0.3 is probably related to the reduction in the jet of the high velocity stream, as reported in Fig. 2.6. The flow tends to reattach to the upper wall, causing the velocity to lower. Beyond x/c = 0.6, such reduction reaches an asymptotic value, stabilizing around an average value of 10^{-16}. The increase in the final part of the curve (i.e. after x/c = 0.9) is due to the increase in the drag force related to the new jet that develops because of the bend after the end of the target wall, as reported by the C-line depicted in Fig. 2.5.

It can be concluded that, from Fig. 5.10, the overall trend is related to the drag force only. The centrifugal effect, in the implementation adopted in this work, is just a linear trend superimposed to the drag detaching moment. The shape of the curve for the other cases is qualitatively similar to the one presented in Fig. 5.10.

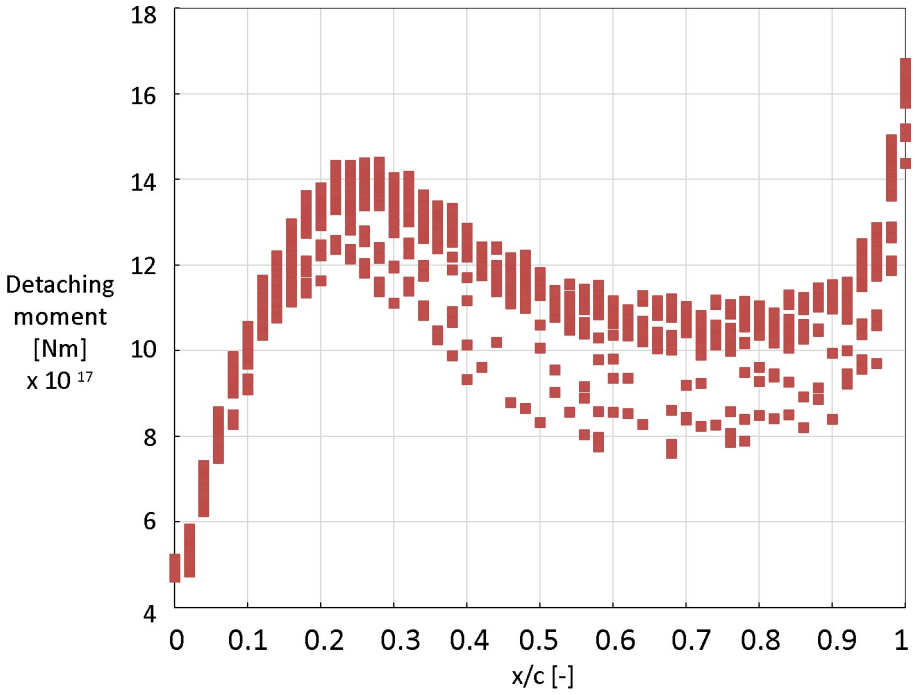

Figure 5.10: Detaching moment variation - 2R = 1 μm, Ma_{in}=0.15, ω=655 rad/s, γ = 0.072 N/m and Ψ=5°

Final Remarks

From this section, it can be concluded that:

- The drag effect is of paramount importance especially for smallest particles. For this kind of particle is basically the only force that can cause the particle detachment, since the the centrifugal force may be not strong enough. In the cases tested, no detachment due to drag force only has been detected even for biggest particles.
- A transonic stage is more prone to be held clean due to higher flow velocities and higher centrifugal forces. Besides, the tangential component of particle velocity is usually higher and this would imply a reduction in the number of impacts resulting in sticking, if a proper criterion is used.
- On the other hand the amount of foulant ingested, keeping the environmental concentration of contaminants fixed, is higher due to higher mass flow rate.
- For particle smaller than the micron (not analyzed in this work) the trend is clearly unfavourable to the detachment, especially on vanes.

The analysis of a real compressor blade/vane geometry subject to fouling can be thus carried out in the track of these remarks. Particularly the centrifugal force has a minor effect if compared to drag for the smallest particles (diameter little or equal to 1μm), whereas the opposite holds when the particles size is above 10 μm. In between these two

values the two forces has the same order of magnitude and thus both of them should be accounted for when the the detaching moment is computed.

5.2 Hot section: detachment and sintering

As the exposure time increases, the deposit on HPT evolves. An increased exposure time means more particulate ingested and therefore build-up accretion. Nonetheless, the drag forces, as the build-up protrudes towards the core flow, are higher and thus they have higher capabilities to detach the deposit. On the other hand, compound of semi-molten particles held at high temperature can form bonds in what is called sintering process.

This section deals with these two aging mechanisms, in order to give a comprehensive overview of the fouling phenomenon on HPT sections.

5.2.1 Deposit detachment modeling in HPT

Deposition of particles on the surfaces entails the build-up of material. The deposit can be detached from the surface as a consequence of the modified flow field. This phenomenon has been analyzed widely in literature and several studies on the mechanisms of detachment are available. Das et al. (1995) compare the three main mechanisms of detachment, namely lifting, rolling or sliding. The authors state that the main mechanism of detachment is the rolling of the deposited particle by breaking the interface particle-surface. There are many theories in the literature trying to find the main cause of the bond breakage. For instance, Reeks et al. (1988) formulated a theory based on the transfer of turbulent energy to a particle. The particle can be resuspended from a substrate after it accumulates enough energy to escape from the adhesive potential well. Turbulent flow lift forces transfer energy by their average component, which modifies the shape and height of the well, and their random fluctuating component, which causes the particle and surface to deform in a random oscillatory fashion from their static equilibrium configurations. In this paper the detachment is thought to be dependent only on the aerodynamic drag, and the well known model reported in Soltani and Ahmadi (1994) is used.

In this work a numerical study is conducted into the consequences of flying through a volcanic ash cloud. In the following sections the following topics will be treated:

- application of an in-house deposition model for the evaluation of a realistic deposition problem on HPT vanes;
- numerical simulation by means of a transient solver which takes into account the

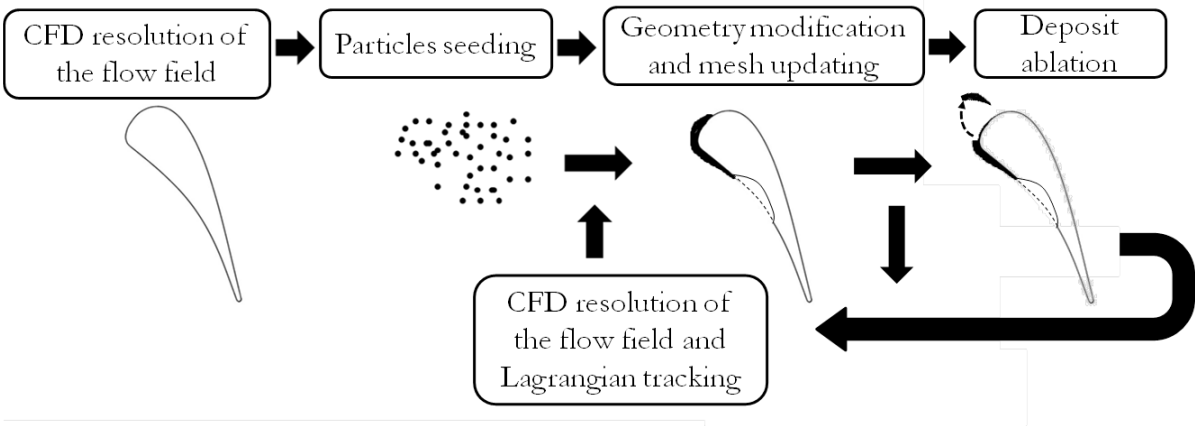

Figure 5.11: Outline of the procedure, nozzle modifications not in scale.

variation of the geometry and its effect on the fluid flow;

- simultaneous analysis of all the consequences the ingestion of a particle cloud can entail, namely erosion, deposition and deposit detachment;
- The starting and final geometry are available in our on-line website to allow the repetition of tests and the validation of the consequences on the flow field.

Deposition and erosion are kept into account as well as the detachment of the deposited layer. The behaviour of the particulate is described in terms of parcels (clusters of particles). Although the particulate ingested by the engine in case of flight through a cloud can be of very high concentration (up to 250 mg/m^3 Dunn 2012), the typical value does not exceed the threshold by which the so called one-way coupling can be safely used Elghobashi (1994). According to this approach the effect the particles have on the fluid flow in terms of momentum and energy transfer is not kept into account.

The geometry evolution of a transonic vane subject to fouling/erosion is numerically investigated by means of a moving mesh technique which accounts for the boundary displacement. Such a kind of vane is usually more subject to fouling with respect to a subsonic one. More details regarding this remark can be found in the *Deposition* section.

The main effects of the ingestion are deposition and erosion of the surfaces exposed to the flow. The approach used in this section is based on the method proposed in the *Deposition* section with modifications to include the effect of erosion and detachment. The present method is outlined diagrammatically in Fig. 5.11 and is explained in detail below.

The flow field is first computed in absence of contaminant until convergence is achieved. At this point particles are seeded at the inlet of the domain and for every time step, both the carrier and the dispersed phase are updated. The particles are tracked via one-way approach and the flow field is solved through the *sonicFoam* solver with a set of given boundary conditions (see paragraph 2.4.2). The deposition or erosion of the vane causes

the mesh nodes on the surfaces to move, in the area-wise approach presented in 5.4, since a 2D approach has been used here . Mesh quality is maintained by solving a Laplace equation for the displacement over the computational domain. The present approach, although more time consuming than integrating the particle trajectories over a frozen flow field, gives more realistic information on the evolution of the geometry of the vane wall. In particular, it gives the more accurate results concerning the rate of change of the passage throat area.

It must be remarked that in this work all the possible effects deriving from particles ingestion are analyzed, namely deposition, erosion and build-up detachment. This is due to the fact that all these phenomena might happen simultaneously in the hot section of a gas turbine, as reported in Bons et al. (2001).

A further assumption is that the same concentration that is ingested by the fan is transferred to the core flow without any changes. In such a way, the particulate flow rate that is processed by the core flow is simply a function of the by-pass ratio. This assumption is very pessimistic since a very high fraction of the foulant agent would be centrifuged towards the by-pass flow, lowering the concentration of particles within the flow processed by the turbine. Nevertheless this condition implies more detrimental effects on the components, and so this "worst case scenario assumption" is deemed suitable for the purposes of this study. This approach is a common assumption when dealing with this kind of problem, and it is also used for the realization of the 'Safe-to-Fly' chart by Rolls-Royce, see Clarkson et al. (2016).

CFD resolution of the flow field

The prediction of the deposition starts with the initialization of the flow field. In this step, no particles are transported through into domain. The numerical analysis have been carried out using the *sonicFoam* solver from the OpenFOAM-v3.0.0®set of compressible solvers is used.

This solver is a pressure-based solver that uses the Pressure Implicit with Splitting of Operators algorithm (PISO). The solver has been validated against the well known LS 89 testcase measured by Arts et al. (1990). More details are reported in section 2.4.2: for the purpose of the ash ingestion study, a set of boundary conditions representative of cruise conditions is selected. These conditions are reported in Tab 5.2.

A k-ε model, with standard wall functions has been employed for the simulation purposes. The wall was considered to be hydraulically smooth both in cases of clean and dirty vane.

Table 5.2: Boundary conditions for the computation of the undisturbed flow field

	Quantity	LS - 89
Inlet	p_0	1,523,000 Pa
	T_0	1708 K
	Turbulence intensity	1 %
	Turbulence mixing length	0.0004 m
Wall	T	1100 K
Outlet	Mis	1.02
	p	911,200 Pa

Particle seeding

In this simulation a mass flow rate of particulate equals to $1.375x10^{-7}kg\,s^{-1}$ have been injected corresponding to roughly 30000 particles per second.

The physical properties of the particles relevant to the calculation are the density ρ=3000 kgm^{-3} and the specific heat c_{part}= 800 J(kg K)−1. The particles are inserted into the flow at the inlet of the domain at random angular positions and with velocity perfectly coupled with the fluid flow at the inlet of the domain. The size distribution is representative of the one which could reasonably reach the exit of the combustor. According to Taltavull et al. (2015), the typical distribution of a volcanic ash cloud is very case dependent. Nonetheless the biggest particles are centrifuged towards the by-pass flow or are split in smaller parts during the impact against the compressor blades. Thus the population that approaches the high pressure turbine vane can be represented by a uniform distribution between 1 μm and 30 μm as can be gathered by Taltavull et al. (2015). The chemical composition of the particles is reported by Taltavull et al. (2015). For this composition the coefficients for the sticking probability according to the EBFOG model are derived.

Once particles are seeded they must be tracked in order to associate the particle position to the computational cell.

The tracking algorithm provided with OpenFOAM-v3.0.0 and described in Macpherson et al. (2009) is used. The motion of the particles is governed by the Basset Boussinesq Oseen (BBO) equation, and as suggested by Rispoli et al. (2015) and Wenglarz and Cohn (1983), the only force to be kept into account is the drag force, implemented as described above. As early mentioned, the equation used for the drag is valid for spherical particles. It is well known that the shape of the volcanic ash is far from being spherical, see for example Taltavull et al. (2015). Nonetheless when particles pass through the combustor they melt and their shape become spherical as reported by Lau and Windand (2014). The time step is limited by the condition that the maximum CFL number is one. This condition is imposed for accuracy reasons related to the particle tracking López et al. (2015) and guarantees that each particle crosses at most one cell boundary at every time

step.

he heat transfer between the gas and the particles is also computed. The Ranz-Marshall equation (see Eq. (5.15)) is used to estimate the Nusselt number for the heat transfer from the fluid to the particle.

$$Nu = \frac{hd_p}{k} = 2 + 0.6\sqrt{Re_p}\sqrt[3]{Pr} \tag{5.15}$$

In Eq. (5.15) Nu is the Nusselt number which characterizes the thermal boundary layer of the particle, h the convection heat transfer coefficient, k is the thermal conductivity of the gas and $Pr = \mu c_p/k$ is its Prandtl Number. If Nu is known, and in this work is evaluated using the right hand side of Eq. (5.15), k is a property of the gas and thus h is derived. Finally $\dot{Q} = hS\left(T_p - T_\infty\right)$ can be evaluated, where T_∞ is the temperature of the gas outside the thermal boundary layer of the particle having a temperature of T_p. The variation in the particle temperature is calculated as reported in Eq. (5.16)

$$\frac{\partial T_p}{\partial t} = \frac{\dot{Q}}{m_p c_{part}} \tag{5.16}$$

Impact modelling, geometry modification and mesh update

The properties of the particle at the end of the time step before the impact are evaluated. The sticking probability is evaluated using the EBFOG model proposed in the *Deposit*. The model uses an Arrhenius-like equation (Eq. (3.27)) whereby the kinetic energy of the particle associated to its motion normal to the solid surface is compared with an energy which represents its state (solid, soft solid, liquid) and which depends exclusively on temperature through a law of corresponding states. The outcome of the model is a number belonging to the range [0–1]. The decision whether a particle sticks or not is taken by a Metropolis - Hasting algorithm. If the Monte Carlo method rejects the hypothesis, the particle does not stick to the surface. It is well known that the ingestion of particle clouds entails deposition as well as erosion Grant and Tabakoff (1975). Thus in this section, the same assumption proposed in the section 4.2 is made: a particle that does not stick to a surface causes erosion. Therefore, all the particles that impinge the vane either cause erosion or stick to it. To model erosion, the method proposed by Tabakoff et al. (1990) is used. The numerical implementation of the model has been discussed in section 4.2 .

Once an impact takes place, the geometry is always modified, by either loss or gain of material according to the characteristics of the impinging particle. In both cases a displacement in the direction normal to the surface is applied. The normal-to-the-surface vector is assumed to be the vector normal to the boundary face where the impact takes place. Since the faces of the cells are flat, this assumption does not imply any interpolation

error. The mesh displacement follows the same considerations proposed in section 4.2. It should be pointed out that the order of magnitude of the displacement due to the boundary motion for each time step is very small (i.e. 10^{-7}), and thus the numerical grid can bear such deformation with the aid of the smoothing without problems.

Deposit Detachment

The growth of the build-up causes a reduction of the passage section, whereas the erosion widens the channel. In both cases of erosion or deposition the effect of the changed roughness is not taken into account. The corresponding additional reduction due to increase of the displacement thickness is therefore neglected. Nevertheless the flow field changes as a response to the changed geometry.

The evolution of the deposition and, consequently, of flow field can cause conditions around the deposit to change. In particular, if the velocity is sufficiently high, the deposit can detach from the surface and resuspend Tippayawong and Preechawuttipong (2011). In this work the detachment is tought to be due only to the aerodynamic drag. This is the main responsible of the detachment according to many authors, for example Soltani and Ahmadi (1994). Thus a momentum balance is carried out in order to evaluate the drag force necessary to overcome the adhesion force. To measure the adhesion work, Soltani and Ahmadi (1994) proposed a model that relates adhesion energy to the radius of the contact area between particle and surface, and the elastic properties of both wall and particle material. The drawback of this approach is that several properties of the materials under investigation must be known.

The adhesion force for ash particles on steel in the present contribution relies on the estimates by El-Batsh (2001). Once the adhesion force is known, the quantity that causes the particle detachment is the wall shear velocity. The critical value above which the deposit detachment happens is defined by Eq. (5.17).

$$u^2_{\tau critic} = \frac{CuW_A}{\rho d_p}\left(\frac{W_A}{d_p K_c}\right)^{\frac{1}{3}} \tag{5.17}$$

where Cu is the Cunningham correction factor, W_A is the work of adhesion, K_c is the composite Young modulus. The critical wall shear velocity as a function of the diameter is determined using the values of the parameters in El-Batsh (2001). The final equation used to determine the critical shear velocity is

$$u_{\tau critic} = 1.111 \times 10^{-4} h_D^{-0.871} \tag{5.18}$$

where h_D is the thickness of the deposit in the cell under investigation. The condition

$$u_\tau \geq u_{\tau critic} \tag{5.19}$$

indicates that the deposit must detach from the surface. The assumption made in this work is that if the condition (5.19) is true, the whole build-up adhering to a boundary face is detached. This might be not completely true since a fracture can be started anywhere inside the deposit rather than at the base. No exhaustive research has been found in the literature on this topic and there seems to be no general behavior. Inspection of the work by Webb et al. (2012) reveals that, depending on the material, the deposit is completely removed in the trailing edge area whereas spalling of the outer layers of the deposit is discernible in some cases. The wettability of the ash/metal interface with respect to the ash/ash interface is most likely the responsible for such a different behaviour. Further research in this track can be found in the final part of this thesis, concerning the non-dimensional analysis.

Effects on vane shape

The simulations are started with a nominal profile and, as illustrated in the previous section, particles are seeded at the inlet of a converged steady solution. The evolution of the deposits and of erosion patches is monitored in time. The evolution of the profile over the first second of exposure is reported in Fig. 5.12.

Pressure Side

It can be seen that the fouled profile after 1 s is quite different from the one after 0.1 s everywhere but around the trailing edge. Here the profile seems to reach the asymptotic value of the displacement already in the first few steps of the simulation. This asymptotic value of the deposit thickness is determined by the balance between the detaching drag force and the adhesion force. The two forces act simultaneously on the deposit and the resulting effect on the trailing edge deposit area is a continuous succession of build-up and detachment. The evolution of the trailing edge area of the pressure side is reported in Fig. 5.13. It can be seen that the displacement is oscillating around the asymptotic value of $3\text{x}10^{-6}$ m. This value remains the same for as long as the simulation had run. Unless the conditions of the deposit upstream on the vane change in such a way that the flow field is considerably modified, this value can be considered as a constant displacement. This result is in agreement with the experimental data found by Dunn (2012), where very little if no deposition at all is found in the trailing edge areas.

The asymptotic value of the displacement on the trailing edge area seems to find

good agreement in the experimental field. For example, the work by Webb Webb et al. (2012) reports the experimental investigation of the consequences of vane exposure to contaminated air. The study is based on a realistic vane (E^3 geometry) subject to fouling by four different types of coal ash. All the tested materials show the same behavior with respect to the trailing edge area: a thinner deposit compared with the rest of the pressure side. This feature can be considered as typical of the fouling of high-pressure turbine vanes, at least for the exposure time investigated. The appearance of a vane exposed to air contaminated with lignite is shown in Fig. 5.14. The circled area is considerably thinner than the other areas of the deposits.

Inspecting the other parts of the vane in Fig. 5.12, it can be clearly seen how the leading edge is the most affected area by deposition. This remark is in good agreement with the literature (e.g. Prenter et al. (2016), Borello et al. (2014) or Casaday et al. (2014)). Borello *et al.* Borello et al. (2014) observe the same trend regarding the deposition. They do not consider the effect of erosion but, from their work, it is clear how the deposit build-up is greater on the leading edge and on the trailing edge areas, whereas no deposition occurs immediately downstream the leading edge. In this area particle velocity components tangential to the surface are pretty high and thus the deposition is less likely. However in Dunn (2012) deposition is reported in this area of the vane for all the engine tested. We can conclude that the prevailing detrimental effect is of deposition here and it is correctly predicted in this work, even if less evident with respect to the leading edge area. Probably carrying on the simulation for longer exposure time, the difference in build-up between this area and the peak deposition at the leading edge would become lower. Other tests, for example the ones by Casaday et al. (2014), show the midspan chord-wise deposition on a real turbine vane geometry. Even if the airfoil differs from the one analysed in this work, the trend is remarkably similar to Fig. 5.12. The areas mentioned above are easily identifiable.

Suction Side

Parker and Lee Parker and Lee (1972) report that the highest deposition rates are found on the suction surface. This is mainly due to the small size of the particles (sub-micrometer). This behaviour has not found agreement in the literature where real engine have been tested Dunn (2012). The other cause of deposition on the suction side is the rebound against the pressure side of the adjacent vane. In this work no deposit on the suction surface is reported since the particle size is well above the sub - micrometer size. On the other hand the rebound on the pressure surface do not cause the particle trajectory to impinge the next suction surface. For the diameters under investigation in this work, the Stokes number is such that the particle is not able to reach that surface and is brought downstream by the core flow. From Fig. 5.12, the suction side is affected only in proximity of the leading edge. Moving along the suction surface from the leading toward

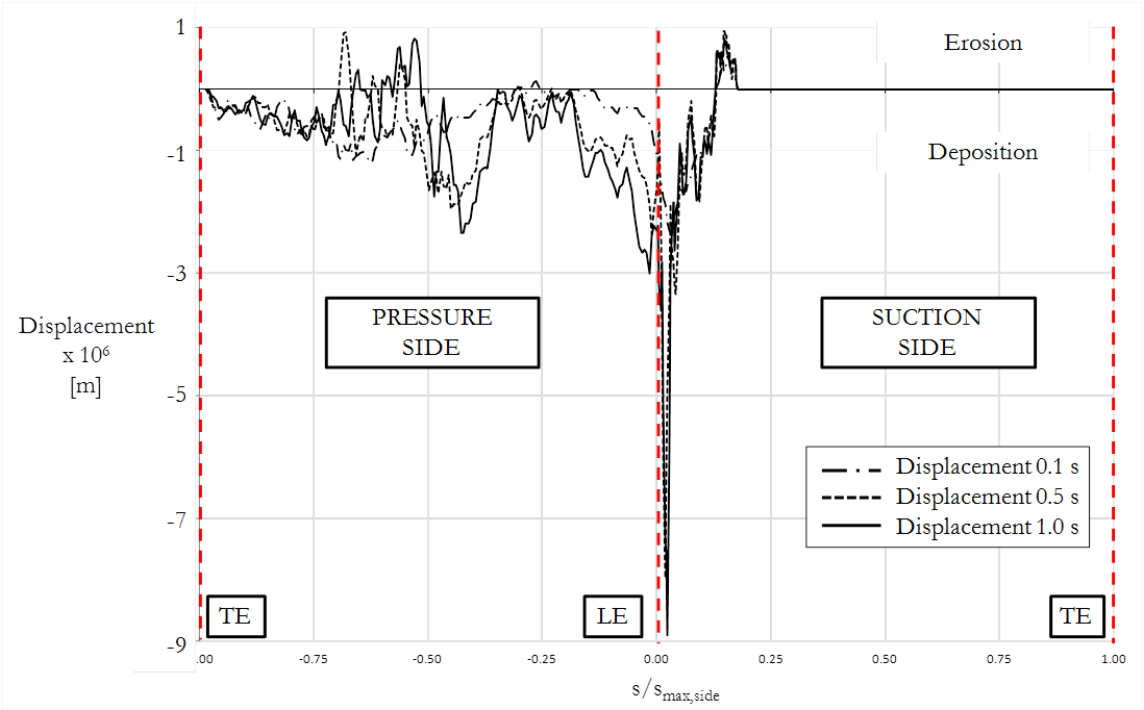

Figure 5.12: Evolution of the deposit during the first second of exposure. $s_{max,side}$ stands for the maximum curvilinear coordinate on the side under investigation. In this way the coordinate s is normalized

the trailing edge, an area of high deposition rate is found. Immediately downstream this area of erosion is found. This area is clearly identifiable from the beginning of the computation and the amount of erosion seems to reach an asymptote after 1 s. It must be remarked that the entity of erosion is very little if compared with the mean deposit build-up. On the top of that, having reach an asymptote, its value is likely to remain the same and to be always less important in terms of effects on the flow field. This result is in agreement with the experiments carried out in Dunn (2012), where very little erosion has been found. Beyond $s/s_{max,side}$=0.25 no changes in shape are reported in the range of time investigated.

Effects on the flow field

The flow field is affected by the presence of the deposit. In agreement with the results reported in Bölcs and Sari (1988), the shock wave is shifted downstream. Figures 5.15 and 5.16 report this shift. The isentropic Mach distribution along the suction side of the vane at the beginning and after 1s of exposure are shown in Fig. 5.16.

The pressure side is not shown since the difference in the pressure distribution before and after the exposure is not noticeable. It is well clear that the overall performances of the vane is not affected except at the trailing edge. The discontinuous pressure rise (and consequent drop in the isentropic Mach number) due to the shock wave also moves

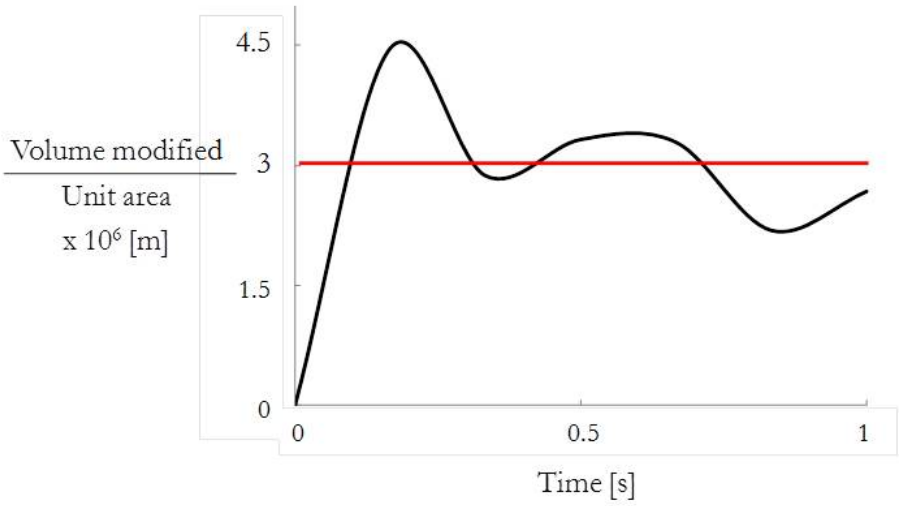

Figure 5.13: Accretion of the trailing edge area

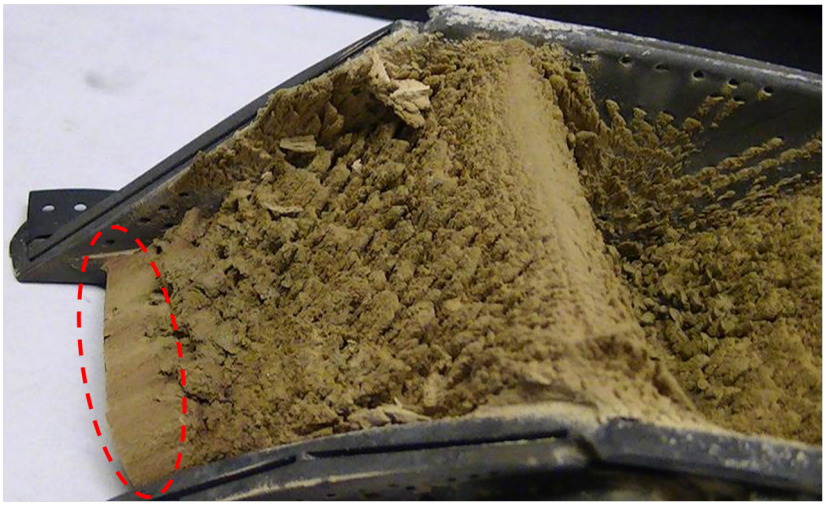

Figure 5.14: Fouled geometry from Webb et al. (2012): particular of the thin deposit in the trailing edge area

streamwise.

Another parameter of paramount importance for the vane performance is the total pressure loss. As it is well known, the parameter which is usually referred to when dealing with losses is the coefficient of pressure, $c_p = (p_{02} - p_{01})/(0.5\rho_2 U_2^2)$ where the subscript 1 refers to the inlet of the computational domain and 2 to the outlet as suggested by El-Batsh (2001). U_2 Is evaluated from the isentropic exit Mach number. In Fig. 5.17 the trend of c_p along a pitch is reported. After the exposure the c_p is lower and this is probably due to the displacement of the shock structures. The Mach number discontinuity across the shock is therefore different and thus a variation in the c_p is the consequence. Furthermore the wake is slightly displaced: the exit flow angle varies with the build-up of deposits on the vane surface. No reports regarding this effect on turbines have been found in the literature so far. Gbadebo Gbadebo et al. (2004) reports the effects of artificially added roughness to compressor vanes on several parameters. The authors identify the

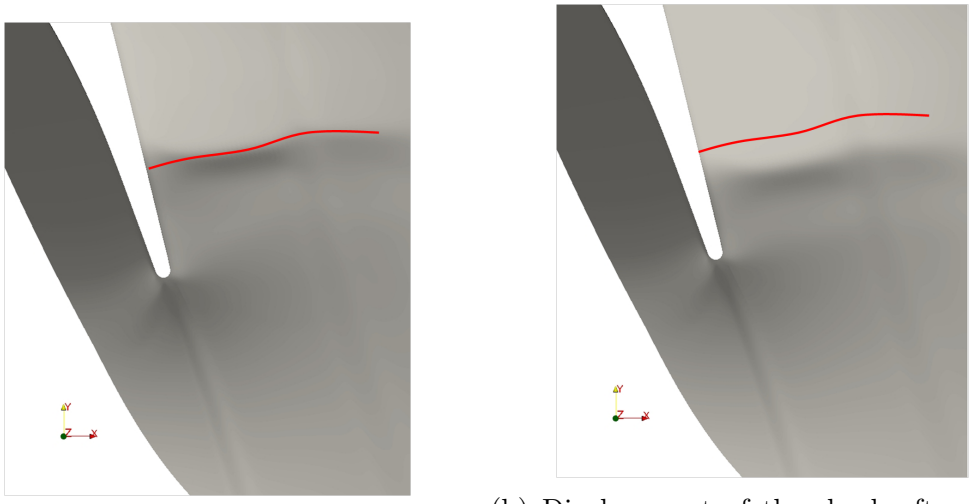

(a) Original position of the shock

(b) Displacement of the shock after 1s of exposure

Figure 5.15: Displacement of the shock wave: depicted in red the initial position

location which affects the flow deviation the most: enlarged roughness at the leading edge seems to have the biggest effect on the outflow angle. In this work, in the leading edge area there is the biggest deposition, as reported in Fig. 5.12 and it is reasonable to expect a slight variation in the outflow angle. Figure 5.17 seems to confirm this trend. It must be remarked that the reason of the variation of the outflow angle could be also the downstream displacement of the shock.

The effects of the ingestion of an ash cloud have been numerically investigated . The model used is an extension of the energy-based EBFOG model which implementation has been changed in order to keep into account also the erosion. The variation of the blade shape due to erosion and sticking is accounted for by modifying the computational mesh. The build-up of the deposit can vary during time as a consequence of the aerodynamic drag. Drag force tends to detach the deposit especially in the trailing edge area where the wall shear stress and thus the friction velocity are higher. The assumption of the total detach of the local deposit rather than outer layer spallation is justified by the presence of an interface metal/non–metal, where the chemical bonds are reasonably weaker.

Some interesting facts about the variation of the blade shape have been found. Particularly two asymptotic values can be detected, one in the peak-valley displacement in the leading-edge suction side area and the other one in the trailing-edge deposit. The asymptotic thickness is a function of the material (since the adhesion force depends on the materials that constitute the two part of the interface). In both the cases after 0.1 s of exposure, the erosion/deposition pattern on this area is remarkably similar to the one at 1 s.

On the top of that, It has been found that geometrical variations and the flow field are strictly coupled. In particular, the shock location changes due to the geometrical variations.

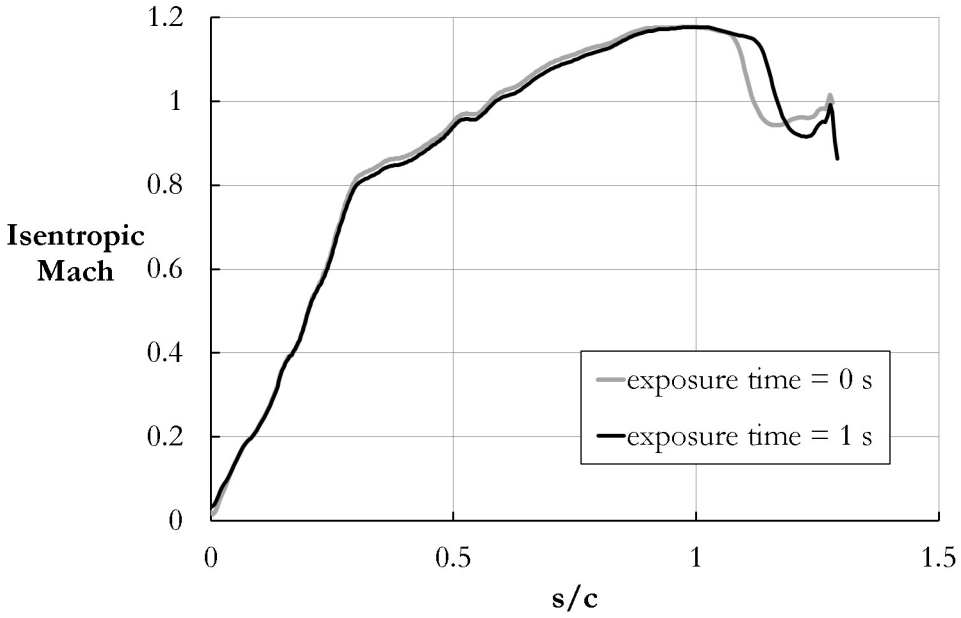

Figure 5.16: Isentropic Mach distribution along the suction side of the vane at different exposure time

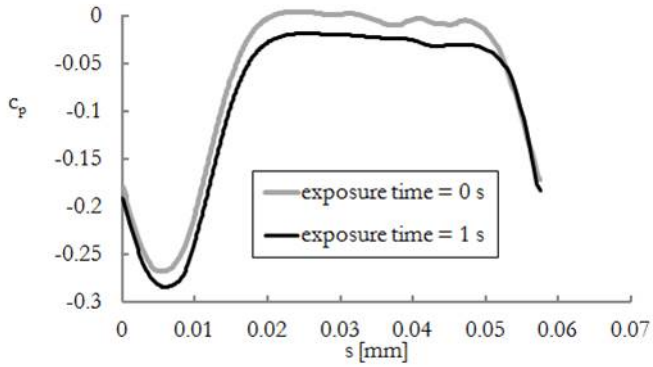

Figure 5.17: Coefficient of pressure in the two cases: peak represents the wake

From this work it can be concluded that during the ingestion of a volcanic ash cloud, the geometry of the High Pressure Turbine Vane changes and these variations affect the flow field in different ways. The displacement of the shock structures and a variation in the coefficient of pressure are the two main consequences.

Future work will be focused on the translation of information obtained from this article to important piece of on-board information for the flight crew. In order to predict the displacement of the operating point on the compressor map, the whole 3d vane should be investigated. Nonetheless useful information can be derived from the fouled geometry reported in Fig. 5.18. For more quantitative analyses the coordinates of the clean and fouled blade are available for downloading at the website Casari et al. (2017b).

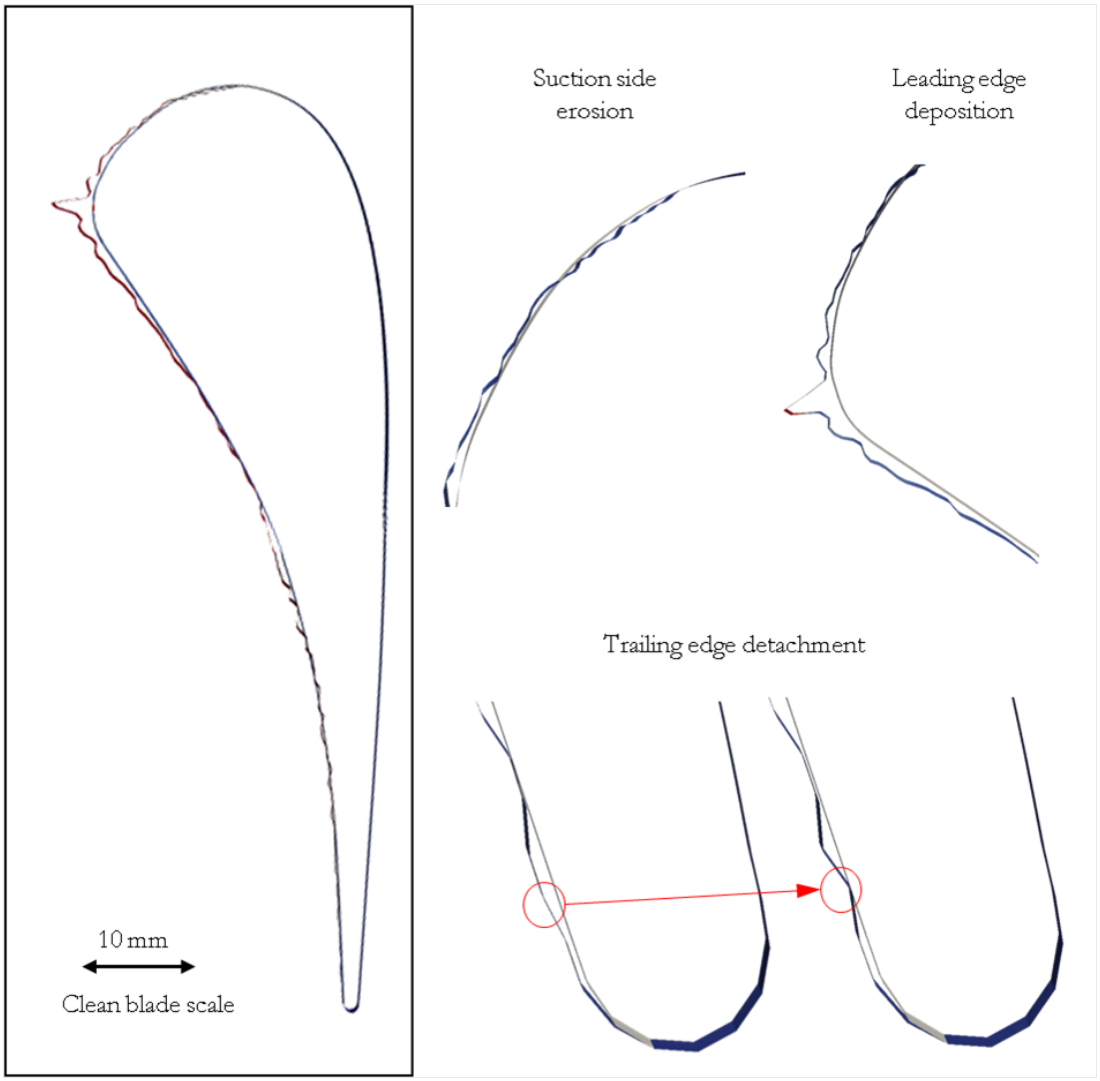

Figure 5.18: Overall of the blade and details of leading edge, suction side and trailing edge. Displacement is magnified of 200 times

5.2.2 Combined sintering and detachment effect in volcanic ash deposits on HPT vanes

A deposit is subjected to several forces that either tend to make it sticking to the surface or to detach from it. In the hot section of the gas turbine, the forces that act on the build-up tending to make it to adhere to the surface can be traced back to the van der Waals forces and, possibly capillary force if a certain amount of liquid phase is present. On the other hand, the detaching mechanism is related to the component investigated: if the particle is deposited on a vane, the drag and the shearing force are the only forces that tend to detach the particle, if a rotor blade is investigated, the centrifugal forces must be considered as well.

On top of that, the deposit evolves over time in what is called sintering. During this process, the single particles deposited can melt together forming necks. If the temperature is sufficiently high, these necks increase in size until the former pores among particles are

completely filled. This process is of paramount importance if the effect of the applied forces on the deposit needs to be investigated. The amount of material detached is indeed strongly dependent on the tension exchanged within various layers that constitute the build-up.

This section focuses on the prediction of the build-up evolution on an HPT nozzle. The sintering process is modeled and related to the resisting strength of the deposit: an increasing sintering time reduces the deposit porosity and thus increase its strength. In order to monitor the stability of the deposit, the balance among detaching and attaching forces is carried out. The evolution of the vane shape is taken into account by using a moving mesh technique.

Particularly, the detachment of the deposit as a consequence of the fluid flow forces is reported, taking into account the variation of the deposit porosity over time. All the calculations reported have been performed implementing the presented models in the software suite OpenFOAM-v1606+.

The methodology employed in this work is the same proposed in section 5.2.1, but for the sintering modeling, that has been added and the detachment evaluation that has been deeply revised. The procedure is concisely reported here to ease the reader.

The flow field is first computed in absence of contaminant until convergence is achieved. At this point particles are seeded at the inlet of the domain and for every time step, the Lagrangian and Eulerian field are updated. The PSD injected in this work is a uniform variable in the range [1,30] μm, as suggested by Taltavull et al. (2015). This is indeed the PSD for which the EBFOG coefficients have been derived. Bigger particles are indeed unlikely to reach the HPT section, either due to fragmentation related to compressor blade impact or centrifuge towards by-pass flow. Smaller particles are unlikely to hit the vane due to their small Stokes number. Particles are tracked via one-way approach and the flow field is solved through the *sonicFoam* solver with a set of given boundary conditions (see Tab. 5.3). The deposition or erosion of the vane causes the mesh nodes on the surfaces to move. Mesh quality is maintained by solving a Laplace equation in order to smooth the boundary displacement over the computational domain. The present approach, although more time consuming than integrating the particle trajectories over a frozen flow field, gives more realistic information on the evolution of the geometry of the vane wall. In particular, it gives more accurate results concerning the rate of change of the passage throat area.

Particle impact modelling

Dealing with particle laden flows, extra care should be paid towards impact modelling. In this section all the models implemented in this work for accounting the impact are briefly explained.

For the sticking and erosion evaluation, the model described in section 5.2.1 are used: the EBFOG for the deposition, and the Tabakoff et al. (1990) model for the erosion.

Boundary displacement

The boundary displacement is the results of the balance between sticking and erosion. When these two phenomena happen, the geometry is updated consequently. In the numerical approach implemented in this work the displacement of the boundary due to particle impact is such that a particle sticking to the blade reflects in a variation in the domain geometry, causing the inflation of the surface inward the domain. This deformation have been implemented as a displacement of the hit face in the normal-to-the-wall direction. The amount of the displacement is given by the particle mass conservation: it is calculated in such a way that the volume swept by the boundary face conserves the particle volume. On the top of that a certain void fraction is considered. The void fraction is representative of the porosity and, as the porosity does, it varies over time due to the shrinkage phase of the sintering process.

In case of erosion, the Tabakoff model (4.2) predicts the amount of material removed by the impact. The mass to be removed corresponds to the volume swept by the boundary face in the outward-to-the-domain direction.

Table 5.3: Boundary conditions for the computation of the undisturbed flow field

	Quantity	LS - 89
Inlet	p_0	1,523,000 Pa
	T_0	1708 K
	Turbulence intensity	1 %
	Turbulence mixing length	0.0004 m
Wall	T	1200 K
Outlet	Mis	1.02
	p	911,200 Pa

Deposit Sintering

Deposit sintering is the process by which particles in contact one another are packed together. This phenomenon is well known in the literature, and some examples are Wadsworth et al. (2016), Namkung et al. (2016) and Al-Otoom et al. (2000). The process of ash packing is essentially a viscous driven flow in which the parameters that play an important role are the surface tension γ and the viscosity μ. These quantities, together with the particle average radius can be employed to guess the timescale of the phenomenon, in order to see if it is relevant for gas turbine applications. Using the relationship reported by Wadsworth et al. (2016), the characteristic timescale associated with viscous flow, driven by interfacial tension, and neglecting inertia and buoyancy, is the capillary relaxation time $t_s = \mu R/\gamma$. Assuming, from Song et al. (2017), a viscosity of 10^4 Pa s, a radius of 10^{-6} m and a surface tension of 0.35 N/m (representative of volcanic ash at 1200K), the order of magnitude of t_s is 10^{-2} s. This is comparable with the time between two successive shedding events of the deposit as evaluated in the section 5.2.1, and thus this phenomenon should be kept into account. It must be added that in the detachment analysis in 5.2.1 a very dense ash cloud was considered, and thus the growth rate of the deposit is very high, lowering the mean time between two successive shedding of the deposit. In the case of lower particulate flow rate, the weight of the sintering consequences is expected to imply more detrimental conditions.

To evaluate the mechanical properties of the build-up, its porosity has to be known. Estimating such value is quite complicate, due to the irregularity of the deposit. An example of the deposit appearance in engine-like condition is reported by Taltavull et al. (2015). Taking a closer look at Fig. 5.19, the deposit is made up by elliptical discs. This is due to the splatting of the particle onto the surface and, since the substrate temperature is quite low (i.e. 600 °C) if compared with the temperature one can expect on the NGV surface, the deposit is only slightly (if not at all) sintered. This situation can thus be considered as the condition of the deposit before the sintering onset. The configuration can be related to the packing of ellipsoids, as shown in Fig. 5.20. The packing problem of such solids have been solved, among the others by Donev et al. (2004).

From their work it is possible to derive the starting packing fraction, Φ, used in this work. The variation of Φ reported by the authors in Donev et al. (2004), in agreement with Delaney et al. (2005) for the 2D case, varies in a narrow range. Delaney et al. (2005) found a variation passing from an aspect ratio (semi-minor to semi-major axes ratio) $\lambda = 0.8$ to 0.1 fitted with a third order polynomial with a maximum packing fraction $\Phi = 0.895$ and a minimum of $\Phi = 0.82$. The non-uniform distribution of aspect ratio applies to this case, since the PSD of the population injected is not a fixed diameter. One can expect as a consequence of such variability a different splatting morphology in addition to a range of sizes. As first guess, a reasonable value of the packing fraction is $\Phi = 0.8$. This equivalent packing value is introduced to keep into account the high disuniformity one finds in the

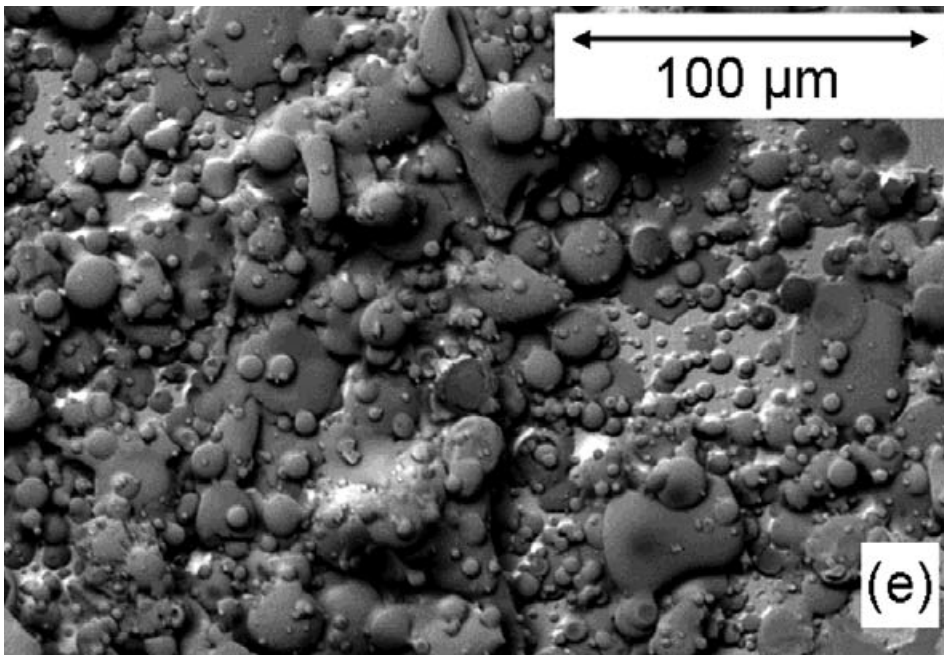

Figure 5.19: SEM micrographs of deposit, from Taltavull et al. (2015)

deposits, as one can see in Fig. 5.19. In a 2D analysis, the packing fraction of elliptical disks is generally higher with respect to the spherical packing. Referring to the results reported by Delaney et al. (2005), an ellipsoids distribution having $\lambda = 1$ (i.e. spheres) has a packing fraction $\Phi = 0.84$. This is not true any longer if a 3D analysis is considered: in that case the spherical jamming implies the densest Φ possible, as suggested by Donev et al. (2004) as high as 0.74. An higher packing fraction implies smaller porosity with consequences that will be described in the following. This means that assuming, in the 2D case, elliptical disks rather than spheres implies more detrimental conditions.

It is interesting to note here that such value of the packing fraction is related to the total volume of the build up with respect to the actual volume occupied by the particles. This reflects on having a total height different than the one theoretically given by the conservation of the particle volume. Assuming $\Phi = 0.8$, the total volume of the deposit is 1.4 times the total volume of the particle deposited, in order to allow for the presence of empty spaces. Besides, the procedure for the boundary displacement employed in this work introduces an extra constraint. In particular, displacing the points of the boundary face affected by deposition, the total volume swept by the boundary is actually greater than the particle volume itself, even without considering the void fraction due to porosity. This is due to the fact that neighbour faces on the wall are sharing points with the faces displaced, and thus they are deformed as well. Assuming three consecutive faces on the boundary have the same lenght and the central face is displaced by a quantity h_{dep}, the total volume swept by the boundary is actually 1.67 times the volume predicted by the conservation of the particle mass. Thus to observe the value of 1.4 above estimated it is necessary to reduce the height of the deposit in the central face to a value $h_{dep,new} = 0.84 h_{dep}$. This fact entails a numerical spreading

Figure 5.20: M&M's candies: the packing of volcanic ash particles can be studied by considering the packing of ellipsoids

of the deposit, that is not representative of what actually happens and tends to mitigate the deposition effects. A way for reducing this numerical spreading is by passing from face-wise displacement to nodal-wise displacement. Further details on this approach are proposed in the Gecko-Like section 5.1.

The initial porosity of the deposit and its evolution over time is of paramount importance for the evaluation of the mechanical properties of the deposit itself. An interesting study evaluating the deposit strength as a function of the porosity was carried out by Kaliazine et al. (1997). In their work, the mechanical properties of build-up are evaluated via scaled-down experiments performed on brittle deposits at room temperature. The reader is referred to the next section for more details regarding the *brittle* property of the deposit. The variation of the tensile strength is ruled by the exponential law reported in Eq. (5.20)

$$\sigma = \sigma_0 e^{-10\epsilon} + 10\,(0.8 - \epsilon)^{3/2} \tag{5.20}$$

where σ is the tensile stress of the deposit, ϵ is the porosity and σ_0 is a constant equal to 35 MPa. This is quite a strong assumption since such values are derived for sintered kraft recovery dust. No similar relation for volcanic ash has been found, and thus such values are used. Equation (5.20) gives the admissible tensile stress over the exposure time, provided the law of variation of the porosity with the temperature. To derive this law, the Frenkel model Frenkel (1945) is used. Such model, formalized for two sintering spherical particles, is thought for the growth of necks between particles that share an initial contact, and is reported in Eq. (5.21)

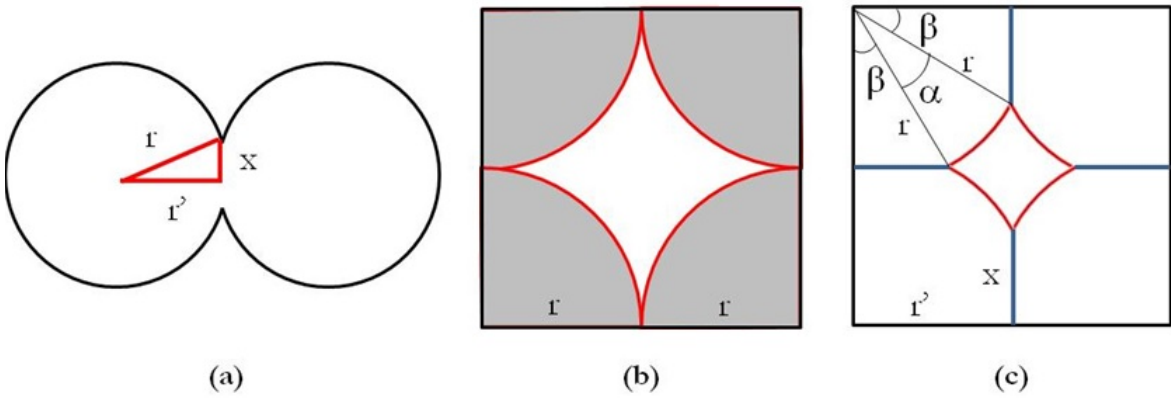

Figure 5.21: (a) Sketch of initial geometry of viscous spherical droplets as considered by Frenkel. (b) Geometry for the evaluation of the porosity at the sintering onset. (c) Progression of the sintering over time

$$\frac{x}{r} = 1.225 \left(\frac{\gamma}{\mu r}\right)^{0.5} t^{0.5} \tag{5.21}$$

where x and r have the meaning reported in Fig. 5.21(a). The former equation is representative of the pore filling procedure due to the temperature and the passing of the time. Temperature affects the surface tension and viscosity values according to the composition of the material under investigation. Several models are available in the literature for its estimation, and in this work the law reported by Song et al. (2017) was used. It must be remarked that the implicit assumption made by using this model is to assimilate the behaviour of elliptical discs (the deformed particle shape used in this work) to spherical particles, from the standpoint of the porosity variation over time. The authors are not aware of sintering laws for shapes different from the spherical, and thus this model has been used. By considering ellipsoids instead of spheres what actually changes is not only the packing fraction, but also the number of contacts per particle. Donev et al. (2004) found an increase in the number of contact points per particle, Z. Z is known to be equal to 6 in case of spheres, and rapidly increase as the particle deflect from the perfect sperical shape, reaching $Z = 10$ for ellipsoids. Higher values of Z entail more nucleation points for the necks among particles in contact. It is thus reasonable to expect an increase in the sintering velocity. This fact has not been taken into account in this work and it is considered a next step in the development of this methodology.

In order to retrieve the porosity variation over time one has to evaluate the evolution of the white area of Fig. 5.21(b), representing a pore in the deposit (that is the area enclosed among four particles in a 2D approach). The variation of the white area of Fig. 5.21(b) over time can be expressed as in Eqn.

$$A = f\left(\frac{x}{r}\right) = 4r'^2 - 2\alpha r^2 - 4\frac{x^2}{tan\beta} \tag{5.22}$$

With the nomenclature of Fig. 5.21(c) and keeping in mind that $r' = x/tan\beta$. The angles α and β can be calculated from the result of Eq. (5.21) and from Eq. (5.23)

$$\alpha = \frac{\pi}{2} - 2\beta \qquad\qquad \beta = arcsin\left(\frac{x}{r}\right) \tag{5.23}$$

In this work the deposit aging has been implemented in such a way that successive layers have different sintering time. Every time a new particle deposits, the porosity of the new layer is initialized as above explained (see Fig. 5.20). The underlying layers, on the other hand, have a porosity that is function of the time passed since they first stuck and of their size, as in Eqn. (5.22). In such a way, depending on the porosity value, the spallation can happen either on the outer layer or can manifest as debonding of the entire build-up. Such a remark attempts to solve the problem of the spallation location addressed in section 5.1.

Shrinkage

The evolution over time of the deposit is such that the change of shape due to sintering entails a reduction in the overall build-up volume Zbogar et al. (2009). Particularly, the pore-filling procedure is reported as one of the main driver of such a process, see Nowok (1996) for further details. In this work the reduction in volume is related to the pore filling procedure described in the previous section. The volume variation and thus the deposit shrinking can be easily retrieved by the porosity variation over two successive time step: the blank area reduction in Fig. 5.21 is the responsible of the overall deflation of the boundary.

Adhesion Forces

Sintering is a phenomenon that is relevant for the build-up resistance, but the bonds with the underlying surface has not been discussed yet. What it must be evaluated is the entity of the forces that keep the deposit attached to the surface. The only force kept into account in this work is the Van der Waals force. The electrostatic force is always small (of at least one order of magnitude) and can therefore be neglected in the analysisBerbner and Löffler (1994). Besides, particle are considered soften but still solid, without liquid phase. This assumption allows to ignore the capillary forces and so no Laplace forces are included.

The London - Van der Waals force is a short range force that originates in the instantaneous dipole generated by the fluctuation of electron cloud around the nucleus of

electrically neutral atoms. It decreases rapidly as the distance increase, but its value has entity similar to the liquid bridge when the particle is in "contact" with the surface Berbner and Löffler (1994). The relation for such a force is reported in Eq. (5.24).

$$F_{VdW} = \frac{A\,2R}{12D^2} \tag{5.24}$$

where A is the Hamaker constant and D is the minimum distance between particle and surface (assumed equal to 4 10^{-10}, as proposed by Israelachvili (2011)). It is common practice to add subscripts to the constant A in order to point out the elements in contact, so in this case the constant A takes the form A_{12} where 1 refers to the particle, 2 to the surface (blade). The database for the A constant is often available only in the form A_{jj}, meaning the contact of spheres of the same materials. In order to obtain the constant representative of the case, the relation proposed by Visser (1972) is used, that allows to derive A_{ij} as the geometric average of the two material.

$$A_{12} = \sqrt{A_{11}A_{22}} \tag{5.25}$$

The values employed in this work are $A_{11} = 1e-20$, from Ontiveros-Ortega et al. (2016) and $A_{22} = 21.2e-20$ for the stainless steel. This force is tought to be applied at the center of the deposit and in the norm al to the surface direction when the torque balance for the detachment is carried out (see the next section for further details).

All the above mentioned considerations may be ill-conditioned if the actual particle shape is accounted for. Referring to the work of Bowling (1988) the van der Waals forces are extremely sensitive to particle shape. In that work, the deformation of a sphere is considered, showing that for a deformation of the 10 % for a 5 μm diameter particle can magnify the van der Waals force of 5 times. Particles impacting the HPT nozzle are splattered on the surface and this will for sure entail an increase in the contact area, as show in Fig. 5.19. An increase in the adhesion force is therefore expected. This aspect is considered a next step of the deposition modeling and is not considered here.

Detaching forces

The decision of whether the particle detaches or not is made after a force balance is carried out on the stuck particle. Particularly the detaching force acting on the deposit is the drag force. Other effects, e.g. turbulent bursts, have not been kept into account since the work of Soltani and Ahmadi Soltani and Ahmadi (1994) proved these are negligible.

The drag force formulation used here is similar to the one proposed by El-Batsh El-Batsh (2001). The only difference is that the comparison is done among forces: there is

no need to evaluate the critical friction velocity as done in the above mentioned works.

The main advantage of this approach resides in the possibility of directly comparing the drag induced by the flow shear with the other forces, as explained in the previous section. The drag force implemented is:

$$F_D = \frac{3\pi}{2}\frac{\rho f R}{Cu}u_\tau^2 \tag{5.26}$$

That must be solved together with $Cu = 1 + Kn[1.257 + 0.4exp(-1.1/Kn)]$, where Kn is the Knudsen number and $f = 1.7$ is the correction factor proposed by O'Neill (1968) in order to account for the presence of the smooth wall.

Detachment

The deposit build-up may be subject to detachment if the flow conditions change or if it protrudes into the core flow. As reported by Zbogar et al. (2009), the deposit may shed away by two different mechanisms: ductile rather than brittle. Brittle break-up may happen when the deposit is poorly sintered. In such a scenario, a single or some layers of the deposit can shed breaking the bonds with the underlying layers. On the other hand, a more sintered build-up promotes a ductile behaviour. Typically the detachment happens by debonding from the metal substrate of the entire deposit.

The implementation of the detachment proposed in 5.2.1 has been modified. Indeed detachment was imposed pointwise: if the wall shear stress was such that the conditions was favourable for the detachment, the deposit in the node was completely removed. This approach has been updated from different standpoints. Firstly, it may happen that not all the deposit sheds away, but rather an outer-layer spallation might occur. Secondly, the detachment is not nodal-wise any longer, since the faces are of interest now. Lastly, the sintering of the deposit may be such that near faces are interested by this phenomenon. This involves the inception of inter-faces bonds. If this is the case, the build-up acts as a unique structure, exchanging tension among adjacent faces. It is well clear thus that even if the deposit is detached as a whole, and thus by debonding mechanism, the porosity of the deposit still plays an important role. Indeed, taking as reference Fig. 5.22, if the build-up on the left hand side of the dashed vertical line tends to detach, the balance at the dashed line itself must be carried out. Particularly, the torque that tends to overturn the left deposit is counteracted by a bending moment. Such a bending moment can keep the deposit stuck until the admissible tension, given by Eqn. (5.20) is overcome. The only admissible breaking locations are the faces between two adjacent cells (represented by the dashed line in Fig. 5.22).

To evaluate the detachment area the following procedure have been adopted:

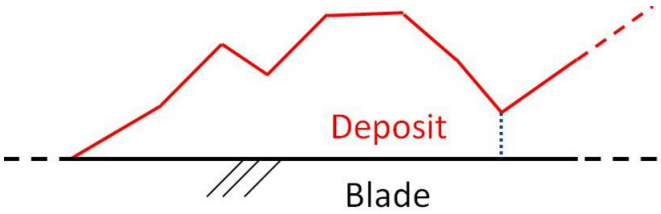

Figure 5.22: Side view of a 2D deposit.

- The shear stress is computed on the boundary face under investigation dividing the drag force by the face area
- If the resulting shear is higher than the admissible shear stress of the outer layer that compose the build-up, assumed to be equal to 0.5 σ (given by Eqn. (5.20)), such a layer is shed away. This assumption derives from simple solid mechanics considerations
- If the admissible stress is higher than the shear induced by the flow friction, the adhesion forces of the deposit on such face are computed
- The resulting torque acting on the lateral faces of the deposit (the faces that separes two adjacent cells, the dashed line in Fig. 5.22) is computed.
- If the bending moment causes higher tension than the admissible one, the deposit debonding on such a face happens

The evaluation is therefore repeated for the next cells reporting adhesion.

Effect on sintering on the deposit and on the flow field

The transient analysis of 0.2 physical seconds of exposure of the LS89 NGV to a volcanic ash cloud has been carried out. Figure 5.23 reports the variation of the vane shape during exposure. The graph reports the unwrapped blade and the x-axis represents the baseline. Negative values of the displacement stand for deposits and positive values are for erosion. This graph can be directly compared with Fig. 5.12, reported in the same graph to ease the reader (labelled as "No sintering"). The difference in the two numerical setup is the wall temperature that has been increased of 100 K in order to promote the sintering effect. The other difference is the change in the erosive behaviour if the particle hits the already formed deposit: in this work, the particles rebound without any consequences. This choice is driven by two different trends reported in literature. On the one hand, Whitaker et al. (2016) carried out experimental tests at 866 K, reporting deposit erosion by larger particle impact. On the other hand, several authors, e.g. Borello et al. (2014), consider the surface as being sticky, owing its own "surface sticking probability". This idea was first introduced by Walsh et al. (1990) , in formalizing the critical viscosity model.

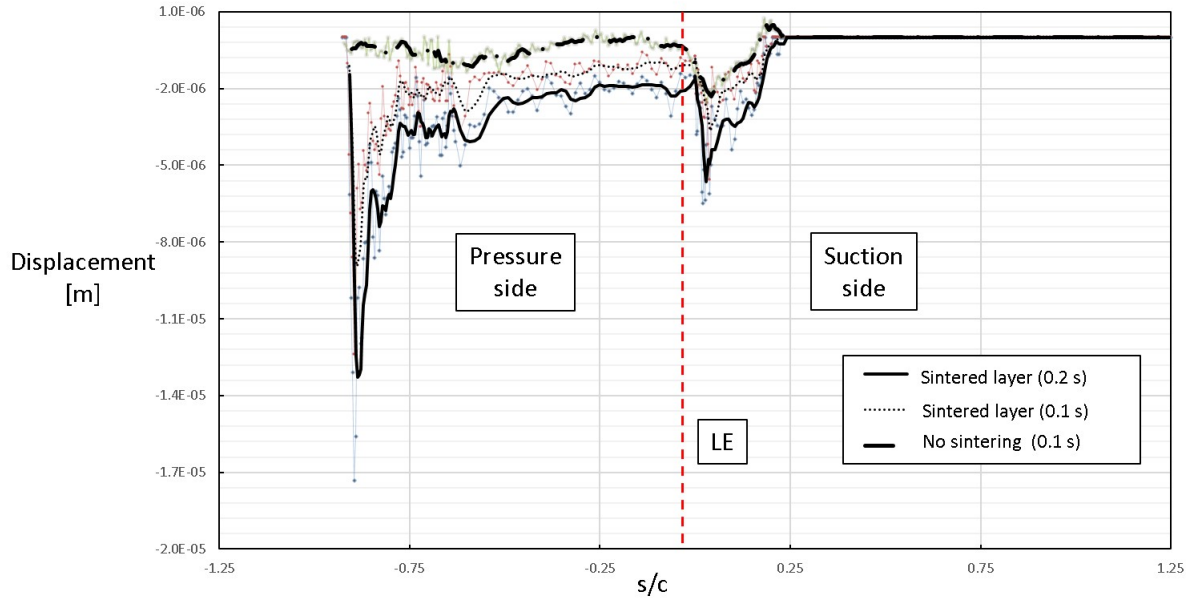

Figure 5.23: Deposition pattern along the unwrapped vane. s is the curvilinear coordinate, c is the chord. The black lines are the moving average carried out on 4 points in order to improve the readability. The solid and dashed lines represents the evolution of the deposit after 0.1 second and 0.2 second of exposure, whereas the no sintering (dash-dot line) is the trend proposed in Fig. 5.12

The differences in the two approaches are probably related to the different characteristic temperature of the phenomenon under analysis. In the first case, the analysis is related to internal cooling deposition where particles are cooler and thus harder. In such a scenario it is reasonable to expect deposit removal by particle impact and thus an erosive behavior. In the latter case, the "sticky" assumption is related to the fact that a rather soften/semi-molten deposit is expected due to the higher temperature on the aerodynamic surfaces, and this tends to favour incoming particle deposition. In light of these considerations, this study considers pure particle rebound on the deposit.

It can be easily seen that the deposition pattern on the suction side is the same for all the cases, showing no impacts for the higher values of s/c. This does not change as the exposure time increases. As the leading edge is approached by decreasing s/c, the vane shape varies noticeably. In particular, the erosion area of the "No sintering" case is not discernible any more. The prevailing mechanism is indeed deposition, and this is probably related to the increased wall temperature, that changes the particle behaviour from erosive to adhesive. Proceeding towards the leading edge, the deposition is more pronounced and in the leading edge area a first deposit peak can be identified. This result is in agreement with the literature, for example with Prenter et al. (2016) or Borello et al. (2014). The combination of an higher blade temperature, the non-erosive behaviour of the particles impacting the deposit and the lower tendency to detach due to the packing considered in this work, reflects in an higher value of deposition in the first 0.1 second of exposure. The shape after 0.2 seconds, in the leading edge area, shows a higher values of

the deposits recorded for the vane at 0.1 second, but somehow retaining the same shape.

Proceeding along negative values of the curvilinear adimensional coordinate s/c, the vane experiences deposition. The deposit height is almost constant along the pressure side evolution. This result is in good agreement with the literature, for example with Casaday et al. (2014). The "No sintering" case shows in this area a remarkably different behaviour. Deposition is still the main effect, but the mean value is lower than the sintered cases. In the authors' opinion this is mostly related to erosion. In this area the shear stress, and thus the detachment, are quite small, as will be described below). The joint effect of increased wall temperature and erosion prevention, promotes a noticeably higher deposition rate in the present work. Approaching the trailing edge area the deposit reaches its global maximum. This is remark is apparently contradictory with what has been found in 5.2.1, where an asymptotic value was identified as balance among the detaching forces and the deposition rate of the particles. Here the sintering and the packing of the particles play a major role and prevents such detachment to occur.

The torque balance described in the previous section is indeed strongly dependent on the admissible tension variation with the porosity. As the porosity lowers, as it happen due to the sintering, the strength the deposit can bear increases. On the top of that, the kinetic energy the particle has when it impinges the deposit is such that the porosity of the deposit is small since the very beginning of the sintering process (as it is shown in Figs. 5.19 and 5.20). Thus it is reasonable to expect that the deposit has to grow far way more with respect to the "No sintering" case. The protrusion towards the core flow increases the drag forces that acts on the deposit, and only in that case the detachment can happen.

In the first 0.2 seconds of exposure the brittle spallation has never verified: the shear tension is indeed very small if compared with the tension predicted by Eq. (5.20). The maximum allowable tension bearable by the deposit is around 4 MPa, for a porosity of 0.2. If the debonding is considered, the maximum "detaching" tension (that occurs in the trailing edge area) is around 0.7 MPa.

The debonding occurrence, as well as the brittle spallation, is closely related to the tensile strength law variation with the porosity, the packing fraction chosen and the sintering law used. In order to give the outcome of this work a more general validity, the non-dimensional detachment moment F^* distribution along the unwrapped vane is reported in Fig. 5.24. F is representative of the detaching moment acting on the deposit, and it is defined as the wall shear stress magnitude measured at the deposit boundary times the deposit height. In other words F is proportional to the detaching torque per unit length. In order to non-dimensionalize such quantity, it is divided by its maximum value, that occurs in the pressure side - trailing edge area.

From the distribution of F^* it is evident that particles lying on the first part of the

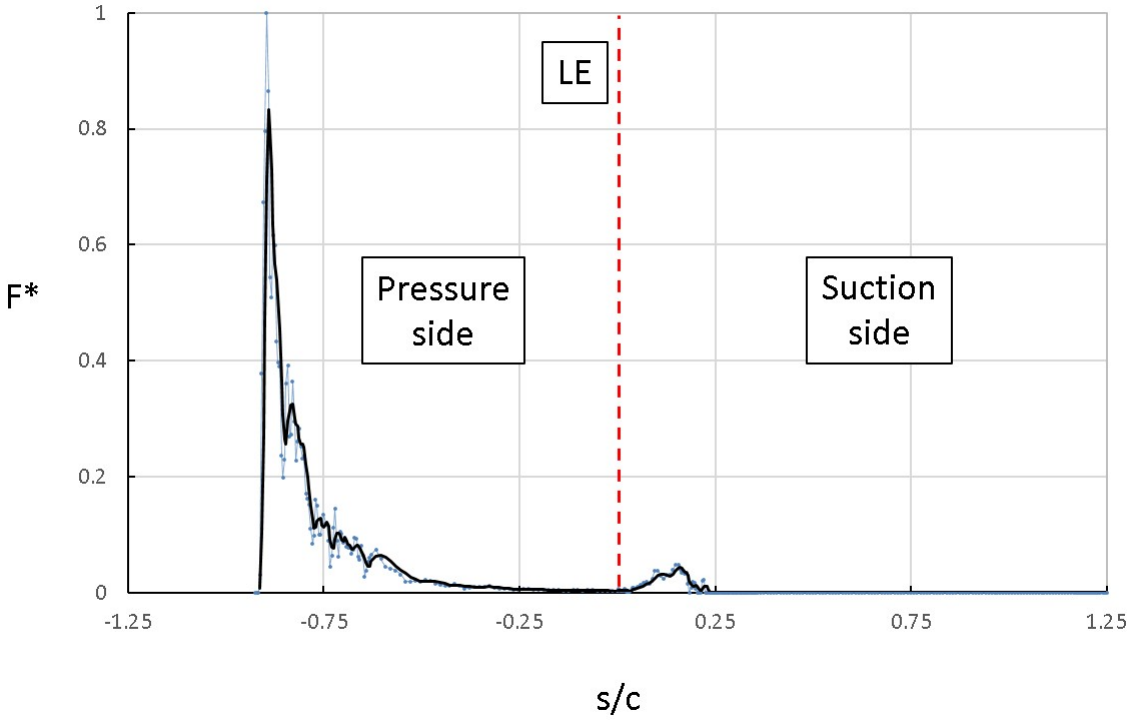

Figure 5.24: Non-dimensional detachment moment distribution along the unwrapped vane after 0.2 s of exposure. The black line is the moving average carried out on 4 points in order to improve the readability. s and c with the meaning of Fig. 5.23

pressure side (at s/c > -0.75) are seldom removed by the shear stress effect. The same remark can be done for the leading edge area in the suction side. F^* grows at the very end of the pressure side. This justifies the fact that the particles in the trailing edge area are more prone to be detaches and it supports the findings reported in section 5.2.1.

By using a different law from the one proposed in Eqn. (5.20), it is thus possible to record detachment. In light of these remarks, one can easily compare the admissible tension such a law would provide with the detaching torque per unit length distribution provided by Fig. 5.24. In order to have dimensional quantities from the distribution of F, it is necessary to multiply F^* times 0.036 Pa m.

In light of this remark it is still justifiable the presence of a trailing edge asymptotic value for the build-up, experimentally found by Webb et al. (2012). The appropriate law for the sintering must be used as well as the proper packing fraction starting value. In order to have balance in the spallation, a brittle fracture must happen. It is therefore reasonable to expect that such fracture should verify in the very first moments of the new particle deposition, otherwise the sintering becomes non negligible and the behaviour of the fracture starts to be ductile, entailing debonding rather than spallation. This statement makes the choice of the starting value of the packing fraction a non-trivial step.

The pressure distribution relative to the fouled geometry is reported in Fig. 5.25.

Qualitatively, the pressure distribution is similar to the one related to the clean profile. Probably, a longer exposure time should be considered in order to appreciate the difference. A downwind displacement and a stronger value of the shock are indeed expected.

Figure 5.25: Pressure distribution on the fouled profile

More quantitative results can be retrieved by subtracting point-by-point the pressure field of the clean profile from the pressure field of the fouled profile, as shown in Fig. 5.26. In Fig. 5.26 Positive values of the pressure difference mean higher pressure in the fouled case. The operation is done starting from the same initial condition with the different geometries. The subtraction is carried out at the same instant, allowing the simulation to run for some time in order to achieve convergence. This approach is chosen in order to compare the two cases without the influence of the transient effects that inevitably arise during the deposition (mainly due to the mesh deformation). The pressure difference is useful to investigate the consequences of deposition on the flow structures. The major

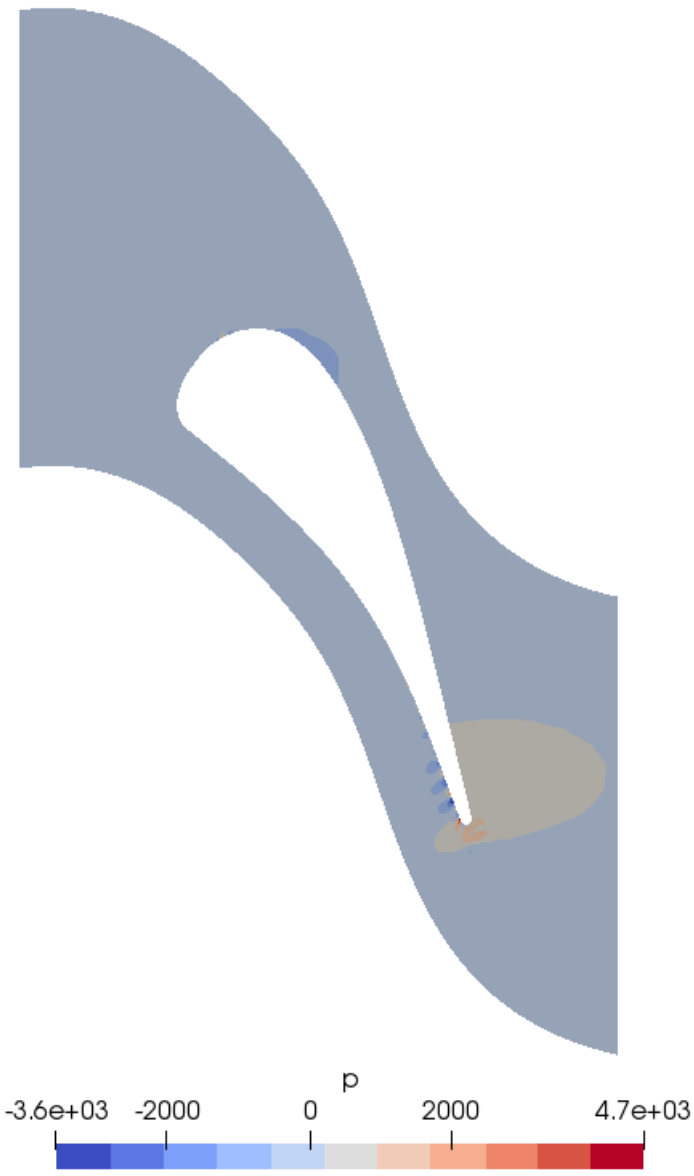

Figure 5.26: Pressure difference distribution on the fouled profile. Positive values imply higher pressure in fouled case

difference is located in the trailing edge, pressure-side area. In the case of fouled profile, an higher pressure area forms in such zone. The over-pressure area, having an average value of 1 kPa, locates just downstream the shock area in the clean case. The strengthening of the discontinuity is therefore correctly predicted. The same procedure, if carried out on the temperature, predicts an increase in the temperature of 1 K, passing from cleaned to fouled profile. An interesting pressure difference pattern that can be noted is around s/c = -0.75 to -1, with reference to Fig. 5.23. In this area, a series of depressions followed by over-pressure zones is present, spanning from -4 kPa to +6 kPa. This pattern follows the peaks-valley distribution of Fig. 5.23. This reflects on a variation of the velocity at the trailing edge, implying a slight deflectuib in the exit angle, as shown in Fig. 5.27. The same point-by-point difference has been introduced here

Figure 5.27: Wake variation due to deposition

Deposition affects the HPT nozzle in such a way that the pressure losses along the gas path increases. The sintering occurrence worsen this aspect since the detachment is more difficult. This, in turn, implies a reduction in the mass flow rate flowing through the nozzle itself. After 0.2 s of exposure a reduction in mass flow of 0.06 % has been recorded in this work. This trend, if assumed to remain constant as the exposure time increases, leads to a reduction in mass flow rate of roughly the 4 % after one minute. This value is capable to demand engine shut-down. This time-scale for the energy life is in agreement with the literature data, as reported by Dunn (2012). It must be remarked that the assumption of constant boundary-growth rate is likely to imply more detrimental consequences with respect to the reality, since the detachment rate is expected to raise as the protrusion towards the core flow increases.

Final Remarks

Although no debonding nor brittle spallation of the outer layer has been recorded over the observation time, the current analysis has outlined some interesting facts.

First of all, the need of a precise guess of the packing factor for the particles that constitutes the deposit has been pointed out. The brittle fracture is indeed promoted by higher porosity and small sintering time, so the way particles get stuck by the reciprocal

shape is of paramount importance. On the top of that, the sintering starts from the porosity this packing entails, and so also the debonding mechanism is affected by this.

The attaching forces and the sintering are thus higher than the detaching force in case of a vane, at least in the very first 0.2 seconds of exposure. This may not be true if a blade is under analysis, since the centrifugal forces are known to have a major effect on the stuck particles.

With respect to the former analysis carried out on the same geometry (section 5.2.1), the regions of erosion are not recorded. This is probably due to the increase in 100 K of the vane temperature to promote sintering, but it is evidence of how closely erosion hot erosion and deposition occur.

Deposition reflects on the pressure losses along the nozzle, implying the reduction in the mass flow rate. The mass flow rate reduction variation has been pointed out, proving the model presented is a reliable approach in predicting the particle deposition and deposit evolution.

The shape variation of the HPT as a consequence of the exposure time is therefore very sensitive to the blade temperature as well as to all the above mentioned factors. To reliably simulate a deposition problem, the evolution of the deposit over time should be kept into account. The characterization of the admissible tensile strength variation with the porosity is a crucial aspect in this perspective.

This page was intentionally left blank.

Chapter 6

First steps towards a robust design for fouling

Fouling and erosion are two problems that severely affect gas turbines. The shape of the blade, its roughness and its structural stability can vary as a consequence of these phenomena. The outcomes of this occurrence can span from the efficiency reduction to the engine shut down according to the nature of the material ingested, to the concentration of contaminant in the air, the cleanliness of fuel and to the particular design of the machine. There is therefore a strong need for improving the capability of designing blades keeping into account the degradation problem. In this work, an axial turbine airfoil is modified according to the requirement of less sensibility to the phenomena above mentioned, utilizing an automatic mesh generator algorithm developed for this purpose.

In this section the first steps in design an HPT section to be the optimal geometric configuration that allows to get to a robust design under conditions of deposition and erosion of solid particles. To solve this optimisation problem, an automated, robust, and fast global optimisation technique needs formalized and exploited.

6.1 Computational details

Two different software suites have been employed for the set-up of the algorithm. Salome-v8.4.0, Bergeaud and Lefebvre (2010), for the robust mesh generation algorithm, and OpenFoam-v3.0.1 have been used for such purpose. Starting with a baseline blade geometry corresponding to a point in the parameters space x, a DOE in the space itself was conducted, and then the geometry is varied, building a new mesh and performing a new simulation, until the optimum geometry was found. The degradation mechanisms considered in this work are deposition and erosion of ash particles deriving from volcanic

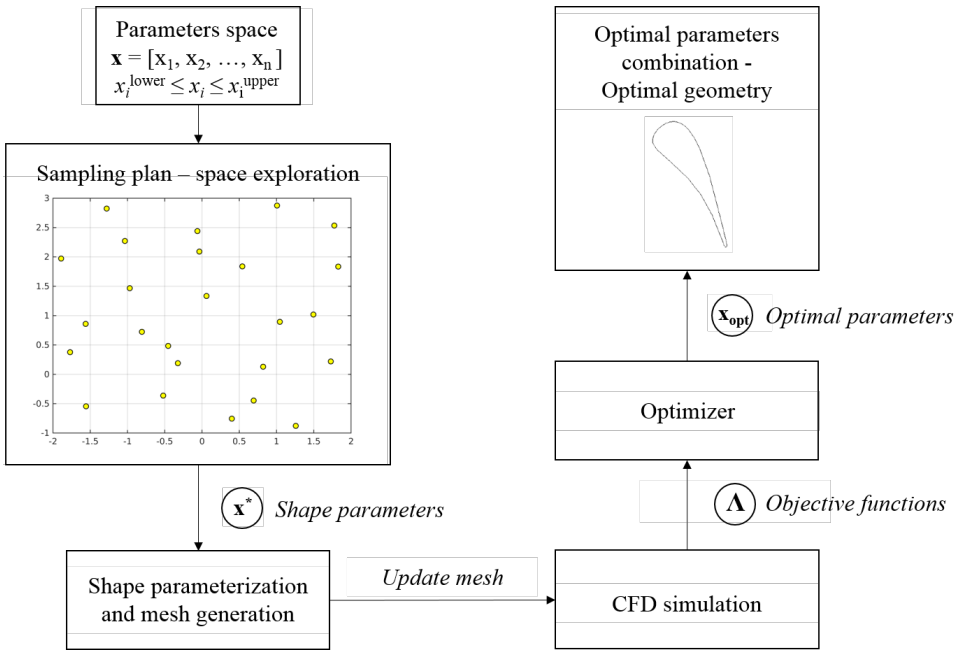

Figure 6.1: Optimization procedure implemented in this work

events, as reported in section 4.2. For counting the geometry variations due to deposition or erosion a mesh morphing was conducted, moving the impact grid points outward for deposition and inward for erosion.

6.1.1 Numerical procedure

Geometric parametrization

In this section, the focus of the analysis is a nozzle of HPT of a two-shaft aero-derivative model gas turbine, looking for an optimum blade geometry against particulate degradation. In order to evaluate the best combination of factors which leads to the best blade shape for this problem, the procedure reported in Fig.6.1 was implemented. Starting from the parameters space, the process works as follows:

Specifically, the blocks of Fig. 6.1 are described in the following.

- Parameters space – Is the set of all possible combinations of values for all the different parameters. Every point in this space is identified by a vector x composed by n components, which is all the parameters of the problem. In this work the parameters will be the coefficients/weights of the polynomial which describes the airfoil, Besides, are imposed upper and lower limits for each parameter, corresponding to a 20 % of variation for each of them.

- Sampling plan – In this step, all the input vectors $\mathbf{x}^*$ composed of the shape pa-

rameters which will be used for the simulations were chosen. This is a crucial step since a large number of samples involves a large number of simulations and so large computation time. On the other hand, a small number of sample reflects in an underrating of the whole space, and so poor accuracy.

- Shape parameterization and mesh generation – Each point sampled in the previous step were used to generate a parameterized blade shape and then a mesh for the simulation step. In this step an automatic algorithm that builds the 2D parameterized turbine blade geometry and mesh it was used.

- CFD simulation – In this step, the flow field and the particle injection effect were analyzed. The output of the step is the objective function Λ, which has to be minimize or maximize by the optimizer.

- Optimizer – after the calculation of the objective function, the optimizer processes the data identifying what the optimal point may be. Such point could not correspond to one of the given set of parameters. When the optimal combination was found, this step gives the best geometry for the given problem. For this step, a surrogate-based optimization was used Skinner and Zare-Behtash (2018).

For this purpose three open-source software suites were used, such as Dakota-v6.4.0 for the sampling and the optimization, Salome-v8.4.0 for the geometry and mesh generation and OpenFoam-v3.0.1 for the CFD simulations. The degradation mechanisms considered in this work are deposition and erosion of ash particles deriving from volcanic events. To take into account the geometry variations due to degradation, the face displacement mesh morphing technique described in chapter 5 was used, moving the impact grid points inward the domain for deposition and outward the domain for erosion.

Geometry definition

Geometry parameterization is the first step for the airfoil optimization, as it leads to a description of the whole shape by a finite number of parameters. Modifying these parameters in conjunction with their constraints, one can obtain different geometries. Many parameterization methods are available in the literature for airfoils, like Ferguson Curves, Hicks-Henne bump functions, B-Splines, PARSEC and CST Ceze et al. (2009). Sripawadkul et al. Sripawadkul et al. (2010) compared all these methods against some criteria and stated that the most suitable are PARSEC and CST for their completeness, which allows the parameterization to describe any airfoil, and orthogonality, which guarantees that

In this work, the CST method (Class Shape function Transformation) was used, in the version proposed by Kulfan and Bussoletti (2006). Such method a two-dimensional geometry represented by the product of a class function, $C(x/c)$, where c is the airfoil

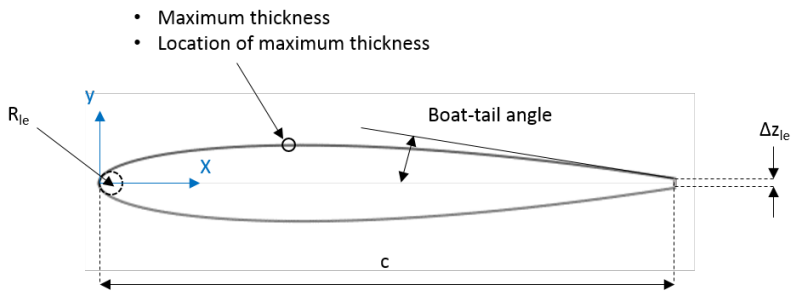

Figure 6.2: Example mesh resulting from the algorithm

chord, and a shape function, $S(x)$ plus a term that characterizes the trailing edge thickness (Δz_{te}). Figure 6.2 shows these five variables/parameters definition for a symmetric airfoil.

$$\frac{y}{c} = C\left(\frac{x}{c}\right) S\left(\frac{x}{c}\right) + \left(\frac{x}{c}\right) \frac{\Delta z_{te}}{c} \tag{6.1}$$

where $C(x/c)$ is given in generic form by:

$$C\left(\frac{x}{c}\right) = \left(\frac{x}{c}\right)^{N_1} \left[1 - \left(\frac{x}{c}\right)\right]^{N_2} \quad \text{for} \quad 0 \leq \frac{x}{c} \leq 1 \tag{6.2}$$

The exponents N_1 and N_2 define the type of geometry to be represented. An airfoil is represented by $N_1 = 1/2$ and $N_2 = 1$. The shape function was built with the constraints:

$$S(0) = \sqrt{\frac{2R_{le}}{c}} \quad S(1) = tan\beta + \frac{\Delta z_{te}}{c} \tag{6.3}$$

where R_{le} is the leading edge radius and β the airfoil boat-tail angle. The shape function acts as a scale function for $C(x/c)$. Kulfan and Bussoletti (2006) have proposed the use of a weighted sum of Bernstein binomials, to represent the shape function $S(x)$:

$$S(\frac{x}{c}) = \Sigma_{i=0}^{n} \left[b_i K_{i,n} \left(\frac{x}{c}\right)^i \left(1 - \frac{x}{c}\right)^{n-1} \right] \tag{6.4}$$

where b_i are the weighting factors and:

$$K_{i,n} = \frac{n!}{i!(n-1)} \tag{6.5}$$

For a 4^{th} order polynomial as S(x), the influence factors for the binomials at each control point was studied by Ceze et al. (2009). They found how much each of the weights influences the overall geometry variation, concluding that only the first and the last weights have the 100% of control respectively to the LE and the TE. All the others terms influence, more or less relevant, the variation of all points of the geometry. For

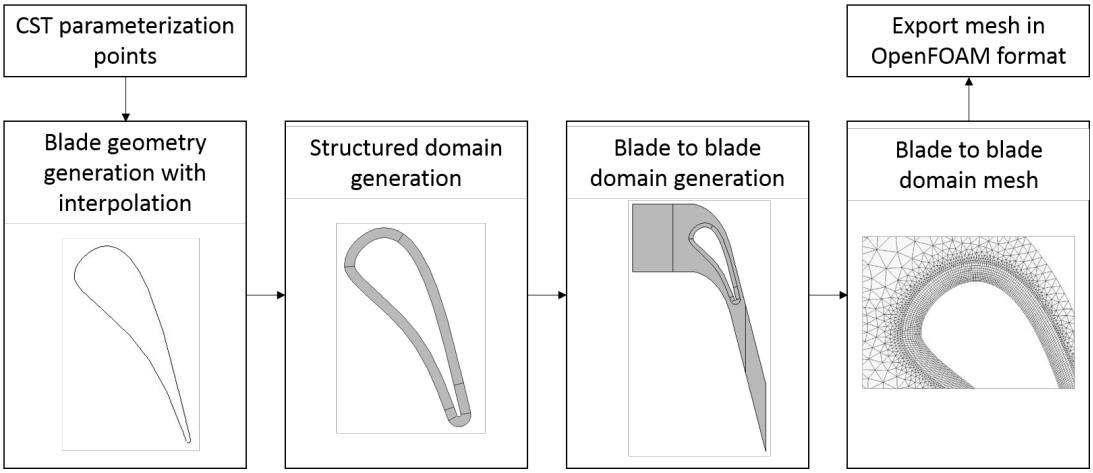

Figure 6.3: Automatic mesh generation algorithm

this work, 5^{th} order polynomials were chosen to describe either the pressure and suction side. Such CST parameterisation has been implemented in a python script and it has been integrated with the automatic mesh generator.

CFD resolution of the flow field

This work limits the study on a 2D problem: the analysis of the mid-span profile is the first step in the optimization problem. To make the processes of geometry and mesh creation robust, an automatic airfoil mesh generator was developed using Salome. This generator builds hybrid airfoil mesh, with a structured zone close to the blade and a non-structured zone in the rest of the blade-to-blade domain. The peculiarities of the developed mesh creator are the robustness against blade profile variations and the possibility to set the thickness of the structured zone. These particularities make the algorithm fully general, and it may be used for different optimization purposes. The algorithm developed is summarily illustrated in Fig. 6.3 Every mesh built by the algorithm has very good quality for OpenFoam-v3.0.1 requirements, even making smoothing unnecessary for cases where the geometry variations are not too big. The numerical analysis was carried out using the sonicFoam solver from Openfoam-v3.0.1 set for compressible flow. For the turbulence modeling the two-equation SST-kω turbulence model was used, thanks to its robustness in the resolution of the near-wall region. Since the domain generation and discretization were conducted by an algorithm developed by the author, a validation of the entire process, including the flow field resolutions, must be done. For this purpose, the VKI-LS89 test case was used as reference Arts et al. (1990). When the validation was satisfied, a scaling of the boundary conditions (BCs) was applied to get closer to the real work conditions of GT. These BCs are reported in Tab. 5.2. In the optimization process, every CFD simulation starts with the initialization of the flow field, in which no particles were seeded until the converged solution was reached. When the latter condition was satisfied the particles were seeded from the inlet patch of the domain.

Concerning the amount of particulate injected, a concentration of 250 mg/m^3 has been considered. The particle size distribution and properties are described in the section 5.2.1. Concerning the impact modelling, the same algorithm proposed in the section 5.2.1 has been applied here.

Optimization Problem

The optimization problem faced in this work was the constrained single-objective optimization formulated as:

$$\text{maximize} \quad \Lambda(\mathbf{x}) \tag{6.6}$$

$$\text{subject to} \quad x_i^{lower} \leq x_i \leq x_i^{upper} \; i = 1, ..., n \tag{6.7}$$

$$\text{where} \quad \mathbf{x} = \begin{bmatrix} x_1 \\ x_2 \\ \vdots \\ x_n \end{bmatrix} \tag{6.8}$$

The vector x is referred to as the vector of design variables. It contains the parameters of the design that can be modified. For the purpose, the design variables chosen are the coefficients of the polynomial that describes the pressure surface. The parameters' space exploration, or Design Of Experiment (DOE), was conducted with Latin Hypercube Sampling (LHS) as shown by Helton et al. Helton et al. (2006), assuming a Uniform distribution of samples for each parameter. The function $\Lambda(\mathbf{x})$ is called objective function. The substantial idea is: the vane shape configuration under deterioration improves its resistance against particulate injection effects by maximizing/minimizing this function (6.6). Equation (6.7) represents the range of variability of the design variables. Every couple of limits contributes to designate the feasible space, which is the space containing all the possible parameters' values, so every possible geometry configuration. Since the computational cost of the simulation is particularly high, optimization was performed by a surrogate-based model.

In this study the objective function to be maximize is the adiabatic efficiency η, calculated as follows:

$$\eta = \frac{h_{inlet} - h_{outlet}}{h_{inlet} - h_{outlet,is}} \tag{6.9}$$

Where, since the study is focused on the stator vane, h is the static enthalpy. This parameter is of paramount importance since a reduction of the performance of the nozzle reflects immediately on its value. For the constraints a 20% variation for each parameter

was chosen. Considering the results of the 3.2 section, only a variation of the LE and of the pressure side was considered.

The constraints reported in Equation (6.7) have been defined in agreement with such considerations. Specifically:

- Fixed throat section area, that governs the maximum mass flow rate of the engine and it's the main responsible for the possible shut down of the compressor part;
- Fixed exit flow angle, that governs the inlet angle of the flow in the rotor part of the stage.

Upper and lower limits of geometric variations are show in Fig. 6.4.

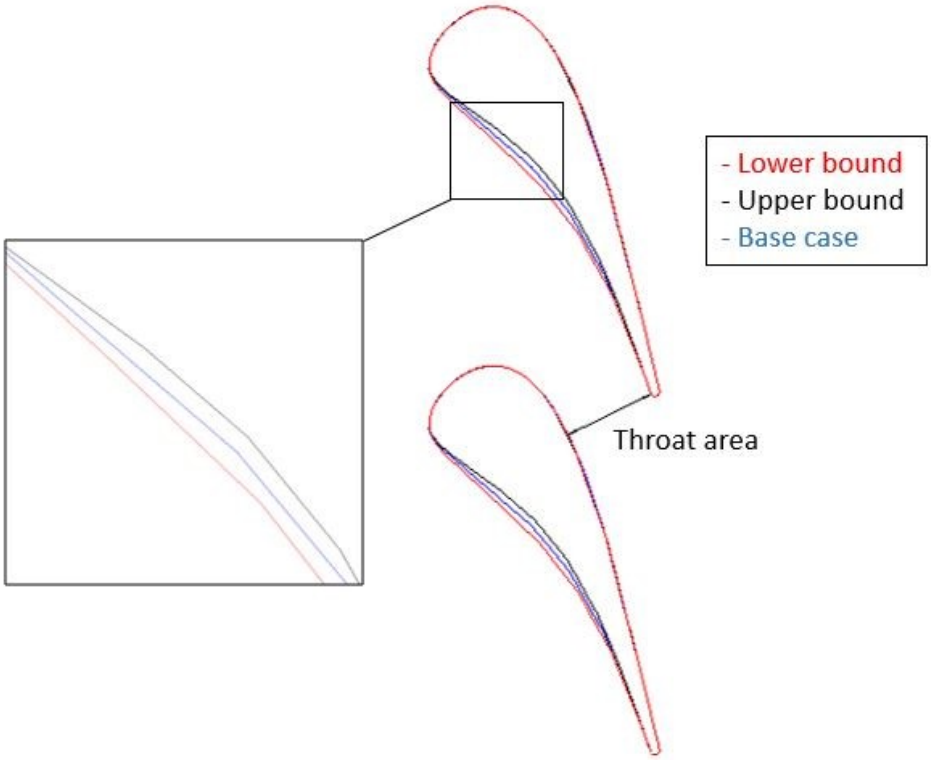

Figure 6.4: Limits for the geometric variation of the blade

Surrogate model

Suppose the simulation results can be written as a function:

$$f(x), \quad f : \mathbb{R}^n \to \mathbb{R}^m \tag{6.10}$$

A metamodel (or surrogate model) is a function:

$$\tilde{f}(x), \quad \tilde{f} : \mathbb{R}^n \rightarrow \mathbb{R}^m \tag{6.11}$$

with much lower computational cost with respect to $f(x)$ and

$$||\tilde{f}(x) - f|| \leq \varepsilon \tag{6.12}$$

Where |||| is an appropriate L_p norm and ε is sufficicently small.

The metamodel used in the current analysis is the Artificial Neural Networks (ANNs) fitting model with stochastic layered perceptron (SLP), designed to have a lower training cost than traditional ANNs Eldred (1998). The main difference between SLP ANNs and traditional ANNs is that, in addition to having transfer function for each perceptron, it also contains an activation function with a stochastic discriminant. The software used for this purpose is Dakota, that implements the SLP ANN model in the form:

$$\tilde{f}(x) = tanh(tanh((xA_0 + \Theta_0)A_1 + \Theta_1)) \tag{6.13}$$

where x is the current point in n-dimensional parameter space and terms A_0, Θ_0, A_1, Θ_1 are the matrices and vectors that correspond to the neuron weights and offset values in the ANN model. The general structure of perceptron is shown in Fig. 6.5. Principal components of neural networks are input layer which receives the shape parameters as input, one or more hidden layer and an output layer. The latter carried out the results of the training, which must be as near as possible to the training points. The training is done using 10 training data points, which is the minimum number for the model chosen Eldred (1998). The algorithm used for the training is the backpropagation.

Each layer is composed by perceptrons, whose logic structure is shown in Fig. 6.5. It can be seen that a perceptron receives as input some features xi, which are linked with the perceptron by weights wi. In the perceptron occurs two calculation steps:

- Transfer function – The weights and the features are combined, often linearly, to form the transfer function:

$$y = \sum_{i=1}^{n} w_i x_i \tag{6.14}$$

- Activation function – An activation function $f(y)$ is applied to the transfer function. In this analysis, the activation function has the form explained above.

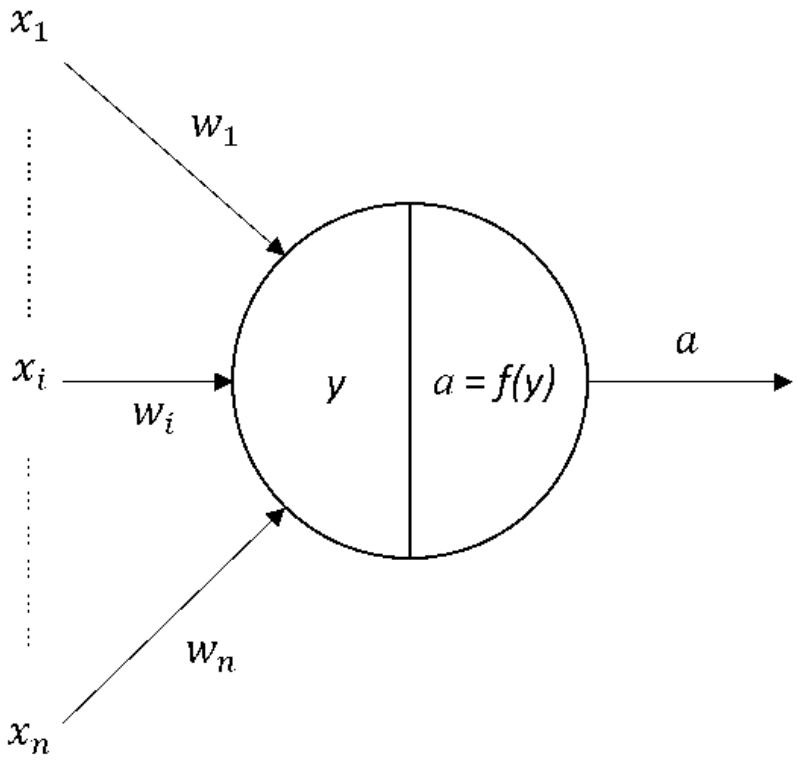

Figure 6.5: Perceptron architecture

An important parameter to choose is the number of hidden layers. If it is too much large the risk is to overfit the data, on the other hand, if it is too much low the risk is to underfit the data. There are different metrics for the evaluation of the quality of surrogate. The metric chosen in this work is the RSM (Root Mean Square), which is the best choice considering the maximum likelihood between the data and the surrogate hypersurface.

Optimization method

The optimization method considered is a gradient-based optimization method called feasible direction method Cheu (1989). This method differs from the classic gradient descent method for the further search step of the best descent or ascent direction. Particularly, the method used by Dakota is inside the CONMIN library Vanderplaats (1973). The drawback of this method is its strong dependence by the starting point, which can lead to a local minimum instead of the global one. The authors tried to fix this problem by using more than one starting point. Precisely the authors start in five different points, chosen with an LHS sampling of the parameter space Thévenin and Janiga (2008). The optimization was applied directly to the surrogate model created with the SLP ANNs method.

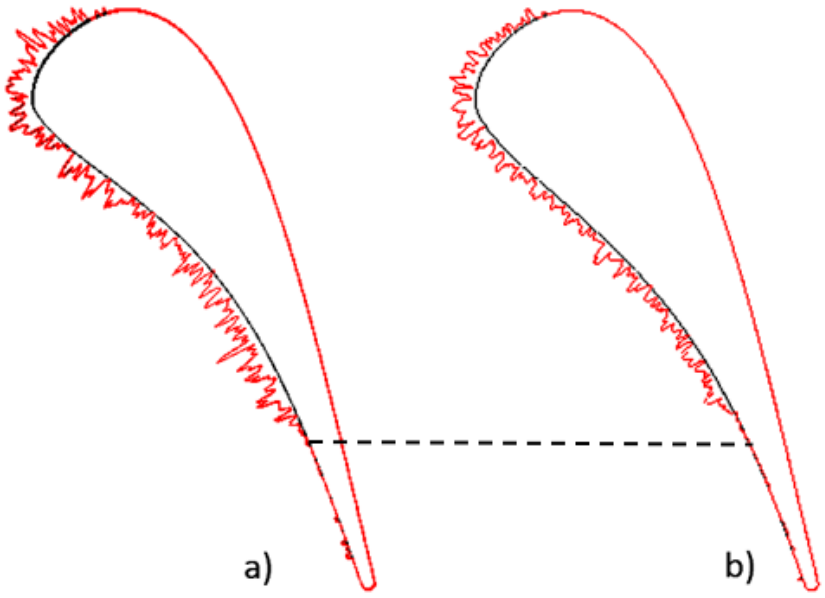

Figure 6.6: Overall of the blade displacement (red) for a) base case and b) lower case. Displacement is magnified of 500 times

Discussion of the results

The procedure described above was applied to a realistic turbine vane section in a bid to optimize it against the particulate injection effects. For the purpose, the first step consists of the study of the feasibility of the problem. In this step, a shape variations of the nozzle's PS are applied in order to highlight the influence of them on the performance of the vane. The second and final step consists of the real optimization of the nozzle through a surrogate based model. Among all the cases considered (samples in the sampling plan), the optimal shape configuration resulting from the process is near to the upper bound in the LE area, and to the lower bound in the remnant part of the geometry. Preliminary analysis. The preliminary analysis was conducted in order to find performance parameters variations once the shape of the nozzle has changed. Specifically, only the base geometry and the two bounds are considered. The results shown in this section are focused on the variation of the performance parameters among such shapes for either the clean and the fouled cases. Performance variation. The parameters monitored for the performance evaluation were the isentropic efficiency calculated as Eq. 6.9 and the loss coefficient (Y) calculated as follows:

$$Y = \frac{p_{01} - p_{02}}{p_{01} - p_2} \tag{6.15}$$

where p_{01} and p_{02} are the inlet and outlet total pressure respectively and p_2 is the outlet static pressure.

The vane shape variation comparison between the base case and the best case due to particle deposition and erosion after 0.5s of exposition is shown in Fig. 6.6 and Fig. 6.12. Figure 6.6 shows the variation of the blade geometry as a consequence of particle impact magnified 500 times. In this picture it can be noted how in the base case the deposition zone expands more toward the TE. It is possible to see the difference in terms of displacement magnitude, which can be more clearly appreciate in Fig. 6.12. The results of the comparisons are shown in Fig. 6.7 and Fig. 6.8 for both the clean (solid line) and fouled (dashed line) cases. For clarity, instead of the isentropic efficiency, the normalized isentropic efficiency ($\eta^N = \eta/\eta_{max}$) was used.

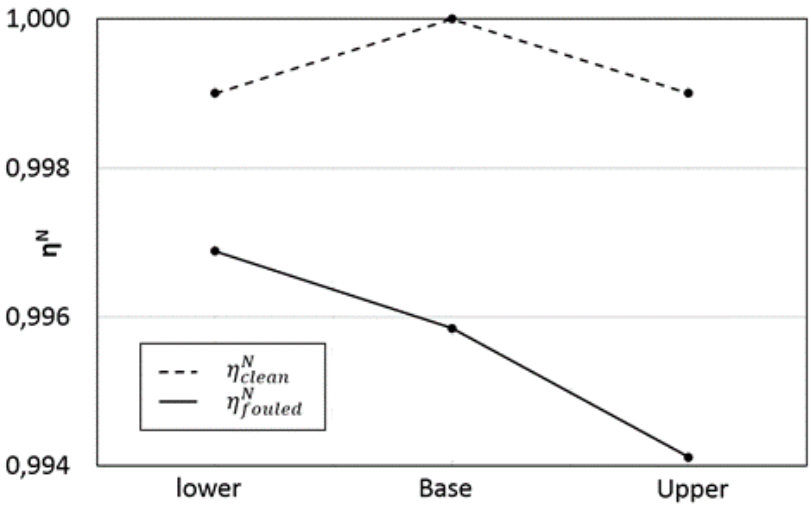

Figure 6.7: Isentropic efficiency comparison between the three fouled cases and the three cleaned cases

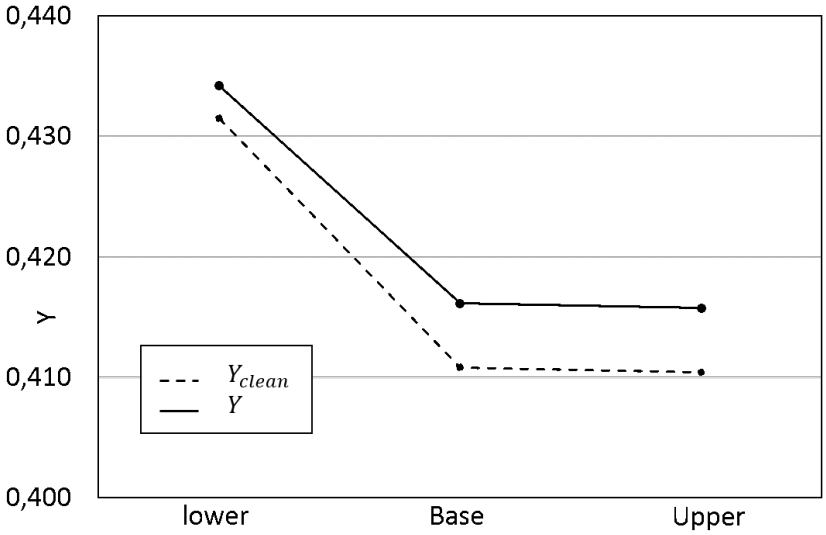

Figure 6.8: Loss coefficient comparison between the three fouled cases and the three cleaned cases

Figure 6.7 shows the values of the normalized isentropic efficiency for the geometry configurations. In absence of particle injections (clean cases) the efficiency reaches the max-

imum for the base geometry. When the deterioration effects (particle adhesion/erosion) are considered, the efficiency increases as one moves toward the lower bound, passing from (upper bound) to (lower bound). Figure 6.8 shows the loss coefficient values for the three geometry configurations. The highest losses occur in the lower case (0.434), being noticeably lower in the upper and base cases (0.415 and 0.416 respectively) when the clean cases are considered. The presence of deterioration effects tends to maintain such a trend. The lower bound remains the shape configuration with a higher value of loss coefficient. However, it can be noticed that the difference between the lower case and the other two cases decrease when deterioration occurs. With this preliminary analysis was underlined the feasibility of the study, therefore the opportunity to proceed with the actual optimization process for founding an optimal shape which can minimize the effects of the degradation

Optimization Results

With the results of the preliminary analysis, the actual optimization procedure was conducted, finding the optimal configuration which will be less sensitive to the deterioration problem. In the section exposed below only base and optimal geometries will be considered, comparing them and highlighting the main dissimilarities. The optimization process was conducted with a surrogate based model, with the feasible direction method as a search technique. The surrogate was built with SLP ANNs having an RMS goodness of fit of $7.33\text{x}10^{-2}$, that is comparable with the order of magnitude of the cost function variation. This suggests the appropriate choice of the number of training loops.

Comparison of vane shape

The optimal geometrical configuration found with the optimization procedure is depicted in Fig. 6.9. In this figure, lower and upper bounds are also shown. Two relevant geometric aspects can be noticed:

- In the LE area the optimal geometry tends to be very close to the upper limit, leading to a reduction of the LE radius;
- The optimal geometry shifts towards the lower limit approaching the TE.

It must be kept in mind that, as it can be noted in Fig. 6.9, the boat-tail angle and the throat section remain constant. In the following paragraphs, the differences between the base geometry (taken as a reference) and the optimal geometry will be described. Concerning the design geometrical parameters comparison, a reduction of 30 % is calculated

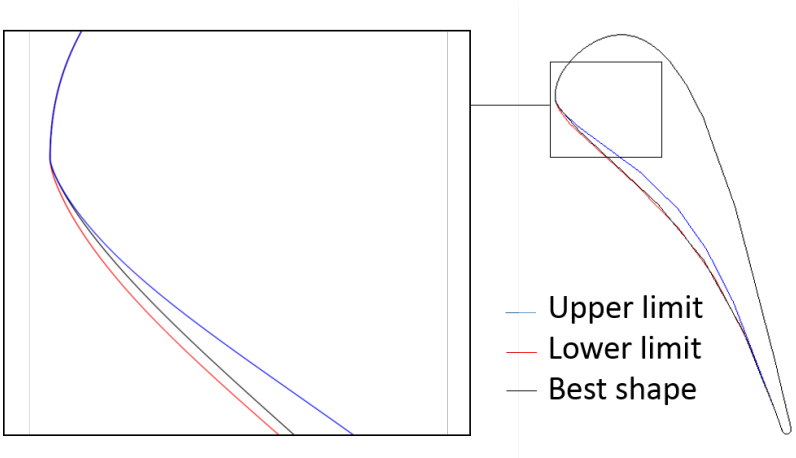

Figure 6.9: Comparison between upper, lower and optimal geometries

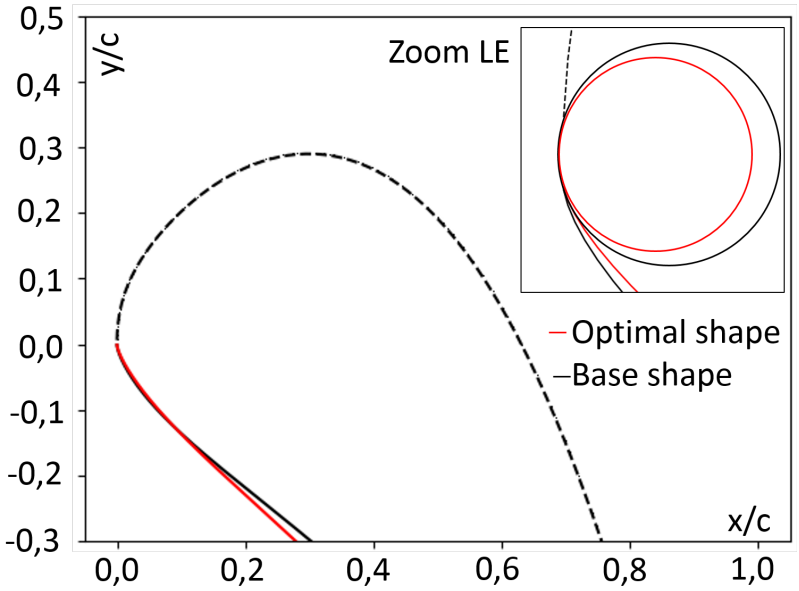

Figure 6.10: LE comparison between base and optimal geometries

for the LE radius. A qualitative comparison of such variation is illustrated in Fig. 6.10, where the two shapes are depicted.

Figure **??** reports the PS of the best and base shapes (solid red and black line respectively) and a close up of the leading edge in the right upper corner. The difference between the two radii can be noticed. Besides the LE radius, a flatter shape of PS can be observed comparing the geometries. Such comparison is reported in Fig. 6.11, which includes the baseline and the optimal configuration (solid black and redline respectively).

Regarding the overall vane shape variation after particle injection, the comparison after 0.5 s of exposure is shown in Fig. 6.12. Figure 6.12 shows the displacement magnitude (bottom) as a consequence of particles impact (erosion or deposition). Positive values correspond to erosion and negative stand for deposition. Analyzing the TE area, it can be noted how the degradation acts mainly as deposition in the base case and erosion in

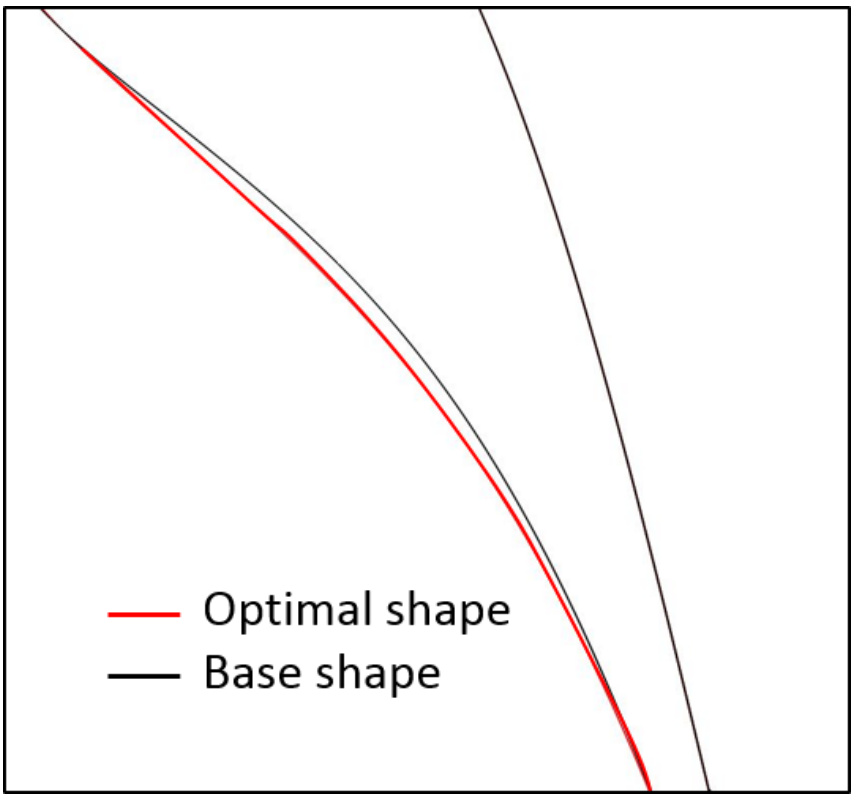

Figure 6.11: PS comparison between base and optimal geometries

the optimal case. Interestingly, small variations in shape, as the ones reported in this work, are such that the particle behavior upon impact changes in nature, passing from deposition to erosion. In Fig. 11 the cumulative deposit mass along the blade (top) is also depicted. This trend shows that the major difference is located in the middle of the PS, where the base case seems to capture higher particulate mass. This effect can also be retrieved in the LE area. In Figure 6.12 it can be noted also the difference in the total stuck mass after exposition: the optimal geometry grants almost 10 % lower deposited mass of contaminant compared with the base geometry. For the purpose of quantifying the difference of adhered particles, the capture efficiency (Ce) calculated as follows was considered:

$$C_e = \frac{\%particlestickonbladesurface}{\%particleseeded} \tag{6.16}$$

The values of this parameter for the base, lower, upper and optimal geometries are shown in Fig. 6.13. As can be seen, the capture efficiency increases as one moves towards the upper bound, passing from 27.3 % (lower bound) to 30.1% (upper bound). The isentropic efficiency trend (Fig. 6.7) seems to be closely related to the capture efficiency variation: decreasing when the latter increases. Besides, it can be seen that the capture efficiency of the optimal geometry (26.7 %) is lower than all other geometries in agreement with the aim of this study. This trend is thought to be related to particle inertia. In this track, the optimal geometry has found to have the following features:

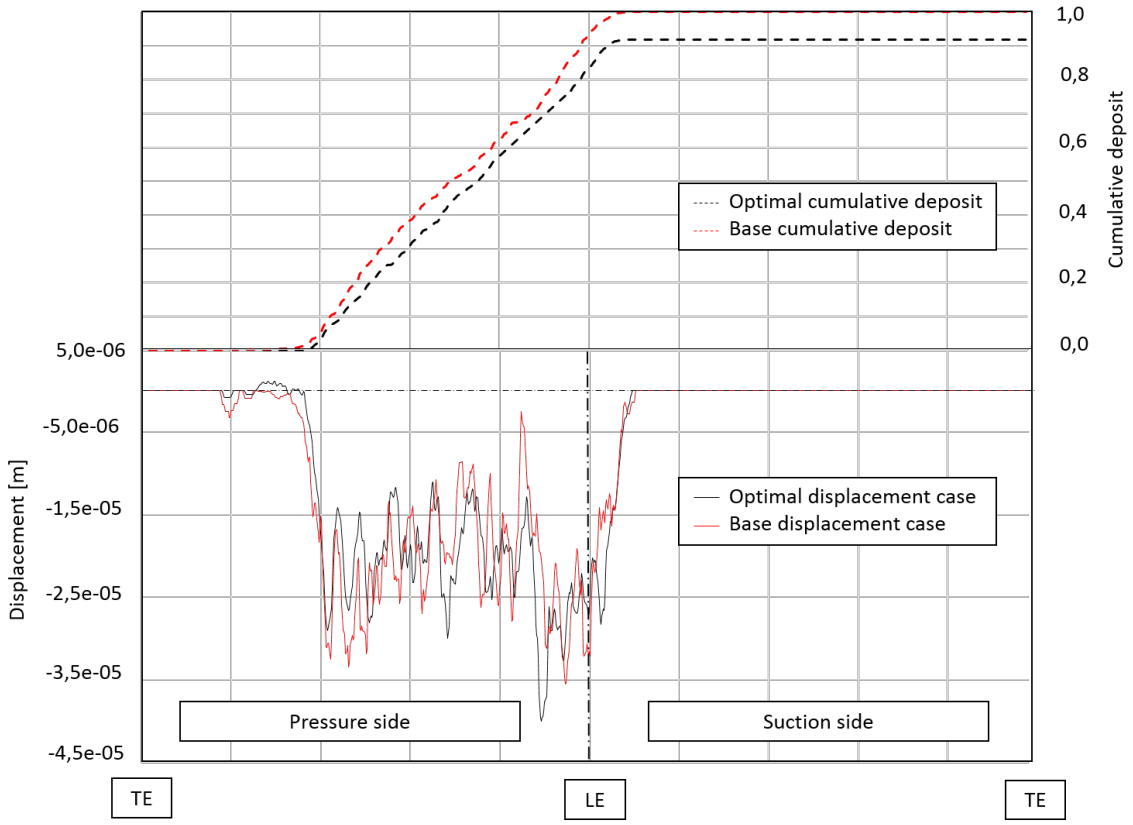

Figure 6.12: deposit evolution after 0.5s of exposure

- the best LE radius decrease approaching the upper limit, reducing the stagnation zone, and so the capture efficiency;
- after the LE, the best geometry become nearer to the lower limit, guiding the flow (so the particle) in a more smoothly way;
- from almost the half onwards, the flow (so the particle) is already guided and the flow angle variation is completed.

Performance variation. The outcome of the optimization process may be of help in the design phase. In this section, the performance dissimilarities between the base and optimal geometry will be analyzed. In Fig. 6.14 the objective function for the base and best cases and the two limits is shown. Looking at Fig. 6.14, it can be asserted that the isentropic efficiency of the fouled optimal case is higher than all other cases ($\eta_{fouled,best}$= 0.957. An important observation on the difference between the fouled and the clean cases can be pointed out here. The efficiency drop of the optimal configuration after degradation is lower than all others, particularly it is 25 % lower than the base case. This means the optimized geometry performances are less sensitive to particulate exposure. The opposite holds for the "upper case".

The considerations made on the isentropic efficiency are still valid also for the loss coefficient. For the clean optimal case the loss coefficient is higher than the clean base

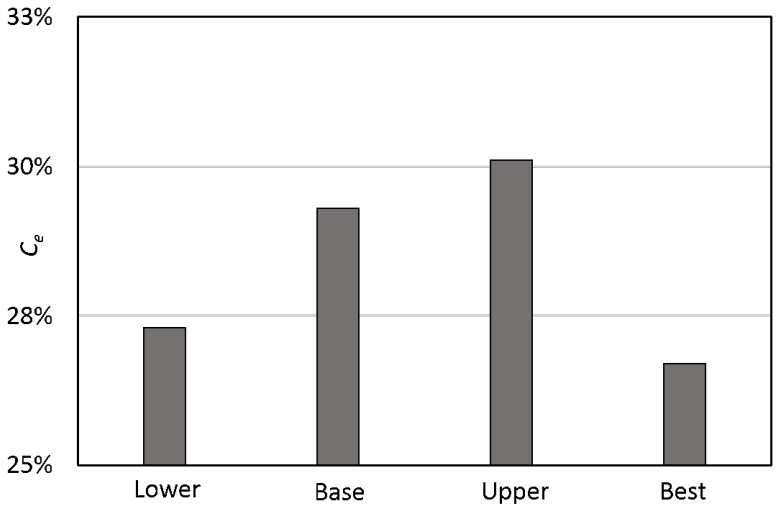

Figure 6.13: deposit evolution after 0.5s of exposure

case ($Y_{clean,best} = 0.417$), but after the degradation, it remains almost constant ($Y_{fouled,best}$ = 0.419) approaching more closely the value of the fouled base case ($Y_{fouled,base}$= 0.416). The remarks pointed out are consistent with the flow field structures analysis explained below. The main source of losses for the considered geometry is the shock. In Fig. **??** the trend of the pressure difference (optimal minus base) is shown. The analysis refers to the two cases when fouled. From Fig. 6.15, the variation in the position where the shock manifests can be retrieved. Specifically, since the positive value of the pressure difference is related to higher pressure in the optimal case, it can be inferred that in such case the shock translates upstream compared to the base case. In other words, if we consider the point to point subtraction of pressure trends, a peak greater than zero means the shock in the optimal case happens closer to the LE. This translation of the shock is also proved by the Mis trend shown in Fig. 6.16, where the zone in which the shock occurs is reported. It can be seen how the position of the shock in the fouled optimal case changes in agreement with the analysis carried out above. Besides, it must be noted that the magnitude of the shock in the latter case is smaller than the one in the base case. This fact is in agreement with the increase of the loss coefficient and the decrease of the isentropic efficiency.

A parameter that can be considered as representative of the load on the vane is the pressure coefficient Cp, calculated as:

$$C_p = \frac{p - p_\infty}{0.5\rho_\infty V_\infty^2} \tag{6.17}$$

where p_∞, ρ_∞ , and V_∞ are the pressure, density and velocity at the inlet of the domain. The C_p trend for clean cases is reported in Fig. 6.17. It can be noted how the pressure coefficient for the two cases maintains almost the same area, with the optimal case slightly smaller than the base one. This means smaller energy for shape effects in the latter is

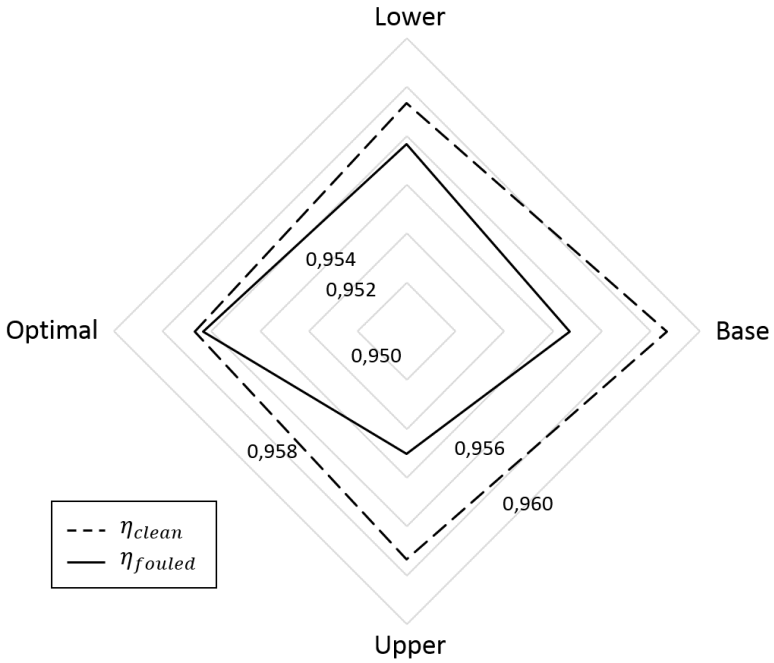

Figure 6.14: Isentropic efficiency for all the fouled and clean cases

lost, but a lower worsening of the performances is guaranteed with the first.

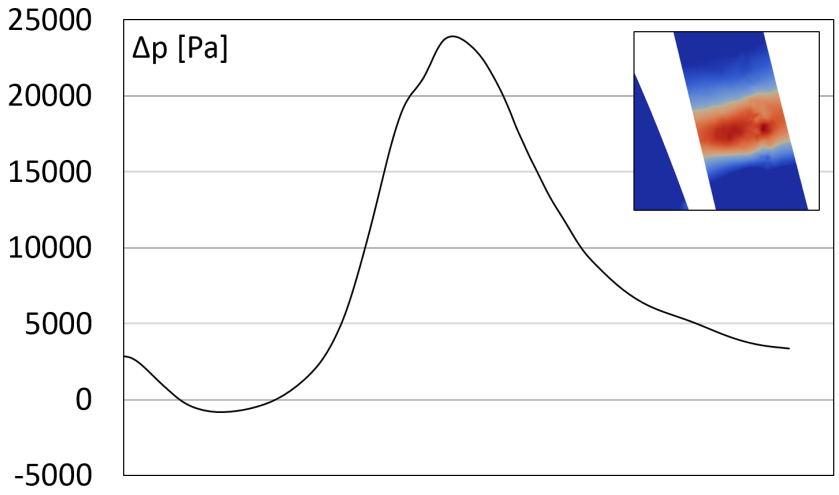

Figure 6.15: Pressure difference (optimal minus base) trend in the shock area

6.2 Final remarks

This chapter reports the first steps in the track of a robust design of an HPT under fouling conditions. A sensitivity study was conducted in order to find the turbine blade geometry which better resists to fouling conditions and at the same time maintains as good as possible performances. Starting from such considerations, a surrogate-based

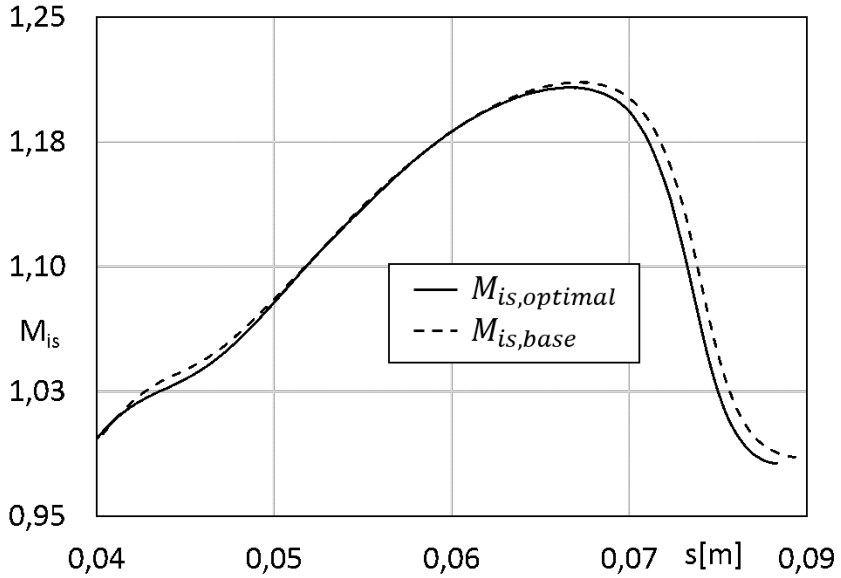

Figure 6.16: M_{is} in the shock zone on the suction side

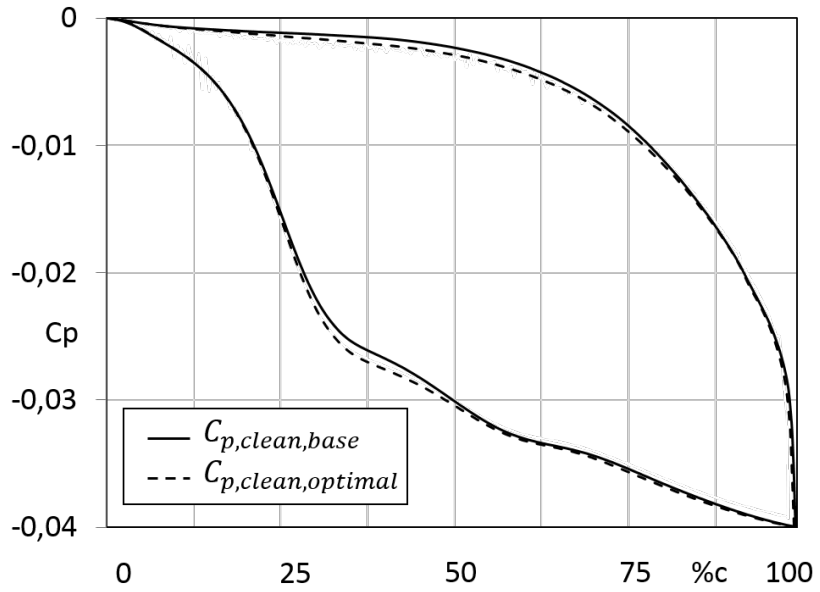

Figure 6.17: C_p trend along the fouled optimal and base cases

constrained optimization algorithm has been built, with an innovative parameterization method and a robust automatic mesh generator

The best shape found leads to a lower capture efficiency and higher isentropic efficiency compared to the base one when the geometries after exposure are considered. Besides, with the best shape, a very small isentropic efficiency reduction due to degradation is expected when degradated and clean situations are compared. These remarks are supported by the flow field analyses and are translated in important design parameters such as C_p and M_{is} distribution along the blade. With respect to the base case, a small reduction in the C_p distribution area resulted in the clean cases, but a greater gain in the performance drops overexposure has been obtained. From the results proposed in this work, it can be

concluded that in the design phase, it is possible to design an HPT nozzle taking into account not only the performance under standard conditions but also behavior due to particular circumstances such as fouling and erosion. This remark is related to the fact that small variations in some geometrical parameters have a high impact on the contaminant capture efficiency, without affecting significantly the nozzle performances. The main design considerations pointed out in the work can be summarized as a reduction of the LE radius and a flatter shape of the PS lead to a geometry less sensitive to degradation. The methodology here developed is fully general and is thought as applicable to different degradation issues, including compressor applications.

This page was intentionally left blank.

Chapter 7

A unified map for the classification of the particle behaviour upon impact

Due to the importance of the particle ingestion phenomenon, several methods to model particle sticking have been proposed in literature. Most models are based on the idea of a sticking probability. Other models investigate the phenomenon from a deterministic point of view by calculating the energy available before and after the impact. The nature of the materials encountered within this environment does not lend itself to a very precise characterization, consequently, it is difficult to establish the limits of validity of sticking models based on field data or even laboratory scale experiments. As a result, predicting the growth of solid deposits in gas turbines is still a task fraught with difficulty. In this section, two non-dimensional parameters are defined to describe the interaction between incident particles and a substrate, with particular reference to sticking behavior in a gas turbine. In the first part of the work, historical experimental data on particle adhesion under gas turbine-like conditions are analyzed by means of relevant dimensional quantities (e.g. particle viscosity, surface tension, and kinetic energy). After a dimensional analysis, the data then are classified using non-dimensional groups and a universal threshold for the transition from erosion to deposition and from fragmentation to splashing based on particle properties and impact conditions is identified. The relation between particle kinetic energy/surface energy and the particle temperature normalized by the softening temperature represents the original non-dimensional groups able to represent a basis of a promising adhesion criterion.

The behavior of solid particles impinging on a wall is determined by the flow conditions, properties of the particles and by the temperature. As demonstrated in Kleinhans et al. (2018), particle adhesion is not a linear phenomenon for which several contributions affect the final results of particle impact at the same time. Depending on the material, temperature and impact conditions (related to both particle and substrate) the adhesion or rebound is not easily extrapolated by using similar experimental tests or numerical

models. Starting from the result collection reported in Kleinhans et al. (2018), in the coal combustion field of research, many efforts have been made in estimating and improving the comprehension of deposition and slagging. Material characterization, experimental procedure, and, sometimes, equation model and basic criteria can be borrowed from this research field to the gas turbine field. Starting from these findings, two main conclusions can be drawn. At low temperature, the particles are likely to bounce off the wall and cause damage by erosion. At high temperatures, the particles become soft and can stick to the wall. As a consequence, erosion is the dominant damage mechanism in fans and compressors or in turbines operating at low (TET). In this case, the damage is irreversible and is related due to an increase in roughness and to uncontrolled modifications of the shape of the blades, typically around the leading edges. Adhesion is the primary damage mechanism at high temperature and takes place mainly around the first turbine stage in machines operating at high TET – where gas and wall temperature values are the highest. Therefore, surface modification afflicts all parts of a gas turbine: coated and uncoated, cooled and uncooled surfaces all experience shape and surface modification from the baseline Bons et al. (2001).

Particle deposition on gas turbine components has attracted much attention because of its practical implications and a large number of experimental studies is available Suman et al. (2018) and Wang et al. (2018). These studies cover the whole range of conditions of (i) full scale gas turbine unit, (ii) wind tunnel testing or hot gas facilities using stationary cascades, able to reproduce the same conditions of gas turbine operation and finally, (iii) wind tunnel testing or hot gas facilities using coupon as a particles target. The experimental analyses have been supported by - and have given inspiration to - increasingly realistic mathematical models. These models are widely used in the computational fluid dynamic analysis for the study of this phenomenon. Two types of model exist according to the approach followed to describe particle sticking. The first model type relies on the definition of a quantity called sticking probability. The sticking probability represents the likelihood a particle has to stick to a substrate (clean surface or pre-deposited layer). This probabilistic approach is required to overcome inaccuracy and the uncertainty of the experimental tests on which these models are based. The sticking probability value may be regarded as the statistically representative outcome of a series of independent experiments carried out under the same conditions. For example, turbulent phenomena may afflict the particle dynamic changing the impact velocity which could assume a different value for every single impact for the same test conditions. In addition, the definition of a probability function may consider the actual variation experienced by the gas turbine in terms of particle size and shape, material compositions, operating conditions and conditions of the blade surface that are difficult-to-be-considered in the laboratory tests. The second model type is related to the comparison of the properties of a particle and a threshold value which considers the particle dynamics, its material properties and energy available before and after the impact. This deterministic approach can only be used when the conditions of the flow, the substrate and the particles are known in detail. The validity of the available

models could be assessed, in principle, by applying them to the wealth of experimental data published on particle deposition. However, these data cover a very wide range of flow velocities, temperatures, particle materials, and target surfaces. Therefore, they cannot easily be grouped or compared to each other unless suitable non-dimensional quantities are defined. Non-dimensional maps describing the behavior of molten or liquid particles are available in literature and can be used with advantage to study the problem at hand because the solid particles ingested in a gas turbine are heated by the combustor and are thereby softened or completely molten before hitting the walls of the turbine. From a physical point of view, the conditions for adhesion, rebound or break-up are determined by how much of the initial kinetic energy of the particle is absorbed by the deformation work upon impact and by the adhesion energy with the substrate and how much is still available to remove the particle, or its fragments, from the wall. In addition to these forces, also the surface tension interacts with the particle deformation, and the resulting surface energy is a function of the contact area between the particle and the substrate [15] which is directly related to the particle deformation. These relations are conveniently expressed in terms of the particle Weber, Reynolds and Ohnesorge numbers

$$We = \frac{\rho\ v^2\ d}{\gamma} \text{ where } \rho, \gamma = f\left(T\right) \tag{7.1}$$

$$Re = \frac{\rho\ v\ d}{\mu} \text{ where } \rho, \mu = f\left(T\right) \tag{7.2}$$

$$Z = We\, Re^{-1/2} \tag{7.3}$$

Both the Reynolds and Weber numbers change with temperature because of the temperature dependence of viscosity, surface tension and, to a lesser extent, density. Using non-dimensional parameters, generalized maps can be formed showing different regimes – stick, rebound, spread, break up, splash - for the interaction between sprays and heated walls Bai and Gosman (1995). Moreover, it is possible to predict the droplet behaviors like stick, rebound, spread, break-up and splash in terms of only two parameters, one non-dimensional (Weber number) and one dimensional (wall temperature). A similar approach has been adopted to describe the performance of droplets deposition for printing Stow and Hadfield (1981). In this case, by using two non-dimensional parameters (Weber number and Reynolds number), it has been possible to define whether ink droplets splash or not during printing Derby (2010).

In light of these remarks, this perspective part aim is to identify particle deposition regimes in the hot parts of gas turbines in terms of non-dimensional quantities. To this effect, over 70 particle deposition tests reported in the literature are studied. The collected

tests are selected because they were conducted using similar materials (silica-based type contaminants, such as silty, coal-like, and volcanic particles) and took place in conditions relevant to deposition on the hot parts of gas turbines. The tests were carried out in a number of configurations, covering full engines, single blades, coupons or blade cooling channels. The tests provide particle sticking results as a function of particle velocity, temperature, dimensions, etc. Only in a few cases, the sticking phenomenon is reported in detail with the quantitative estimation of mass deposits determining the per-order-of-magnitude approach adopted in the present work. Details about particle size and chemical composition used in each experimental test are listed as well as the flow conditions such as velocity and temperature values. In addition, the target typology and its dimension are reported (if available in the literature) in order to characterize each impact test. Starting from this collection, a critical post-process is carried out by means of dimensional (e.g. particle kinetic energy, temperature, etc.) and non-dimensional groups (e.g. particle Reynolds number, particle Weber number, etc.). With more details, the first part of the present review paper includes the following points:

- collection and comparison of the literature on experimental particle impact tests related to gas turbine fouling;
- application of the most used particle sticking models for gas turbine particle adhesion, highlighting how each model works and where it fails if compared with the actual test results;
- a detailed review of the predictive model for particle viscosity is added and a sensitivity analysis coupling particle characteristics (e.g. chemical composition) and impact conditions (e.g. temperature) with the experimental results is proposed in order to highlight the implications of the use of different sticking models together with particle viscosity models.

In the second part, an innovative approach gives the opportunity to link the present experimental results with some new perspective. The phenomenology reported in literature dating back 30 years is summarized in terms of two non-dimensional parameters representing the ratio between the particle temperature and the glass transition temperature on one hand, and the ratio between the available kinetic energy and the surface energy on the other hand. The non-dimensional map clearly shows a number of different regimes, fitting very well with reported observations in terms of deposition and erosion phenomena. Furthermore, the map shows that the phenomena taking place in gas turbines are amenable to generalizations in different fields of research (e.g. printable fluids). The non-dimensional map proposed by the Authors represents a prediction tool in relation to the particle deposition and erosion phenomena and give a new insight into the gas turbine fouling prediction. The conceptual steps, as well as the overall scenario in which the present work is developed, are reported diagrammatically in Fig. 7.1.

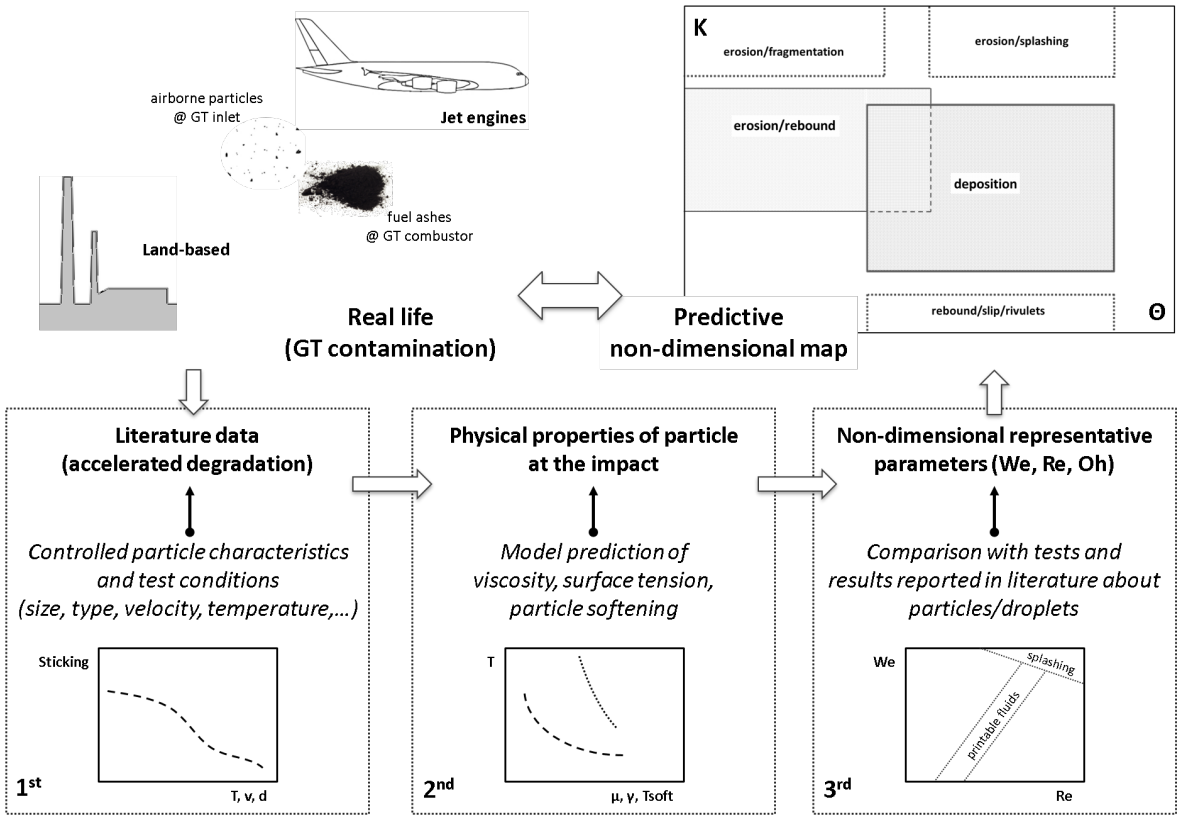

Figure 7.1: Conceptual framework: the predictive model of real-life behavior is based on non-dimensional parameters achieved by specifically-designed tests

7.1 Particle sticking mechanisms and models

The adhesion of contaminant particles to the blade surfaces is determined by (i) the material of the interacting bodies (particle, surface, third substance and carrying medium), (ii) the surface conditions, (iii) the particle size, (iv) the impact velocity and (v) the impact angle. The conditions under which these contaminants stick to blade surface are still unclear. Over the years, several contributions related to the fouling phenomenon have been proposed and this paragraph aims to summarize the models describing the particle sticking. Three particle sticking models have been considered for the data post-process, which is mainly referred to as the basic criteria, such as particle viscosity, velocity, and energy. Other formulations which are derived from these basic criteria are listed as well, but they are not considered for the data-process. The present section reports in detail (i) the sticking models used for predicting particle adhesion on hot gas turbine sections and (ii) the predictive models for estimating particle characteristics (viscosity, surface tension and softening).

Particle Sticking Models

The first model considered is the critical viscosity model, widely used in the literature, that compares particle viscosity to a reference viscosity at which sticking starts. In addition, the model could account for the stickiness of the deposit itself Walsh et al. (1990). The sticking probability was assumed to be inversely proportional to viscosity. In terms of sticking probability, viscosity at or below the critical viscosity is assumed to have a sticking probability of unity whereas at other particle temperature, according to the relation

$$P_{visc} = \mu_c/\mu \tag{7.4}$$

$$P_{visc} = \begin{cases} \mu_c/\mu & \text{if} \quad \mu_c < \mu \\ 1 & \text{if} \quad \mu_c \geq \mu \end{cases} \tag{7.5}$$

where P_{visc} is the sticking probability related to the viscosity effect and μ_c is the particle critical viscosity while μ is the viscosity of the particle at its temperature. This model is implemented assuming that the critical viscosity value corresponds to the particle viscosity at the softening temperature (μ_{soft}). Softening temperature is a predetermined temperature value, and it is a function of the particle material that could be calculated/measured according to the standard ASTM – D1857-04 (Standard test method for fusibility of coal and coke ash) Standard (2003). This standard definition allows a univocal and reproducible application of the critical viscosity method. Many authors have applied this method and, in some cases, validated its results with experimental tests Sreedharan and Tafti (2010); Barker et al. (2013); Birello et al. (2013); Borello et al. (2014); Prenter et al. (2016); Zagnoli et al. (2015). Other contributions have improved the model by introducing a transition across the critical viscosity value Sreedharan and Tafti (2010), and by extending its validity at a lower temperature (lower compared to the melting temperature) Singh and Tafti (2016). A detailed explanation of these models can be found in the paragraph Predictive models for particle properties of the present Chapter. At a lower temperature, energy losses due to particle-surface impact will determine whether an impacting particle will be able to leave the surface. These energy losses are a function of impact parameters such as the properties of the particle, impact velocity and angle. This last formulation of the model states the probability of sticking should be a function of energy losses during a collision and is calculated from the coefficient of restitution model as

$$P_e = f\,(e) = e^{-c\ R} \tag{7.6}$$

The coefficient of restitution R is therefore considered as an index of the energy dissipated at the impact: the lower it is the higher the dissipative viscous effect of the impact. Its

effect is accounted for through an exponential law where the coefficient c ≅6.5. Since the model for the sticking must still depend on the viscosity of the particle (with respect to μ_{soft} considered as the threshold for ideal adhesion), the final formulation of this model is the one reported in Eq. 7.7

$$P = min\left(P_e + P_{visc}; 1\right) \tag{7.7}$$

Another formulation is related to the definition of the critical value of the viscosity, which could relate the effects of particle softening with the particle kinetic energy. In this case, the definition of the critical viscosity is the following

$$\mu_c = A\ E_{kin}^B \tag{7.8}$$

where A and B are two coefficients able to fit the experimental results related to the specific material. For example, in the case of glass particles Srinivasachar et al. (1991), A=5 10-12 and B=-1.78. This model is strongly dependent on the particle material composition. Low-melting elements or mixtures could be responsible for early particle adhesion. For this reason, this model is only suitable when the characterization of the material particle and its behavior according to the temperature is available.

The second model considered is the critical velocity method. This model is based on the comparison between a threshold value of velocity and the particle velocity Brach and Dunn (1992). Other contributions are related to the representation of the particle-boundary layer interaction. Numerical studies on the interaction between the particle and boundary layers are reported in the literature Gökoğlu and Rosner (1984), with greater attention to the effect of turbulence on particle dispersion, deposition on turbine blade surfaces and detachment from the surfaces El-Batsh and Haselbacher (2000, 2002). As mentioned, the velocity of an impinging particle is one of the parameters that drive the sticking process. If its value is lower than a threshold (critical velocity) the particle sticks to the surface. The threshold value is strongly dependent on the particle material and its mass. The formulation suggested in Brach and Dunn (1992) for the critical velocity uses the following equation

$$v_c^2 = \frac{-1 + \mu^2}{R^2} \frac{2W_A}{m} \tag{7.9}$$

where W_A is the work of adhesion and R is the coefficient of restitution. According to the formulation of Brach and Dunn (1992), the critical velocity is referred to the normal direction with respect to the target surface. The work of adhesion Johnson et al. (1971) could be expressed as

$$W_A = -\left[\frac{5}{4}\rho\pi^{\frac{9}{2}}\left(k_1 + k_2\right)\right]^{\frac{2}{5}} \gamma r^2 \left|v\right|^{\frac{4}{5}} \tag{7.10}$$

and the restitution coefficient $R = C/C + |v|^p$ where C and p are constants that can be derived from experimental tests, while the parameters k_1 and k_2 are referred to the substrate and particle characteristics respectively. Assuming the subscript i as a material

index (particle or substrate), the parameter k_i is defined according to Young's modulus E_Y and Poisson's coefficient ν as

$$k_i = \frac{1 - \nu_i^2}{\pi E_{Y,i}} \tag{7.11}$$

Also for this model, the particle properties, and in particular its Young's modulus, are sensitive to the temperature and need to be estimated using empirical correlations. This model was applied in the case of gas turbine contamination by ash using the following relation for the particle's Young modulus El-Batsh (2001)

$$E_{Y,p} = 120\,(1589 - T)^3 \qquad for \quad T > 1100\ K \tag{7.12}$$

and in the case of coal-particle contamination Ai (2009) using $E_{Y,p} = 3 \cdot 10^{20} e^{(-0.02365T)}$ The critical velocity model was applied to study the gas turbine hot section fouling Ai (2009), using simplified relations for critical velocity

$$v_c = \left(\frac{2E_Y}{d}\right)^{\frac{10}{7}} \tag{7.13}$$

based on a composite Young's modulus E_Y obtained as

$$E_Y = 0.51 \left(\frac{5\pi(k_1 + k_2)}{4\rho^{3/4}}\right)^{\frac{2}{5}} \tag{7.14}$$

by considering the parameters k_1 and k_2 defined in the Eq. 7.11 for particle and substrate characteristics. Therefore, E_Y represents the material characteristic generated by the pair of particle and substrate. The application of the present model requires accurate values of the Young modulus of the particle and surface. This procedure is not a standard (contrary to the critical viscosity method for which the definition of the critical viscosity equal to the particle viscosity at the softening temperature allows the results standardization). The lack of universally accepted ways to evaluate material properties may be the reason for discrepancies in predictions obtained (i) in different conditions with the same material or (ii) with different materials for the same test conditions. A deposition model that includes elastic deformation, plastic deformation, adhesion, and shear removal is reported by Bons et al. (2017). Its predictions were compared to five literature cases: quartz on aluminum, ash on stainless steel, sand on stainless steel, ash on Inconel at high temperature and ash on vane cascade. This model it is used in the numerical analysis reported by Prenter et al. (2017) and Forsyth et al. (2018) after tuning the model parameters. A different model was proposed by Agati et al. (2016) for the numerical modeling of particle deposition that occurs in gas turbine hot sections over between 500 K to 1500 K. The transition between these two extreme conditions is modeled

through a temperature-driven modification of the mechanical properties of both particles and target surface. A third method is proposed by Yu and Tafti (2017) as a modification of the former model Yu and Tafti (2016) and it is based on the relation between particle temperature and yield stress at a high temperature starting from 1000 K. The model prediction was compared against experimental data obtained with sand particles. As mentioned, more details about these models are reported in the section Predictive models for particle properties of the present section.

The third category of models are referred to as Energy-Based models. Energy balance models are based on comparing the available energy just before the impact to the energy dissipated by the particle during its deformation. The model predicts sticking if all the available energy is dissipated to deform the particle and to adhere to the surface. The main parameters are the kinetic energy of the particle, its viscosity and surface tension, and the surface energy or contact angle Kleinhans et al. (2016) and Ni et al. (2011). The method can study deposition on an existing layer by a suitable choice of the properties of the substrate and can even be used to obtain the restitution coefficient for use in critical viscosity model calculations Singh and Tafti (2013). This model takes into account the particle deformation due to the impact, without considering the behavior of particle viscosity such as non-Newtonian effects or possible sintering effects after particle impact. Figure 3 reports the phases involved in the particle impact phenomenon. The model is based on the estimation of the parameter E^* that stands for the excess of energy and indicates whether all energy is dissipated during wetting and deformation. The particle will rebound if $E^* > 0$ and it will stick otherwise. The parameter E^* is defined according to Kleinhans et al. (2016)

$$E^* = \frac{25}{172}\xi^2(1-\cos\theta + \frac{50}{129}\xi^{-1} - \frac{3}{43}\xi^{2.3}(1-\cos\theta)0.63 - 1 > 0 \tag{7.15}$$

where θ is the contact angle and ξ is the particle spread factor. The spread factor represents the particle maximum deformation and, if d_{max} is the maximum footprint particle diameter when the particle hits the surface, the spread factor is defined as

$$\xi = \frac{d_{\max}}{d} \tag{7.16}$$

Several empirical tests and spread factor quantifications are reported in the literature Jones (1971); Pasandideh-Fard et al. (1996); Chandra and Avedisian (1991); Mao et al. (1997); Scheller and Bousfield (1995) and, for this reason, a detailed evaluation of the particle spread factor value predictions will be carried out in the present work.

As mentioned, the model compares the kinetic energy to the energy dissipated by viscosity and the work done against surface tension to modify the surface area of the particle. These energies are evaluated using semi-empirical correlations. The criterion E^*¿0 is determined mainly by the value of the spread factor ξ. This can be appreciated by inspecting Figure 4, where E^* is shown as a function of ξ for different values of θ. In

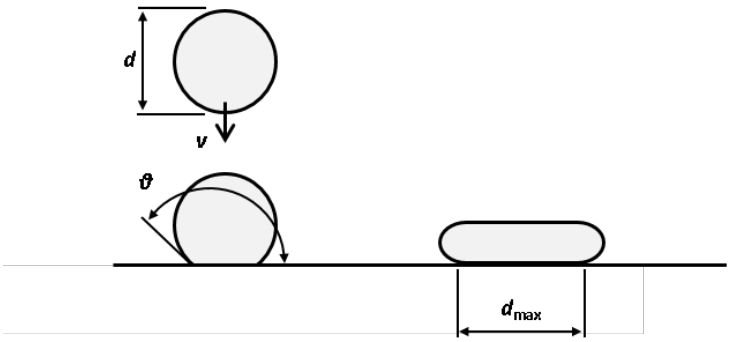

Figure 7.2: Particle deformation at the impact: d_{max} is the maximum footprint particle diameter

particular, it can be seen that particle adhesion takes place for ξ >0.4 for most values of θ of practical interest. Therefore ξ=0.4 will be used as threshold value in the present work for particle adhesion.

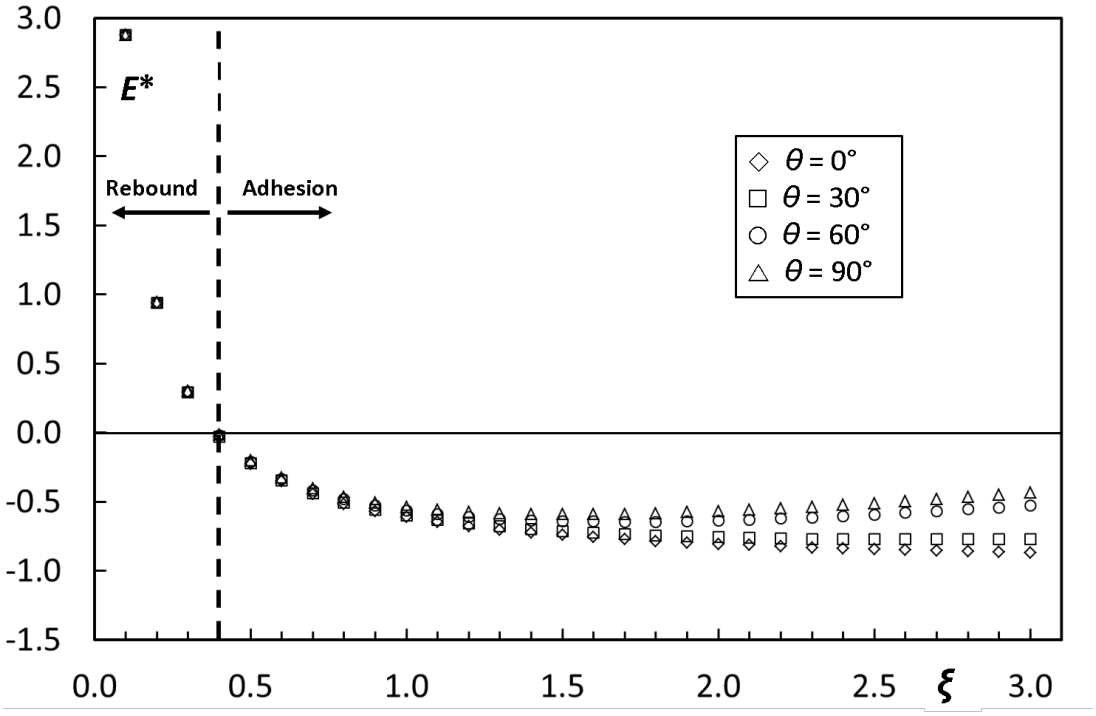

Figure 7.3: Sensitivity analysis of the contact angle on E^* calculation

Sticking mechanisms and deposit formation mechanisms are based on the presences of a third substance or second phase at the particle/surface interface Mezheritsky and Sudarev (1990). The presence of a third substance is usually invoked at low temperature. An example is the formation of deposits on compressor blades, where particles come into contact with water droplet or oily substances Zaba and Lombardi (1984). The third substance could generate favorable conditions for particle sticking especially when the particle is solid and its adhesion is driven only by electrostatic forces. In this case, in fact, the presence of third substance could change the action of capillary forces as well as the effects of the inertia and the correspondent energy dissipation during impact allowing particle sticking. The presence of a second phase is invoked also to model deposition

Table 7.1: Predictive sticking model

Basic criterion	Authors	⇑ Pros / ⇓ Cons
Critical viscosity	Srinivasachar et al. (1991)	⇑Influence of the kinetic energy on the particle sticking ⇓Critical viscosity values related only to a single coal sample
	Sreedharan and Tafti (2010)	⇑Accounts for the particle softening effects ⇓Only representative of molten particles
	Singh and Tafti (2015)	⇑Accounts for the energy absorbed by the particle at the impact ⇓ Detailed characterization of the temperature-material characteristics relations
	Jiang et al. (2018)	⇑Influence of the wall temperature on the particle sticking Model equations and constant do not account for the particle kinetic energy
Critical velocity	Agati et al. (2016)	⇑Extended range of temperature ⇓Detailed characterization of the temperature-material characteristics relations
	Yu and Tafti (2016)	⇑Accounting for the elastic/plastic deformation ⇓Sensitive to the on the mechanical properties of sand to the grain size.
	Bons et al. (2017)	⇑Accounting for the elastic/plastic deformation, adhesion and shear removal ⇓Tuned by case-dependent coefficients
	Yu and Tafti (2017)	⇑Temperature dependency on the yield stress for sand particles ⇓Sensitive to the on the mechanical properties of sand to the grain size.
Activation energy	Casari et al. (2017a)	⇑General approach based on an energy content comparison ⇓Lack of validation of the model constants and applicability limits

on hot gas turbine sections in which contaminants are softened or completely molten Senior and Srinivasachar (1995). For adhesion of particles to occur, either they must be semi-molten or a molten phase must be present on the blade surfaces. The low-melting compounds generated by the increment of the particle temperature act as a bridge between the particle and the blade surface. Therefore, the sticking probability is dependent on a number of characteristics, such as particle temperature, viscosity, surface tension and wettability Ahluwalia et al. (1989), Ahluwalia et al. (1989). In the light of this background, the prediction of particle adhesion is based on a two-step approach. The first step deals with the prediction of the particle/surface properties while the second step deals with the estimation of the sticking probability (or any other measure of adhesion) based on them.

With the reference of basic models presented in the latter paragraphs (critical viscosity, critical velocity, and energy-based models), it is interesting to compare the exisiting predictive sticking models, starting from the basic ones and tuned according to the experimental results obtained. All of these models were used for estimating the particle deposition in the gas turbine and in agreement with their hypothesis, they could be used for fouling prediction with a certain confidence. In Tab. 7.1, these models are listed together with their peculiarities, such as, the basic criterion on which the model is based and the main positive and negative peculiarities. The analysis proposed by Srinivasachar et al. (1991), shows that the particle kinetic energy affects the critical viscosity value at which sticking starts. The experiments have shown, for a single sample of coal, that the critical viscosity value decreases for a specific particle impact velocity and diameter. The sticking efficiency transition as a function of temperature was not as sharp, due to the overlaying effects of ash size and composition distributions. It increases the reliability of the former critical viscosity model. The models proposed by and Singh and Tafti (2015) are based on the critical viscosity criterion as well, but, in these attempts, the Authors have extended the prediction capability of the model to lower temperature. Hypothesis related to the energy dissipation at the impact imposes to the precise characterization of the particle structural characteristics. The last model based on the critical viscosity

criterion is that proposed by Jiang et al. (2018), and is able to account for the wall temperature effects on the particle sticking capability. The model takes into account ash thermo-physical properties, particle viscosity and metal wall temperature by means of simplified relation and two model constants. Moving to the critical viscosity criterion, the proposed model involves the mechanical properties of the particles. The model proposed by Agati et al. (2016), is based on the critical velocity criterion: the model is developed according to the correlation between temperature and material properties by means of the chemical composition, Temperature based model considers material properties (E and ν) and material composition for a temperature range between 500 K and 1500 K. This interval is modeled through a temperature-driven modification of mechanical properties of particles and target surfaces. The model can also predict the coefficient of restitution for particles bouncing region. Based on the aim of estimating the coefficient of restitution, four models are developed. In this case, the sticking phenomenon can be detected when the restitution coefficient is null. The model reported in Yu and Tafti (2016), takes into account the contact models for elastic, elastic–plastic and plastic compression stages, followed by a recovery model based on the model of Stronge (2018). Then, a new elastic recovery model is proposed with molecular adhesive forces acting on the contact area. The model is more accurate in predicting the coefficient of restitution compared to the Stronge (2018) and Jackson and Green (2005) models. The model is largely sensitive on the mechanical properties of sand to the grain size. With the reference of this model Yu and Tafti (2016), the Authors have improved the formulation in Yu and Tafti (2017) for modeling the collision of micro-sand particles by means of the adhesion forces, size and temperature dependency of particle mechanical properties. The base model is validated and the proposed temperature-dependent model is validated against experiments on the impact of micro-sand particles for impact velocities at different temperatures. However, it is validated only against experiments that involve sand particles. Bons et al. (2017) proposed a physics-based model which includes elastic deformation, plastic deformation, adhesion, and shear removal. The model accounts for fluid shear removal, elastic and plastic deformation, and adhesion. The model is not fully validated in terms of the deposition prediction because of the dependency between temperature and material properties. A different approach is adopted in Casari et al. (2017a), that investigates the deposition process under a statistical perspective. This fouling model uses only the energy content of the particles, based on temperature and kinetic energy, to estimate the sticking probability. However, in a similar way of previous models, the model constants and the applicability limits are not checked against experimental results. After this brief review of the present sticking models, it is clear how the major issue is related to the extension of predictive capability as a function of different particle chemical compositions, mechanical properties etc. Therefore, it is necessary to improve the models in order to extend the prediction capabilities together with the limitation of the use of model constants which are usually specifically tuned for each application.

Different predictive models used for particle characteristics such as viscosity, surface

tension, softening and density are reported. The formulations reported in the following sections are useful for the subsequent data post-process based on literature experimental data. The particle deposition on hot gas turbine section experiments was carried out using similar materials that affect the power unit in the actual operating conditions such as sandy, volcanic and coal-type particles. All of these contaminants belong to the class of material called silica-based and are characterized by well-known interaction between their constitutive ions. Silica melts are based on the strong covalent bonding between silicon and oxygen forming a network structure. The glassy silica network can accommodate many different cations. Three main categories exist, depending on the interaction of cations and network: (i) glass formers (Si^{4+}, Ti^{4+}, P^{5+}) which form the basic anionic polymer unit, (ii) modifiers (Ca^{2+}, Mg^{2+}, Fe^{2+}, K^{+}, Na^{+}) which disrupt the polymeric chains by bonding with oxygen and terminating chains, and (iii) amphoteric (Al^{3+}, Fe^{3+}, B^{3+}) which act either as glass formers or as modifiers. Modifier ions disrupt the glass structure and thus tend to lower viscosity. Amphoteric ions can act as glass formers when they combine with modifiers ions which balance their charge, thus forming stable metal-oxygen anion groups that can fit into the silicate network. If insufficient modifier ions are present in the glass, amphoteric cations (Al^{3+} and Fe^{3+}) can act as modifier ions Mysen (1988).

Several test methods exist to measure silica melts viscosity: rotating crucible, rotating bob, falling body, oscillating plate, oscillating viscometer and Static Light Scattering (SLS) Seetharaman et al. (2005). The methods contain provisions to guarantee uniform temperature zone during the measuring processes. Each method has its applicability range, confidence band and requires additional data (such as density and surface tension). The rheological behavior of silica melts Hsieh et al. (2016) can be assess using standard test methods, according to ASTM D 2196-15 D 2196-15 (2015), which are able to evaluate whether the slag has transitioned from Newtonian to non-Newtonian flow at the measurement temperature. Unfortunately, these test methods are defined for a specific range of shear rate (0.1 – 50) s^{-1} and developed for measuring the rheological properties of the liquid phase only. Each material has its own temperature-dependent characteristics, furthermore, each particle is subjected by different temperature-history in a gas turbine flow path. For this reason, the aim of the present analysis is to compare the experimental data with dimensional and non-dimensional parameters using the available data reported in the literature. Over the past century, several equations have been proposed relating the viscosity of arbitrary melts to temperature-dependent characteristics and to specific composition constants Vargas et al. (2001). Most of these are proposed for predicting material viscosity for a specific material composition and sometimes, their validity is limited to a certain viscosity ranges. In the present review, seven (7) methods are considered. They are based on data extrapolation from temperature-viscosity trends of coal and volcanic samples similar to those responsible for gas turbine hot section fouling. In addition, all of the selected methods are able to predict the particle viscosity based on the composition and temperature. Each method is applied considering its limits according

to the particle composition, beyond of the absolute value of the predicted viscosity Mills and Sridhar (1999); Hoy et al. (1964); Watt and Fereday (1969); Sreedharan and Tafti (2011); Riboud et al. (1981); Streeter et al. (1984); Giordano et al. (2008). In this way, each method can be included or excluded a priori only based on the particle composition useful for automated calculation or routine easy-to-be-implemented in numerical simulations. The considered models are based on different correlations obtained considering different physical-chemical criteria. The S2 Hoy et al. (1964) and Watt-Fereday (WF) Watt and Fereday (1969) postulate that the viscosity depends on temperature following Arrhenius' law. This corresponds to a description of the flow of silicates in terms of transition probability and vacancy distribution in the structural lattice. The NPL model by Mills and Sridhar Mills and Sridhar (1999) is also based on the Arrhenius equation used to describe the temperature dependence of slag viscosity and correlates the slag composition to the optical basicity of the material. Weymann (1962) proposed another equation resulting from the same deduction considered for the Arrhenius model with the addition of an extra temperature-dependent parameter. This model demonstrated a valid correlation with experimental data and a successful description of the relationship between viscosity and temperature. The models that are based on Weymann equation Weymann (1962) are Sreedharan and Tafti (2011) (S&T), Riboud et al. (1981) (RRLG) and Streeter et al. (1984) (SDS). Another equation that links the viscosity with temperature was independently proposed by Vogel (1921), Fulcher (1925) and Tammann and Hesse (1926) in the 1920s and it is the base of the model presented by Giordano et al. (2008) (GRD). In this case, a third adjustable composition parameter is introduced into the equation to improve the performance of the model and to better emphasize the dependence of temperature on silicate melts viscosity. This model is specifically realized for predicting temperature-viscosity trends of volcanic ashes.

In addition to the particle viscosity, another basic particle characteristic is the particle softening temperature. This property is the key value for calculating particle adhesion according to the critical viscosity method. In order to post-process the literature data related to the particle deposition on hot gas turbine sections, the calculation of the present quantity is required. For the estimation of the softening temperature, three main approaches exist. The first one is related to a visual method described in the standard procedure of ASTM – D1857-04 (Standard test method for fusibility of coal and coke ash) Standard (2003), the second one is carried out with a ThermoMechanical Analysis (TMA) approach while the third one is related to a thermal analysis by means of Differential Scanning Calorimetry (DSC) approach. The setup of these different methods has been carried out over the years due to the controversial question related to the deformation temperature. In the literature, in fact, it has been emphasized that the initial deformation temperature is not the temperature at which the ash melting begins, and many coal ashes have been found to start melting at temperatures far below the initial deformation temperatures Hansen et al. (2002). Therefore, in this section, the three approaches are briefly described. In accordance with Standard (2003), the softening temperature (ST)

is defined as the temperature at which triangular pyramid prepared from the material (see sketch n°1 in 7.4) has fused down to a spherical particle which is characterized by the height equal to the width at the base (see sketch n°3 in Figure 7.4). The softening temperature has been accepted as the critical temperature which is commonly referenced in the evaluation of the characteristics of coal ash Speight (2015). The ash fusion test (AFT) is considered the most widely used procedure for determining the temperature at which the different stages of the ash transformations (softening, melting and flow) take place in order to assess the deposition characteristics of the material Degereji et al. (2012). The fusion temperature values are determined by heating a prepared sample of molded coal in a gas-fired or electric furnace conforming to Standard (2003). The deformation of the molded ash cone is monitored during the increase of temperature and, according to Figure 5, the four (4) critical temperature points (fluid – FT; hemispherical – HT; initial deformation – IT; softening – ST) are determined. Moreover, the response of the sample to thermal treatment is generally quantified by optical pyrometer or thermocouple. An alternative approach for the evaluation of the four (4) critical temperature values, applied to volcanic ash samples, consists in the use of thermogravimetry and differential scanning calorimetry (DSC) Song et al. (2017) and Kueppers et al. (2014). Mechanically, the evolution of characteristic temperature and the geometrical transformations of the cone define the ability of the sample to sinter, to stick or to spread and wet the surface Song et al. (2016). Nevertheless, the standard test Standard (2003) can be susceptible to subjective assessment because of the visual evaluation of critical temperature points Gupta et al. (1998). The standard procedure is recognized as not a very precise method failing the prediction of the fusibility temperature by over 40 K Gupta et al. (2002) as a function of the amphoteric content. In addition, it was found that the deformation temperature is not the temperature at which initial melting begins as normally perceived and the hemisphere temperature is below the liquidus temperature.

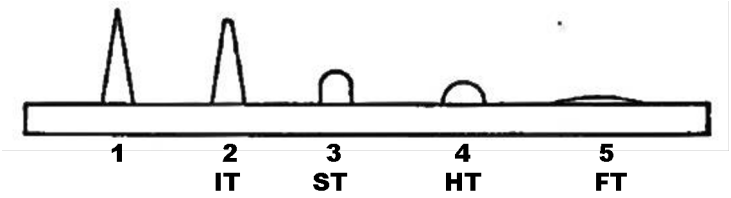

Figure 7.4: Critical temperature points. From Standard (2003)

The TMA methodology evaluates the progressive shrinkage of ash and it is suitable for characterizing the sintering and melting behavior at temperatures lower than the standard method. In addition, the precision of this technique is greater than the standard one, reducing the inaccuracy due to the measurement method. However, this accurate methodology can not be applied to ashes from biomass combustion Hansen et al. (2002) and in this case, the use of the DSC technique appears the best solution. This methodology is based on the evaluation of any mass changes by means of the comparison between the ash behavior against the reference material. With this procedure, any deviation in terms of energy corresponds to an evaporation or melting process with an accurate estimation

of the most ash fusibility temperature values. Despite the background of conventional techniques for determining the transformation temperature, the evaluation of the critical temperature values from the chemical composition can be a difficult task because of the unknown correlation between the interacting factors. In the present paper, starting from the particle characteristics reported in the literature, empirical relations to compute the particle softening temperature as a function of the composition proposed by Yin et al. (1998) were used. This model is much easier and direct than other statistical methods through the possibility to omit the mathematical correlation between the variables. In addition, the aim of the present study is to compare the experimental literature data and, for this reason, particle softening temperature has to be computed only by the use of the particle chemical composition. According to the particle composition, different relations are proposed. When the content of SiO_2 is less than or equal to 60 %, and the content of Al_2O_3 is larger than 30 %

$$T_{soft} = 69.94\mathrm{SiO_2} + 71.01\mathrm{Al_2}O_3 + 65.23\mathrm{Fe_2}O_3 + 12.16CaO + 68.31MgO + 67.19a - 5485.7 \tag{7.17}$$

when the content of SiO_2 is less than or equal to 60 %, the content of Al_2O_3 is less than or equal to 30 % and the content of Fe_2O_3 is less than or equal to 15 %

$$T_{soft} = 92.55\mathrm{SiO_2} + 97.83\mathrm{Al_2}O_3 + 84.52\mathrm{Fe_2}O_3 + 83.67CaO + 81.04MgO + 91.92a - 7891 \tag{7.18}$$

when the content of SiO_2 is less than or equal to 60 %, and that of Al_2O_3 is less than or equal to 30 %, and that of Fe_2O_3 is larger than 15 %

$$T_{soft} = 1531 - 3.01\mathrm{SiO_2} + 5.08\mathrm{Al_2}O_3 - 8.02\mathrm{Fe_2}O_3 - 9.69CaO - 5.86MgO - 3.99a \tag{7.19}$$

and finally, when the content of SiO_2 is larger than 60 %

$$T_{soft} = 10.75\mathrm{SiO_2} + 13.03\mathrm{Al_2}O_3 - 5.28\mathrm{Fe_2}O_3 - 5.88CaO - 10.28MgO - 3.75a + 453 \tag{7.20}$$

The constant a is defined according to the weight fraction wt% of each component as

$$a = 100 - (\mathrm{SiO_2} + \mathrm{Al_2}O_3 + \mathrm{Fe_2}O_3 + CaO + MgO) \tag{7.21}$$

The third particle characteristic useful for applying the particle sticking methods is the particle surface tension. In the literature, several contributions are related to the measurement of surface tension values of slags and silicate melts Sukenaga et al. (2011); Shin and Gulyaeva (1998); Vadasz and Havlik (1995); Nakamoto et al. (2007); Choi and Lee (2002); Melchior et al. (2009); Clarkson et al. (2016). Ternary or more complex slags, as well as coal ashes, are taken into consideration. These analyses are mainly focused on

Table 7.2: Surface tension of single oxides

Component	$\gamma = f(T)$ [mN/m]
SiO_2	243.2+0.0031 T [K]
CaO	791-0.0935 T [K]
Al_2O_3	1024-0.177 T [K]
MgO	1770-0.636 T [K]
Na_2O	438-0.116 T [K]
Fe_2O_3	504-0.0984 T [K]

the estimation of the temperature effects on the surface tension values. Even if, these contributions report very detailed slags and ashes characterizations, both in terms of chemical composition and surface tension values, they are mainly focused on the high-temperature values at which these materials are characterized by the liquid phase. For this reason, the actual slag and ash characterization can not be applied to the present study, due to the different temperature ranges at which gas turbine operates (lower temperature values than the slag/ash characterization). Therefore, in the present work, the particle surface tension is calculated using a chemical-temperature dependent correlation based on the principle that the surface tension can be expressed as a linear function of the composition Rezaei et al. (2002)

$$\gamma = \Sigma \ (\gamma_i \ m_i) \tag{7.22}$$

where γ is the surface tension corresponding to each oxide i and m is its molar fraction. The surface tension of each oxide is taken from literature correlations Hanao et al. (2007); Wu et al. (2014). Tab. 7.2 reports the equation of the relation $\gamma = f(T)$ used in the present analysis. The contribution of potassium oxide and titanium dioxide are not considered.

Particle density model

Several models for density calculation have been provided through the years Grau and Masson (1976); Courtial and Dingwell (1995); Persson et al. (2007). One of the most common methods is proposed by Bottinga et al. (1982), which calculates the densities, ρ, of molten slags from the following two equations

$$V_m = \Sigma \ \left(X_i \ V_i^0\right) + X_{Al_2O_3} \ V_{Al_2O_3}^0 \tag{7.23}$$

$$\rho = \frac{M}{V_m} \tag{7.24}$$

where the sum of Eq. 7.23 is taken over all oxide components except the aluminum trioxide. In the Eq. 7.23 X is mole fraction of component i, while V^0 terms represent the apparent partial volume of slag constituents. They are constant and derived independently

Table 7.3: Recommended values for apparent partial molar volume V^0 of slag constituents [cm^3/mol]

Component	V^0 at 1673 K Bottinga et al. (1982)	V^0 at 1773 K Mills and Keene (1987)
SiO_2	26.75	$19.55 + 7.966X_{SiO_2}$
TiO_2	22.45	24.0
Al_2O_3	-	$28.31 + 32 - 31.45X_{Al_2O_3}$
Fe_2O_3	44.40	38.4
MgO	12.32	16.1
CaO	16.59	20.7
MnO	14.13	15.6
Na_2O	29.03	33.0
K_2O	46.30	51.8

from an analysis of volume-composition relations in alumina-free silicate liquids. In Eq. 7.24, M represents the sum of the molar weight for the given slag. The apparent partial molar volumes of SiO_2 and Al_2O_3 are polynomial functions of composition in the density model proposed by Mills and Keene (1987) for multicomponent slags. Based on Bottinga et al. (1982), the Authors adjust the partial molar volume values (V^0) achieving certain success in calculated data with an uncertainty of 2 %. Different model constants provided by Bottinga et al. (1982) and Mills and Keene (1987) for calculating V^0 of various slag constituents are listed in Tab. 7.3 . In the present work, the apparent partial volume of slag constituents reported Mills and Keene (1987) are used.

7.2 Experimental data of gas turbine particle deposition

Deposition tests in conditions representative of the hot parts of a gas turbine have been conducted over the years with a number of different materials. The tests involve five principal types of particles Allaby (2013): sand, ash, coal, bituminous coal and lignite. Sand is defined as mineral particles of diameter 2 mm to micronized powder. In the gas turbine field of research, sandy particles are usually referred to Arizona Road Dust (ARD) sand samples. This sandy powder takes inspiration from the standard powder of ISO 12103-1 (A1, A2 A3, and A4) ISO 12103-1:2016 (2016), but the size and chemical composition of particle used in the deposition tests could be different from the standard one due to the mixing, filtration, sieving, and processes applied before the tests. Ash comprises all pyroclastic particles or fragments ejected from a volcano, irrespective of size, shape or composition. The term is usually applied to an air-fall material characterized by a characteristics diameter less than 2 mm. Coal is a carbon-rich mineral deposit formed from the remains of fossil plants. The process of coalification results in the production of coals of different ranks such as bituminous coal, lignite, and anthracite. Each rank

marks a reduction in the percentage of volatiles and moisture and an increase in the percentage of carbon. According to this definition, ASTM standard D388 (2013) proposed a detailed coal classification based on the content of carbon, volatile matter and calorific limits. Unfortunately, this classification is not completely useful to understand the physical characteristics of the contaminants involved in gas turbine degradation. Physical characteristics such as viscosity and surface tension are dependent on the chemical composition and structure (e.g. crystalline or amorphous) of the contaminants. In addition, it is important to note that the chemical composition of slag and its correspondent original coal ash could be different. As reported by Streeter et al. (1984), slags chemical composition could change due to the depletion of iron oxides species or to the enhancement in alumina content during heating/melting processes. At the same time, high-temperature values generate the volatilization of the sodium oxide that could change the slag viscosity. These behaviors enhance the difficulties related to the characterization and classification of the contaminants that affect hot sections. Particle deposition is investigated in order to understand turbine section contamination and the interaction between cooling holes and particle deposition. Accelerated tests are frequently used to recreate the actual gas turbine condition using in-house experimental test bench. For example, accelerated deposition testing is realized within 4 hours which cover 10,000 hours of actual gas turbine operation Jensen et al. (2005). Sometimes, in order to study specific problems, deposition tests are conducted using a coupon instead of gas turbine cascade Anderson et al. (1984, 1990); Ross et al. (1988); Richards et al. (1992); Weaver et al. (1996); Bons et al. (2007); Wammack et al. (2008); Crosby et al. (2007); Ai et al. (2009, 2012b,a); Laycock and Fletcher (2013, 2016); Boulanger et al. (2016); Barker et al. (2017).In this type of test, the particle deposition occurs on specifically-designed target, usually characterized by simplified geometry in order to guarantee a certain flow and temperature fields. In this case, the experimental procedure allows the proper correlation between particle impact conditions and deposition phenomenon based on the criterion that, all of the injected particles are characterized by the same impact conditions such as temperature, velocity, and incoming angle. In addition, given the simplified geometry of the coupon, detailed evaluation of several peculiarities such as (i) surface roughness of the deposited layer, (ii) effects of the cooling hole array, (iii) deposits thickness and (iv) influence of the substrate temperature on the particle sticking capability can be easily carried out. In Figure 6 an example of this evaluation is reported. In particular, Figure 6a shows the evaluation of deposit surface roughness, Figure 6b depicts the influence of the presence of cooling holes on the particle deposition pattern and, finally, Figure 6c reports an evaluation of the deposit thickness by means of a three-dimensional detection carried out with a laser scanner.

Earliest contributions are related to deposits due to fuel contamination. Several studies can be found in literature Cohn (1982); Whitlow et al. (1983); Wenglarz and Cohn (1983); Wenglarz (1987); Kimura et al. (1987); Spiro et al. (1987); Wenglarz and Fox (1990); Wenglarz (1991); Chin and Lefebvre (1993) but no specific details about particle

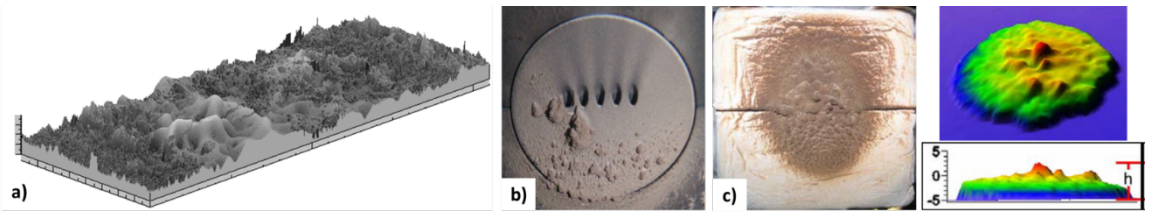

Figure 7.5: Experimental particle deposition tests carried out on coupons: a) evaluation of the surface roughness Bons et al. (2017), b) effects of the cooling hole array Ai et al. (2012b) and c) measurement of the deposit thickness by means of the three-dimensional reconstruction based on laser scanner detection

sticking probability is reported, or the chemical compositions is too different from the silica-based materials Laycock and Fletcher (2018). Analytical schemes were developed for extracting sticking coefficients from the measured weight gain data, particle size spectrum, and particle density and composition Ahluwalia et al. (1986). The influence of the particle temperature was one of the first studies reported in the literature Nagarajan and Anderson (1988). The particle temperature determines the appearance of different composites with different characteristics. For example, in the temperature interval (800 – 1800) K, the multi-component solution comprises oxides, sulfates, silicates, and aluminosilicates. Below 1100 K, low-melting alkali sulfate solutions are the predominant components, whereas above about 1500 K, molten oxides constitute most of the liquid phase. At high temperature, vapor deposition driven by thermophoresis force becomes important. Differences in deposits were encountered for pressure and suction sides where diffusion phenomenon works as a leading actor Fackrell et al. (1994b) and Fackrell et al. (1994a). At the same time, the first studies on the effects of volcanic ash on aero-engines were published. Tests with different power unit using a unique facility able to generate realistic environmental conditions of particle-laden clouds under controlled laboratory conditions are carried out Dunn et al. (1987); Kim et al. (1992); Dunn (2012). The results show the variation of the power unit performance during the test (a few minutes) highlighting the deterioration over a small period. Evaluations of blade erosion and deposition patterns are also proposed. This type of studies are not widespread in literature and only in the last years, new studies have been proposed related to simply particle deposition Taltavull et al. (2015); Dean et al. (2016); Giehl et al. (2017), cooling holes blockage Wang et al. (2016); Whitaker et al. (2017) and internal cooling hole clogging Wylie et al. (2017). Cooling holes clogging represent the most detrimental phenomenon that occurs in gas turbine hot section, especially for aero-engines. Figure 7.6 reports literature experimental results showing the occupied area due to particle adhesion inside the cooling hole. More recently, Shinozaki et al. (2013) and Naraparaju et al. (2018) use a micro gas turbine for studying volcanic ash adhesion at different load and for different blade coating material, respectively.

With the increase in usage of gas turbines for power generation and given that natural gas resources continue to be depleted, alternative types of fuel have been tested.

Figure 7.6: Internal cooling hole clogging Wylie et al. (2017): deposition in first four cooling holes of HD45 running at 1310 K

Examples of alternative fuels are coal-derived synthetic fuels. Coal-derived fuels could contain traces of ash and other contaminants that can deposit on vane and turbine surfaces. Experimental tests and numerical analyses are devoted to the comprehension of the effects provided by bituminous and sub-bituminous particles on the gas turbine nozzle Casaday et al. (2014). Several studies were realized in order to increase the effects of these contaminants on gas turbine hot section fouling, especially in the presence of film cooling. Different types of ash (e.g. coal bituminous, lignite, etc.) have been used for performing particle deposition on a gas turbine nozzle Webb et al. (2013); Prenter et al. (2014); Smith et al. (2010). Such tests allow the proper analysis of the flow dynamic behavior in the particle impact and adhesion phenomena, giving the possibility to realize the same flow conditions of the actual application. By contrast, the complexity of the flow structure and the effects of geometric features that characterize an actual gas turbine nozzle could represent an obstacle in the definition of general rules and trends related to particle sticking. In Fig. 7.7 the comparison between the deposits pattern without and with film cooling using bituminous ash is reported. The effect of cooling holes on particles deposition pattern is still under investigation. Experimental tests Whitaker et al. (2016), also run with high gas temperature Lundgreen et al. (2016), attempt to improve the comprehension of particle deposition.

Other specific contributions can be found in relation to the effects of the electrostatic charge on particle deposition Raj (1983); Raj and Moskowitz (1984) or the influence of the deposit on the heat transfer and the influence of the free-stream turbulence on the particle deposition Whitaker et al. (2015). The deposits thickness influences the heat transfer and, through experimental tests, it is possible to correlate the thickness and the heat transfer over the operating time Bons et al. (2008). Finally, some attempts to

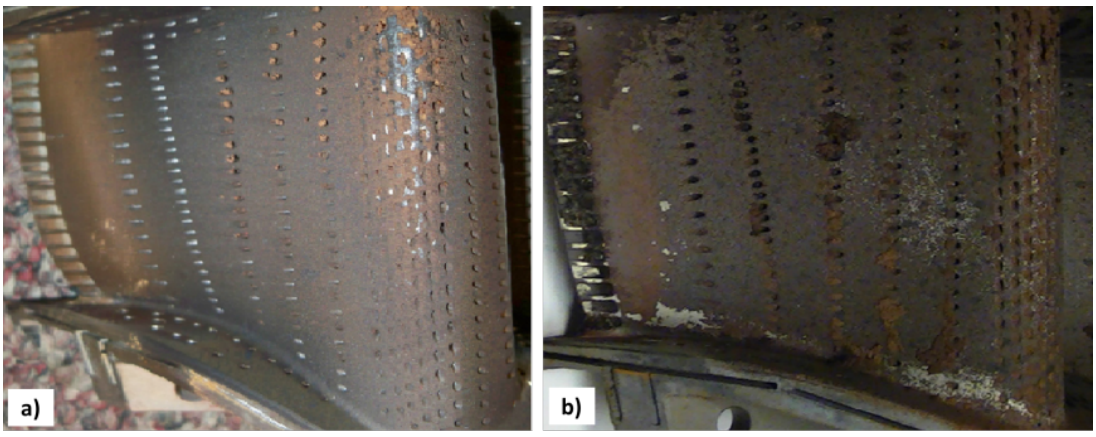

Figure 7.7: Comparison of coal bituminous particle tests (a) film cooling (b) non-film cooling. From Webb et al. (2013)

use a sort of thermal similitude for studying particle adhesion were proposed Lawson and Thole (2009); Wood et al. (2010); Lawson and Thole (2010). These experimental tests were based on the similarities between melting ash and wax/PVC particles. Latter materials have lower values of melting temperature and, using thermal scaling techniques, the deposition pattern could be assumed as representative of actual gas turbine particle deposition.

7.3 Literature data collection

The experimental results related to particle deposition on cascade and/or coupon reported in the literature, are obtained with different (i) material (ii) size and (iii) working conditions such as velocity and temperature. These different working conditions imply several difficulties in comparing deposition results obtained from different experimental tests. Different material compositions determine, for example, different values of particle viscosity even if the tests are carried out at the same particle temperature. The same phenomenon affects also the surface tension value (closely related to the surface energy), that, in addition with the viscosity, drives the adhesion phenomena at the particle/surface interface Johnson et al. (1971). On the other hand, differences in impact velocity and particle dimension values determine different impact mechanisms and particle deformation related for example to the particle kinetic energy. In the light of these considerations, in this paragraph, all the experimental results related to particle deposition on hot gas turbine section are summarized. Starting from the information reported in every single work, particle composition and temperature are used to calculate viscosity and surface tension based on the relations available in literature and reported earlier. Coupling these values with particle velocity, density, and dimension, the calculation of the particle adhesion according to the analytic models (critical viscosity, critical velocity and energy-based models) are performed, highlighting pro and cons of each method. Special attention

is given to the particle viscosity which is considered the most important parameter for judging the particle adhesion or rebound phenomena.

Tab. 7.4 reports the experimental data available in literature related to particle deposition in gas turbine hot sections. Each material is indicated with the same name used in the respective reference. In the case of more than one contribution that uses the same material, with different test conditions, a progressive number is adopted. For each test (grouped according to the reference), the particle characteristics such as dimension and density are reported. The particle dimension indicates the variability range or the mean mass diameter used in each test (if provided). Unfortunately, detailed data on other interesting parameters such as d_{50} and d_{75}, which represents the diameters for which the 50 % and 75 % of the particles measured are less than the stated size, are not reported. The test conditions are also indicated and, in absence of detailed information, particle velocity is assumed equal to the gas velocity and particle temperature is assumed equal to the gas temperature. Fixed value or the indicated variability range is also specified. Regarding the velocity, in the case of test realized on a full-scale gas turbine, a representative particle impact velocity of 100 m/s is chosen because no-data related to this variable is reported Kim et al. (1992); Dunn (2012). Finally, Tab. 7.4 reports also the type of target, tg, used in the experimental tests, with a reference of:

- T, the test is realized on a full scale gas turbine;
- B, the test is realized on wind tunnel provided with cascade or single blade target;
- C, the test is realized using a coupon;
- I, the test is realized in order to discover particle deposition inside the internal cooling hole.

All of this information (dimension, density, velocity, and temperature) provide the first overview of the experimental contribution related to particle deposition and fouling on gas turbine hot sections. Particle velocities span from 15 m/s to 350 m/s while the temperature values range from 850 K to 1900 K, approximately. Wind tunnel tests allow the best control in terms of test parameters but, at the same time, could imply certain limits related, especially to a maximum temperature value.

The uncertainty related to the experimental test conditions and at in turn, the accuracy of the particle deposition results, are not always reported in literature even if a considerable number of tests indicate the experimental uncertainty Webb et al. (2012); Prenter et al. (2014); Ahluwalia et al. (1986); Jensen et al. (2005); Anderson et al. (1990); Richards et al. (1992); Wammack et al. (2008); Crosby et al. (2007); Ai et al. (2012b); Aldi et al. (2017a); Laycock and Fletcher (2013); Boulanger et al. (2016); Wylie et al. (2017); Smith et al. (2010); Whitaker et al. (2016, 2015). The difficulties are especially related

to the not-clear correlation between the uncertainties related to test conditions like flow velocity and temperature and mass deposits or sticking coefficients. Measurement uncertainties have to be considered different from the variability of the test conditions even if, both of them determine the amount of deposits. The present data collection allows the definition of a sort of tolerance band of the experimental data reported in the present review. Given the sticking model relations which are based on the particle characteristics strongly related to the temperature, one of the most important uncertainties related to the experimental results is that which characterizes the temperature measurements. Uncertainties related to the temperature values are estimated equal to 0.11 % Wylie et al. (2017), 1.3 % Crosby et al. (2007)and 2 % Webb et al. (2013); Prenter et al. (2014); Smith et al. (2010); Whitaker et al. (2015). These values have to be correlated with the actual temperature in order to highlight the influence of the measurement uncertainty on the particle characteristic and thus, on their sticking capability. According to the aforementioned percentage values, the uncertainty in terms of Kelvin become equal to 1 K Wylie et al. (2017), 19 K Crosby et al. (2007), and 27 K Webb et al. (2013); Prenter et al. (2014); Smith et al. (2010); Whitaker et al. (2015). Given the high temperature at which the tests were carried out (up to 1500 K), these uncertainty values appear in line with those reported in literature even if, according to the analysis reported in the following paragraphs, a slight deviation could be determined between the sticking prediction provided by the models and the actual results of the experimental tests. In the same way of the temperature measurement, even the uncertainties related to the mass flow rate are useful to improve the comprehension of the experimental results. In particular, these uncertainty values could be used to estimate the uncertainty in the particle impact velocity. For the collected data, these uncertainty are estimated to be equal to about 0.80 % Wylie et al. (2017) and 4 % Webb et al. (2013); Prenter et al. (2014); Wammack et al. (2008); Whitaker et al. (2015). According to the percentage values, the uncertainty of the mass flow rates in Wylie et al. (2017) is equal to 0.0074 g/s, while in Webb et al. (2013); Prenter et al. (2014); Wammack et al. (2008); Whitaker et al. (2015), the maximum uncertainty value is equal to 0.015 kg/s. Regarding the uncertainty of the particle concentration used to contaminate the main air flow, data are not commonly reported. Only in [106] and Jensen et al. (2005); Wammack et al. (2008) the accuracy in the particle contamination is reported and is equal to 6 ppmw. Other uncertainties are related to the geometry and position of the target Laycock and Fletcher (2013); Boulanger et al. (2016), in the capture efficiency evaluation Ai et al. (2012b,a), and mass measurements Crosby et al. (2007). Proper methods for uncertainty estimation are adopted in Wylie et al. (2017) by applying Kline and McClintock (1953) and Smith et al. (2010); Webb et al. (2013) using the procedure reported in Coleman and Steele (2018). In other cases, the uncertainties were estimated by duplicating the tests as reported in Richards et al. (1992); Ai et al. (2012a). In relation with the variability of the tests condition during the deposition tests, the variability of the flow temperature is between 3 K Whitaker et al. (2015) (for a tested flow temperature of 1353 K), 6 K Webb et al. (2013) (for a tested flow temperature in the range of 1314 K – 1385 K) and 5 K in Whitaker et al. (2016) (for

a tested flow temperature of 866 K). Regarding the variability of the mass flow rate, in Whitaker et al. (2015) is declared equal to 0.005 kg/s (that corresponds to the 2.8 % and 1.4 % for a tested mass flow rate values of 0.181 kg/s and 0.363 kg/s, respectively) while in Webb et al. (2013) is declared equal to 0.01 kg/s (that corresponds to the 1.8 % and 2.7 % for a tested mass flow rate values of 0.557 kg/s and 0.365 kg/s, respectively). Other inaccuracies are especially related to the effects of radiation on the flow temperature measures Ahluwalia et al. (1989); Anderson et al. (1990); Crosby et al. (2007). Data collection covers about thirty (30) years of particle deposition tests, realized using several different facilities and instrumentations. The amount of data, their variability, and their different nature give the possibility to discover the widest view of particle deposition on gas turbine hot section. The present analysis is based on the data available in open literature, and the data post-process reported in the following paragraph allows the comprehension of the basic phenomena using per-order-of-magnitude variations.

The particle behavior depends on the relationship between particle viscosity and temperature and this is strongly dependent on the chemical composition. Table 7.4 reports the chemical composition as a weight fraction of sodium oxide Na2O, potassium oxide K_2O, calcium oxide CaO, magnesium oxide MgO, silicon dioxide SiO_2, aluminum oxide Al_2O_3, titanium dioxide TiO_2, and iron oxide Fe_2O_3. Obviously, these oxides do not cover the entire composition for each material but these components characterize each ash, powder, and particle determining their physical characteristics. This wide compositional range is related to the process formation of the ash or powder and might include particles formed from new materials as well as those derived by the fragmentation of pre-existing components which are subjected to degradation or combustion processes. In this context, Srinivasachar et al. (1991) have carried out combustion and deposition experiments with a coal (San Miguel Texas lignite) to assess critical viscosity hypothesis for deposition processes. These experiments have highlighted that final ash composition is independent of combustion conditions and the analysis of individual combustion ash particle have shown that there are negligible interactions between the particles which are characterized by similar final chemical composition. In light of the above, bulk composition can thus provide an overall indication of each particle behavior and its relation between viscosity, temperature, and chemical composition. However, a certain degree of non-uniformity could be represented by the initial formation of liquid phase due to the low temperature eutectic during the particle heating, such as the combination between sodium oxide with silica and aluminum dioxides, that generates a liquid fraction starting from 1200 K. Similar findings are reported in Lee et al. (2002), where the presence of sodium sulfate generates a condensed phase that increases the particle sticking capability. This sort of inhomogeneity represents the first phase of particle softening process, that represents one of the most important parameters for estimating the particle adhesion capability. A graphical description of this occurrence can be realized by means of the ternary plot. Figure 7.8 depicts two different ternary plots according to the triplets Al_2O_3-SiO_2-CaO and SiO_2-MgO-Fe_2O_3 with the indication of the liquidus curves Atlas (1995) together with the

Table 7.4: Particle deposition data. Material composition in term of weight fraction. Notes in Tab. 7.5

	Authors	Material	d [μm]	ρ [kg/m^3]	v [m/s]	T [K]	TT	Na_2O	K_2O	CaO	MgO	SiO_2	Al_2O_3	TiO_2	Fe_2O_3
'18	Naraparaju et al.	EYJA	0.5–10	849	200	1773	T	3.6	2.7	1.6	1.3	78.6	11.3	0.3	0.7
2017	Giehl et al.	Basalt	5–125	2800	15	1373–1773	C	3.0	0.5	10.2	5.9	52.0	13.0	2.8	12.4
		Andesite	5–125	2600	15	1373–1773	C	3.7	0.7	8.8	5.6	53.9	18.7	1.0	7.4
		Dacite	5–125	2700	15	1373–1773	C	4.4	2.4	3.7	0.8	63.7	13.5	0.8	7.8
		Rhyolite	5–125	2500	15	1373–1773	C	6.4	2.4	2.9	1.0	73.4	11.9	0.9	2.8
	Barker et al.	ARD$^+$	10–35	2560	80	1373	C	2.3	3.3	3.8	1.3	72.8	10.8	0.3	5.3
	Boulanger et al.	ARD 2$^+$	20–40	2560	70	1273–1373	C	2.3	3.3	3.8	1.3	72.8	10.8	0.3	5.3
	Whitaker et al.	ARD 3$^+$	0–10	2560a	40	920–1262	I	2.3	3.3	3.8	1.3	72.8	10.8	0.3	5.3
	Wylie et al.	EYJA 2 °	4.8–34.9	849b	80	1163–1293	I	2.0	2.0	4.6	0.0	51.3	10.9	1.4	9.5
		Chaiten VA	4.8–34.9	849b	80	1163–1293	I	2.9	2.9	1.6	0.0	73.9	14.0	0.2	1.6
2016	Boulanger et al.	ARD 4$^+$	20–40	2560	70	1273–1373	C	2.3	3.3	3.8	1.3	72.8	10.8	0.3	5.3
	Whitaker et al.	ARD 5$^+$,*	0–20	2560	21	866c	I	0.0	0.0	3.3	0.0	84.8	9.9	0.0	2.1
	Lundgreen et al	ARD 6$^+$,*	0–5	2560	70	1363–1623	B	0.0	0.0	3.0	0.0	85.0	10.0	0.0	2.0
	Dean et al.	Laki^x	5–50	2400	106	1043–1295	C	6.4	0.3	6.3	8.3	52.6	18.8	1.3	6.1
		Hekla2^{2x}	5–50	1500	106	1043–1295	C	7.3	1.2	2.0	1.4	67.4	18.1	0.0	2.6
		Eldgja^{3x}	5–50	1900	106	1043–1295	C	6.9	0.3	6.2	7.1	50.3	19.7	2.4	7.3
		Askja^{4x}	5–50	1400	106	1043–1295	C	5.6	1.5	1.7	1.8	71.9	15.5	0.0	2.0
	Laycock and Fletcher	JBPS A	4	2330	200	1523–1673	C	2.5	0.9	5.1	1.6	63.6	17.3	1.1	4.2
	Taltavull et al.	Laki 2^{5x}	10–70	2400	91	1043	C	1.2	0.1	7.8	3.1	47.2	11.6	3.7	25.2
		Laki 3^{5x}	10–70	2400	106	1160	C	1.2	0.1	7.8	3.1	47.2	11.6	3.7	25.2
		Laki 4^{5x}	10–70	2400	127	1295	C	1.2	0.1	7.8	3.1	47.2	11.6	3.7	25.2
'15	Whitaker et al.	JBPS B	4.63; 6.48	2320	70	1353	B	3.7	1.6	9.4	1.7	49.9	11.5	3.0	14.5
'14	Prenter et al.	JBPS B	6.48	2320	70	1353	B	3.7	1.6	9.4	1.7	49.9	11.5	3.0	14.5
2013	Casaday et al.	JBPS B 2	11.6	2320	79	1366	B	3.7	1.6	9.4	1.7	49.9	11.5	3.0	14.5
	Laycock and Fletcher	JBPP **	3; 13	1980	200	1523	C	3.9	1.7	9.9	1.8	52.4	12.1	3.1	15.2
	Shinozaki et al.	Laki 5	20–100	2400	365	1343	T	1.2	0.1	7.8	3.1	47.2	11.6	3.7	25.2
2012	Webb et al.	Lignite	12.5	2818	70	1314–1371	B	0.8	1.0	31.7	3.6	32.8	14.2	2.6	9.8
		Bituminous	14.1	1980	70	1339–1366	B	0.3	2.0	2.3	0.6	25.3	11.0	1.9	52.7
		PRB	18.3	2989	70	1315–1385	B	1.8	0.5	42.2	6.9	22.1	10.5	2.2	6.1
		JBPS B 3	12.5	2320	70	1317–1343	B	3.7	1.6	9.4	1.7	49.9	11.5	3.0	14.5
	Ai et al.	Coal (bit.)	13.4	1980	170	1456	C	6.9	2.6	8.7	3.6	47.4	17.8	1.6	6.4
	Aiet al.	Coal (bit.) 2	16	1980	180	1453	C	6.9	2.6	8.7	3.6	47.4	17.8	1.6	6.4
'11	Ai et al.	Coal (bit.) 3	4, 13.4	1980	170	1453	C	6.9	2.6	8.7	3.6	47.4	17.8	1.6	6.4
'10	Smith et al.	BM 14	14	1980	70	1181–1272	B	0.0	2.5	2.9	0.0	32.9	20.3	0.0	40.6
2008	Crosby et al.	Coal (bit.) 4	3.1–16	1980	170	1133–1456	C	6.9	2.6	8.7	3.6	47.4	17.8	1.6	6.4
		Petcoke	6.3	2900	170	1133–1456	C	4.3	2.5	7.5	2.2	38.3	14.5	0.8	22.9
	Wammack et al.	BYU SEM	16	2500	220	1423	C	0.0	7.3	13.7	0.0	60.2	4.5	0.0	10.7
2007	Bons et al.	Coal (bit.) 5	13.3	1980	200	1423	C	6.9	2.6	8.7	3.6	47.4	17.8	1.6	6.4
		Petcoke 2	33.0	2900	200	1423	C	4.3	2.5	7.5	2.2	38.3	14.5	0.8	22.9
		Straw	17.6	1680	200	1423	C	1.7	23.4	7.8	2.5	48.4	1.8	0.0	5.0
		Sawdust	19.7	960	200	1423	C	5.9	10.7	42.9	12.4	11.6	5.1	1.3	1.0
'05	Jensen et al.	BYU SEM	16	2500	220	1423	C	0.0	7.3	13.7	0.0	60.2	4.5	0.0	10.7
'96	Dunn et al.	St Helens	23	2700	100	1283–1558	T	4.5	1.6	4.5	1.6	63.2	16.4	0.6	4.1
		Twin Mountain	73	2730	100	1283–1558	T	0.5	4.2	10.6	1.5	50.3	13.2	1.9	15.3
'93	Kim et al.	St Helens 2	23	2700	100	1394–1494	T	4.5	1.6	4.5	1.6	63.2	16.4	0.6	4.1
1992	Richards et al.	Arkwright	0–40	1980	300	1373	C	0.9	1.2	5.8	1.3	48.1	25.1	1.3	11.0
		Blue Gem	0–40	1980	300	1373	C	1.5	0.5	7.0	2.5	16.9	22.8	2.0	29.6
		Arkwright 2	0–20	1980	300	1573	C	0.9	1.2	5.8	1.3	48.1	25.1	1.3	11.0
		Blue Gem 2	0–20	1980	300	1573	C	1.5	0.5	7.0	2.5	16.9	22.8	2.0	29.6
1990	Anderson et al.	Arkwright	0–40	1980	300	1373	C	0.9	1.2	5.8	1.3	48.1	25.1	1.3	11.0
		Blue Gem	0–40	1980	300	1373	C	1.5	0.5	7.0	2.5	16.9	22.8	2.0	29.6
		Arkwright 2	0–20	1980	300	1573	C	0.9	1.2	5.8	1.3	48.1	25.1	1.3	11.0
		Blue Gem 2	0–20	1980	300	1573	C	1.5	0.5	7.0	2.5	16.9	22.8	2.0	29.6
	Wenglarz and Fox	Ash-fuel 1	10.2	1900	150	1253–1373	C	0.6	1.2	3.8	0.0	12.0	14.2	0.8	20.4
		Ash-fuel 2	8.5	1900	150	1253–1373	C	0.7	1.0	3.4	0.0	11.5	13.9	0.8	21.9
		Ash-fuel 3	14.5	1900	150	1253–1373	C	1.0	0.9	4.7	0.1	7.5	10.9	1.0	23.1
1989	Ahluwalia et al.	Ash-fuel 1	10.2	1900	150	1253–1373	C	0.6	1.2	3.8	0.0	12.0	14.2	0.8	20.4
		Ash-fuel 2	8.5	1900	150	1253–1373	C	0.7	1.0	3.4	0.0	11.5	13.9	0.8	21.9
		Ash-fuel 3	14.5	1900	150	1253–1373	C	1.0	0.9	4.7	0.1	7.5	10.9	1.0	23.1
1988	Ross et al.	Arkwright3	20	1980d	100	1400–1500	C	0.9	1.2	5.8	1.3	48.1	25.1	1.3	11.0
		Kentucky	20	1980d	100	1400–1500	C	9.5	0.3	1.3	0.6	25.5	15.9	7.8	32.4
		Spring Montana	20	1980d	100	1400–1500	C	13.1	0.1	26.5	6.5	18.6	13.5	1.3	4.7
		North Dakota$d$	20	1980	100	1400–1500	C	8.3	0.3	22.9	6.7	20.1	11.2	0.5	13.2
1987	Spiro et al.	AMAX	0–15	1900	100	1366	B	6.7	5.8	3.2	0.0	17.9	11.5	2.9	37.6
		Otisca coal	0–11.5	1900	100	1366	B	0.5	0.5	11.6	0.0	16.1	23.2	1.1	28.2
	Wenglarz	Ash-fuel 1	10.2	1900	150	1253–1373	C	0.6	1.2	3.8	0.0	12.0	14.2	0.8	20.4
		Ash-fuel 2	8.5	1900	150	1253–1373	C	0.7	1.0	3.4	0.0	11.5	13.9	0.8	21.9
		Ash-fuel 3	14.5	1900	150	1253–1373	C	1.0	0.9	4.7	0.1	7.5	10.9	1.0	23.1
	Kimura et al.	Otisca coal	0–11.5	1900	100	1366	B	0.5	0.5	11.6	0.0	16.1	23.2	1.1	28.2
1984	Raj and Moskowitz	Coal	0–6	1900	244	1144–1422	B	2.2	2.8	0.3	1.1	28.9	29.4	1.7	25.6
	Anderson et al.	Pittsburg	15	2500	53	1590	C	0.9	1.2	5.8	1.2	47.9	25.0	1.3	10.9
		Pittsburg 2	15	2500	149	1590	C	0.9	1.2	5.8	1.2	47.9	25.0	1.3	10.9
		Pittsburg 3	15	2500	215	1590	C	0.9	1.2	5.8	1.2	47.9	25.0	1.3	10.9
'83	Raj	Coal 2	0 – 6	1900	244	1700–1922	B	2.2	2.8	0.3	1.1	28.9	29.4	1.7	25.6

$^{+}$	The particle diameters used in these tests could be different from the standard ones reported in the ISO 12103-1 (A1, A2 A3, and A4) ISO 12103-1:2016 (2016) due to filtration, sieving and processes applied by the Authors
$^{\circ}$	EYJA 2 has different chemical compositions with respect to EYJA
*	ARD 5 and ARD 6 have different chemical compositions with respect to ARD, ARD 2, ARD 3 and ARD 4
^{a}	Temperature values refer to the surface wall temperature. Gas temperature was set equal to 866 K
^{b}	Temperature values refer to the surface wall temperature. Gas temperature was set equal in the range (800-900) K
^{c}	Temperature values were set in the range (700 – 866) K but particle deposition was founded for the highest temperature value (866 K)
^{x}	The chemical composition in terms of oxide weight fraction was derived starting from the element count % reported in Dean et al. (2016) (Si 17.5 %, Al 7.1 %, Na 3.4 %, Ca 3.2 %, Mg 3.6 %, Ti 0.6 %, K 0.2 % and Fe 3.4 %)
^{2x}	The chemical composition in terms of oxide weight fraction was derived starting from the element count % reported in Dean et al. (2016) (Si 21.4 %, Al 6.5 %, Na 3.7 %, Ca 1.0 %, Mg 0.6 %, Ti 0.0 %, K 0.7 % and Fe 1.4 %)
^{3x}	The chemical composition in terms of oxide weight fraction was derived starting from the element count % reported in Dean et al. (2016) (Si 16.0 %, Al 7.1 %, Na 3.5 %, Ca 3.0 %, Mg 2.9 %, Ti 1.0 %, K 0.2 % and Fe 3.9 %)
^{4x}	The chemical composition in terms of oxide weight fraction was derived starting from the element count % reported in Dean et al. (2016)(Si 23.6 %, Al 5.8 %, Na 2.9 %, Ca 0.9 %, Mg 0.8 %, Ti 0.0 %, K 0.9 % and Fe 1.1 %)
^{5x}	The chemical composition in terms of oxide weight fraction was derived starting from the element count % reported in Taltavull et al. (2015); Shinozaki et al. (2013) and is different from the Laki composition in Dean et al. (2016) (Si 24.0 %, Al 6.7 %, Na 1.0 %, Ca 6.1 %, Mg 2.0 %, Ti 2.4 %, K 0.1 % and Fe 21.3 %)
**	The details about the composition are based on the erratum Laycock and Fletcher (2017). The powder belongs to the Jim Bridger Power Plant as well as the tests named JBPS A, JBPS B, 1, 2 and 3 but has a slightly different chemical composition. The weight percent values reported in the table were calculated starting from the following molar percentages (SiO_2 60.2 %, Al_2O_3 8.17 %, Na_2O 4.3 %, CaO 12.2 %, MgO 3.1 %, TiO_2 2.7 %, K_2O 1.2 % and Fe_2O_3 6.6 %)
^{d}	Temperature range obtained as a function of the distance between nozzle and target
^{e}	Maximum firing temperature

Table 7.5: Notes for Tab. 7.4

correspondent temperature value. The liquidus temperature can be compared with the temperature value at which the deposition test is carried out. The deposition tests are reported by means of different markers based on the chemical composition reported in Tab. 7.4. A higher content of silica dioxide corresponds to higher liquidus temperature, and in turn, the deposition test is carried out when particles are not melted yet. Another element of information that can be drawn, is related to the effects of each oxide on the particle behavior. For example, for the majority of the considered tests reported in Tab. 7.4, the presence of iron dioxide does not influence the liquidus temperature that can be assumed equal to 1673 K due to the higher presence of silica dioxide. In addition, it can be highlighted that the ash composition of several tested coals occurs in mullite phase field. Mullite is the predominant phase of coal ash which is formed due to kaolinite and other clays decomposition during combustion Bandyopadhyay et al. (2014). With this qualitative data representation (due to the approximation of this data post-process based on only three oxides) it is clear how the correlation between particle composition and

temperature could determine different phenomena during the impact process. The different amount of oxide content in each test increase the complexity of the result comparison process and thus, each test condition has to be considered as a fundamental information coupled with the particle chemical composition. The final consideration is related to the literature data. The material characterization is often reported but sometimes it is not complete or, in the worst cases, completely absent. Material characterization is fundamental for calculating physical properties such as viscosity and surface tension which are the most important parameter in the particle adhesion phenomenon. For this reason, in this work, two characterizations related to the volcanic rock, are taken from literature. In details, the composition of Twin Mountain basaltic rock Ciprian and Grigore (2013) and St. Helens rock Taylor and Lichte (1980) are taken from literature.

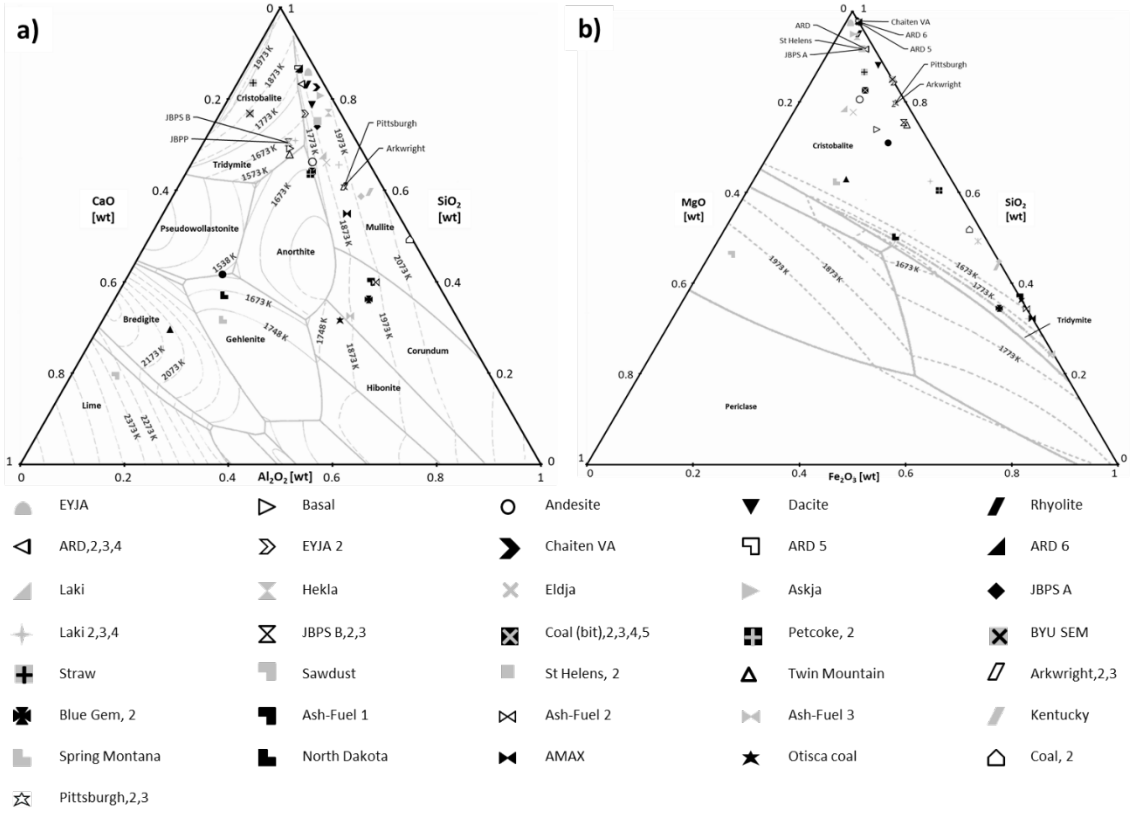

Figure 7.8: Ternary diagrams with liquidus curves of the triplets: a9 Al_2O_3-SiO_2-CaO and b)SiO_2-MgO-Fe_2O_3

With the reference of the data reported in Tab. 7.4, it is clear how each test is characterized by several peculiarities, as well as different particle size and temperature. This evidence introduces some critical aspect into the determination of a proper framework under which a useful comparison can be carried out. According to the contamination source, three families can be recognized such as silty, coal and volcanic particles even if, only the volcanic ash particles, are created by instantaneous and, in many cases, explosive processes. For these reasons, in the literature, detailed analyses are reported in relation to their dimension and material structure. Volcanic ashes are characterized by different fractions of crystals and amorphous solids (juvenile fragments) created during explosive volcanism phenomena. Specific volcanic events (phreatomagmatic eruptions,

pyroclastic density currents, and explosive eruptions) determine variations in terms of crystals/volcanic glasses fractions and changes in chemical compositions. The intrinsic structural nature of the ash, comprised of fine fragments of magmatic glasses, magmatic crystals, and other lithic materials, influences the temperature-dependent material characteristics causing, for example, significant modification in sintering and/or melting conditions of ash particles. This wide variability in chemical and physical ash characteristics makes it difficult to evaluate the behavior of volcanic ash and the proper characterization of the material structure is often tedious due to the structurally complex nature of ash components. Regarding the coal-like particles, a description of the generation of ash particles is reported in Lee et al. (2002). Large particles are formed by the mechanism of coalescence, while fine particles are the result of vaporization and the subsequent condensation of volatile inorganic elements. This implies that a certain degree of inhomogeneity in terms of size and composition can be found after the combustor, but, no detailed analysis are available in this sense, especially related to the combustion process in a gas turbine. A lack of contaminant characterization in terms of temperature-dependent material characteristics implies hypotheses and unavoidable inaccuracies that should be the main reason for pushing new strategies and tests procedures forward. For example, in volcanic ash analysis, the relation between ash composition and melting temperature (and in turn, ash viscosity) is very difficult to predict in detail Taltavull et al. (2015). Other contributions (Song et al. 2014; Kueppers et al. 2014; Song et al. 2017) show the influence of the heating rate on the evolution of the wettability and spreading of volcanic ash. More specifically, the wetting efficiency of volcanic ash is dependent on particle size and particle temperature together with mineral/glass ratio Giehl et al. (2017). As reported by Taltavull et al. (2015), these factors are related to the adhesion rate for normal surface incidence. Regarding the dimension, as mentioned before, non-precise data are reported but, some general consideration can be drawn. It is clear that the adhesion rate is more influenced by a larger particle because its weight is comparable to that of several smaller particles (e.g. one 50 μm particle weighs the same as a thousand 5 μm particles). Particle size also affects the rate at which the particle temperature achieves the substrate temperature: fragments with smaller diameters are capable of reaching more quickly the substrate temperature compared to larger particles and this is at the base of the theoretical effect of heat transfer to different particle sizes Giehl et al. (2017); Clarkson et al. (2016). In this context, the mineral/glass content of the ash can play a key role in the deposition rate. When glass transition temperature is reached, most of the amorphous (glassy) particles are expected to rapidly become very soft promoting the particle adhesion phenomenon. Finally, the mechanical properties are related also to the particle diameter. As reported in Portnikov and Kalman (2014), the particle Young modulus may increase when particles are smaller. In particular, in Portnikov and Kalman (2014), an exponential dependence of the particle Young modulus on the grain size is reported due to the fact that, when the particle is small, the material structure is less affected by inhomogeneity and defects. All of these effects affect the experimental results carried out over the years and, in turn, influence the present data post-process. By contrast, given the number of tests which

involve several materials, particle sizes and test conditions, can be concluded that the present data post-process can be considered robust against these effects within a certain tolerance band, allowing the comprehension of the particle deposition phenomenon based on per order of magnitude considerations

7.4 Particle sticking models and viscosity method: mutual interaction and critical analysis

The previous analysis has shown that the deposition tests listed in Tab. 7.4 are carried out with temperature values lower than liquidus temperature and, thus, they are characterized by semi-molten particles which impact on a solid surface. For this reason, the measurement of the particles viscosity is not straightforward and, it implies several difficulties. Figure 7.9 shows the iso-viscosity contour plot based on the ternary plots of the triplet Al_2O_3-SiO_2-CaO and gives the possibility to compare the collected data with the viscosity values measured at 1773 K Atlas (1995). The regions not covered by the iso-viscosity lines are due to the lack of literature data and, in some instances the presence of solid matter (higher content of silica dioxide). Despite the fact that this qualitative representation is not useful for carrying out the analysis of the deposition process (the temperature value is constant and higher than the experimental particle temperature), it gives the opportunity to highlight how the particle chemical composition influences the particle impact behavior. By a slight modification of mass fraction oxide content, the particle viscosity changes by an order of magnitude for the same temperature value.

Based on the chemical composition of the material, in this section, the particle viscosity is calculated as a function of the temperature. Using the listed models (NPL, S2, WF, S&T, RRLG, SDS and GRD) it is possible to calculate the viscosity values as a function of the material composition and temperature. This allows the comparison between different tests (carried out with different materials and temperature) in terms of viscosity. The viscosity values are calculated for all materials reported in Tab. 7.4 following the models reported. As mentioned, based upon the viscosity model analysis the NPL model works with all the considered materials due to the absence of specific applicability limits (in terms of chemical composition) allowing for the comparison among the deposition tests without restrictions. Due to this, for the cross-comparison between the viscosity model reported in the following paragraph, the NPL model represents a sort of reference giving the chance to compare several models (applied according to their applicability limits) with respect to the same reference values. For each analysis, all the viscosity models which are suitable (in terms of particle composition) for the analysis are used, in order to improve the completeness of the present data post-process. Figure 7.10 reports the variation of the particle viscosity as a function of the temperature, according to the NPL model. For a given temperature, the viscosity variation is almost six (6) orders of magnitude

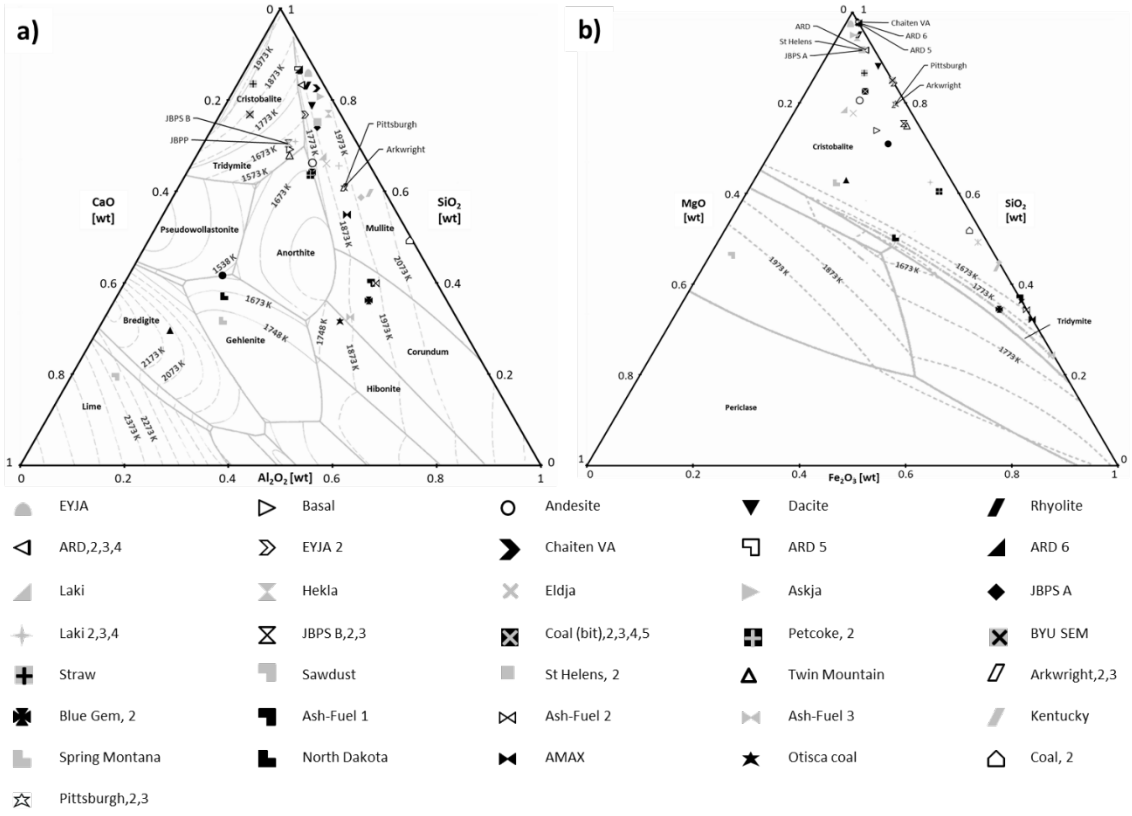

Figure 7.9: Iso-viscosity [Pa s] contour of CaO-Al_2O_3-SiO_2 at 1773 K

for lower temperatures and three (3) orders of magnitude for higher temperatures while the majority of the data is localized in the range of (1 – 104) Pa s. Figure 7.11 reports the viscosity prediction according to the different models (S2, WF, S&T, RRLG, SDS and GRD). Each model is applied within its validity limits and, in order to highlight the differences, the viscosity prediction obtained with the NPL model are reported in red. Therefore, the shape and grey-scale color (empty with black bound, solid black and grey) represent the model predictions according to the chart label, while the red-scale (empty with red bound, solid red and pale red) represent the NPL predictions. Considering all predictions, the viscosity values vary in a sixteen-orders-of-magnitude-wide range. The trends are very similar to each other, even if the predictions provided by the WF model show a different trend. Based on viscosity calculation and by applying the critical viscosity method, it is possible to define the capability of each particle to adhere comparing the instantaneous particle viscosity and the critical viscosity value. The critical viscosity values could be calculated using one of the viscosity model reported where the particle temperature corresponds to the softening temperature T_{soft}. According to Eqs. (7.17) to (7.21), the particle softening temperature is calculated according to the materials compositions. Even if in some instances the particle softening temperature is reported, in order to compare all tests under the same conditions, the particle softening temperature is calculated for all tests. Table 7.6 shows the softening temperature for all materials listed in Tab 7.4. Therefore, starting from the particle characteristics such as particle viscosity, reported in Fig. 7.10 and Fig. 7.11, it is now possible to compare the viscosity ratio (μ/μ_c) trends at the critical condition related to the sticking model. This means

that starting from a particle characteristic, the information changes, moving toward the particle sticking phenomenon.

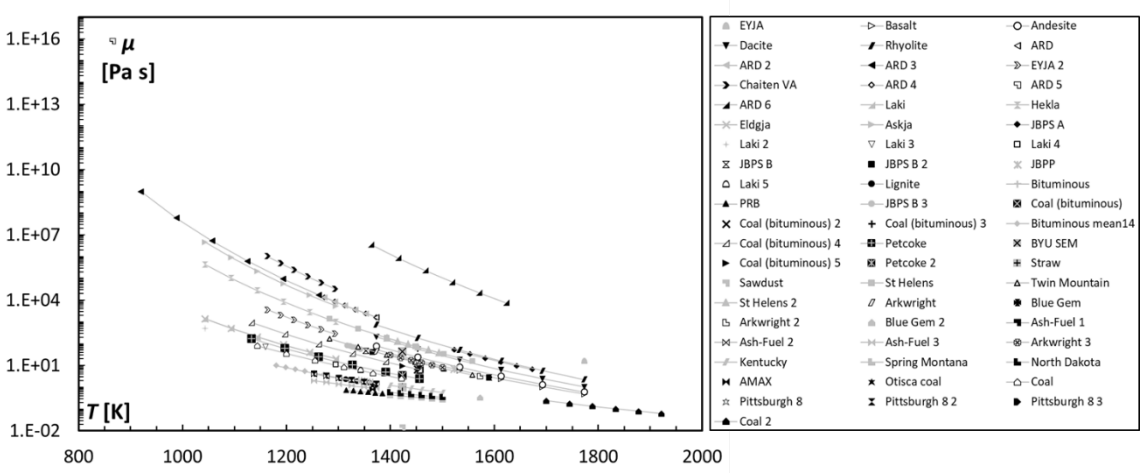

Figure 7.10: Viscosity values as a function of the temperature calculated according to the NPL model

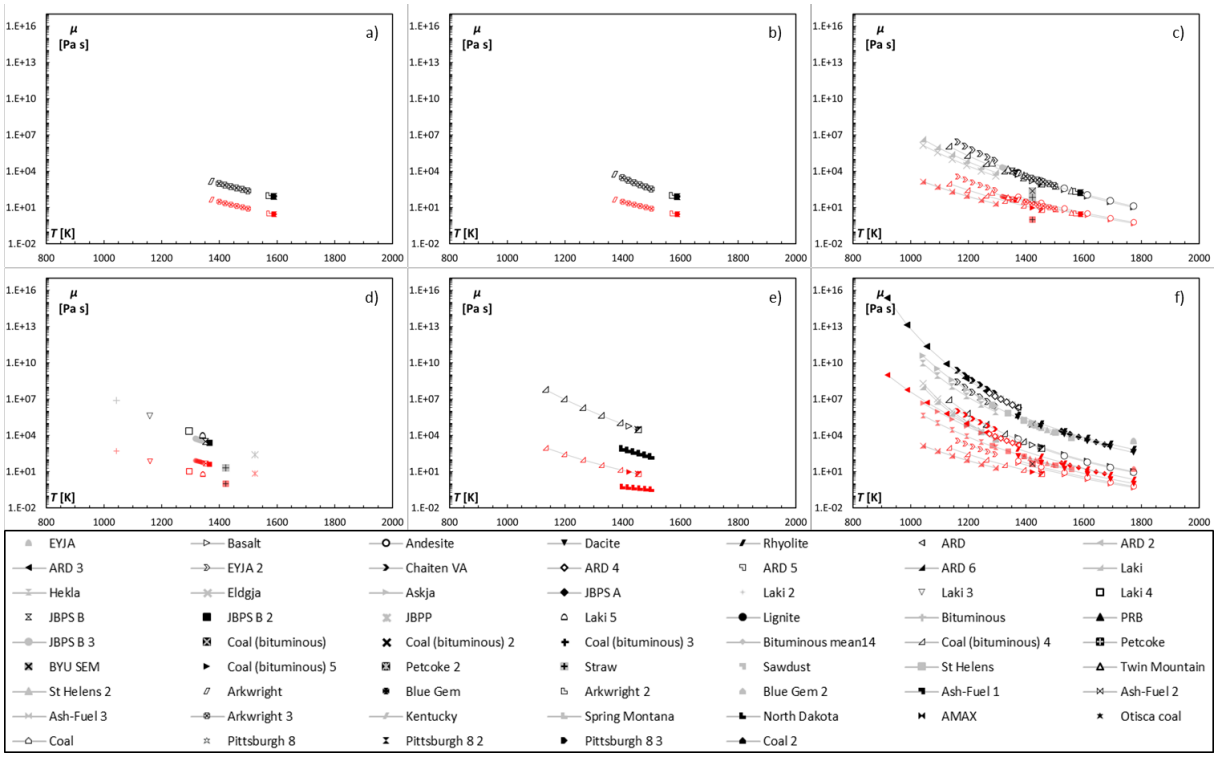

Figure 7.11: Viscosity values as a function of the temperature: a) S2, b) WF, c) S&T, d) RRLG e) SDS and f) GRD

The viscosity ratio (μ/μ_c) trends according to the temperature values are reported in Fig. 7.12 where the particle viscosity and the critical ratio are calculated according to the NPL model. According to the critical viscosity method, two regions for each material can be defined according to the viscosity ratio (μ/μ_c) identifying the sticky and rebound conditions. As can be seen in Figure 13, experimental tests are mainly conducted in the sticky regions excluding a few cases in which the results of test conditions lie inside the rebound region due to the lower particle temperature of deposition tests.

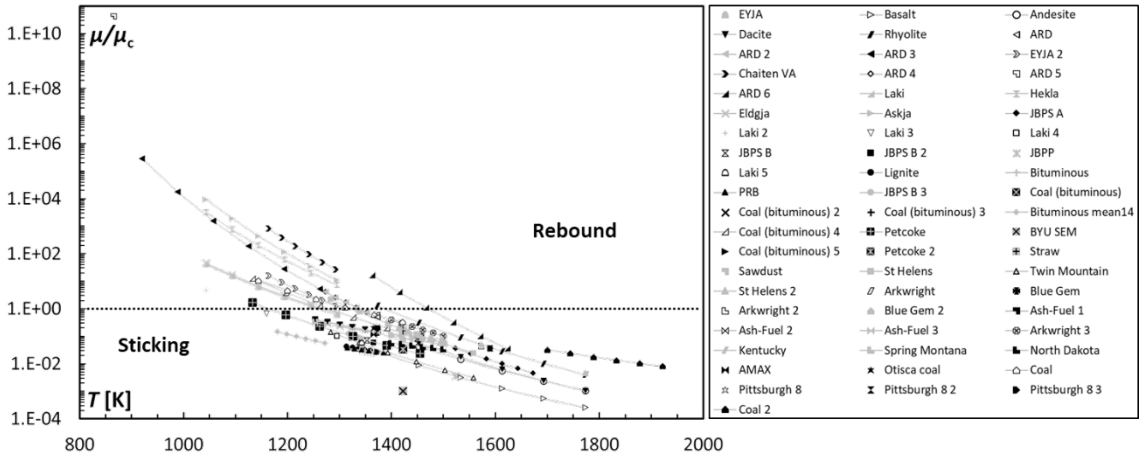

Figure 7.12: Critical viscosity method (rebound and sticking regions are divided by the dashed line) calculated according to the NPL model

With the same criterion, Fig. 7.13 reports the viscosity ratio (μ/μ_c) trends according to the temperature values obtained with the other viscosity methods . Each model is applied within its validity limits. State the analysis of Figure 7.12 and Fig.7.13 , it is clearly visible the immense variability in the viscosity obtained for the same substance from different models and also that, using such widely different values will result in contrasting predictions if different sticking models are applied.

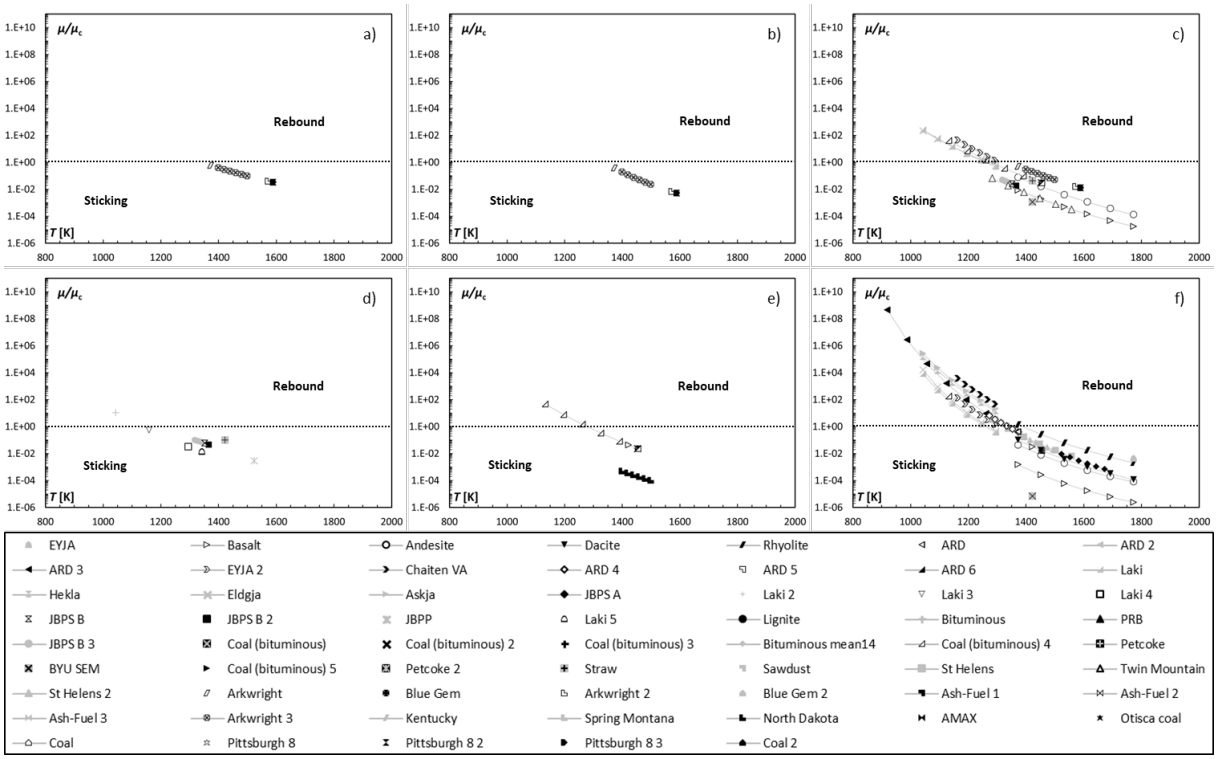

Figure 7.13: Critical viscosity method (rebound and sticking regions are divided by the dashed linea) S2, b) WF, c) S&T, d) RRLG e) SDS and f) GRD

In details, the following analysis reports a distinction between the tests according to the viscosity method. At the same time, the softening temperature is calculated with the same aforementioned model proposed by Yin et al. (1998). The first analysis, reported

Table 7.6: Values of particle softening temperature obtained according to Equations (7.17) to (7.21) compared with literature (if available)

Material	T_{soft} [K] (calculated)	T_{soft} [K] (literature)	Material	T_{soft} [K] (calculated)	T_{soft} [K] (literature)	Material	T_{soft} [K] (calculated)	T_{soft} [K] (literature)
EYJA	1445	-	JBPS A	1329	-	Twin Mountain	1176	-
Basalt	1170	-	Laki 2, 3, 4, 5	1132	873 - 973	Arkwright, 2, 3	1337	1589
Andesite	1257	-	JBPS B, 2, 3	1197	1422*	Blue Gem, 2	1191	1581
Dacite	1284	-	JBPP	1172	1500	Ash-fuel 1	1169	-
Rhyolite	1387	-	Lignite	1032	-	Ash-fuel 2	1162	-
ARD, 2, 3, 4	1337	-	Bituminous	1030	-	Ash-fuel 3	1118	-
EYJA 2	1305	1123 – 1323	PRB	909	-	Kentucky	1162	-
Chaiten VA	1446	1123 – 1323	Coal (bitum.), 2, 3, 4, 5	1278	1278**	Spring Montana	1068	-
ARD 5	1465	-	Bituminous mean14	1030	-	North Dakota	1021	-
ARD 6	1471	-	Petcoke, 2	1162	-	AMAX	1084	-
Laki	1258	923	BYU SEM	1071	-	Otisca coal	1179	-
Hekla	1394	1023	Straw	1213	-	Coal, 2	1320	-
Eldgja	1341	973	Sawdust	842	-	Pittsburgh, 2, 3	1337	1589
Askja	1161	973	St Helens, 2	1323	-			

in Fig. 7.14 and Fig. 7.15, shows silty and coal particle tests respectively. The marker shape indicates the test while the color indicates the viscosity method. In this case, silty particle tests mainly belong to the rebound region, while coal particle tests are located in the sticky region even if, some of these tests are conducted with the same temperature as silty tests. This difference is due to the different relationship between particle viscosity and temperature generated by the different chemical compositions. As reported by Kueppers et al. (2014), differences in chemical composition must be taken into account and the similarities between different particle impact tests have to be drawn considering these differences. Therefore, the use of ARD particles instead of coal particles for carrying out experimental tests in laboratory test facilities could generate several mismatches with respect to the actual applications. Figure 7.14 and Figure 7.15 show, in addition, the different viscosity ratio predictions provided by the viscosity methods. The variations between the NPL model and the GRD and S&T models increase towards lower temperature. In addition, the NPL predictions appear more close to the critical value (μ/μ_c=1) than other models. Considering the comparison reported in Fig. 7.16, it can be noted that predictions are not aligned with the straight dashed line (provided as a reference for the reader), but the trends change according to the tests and according to the viscosity ratio μ/μ_c. For high values of viscosity ratio, NPL and GRD model predictions (see Fig. 7.16a) are very different (several orders of magnitude), while, across the critical point (see Fig. 7.16a and b), the predictions appear similar even if characterized by different slopes. A detailed description of the relations between the viscosity method, sticking model and particle characteristics will report in the following sections.

Given that there have been a considerable number of tests of volcanic ash deposition, a dedicated analysis is carried out. The viscosity method proposed by Giordano et al. (2008) is expressly based on several volcanic ash samples (see section 7.11 for completeness) and, in this section, it will be compared with the more general method proposed by Mills and Sridhar (1999). According to the chemical classification proposed in BAS et al. (1986), Fig. 7.17 reports the Total Alkali-Silica (TAS) diagram with the superimposition of the

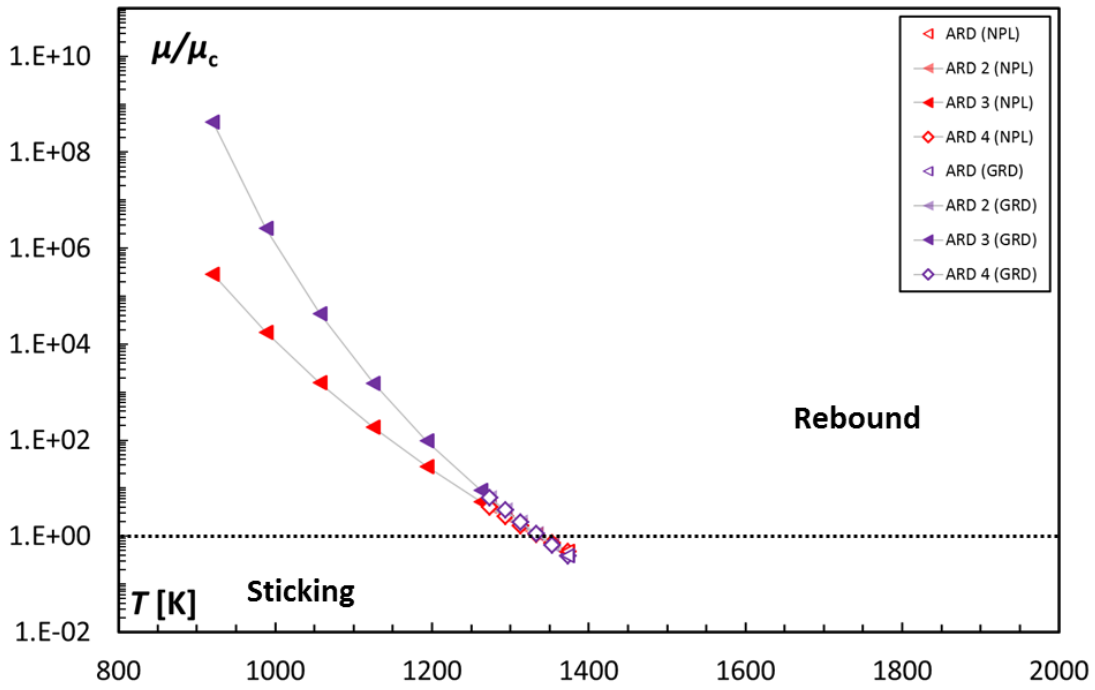

Figure 7.14: Critical viscosity method for silty particles (four tests with ARD) calculated according to the NPL and GRD models

fourteen (14) volcanic ashes considered in this review. Tests can be classified according to six (6) different categories called basalt, basaltic-andesite, dacite, rhyolite, basaltic trachy-andesite, and trachydacite. These subalkaline series are characterized by a lower amount of alkali and a progressive increase in silica dioxide content and are included in the GRD model limits.

Figure 19 reports the viscosity ratio as a function of the temperature for volcanic ashes using the GRD and NPL models. Thirteen (13) tests out of seventeen (18) are shown. Laki 2, 3, 4 and 5 and Twin Mountain tests are characterized by a particle composition out of the validity range indicated by Giordano et al. (2008). In a different way of coal particles, about half of these tests belong to the sticky region. As mentioned above, by using different viscosity prediction models, the viscosity ratio can vary noticeably, but the mutual variation between NPL and GRD methods appears very similar to those reported for silty and coal particles (see Fig. 7.14 and Fig. 7.15). This means that even if the GRD model is based only on volcanic ash materials (by means of a data regression, as reported in section 7.11), it performs similar prediction, in comparison with the NPL model, even for the material derived from different sources (silty and coal particles). Figure 7.19 shows the comparison between the critical viscosity ratio calculated according to the NPL and the GRD viscosity models. Sticking and rebound regions are superimposed onto the graph dividing the two regions as a function of the viscosity model. The comparison highlights how the choice of the viscosity model affects the particle adhesion prediction. It can be noted that predictions are not aligned with the straight dashed line (provided as a reference for the reader), but the trends change according to the tests and according to

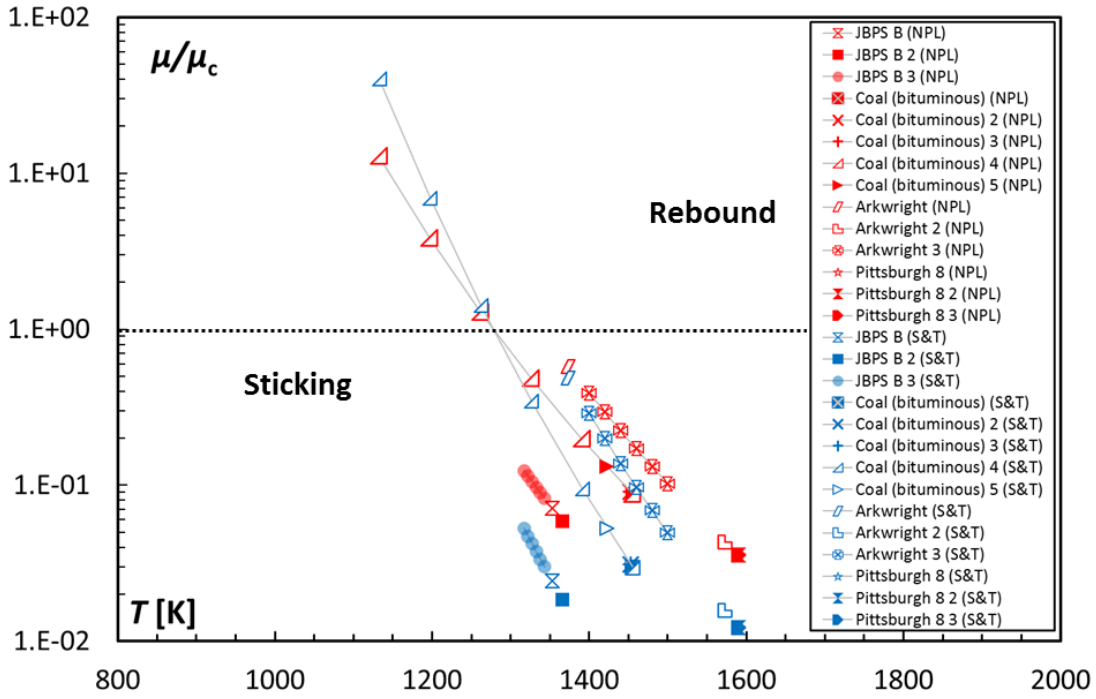

Figure 7.15: Critical viscosity method for coal particles (three tests with JPBS B, JBPP, five tests with Coal (bituminous), three tests with Arkwright and three tests with Pittsburg particles) calculated according to the NPL and S&T models

the viscosity ratio. This evidence has to be matched with the trends reported in Fig. 7.18: by changing the test temperature by 50 K, the particle viscosity may change by an order of magnitude and, by considering the different relation between viscosity and temperature, this could imply different predictions in terms of a particle sticking or rebound. This analysis shows how important the correct estimation of particle temperature is, as well as the choice of the viscosity and sticking models in the prediction of particle adhesion.

7.5 Particle velocity: application of the critical velocity method

In line with the viscosity analysis, it is possible to apply the critical velocity method defining the rebound/adhesion regions. This analysis is carried out using Eq. (7.14) for the calculation of the Young modulus and using Eq. (7.13) as a reference. This relation is used in literature for both ash contaminants Ai (2009) and JBPS B 2 particles Barker et al. (2013). The Young modulus of the surface is set equal to 200 GPa, while the Poisson coefficient is equal to 0.3 for both particle and surface. The Young modulus for the particle is calculated according to Eq. (7.12) that is suitable for coal-ash contamination. Figure 7.20 shows the comparison between a representative test (JBPS B 2) condition at v = 79 m/s and the consequent critical velocity. The dashed line in the picture is representative of the particle velocity used in the tests and the critical velocity is reported as a function

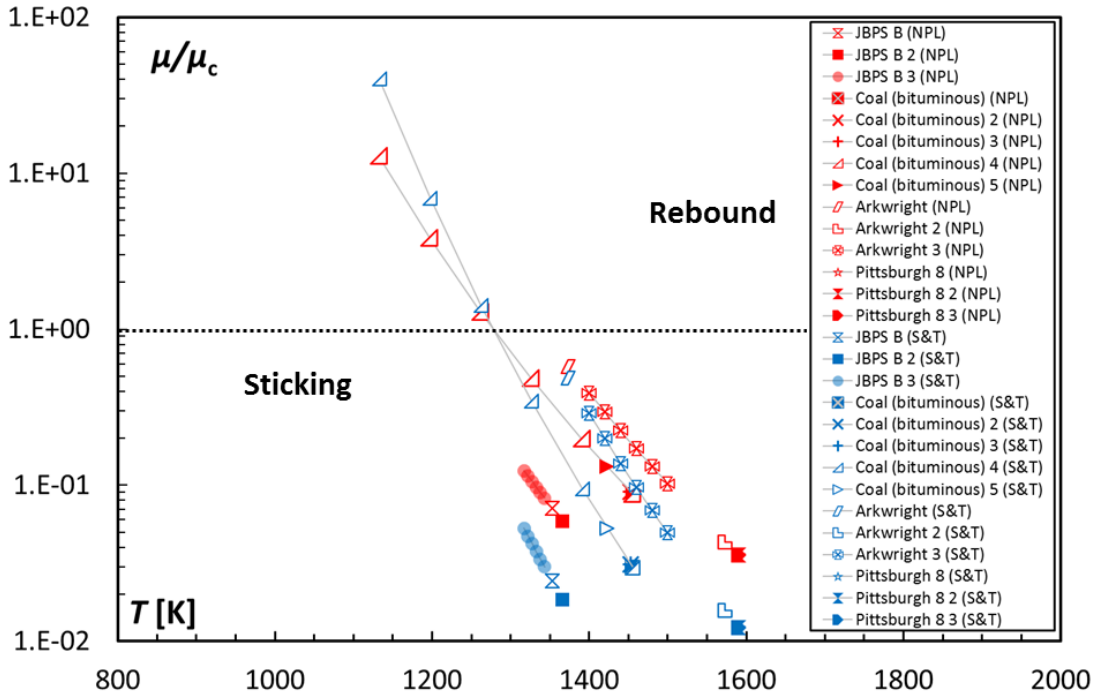

Figure 7.16: Comparison of the critical viscosity ratio (μ/μ_c): a) NPL and GRD models for silty particles and b) NPL and S&T models for coal particles. The straight dashed line allows the data comparison

of temperature and diameter. In this case, the overall range of particle diameter (2 – 20) μm, instead of the mass mean average diameter equal to 11.6 μm has been considered. In the same way, a temperature values in the range of 1273 K 1373 K instead of single temperature value equal to 1366 K have been considered for the analysis. This assumption is based on the experimental evaluations reported in Casaday et al. (2014). The Authors in Casaday et al. (2014) reported the temperature map across the vane, showing a non-uniform temperature pattern. If the particle velocity is lower than the critical velocity value, the particle is able to stick to a surface. Taking into consideration the critical velocity trends, for a given particle diameter, the particle velocity ranges for which the particle is able to stick increases according to temperature values. This trend is related to Young modulus variation with temperature (see Eq. (7.12)). Analogous results can be obtained by fixing particle temperature and decreasing particle diameter. In this case, the critical velocity value is inversely proportional to the particle diameter (see Eq. (7.13)). As can be predicted by the critical velocity model, particle adhesion occurs in the case of smaller diameter and higher temperature values. In this case, according to the critical velocity model, several experimental conditions lie outside the adhesion region. In this case, the actual non-uniform temperature pattern, instead of the single value taken as the reference for this test, shows how for a single adhesion test, different predictions may occur as a function of the local flow conditions. Critical velocity model takes into account particle diameter while the classic formulation of the critical viscosity model accounts only for the particle temperature and its composition. In literature, several analyses show that increasing particle diameter the average sticking coefficient decreases, probably due

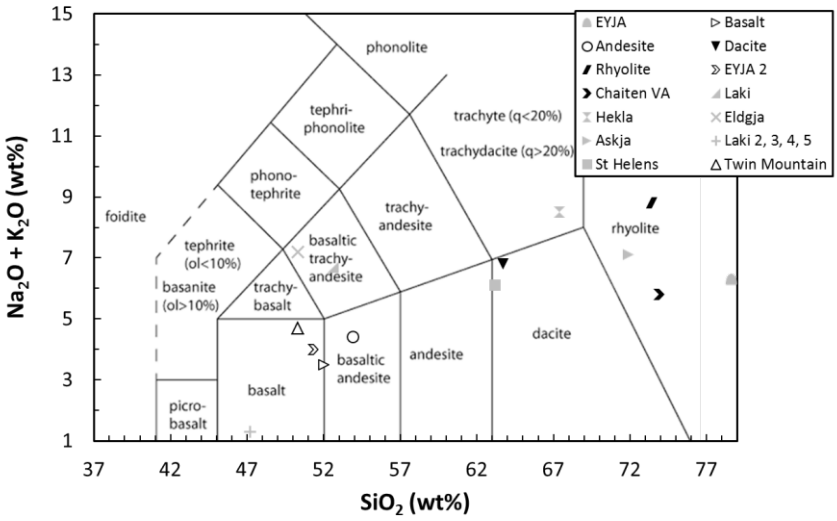

Figure 7.17: Classification of volcanic tests according to the TAS diagram

to a not-complete particle heating during the experimental tests Naraparaju et al. (2018). Analytical observations have highlighted the influence of the surface temperature Johnson et al. (1971). In particular, in presence of blade cooling, the sticking coefficient decreases due to the increment of the Young modulus (molten particle starts to solidify).

7.6 Energy-based model: particle spread factor and overall comparison

The last analysis related to particle adhesion/rebound using literature sticking model refers to the energy-based model. This model is based on the estimation of particle deformation during the impact and its correspondent energy balance between the dissipative and conservative forces. The peculiarity of this approach is related to the estimation of particle deformation as a consequence of the impact. Beyond the target characteristics (such as elasticity, hardness, surface roughness, etc.), one of the major challenges is represented by the identification of the particle condition (such as solid particle, liquid particle or semi-molten particle) upon impact. As reported in the literature Ravi et al. (2010) the deformation process is strongly dependent to the particle/droplet viscosity and surface tension.

Figure 7.21 reports the variation of the particle surface tension as a function of the temperature according to the material reported in Tab. 7.4. Therefore, each trend includes the particle surface tension variation due to the composition and temperature, while, each dot provides the particle surface tension value fixing both temperature and composition when that material is tested at a fixed temperature. The particle surface

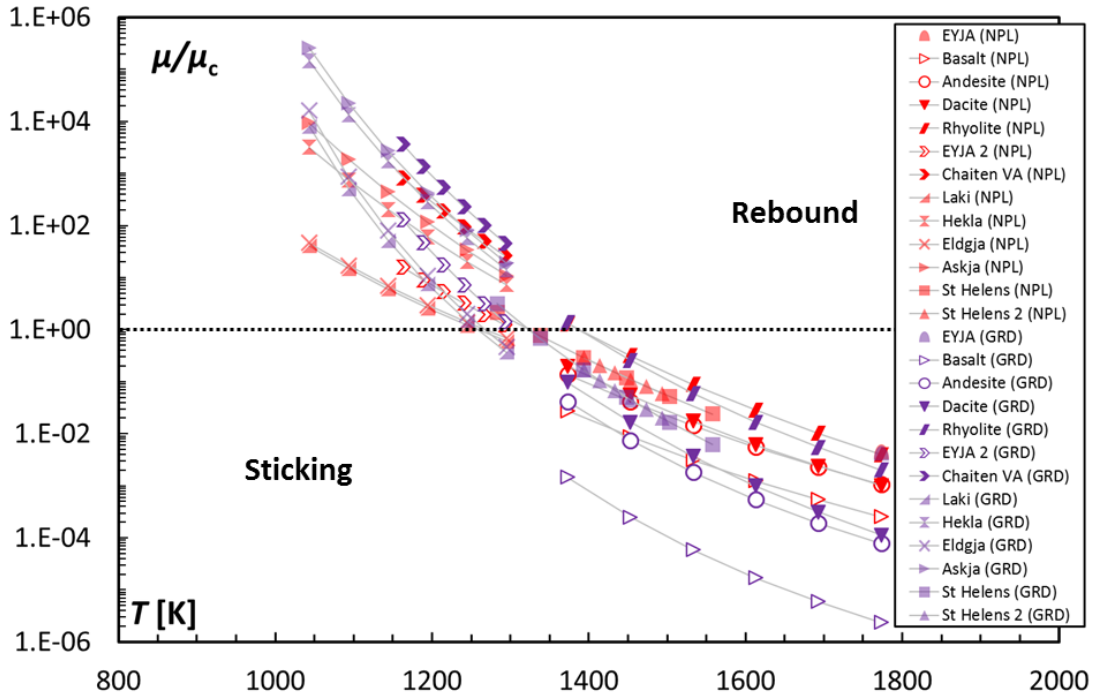

Figure 7.18: Critical viscosity method for volcanic ash particles calculated according to the NPL and GRD models

tension values are estimated in agreement with Eq. (7.22) and the model coefficient collected in Tab. 7.2. In the same fashion as seen for viscosity, particle surface tension values decrease according to the temperature even if, the variation over the temperature range is lower. The majority of data are comprised within 0.35 N/m to 0.45 N/m.

Particle spread factor analysis

Several researches are devoted to model the particle/droplet deformation process by means of the non-linear relationship between non-dimensional numbers such as We and Re and the contact angle realized on the target. As demonstrated by Kleinhans et al. (2016) relationship derived from droplet impact Mao et al. (1997) could be used for representing semi-molten particle impact, successfully. In particular, in Kleinhans et al. (2016), the sticking behavior of soda lime glass particles are well represented using the non-linear equation reported in Mao et al. (1997) obtained for water mixture with a viscosity value in the range (1–100) mPa s. Starting from this result, in this section, a collection of the relationships able to model the particle deformation process are reported. In order to give an overall overview how these models tackle the problem of semi-molten particle impact, six (6) relationships are used to calculate the particle spread factor for three (3) representative tests taken from Tab. 7.4, named ARD 2 (sandy particle), Eldgja (volcanic particle) and Coal (bituminous) 4 (coal particle) are considered. Spread correlations available in the literature refer to the different type of fluid/semi-molten substances and, as reported in Ravi et al. (2010) are characterized by some limitations. Most of these

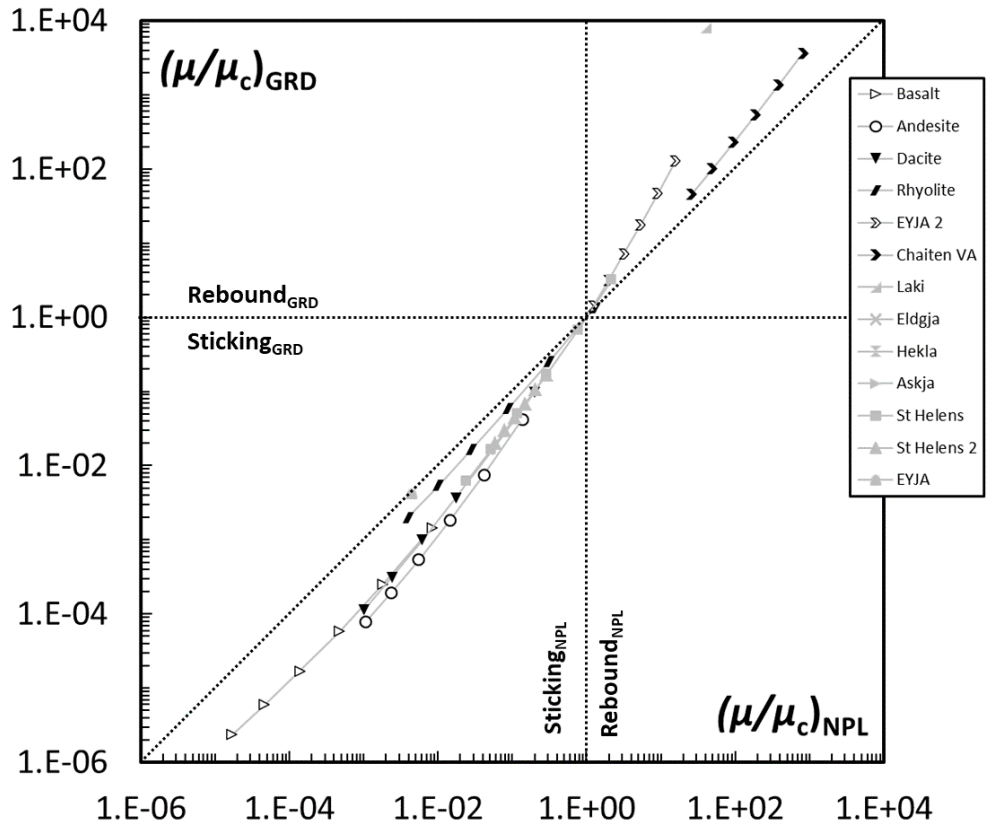

Figure 7.19: Comparison of the critical viscosity ratio calculated according to the NPL and GRD viscosity models where straight dashed line allows the data comparison

are related to the difficulties of scaling the complex interactions of liquid properties, surface wettability, dynamic contact angle and liquid velocity implying several difficulties to extend the validity beyond the fluid tested. Unfortunately, all the models available in the literature are based on studies of droplet impact having viscosity values lower than that involved in the present study (see Fig. 7.4 and Fig. 7.13). For example, very low viscosity fluid (3.9e-5 Pa s) was used by Jones (1971) taken inspiration from the Madejski (1976) model characterized by higher viscosity value (about 1 Pa s). Other models as Pasandideh-Fard et al. (1996) and Ukiwe and Kwok (2005) are based on experimental results obtained with droplet water. Similar fluid viscosity (n-heptane) is adopted also by Chandra and Avedisian (1991) while, fluids with higher viscosity values, are used by Mao et al. (1997) (fluid viscosity equal to 100 mPa s) and Scheller and Bousfield (1995) (fluid viscosity equal to 300 mPa s). Table 7.7 shows the non-linear equations used for calculating particle spread factor for the three (3) considered experimental tests. As reported, each equation depends on non-dimensional numbers (particle Reynolds and/or Weber numbers) and, in some cases, on the contact angle θ assumed equal to $\pi/2$ in the present study.

According to the relations reported in Tab. 7.7, Figure 7.22 and Figure 7.23 show the spread factor trend as a function of particle diameter and particle viscosity, respectively. In order to simplify the analysis, particle viscosity is calculated according to the NPL model, only. Each figure reports the results obtained for the three considered tests (ARD

Table 7.7: Non-linear equations for particle/droplet spread factor calculation

Author	Equation	Characteristics of liquid
Jones (1971)	$\xi = \left(\frac{4}{3}Re^{0.25}\right)^{0.5}$ (7.25)	Viscosity equal to 3.9e-5 Pa s
Pasandideh-Fard et al. (1996)	$\xi = \left(\frac{We+12}{3(1-cos\theta)+4WeRe^{-0.5}}\right)0.5$ (7.26)	Water
Ukiwe and Kwok (2005)	$(We+12)\xi = 8+3(1-cos\theta)+4WeRe^{-0.5}\xi^3$ (7.27)	Water
Chandra and Avedisian (1991)	$\frac{3We}{2Re}\xi^4 + (1-cos\theta)\xi^2 - \left(\frac{1}{3}We+4\right) = 0$ (7.28)	N-heptane
Mao et al. (1997)	$\left(\frac{1-cos\theta}{4}+0.2\frac{We^{0.83}}{Re^{0.33}}\right)\xi^3 - \left(\frac{We}{12}+1\right)\xi + \frac{2}{3} = 0$ (7.29)	Viscosity up to 100 mPa s
Scheller and Bousfield (1995)	$\xi = 0.91(ReWe^{0.5})^{0.133}$ (7.30)	Viscosity up to 300 mPa s

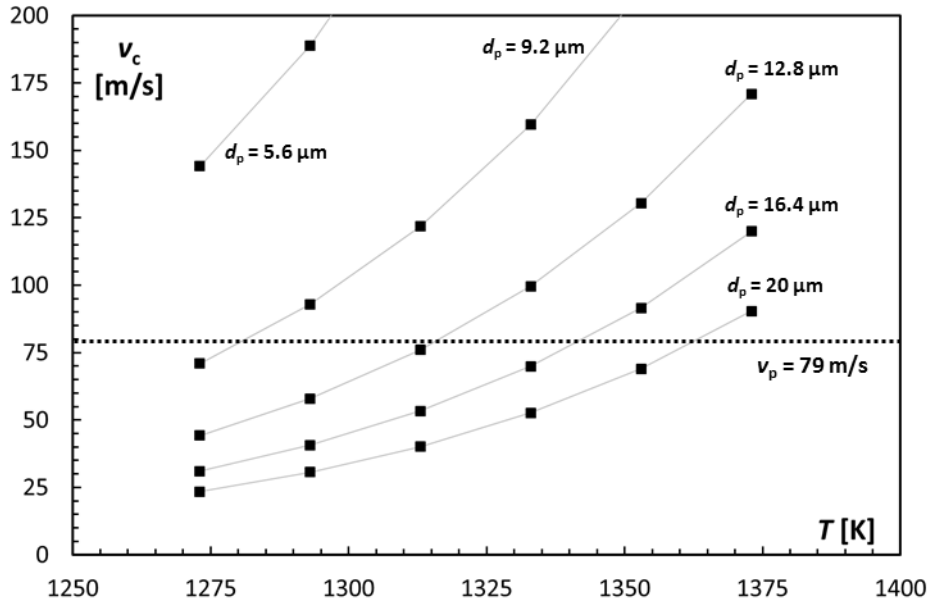

Figure 7.20: Application of the critical velocity method for JBPS B 2. Sticky conditions refer to the case when particle velocity vp is lower than the critical velocity value

2, Eldgja and Coal (bituminous) 4). Taken into consideration Fig. 7.22, trends appear very similar for particle diameter higher than 20 μm, even if, the spread factor values are widespread. In the case of smaller diameter, the trend provided by Jones (1971) deviates significantly with respect to the other. Therefore, in the case of small particle diameter, data dispersion is greater and the prediction of particle spread factor become more affected by the selection of the spread factor model.

Similar evidence can be found by considering the sensitivity analysis reported in 7.23. In this case, spread factor values are shown as a function of the particle viscosity values, and, it is visible that for lower particle viscosity, the model predictions of particle spread factor values are very close to each other (see Fig. 7.23c, for example). Moving towards higher viscosity values, the data appear very dispersed highlighting the variation of the slope among the models (see Fig. 7.23a). The trends ξ/μ appear very different from each other and it is in the opposite way than that reported in Fig. 7.22, where, the ξ/d trends show very similar slopes. This result derives from the relationship between particle spread factor and the non-dimensional numbers Re and We (see Tab. 7.7). Particle viscosity contributes only to the particle Reynolds number while particle diameter contributes in both characteristic numbers (Re and We). This implies that, from a particle deformation estimation point of view, the variation of particle viscosity in more detrimental than particle diameter. Taking into consideration the analyses reported in Fig. 7.22and Fig. 7.23, trends can be identified and correlated with the droplet characteristics used for obtaining model equations (Eqs 27 – 32), reported in Tab. 7.7). Models based on liquid droplet characterized by lower viscosity (Jones (1971); Pasandideh-Fard et al. (1996); Ukiwe and Kwok (2005)) predict lower particle spread factor values than the other models, which are obtained with higher droplet viscosity. The energy-based models are built on the defini-

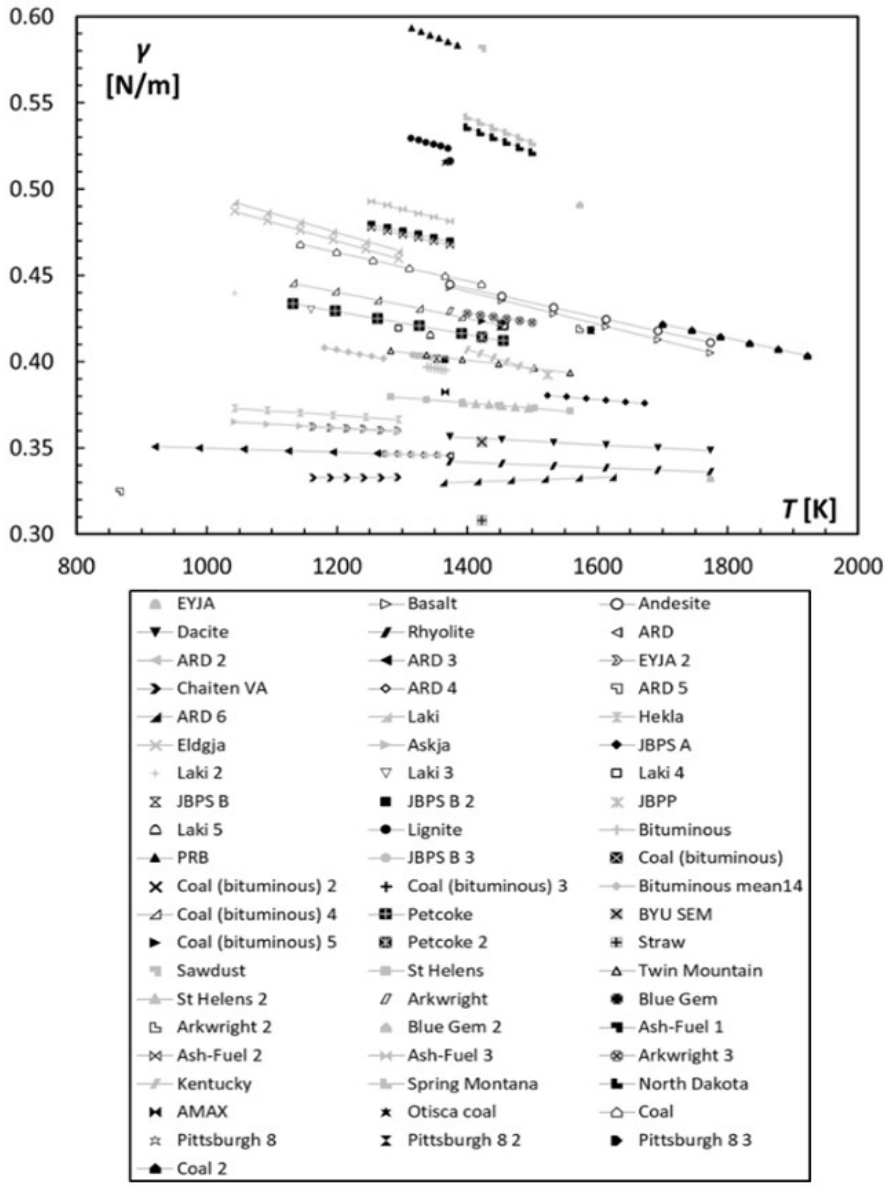

Figure 7.21: Particle surface tension as a function of particle temperature

tion of a particle spread factor threshold value (ξ=0.4 for the present work, see Fig. 7.3 for the full explanation), and with the reference of particle sticking phenomenon, different spread factor models give a different prediction of particle deformation for the same particle in the same impact conditions. According to the energy-based model, for a particle spread factor ξ equal or less than 0.4, particle sticks to the surface, otherwise it bounces. On the basis of these analyses, the model prediction of particle spread factor plays a key role when particle sticking prediction is based on the estimation of the energy dissipation provided by the particle deformation during the impact. Therefore, with this approach, particle sticking prediction is affected by (i) the model assumptions related to the spread factor equation and, taking into consideration also the estimation of particle viscosity and surface tension, (ii) the models used for estimating the particle characteristics upon the impact. In the following sections, the model of Mao et al. (1997) is taken as a reference

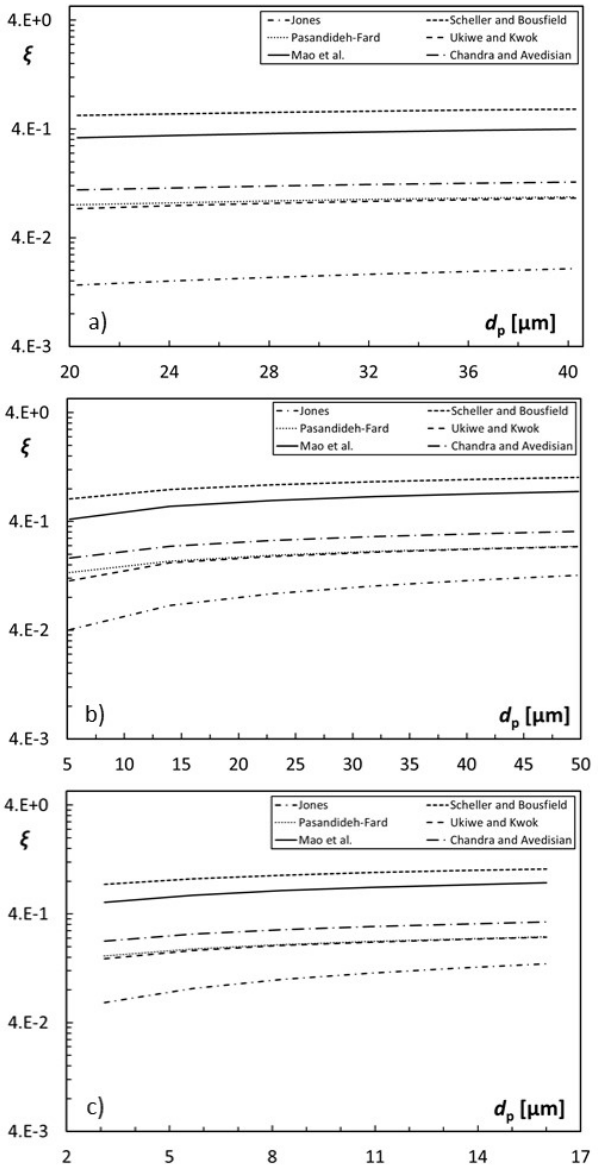

Figure 7.22: Particle diameter sensitivity analysis: a) ARD 2, b) Eldgja, and c) Coal (bituminous) 4

for analyzing the literature results, comparing the spread factor values with a threshold value (ξ=0.4). As reported by Kleinhans et al. (2016),Mao et al. (1997) model is able to well-recognized particle sticking in the case of high viscous substance (e.g. soda lime glass particle).

Starting from the particle Reynolds number and particle Weber number and using Eq. (7.29) it is possible to calculate the correspondent spread factor for each deposition test. To perform this, the particle surface tension has to be calculated according to the Eq. (7.21) with the reference of Tab. 7.3. Based on the derived particle surface tension values, Figure 7.24 reports a three-dimensional variation of the spread factor as a function of We and Re for a representative fixed value of contact angle Mao et al. (1997) equal to 90°. In Fig. 7.24, red and black dots represent all the data reported in Tab. 7.4. The threshold value of the spread factor (ξ = 0.4) is marked with a white line that divided

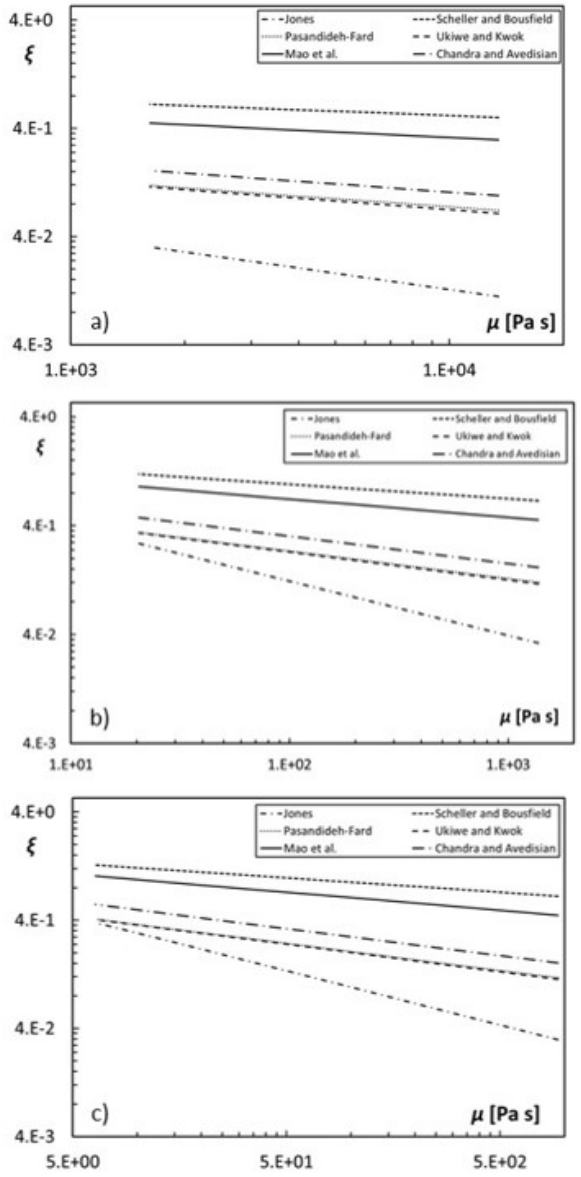

Figure 7.23: Particle viscosity sensitivity analysis: a) ARD 2, b) Eldgja, and c) Coal (bituminous) 4

the grey region from the pale-grey region. The grey region represents the sticking region ($\xi \geq 0.4$) in which the red dots represent the energy-based model prediction in agreement with the literature deposition tests, while the pale-grey region represents the rebound region ($\xi < 0.4$) in which the black dots represents the energy-based model prediction in disagreement with the literature deposition tests. Therefore, some deposition tests belong to the rebound region instead of the sticky region. In this case, particle diameter, velocity, and temperature are the main contributors in the to spread factor values. The three-dimensional surface We-Re-ξ shows, in correspondence of lower values of particle Weber number, a curvature variation due to the roots of the cubic relation reported in Eq. (7.29).

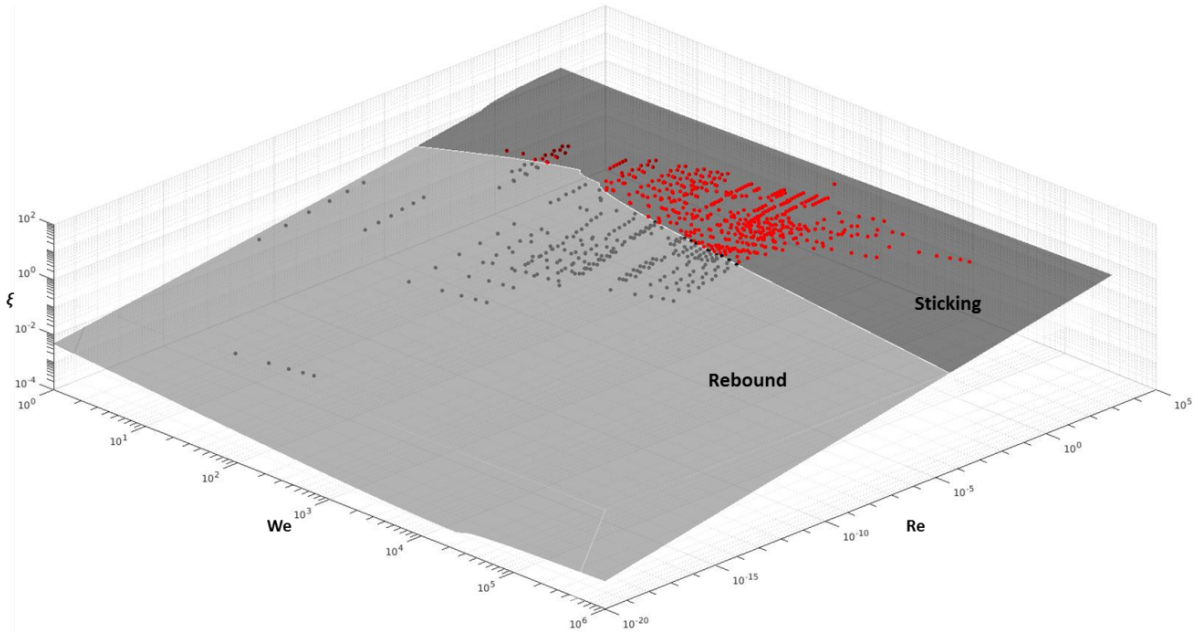

Figure 7.24: Application of the energy-based model. Sticky conditions refer to the case when particle spread factor ξ is higher than 0.4. Particle viscosity is calculated according to the NPL model

7.7 Comparison between critical viscosity and energy-based sticking models

The comparison proposed in Fig. 7.25 is related to the critical viscosity method and the energy-based model calculated according to the NPL viscosity model. Trends are related to a fixed particle diameter and particle temperature variation (if present) that implies the contemporary variation of particle viscosity and spread factor values. The trend lines report the variation of particle spread as a function of the viscosity for a fixed particle diameter. In some cases, experimental tests are conducted with a certain particle diameter dispersion with a constant temperature value. In this case, no trend-lines are depicted because no-relation between particle spread and particle viscosity depend on the diameter. The data summarized in Fig. 7.25 are subdivided according to two lines: the vertical line divides rebound/adhesion regions according to critical viscosity method while the horizontal line divides rebound/adhesion regions according to energy-based model. From the comparison, it is clear the difference in the particle sticking prediction related to these models. From the present subdivision, two regions could be clearly detected according to the two models. The adhesion region is recognized using the simultaneous conditions of $\mu/\mu_c < 1$ and $\xi \geq 0.4$ for which both methods predict adhesion as a result of the particle impact. The other region, characterized by $\mu/\mu_c > 1$ and $\xi < 0.4$, is the region of particle rebound. For the other two combinations ($\mu/\mu_c > 1$; $\xi \geq 0.4$ and $\mu/\mu_c < 1$; $\xi < 0.4$) the two models are in disagreement, showing opposite predictions. It can be remarked that all data collected in Tab. 7.4 refer to experimental tests showing particle

adhesion. The overall analysis of the (μ/μ_c ;ξ) trends is reported in Fig. 7.26 where the viscosity ratio and the spread factor values are calculated according to the other six viscosity models considered. As highlighted, different viscosity models predict different results (see for example the test called Arkwright and Arkwright 3 with the reference of Tab. 7.4) that could differ from sticking to rebound results (see the predictions of S2 and WF). Therefore, the analyses reported in Fig. 7.25 and Fig. 7.26 show the effects of the viscosity model on the particle sticking probability as a function of particle composition. In the next sections, a detailed analysis of their mutual interaction is proposed according to material composition.

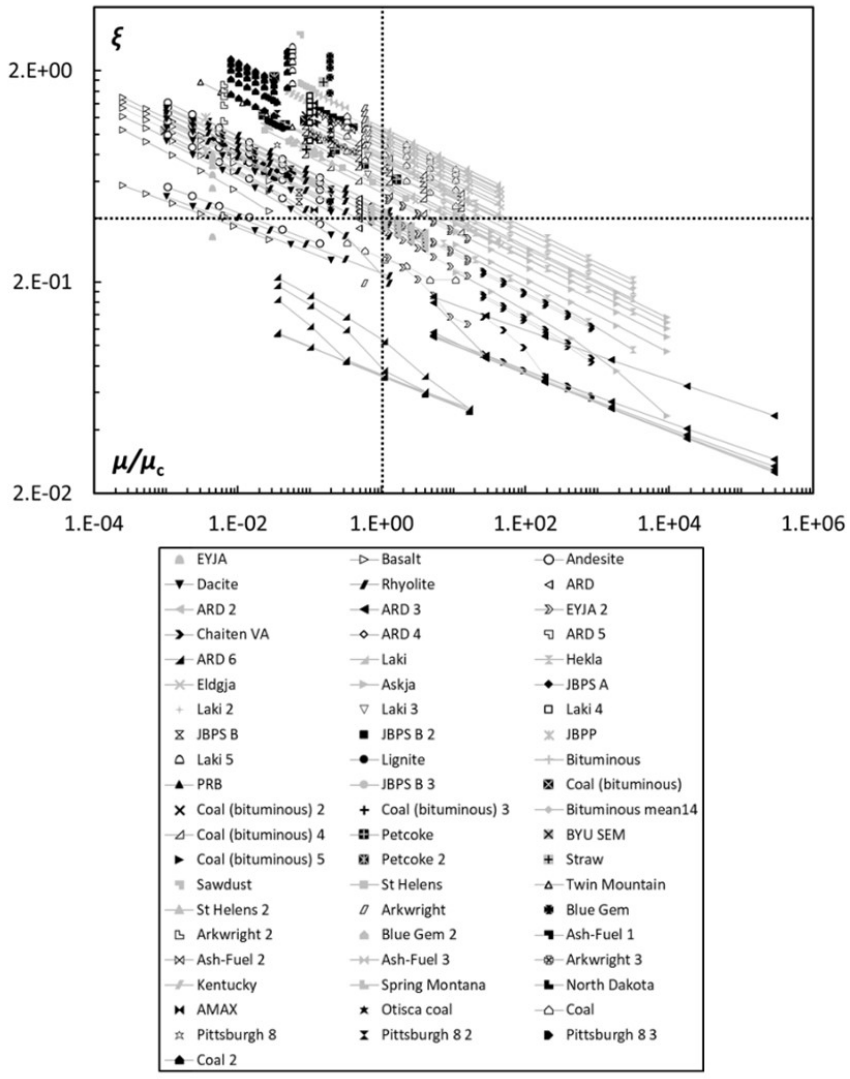

Figure 7.25: Model comparison critical viscosity/energy-based (data obtained using NPL model).The vertical line divides rebound/adhesion regions according to critical viscosity method while the horizontal line divides rebound/adhesion regions according to energy-based model (for an easier visualization of the chart, ARD 5 tests (characterized by μ/μ_c= 4.1e16 and ξ = 0.010 – 0.004) are not shown)

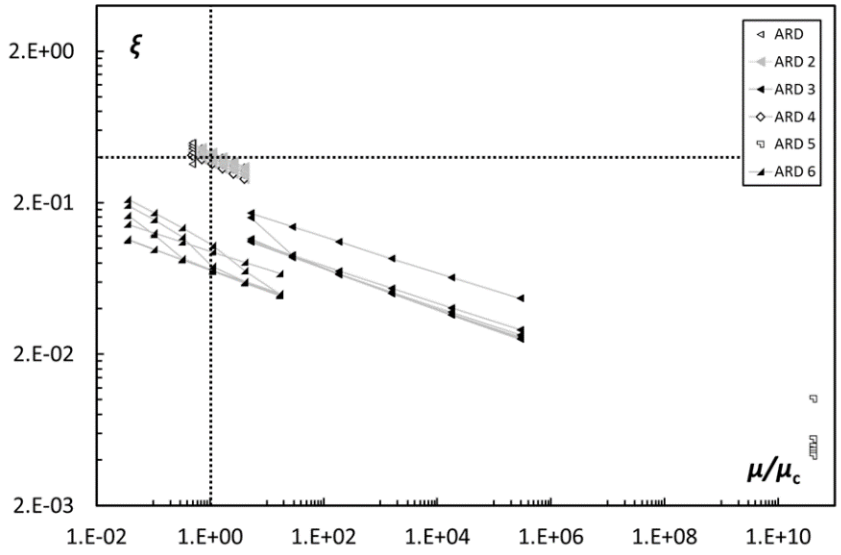

Figure 7.26: Model comparison critical viscosity/energy-based: a) S2, b) WF, c) S&T, d) RRLG, e) SDS and f) GRD. The vertical line divides rebound/adhesion regions according to the critical viscosity method while the horizontal line divides rebound/adhesion regions according to energy-based model

Arizona Road Dust tests

The first analysis is devoted to the ARD tests. This material is largely used in the experimental tests due to its ready availability and standardization (e.g. ISO 12103-1:2016 2016). This material is characterized by a high value of silica dioxide comprises in the range of (72.8 – 85.0) wt% and for this reason, in the present analysis, only the NPL viscosity model is applied to the six (6) experimental tests (see Tab. 7.4). Based on literature characterization, the same material (ARD) is characterized by three different compositions (see ARD, 2, 3, 4 with respect to ARD 5 and ARD 6 tests). In addition, due to the preparation processes (e.g. filtration), different particle diameter ranges characterize the literature value. Figure 7.27 shows the (μ/μ_c ;ξ) trends superimposed on the thresholds sticking condition (μ/μ_c=1 and ξ=0.4). As reported above, several tests belong to the rebound region for which both sticking models fail the prediction. In particular, even if the ARD and ARD 6 tests are conducted with the same particle temperature 1373 K and 1363 K respectively, the viscosity ratio is one order of magnitude different. The ARD 6 particles are characterized by a higher silica dioxide content that reflects in higher softening temperature (see Tab. 7.6). This mismatch between the actual experimental results and the model prediction can be explained with two reasons: (i) the sticking models are not able to represent all of the ARD deposition tests and/or (ii) for a specific test, the deposits are generated by a certain combination of particle diameter, temperature, and velocity. Therefore, even if the particle impact tests give particle adhesion, this results could be generated by a small portion of powder (in term of diameter) or by specific flow conditions (in term of temperature).

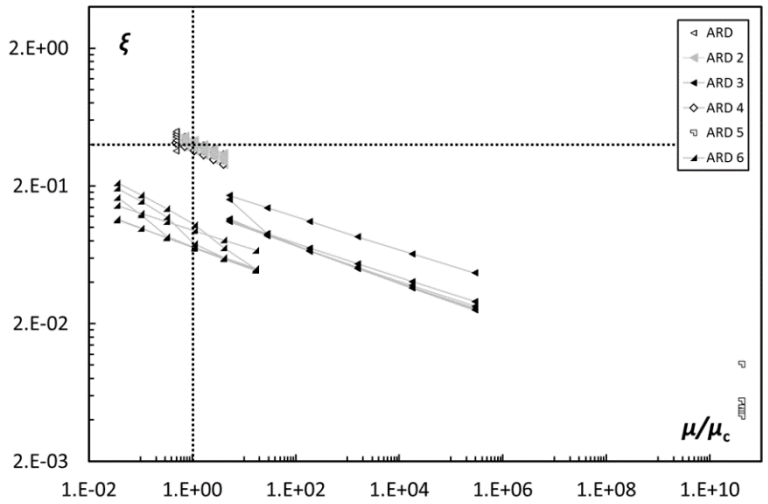

Figure 7.27: Model comparison critical viscosity/energy-based (data obtained using NPL model) for Arizona Road Dust tests

7.7.1 Volcanic ash tests

In this section, several specific analyses are realized considering volcanic ash tests. Volcanic ashes are characterized by a lower content of silica dioxide than ARD, allowing the application of three viscosity models (NPL, S&T, and GRD) matching the ash composition and the applicability limits. Figure 7.28 shows the (μ/μ_c ;ξ) trends superimposed on the thresholds sticking conditions (μ/μ_c=1 and ξ=0.4). Taking into consideration the critical viscosity method, the three viscosity models provide different predictions. Three tests (Eldja, EYJA 2 and Laki) belong to rebound region for which the critical viscosity method fails the prediction. Referring to the energy-based sticking method, it can be appreciated that NPL viscosity model gives higher spread factor values for the same test conditions and it seems the best viscosity model for predicting particle sticking with the energy-based method. By contrast, GRD model predicts the lowest values of particle spread-factor and for this reason appear not suitable for the energy-based model. Figure 7.29 reports a detailed analysis of Basalt and Andesite tests according to NPL, S&T, SDS, and GRD viscosity models. With the same criterion adopted earlier, the marker shape indicates the test while the color indicates the viscosity method. According to the volcanic ash classification, basalt and andesite are characterized by a different content of silica dioxide. With this comparison, clearly visible is the effects of the viscosity model on the sticking/rebound prediction. The NPL method gives higher values of particle spread factor, but at the same time, provides a viscosity ratio (μ/μ_c) prediction closer to the threshold μ/μ_c =1. The SDS model provides the lowest values of particle spread factor determining conflicting predictions in the case of energy-based sticking model. A specific analysis of the influence of viscosity methods and their effects on particle sticking prediction will be reported in the next section.

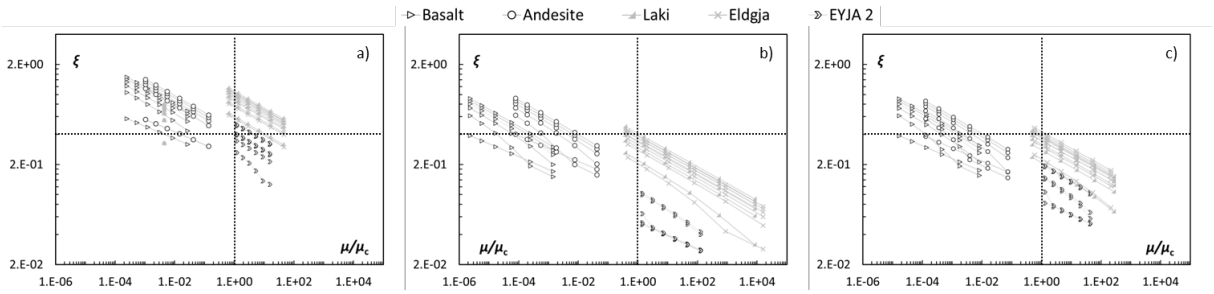

Figure 7.28: Model comparison critical viscosity/energy-based for volcanic ash tests: a) NPL, b) S&T and c) GRD

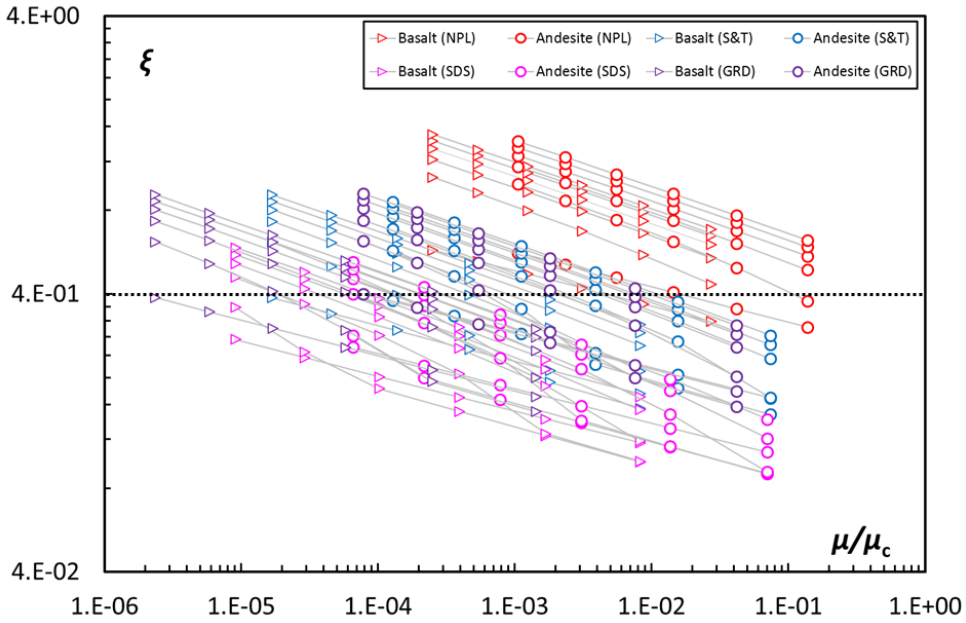

Figure 7.29: Model comparison critical viscosity/energy-based for Basalt and Andesite volcanic ash tests with NPL, S&T , SDS and GRD viscosity models

Influences of particle composition

Thanks to the availability of the particle chemical characterization (see Tab. 7.4) it is possible to analyze the different behavior of viscosity models and chemical composition on the sticking methods. In Fig. 7.30, 7.31 and 7.32 the application of different viscosity models to different tests are reported. The marker shape indicates the test while the color indicates the viscosity model. These comparisons are dedicated to discovering the relationship between model predictions and the influence of single constitutive element. The analysis reported in Fig. 7.30 considers Coal (bituminous) and North Dakota tests. These materials are characterized by the different content of silica dioxide and calcium oxide: Coal (bituminous) particles have about 50 %wt of SiO_2 and 9.5 %wt of CaO while North Dakota particles have about 20 %wt of SiO_2 and 23 %wt of CaO. As can be seen from the graph, similar effects on the viscosity ratio and spread factor values are generated by the viscosity models. The NPL formulation determines a viscosity ratio (μ/μ_c) prediction closer to the threshold μ/μ_c =1 for the same test condition. This effect is

more visible in the case of North Dakota test characterized by a lower amount of SiO_2 and a higher amount of CaO. Given that the present analysis, for a particle material similar to North Dakota, SDS model appears more suitable for calculating particle adhesion according to the critical viscosity method. Opposite results can be obtained with the reference of the energy-based method. North Dakota tests appear closer to the threshold value ($\xi = 0.4$) if the particle viscosity is calculated with the SDS model.

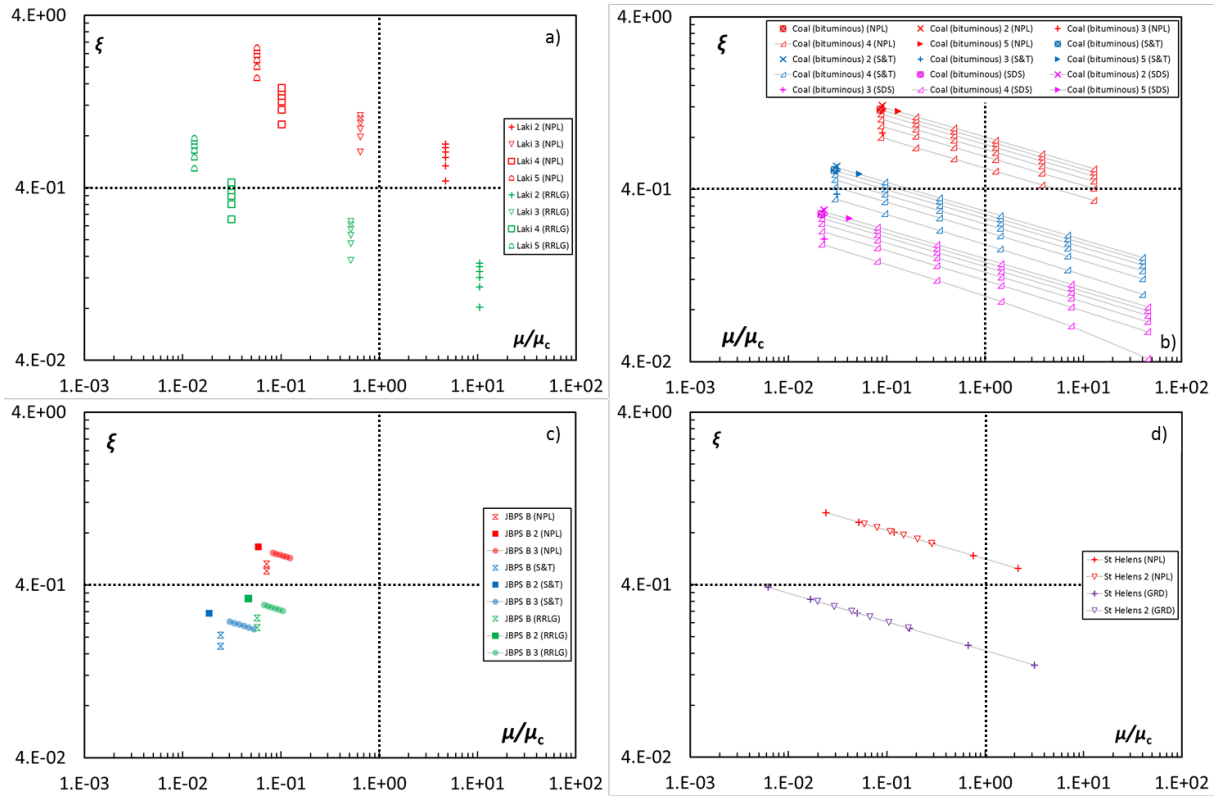

Figure 7.30: Model comparison critical viscosity/energy-based for Coal (bituminous), 2, 3, 4, 5 and North Dakota tests (NPL and SDS viscosity models) characterized by a different content of silica dioxide and calcium oxide

The analysis reported in Fig. 7.31 considers JBPS B, 2, 3 and Straw tests. These materials are characterized by the different content of potassium oxide: JBPS B particles have about 1.6 %wt of K_2O while Straw particles have about 23.4 %wt of K_2O. Both materials have a similar content of silica dioxide in the range of 48 – 50 % wt Considering the critical viscosity model, the NPL and RRLG predictions appear very similar for the JBPS B particles (lower content of K_2O) while, in the case of Straw particles (higher content of K_2O) the two predictions appear not so close. Therefore, NPL and RRLG models work in a similar way in the presence of lower content of potassium oxide. Regarding the S&T model, the variations between its predictions and the other obtained with NPL and RRLG methods appear not so influenced by the different chemical composition of JBPS B, and Straw particles.

The analysis reported in Fig. 7.32 considers JBPS B, 2, 3 and Arkwright, 2, 3 tests. These materials are characterized by the different content of aluminum oxide and silica dioxide: JBPS B particles have about 50 %wt of SiO_2 and 12 %wt of Al_2O_3 while

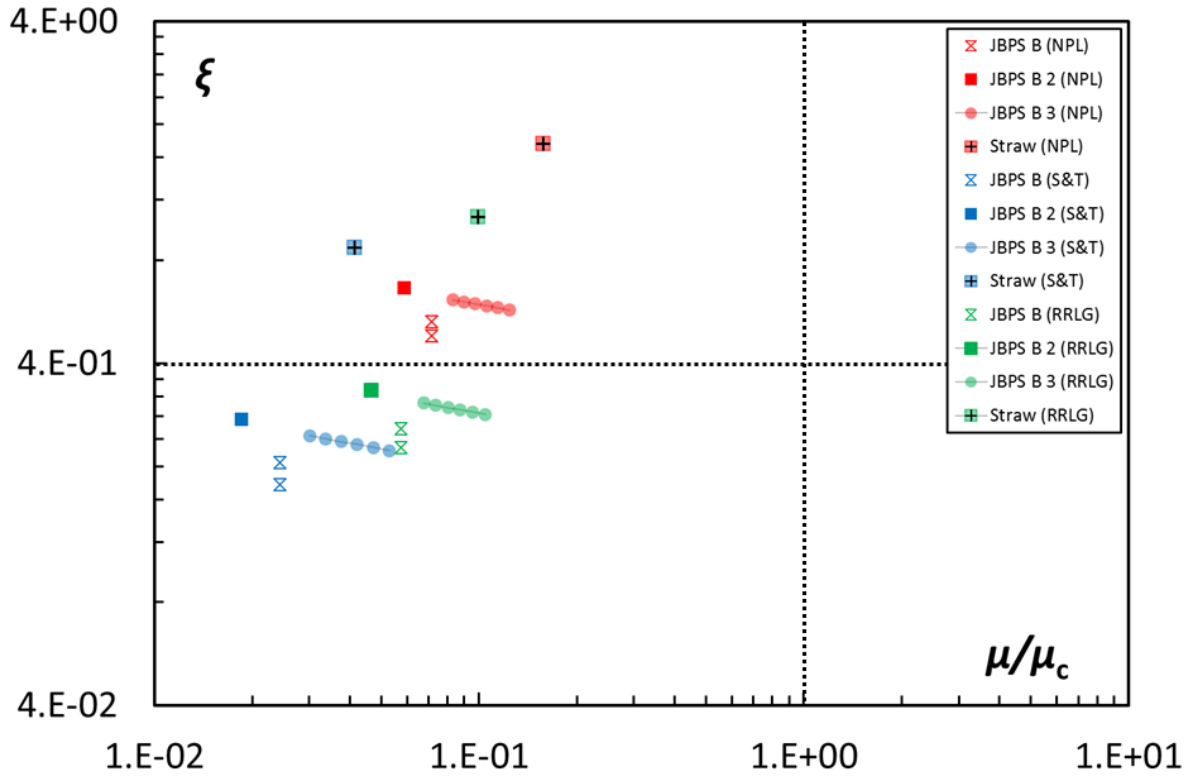

Figure 7.31: Model comparison critical viscosity/energy-based for JBPS B, 2, 3 and Straw tests (NPL, S&T, and RRLG viscosity models) characterized by a different content of potassium oxide

Arkwright particles have about 48 %wt of SiO_2 and 25 %wt of Al_2O_3. In this case, no particular effects can be highlighted due to the presence of a different content of aluminum oxide. The S&T model better performs the sticking predictions in the case of a critical viscosity model. The behavior of the viscosity model on the particle sticking model will be described in the next section.

Critical analysis of the viscosity models

Figure 7.33 reports four analyses dedicated to four different tests (Laki, Coal (bituminous), JBPS B, and St. Helens tests) for which the applicable viscosity models (according to the proper applicability limits) are used to calculate the viscosity ratio and particle spread factor. Also, in this case, the marker shape indicates the test while the color indicates the viscosity method. Regarding the energy-based model, and thus the spread factor and its threshold value (ξ= 0.4), NPL model predicts the highest values in all cases. The other models (S&T, RRLG, SDS, and GRD) provide lower values of ξ with unavoidable effects on the particle sticking prediction. For example, tests for which the NPL model predicts particle sticking, RRLG predicts particle rebound (see for example Laki 3 and JBPS B 3 tests) or again, by comparing the prediction provided by NPL and S&T models in the case of tests with JBPS B particles. As mention in the previous sections, NPL model determines closer viscosity ratio value to the threshold (μ/μ_c=1) in the sticking

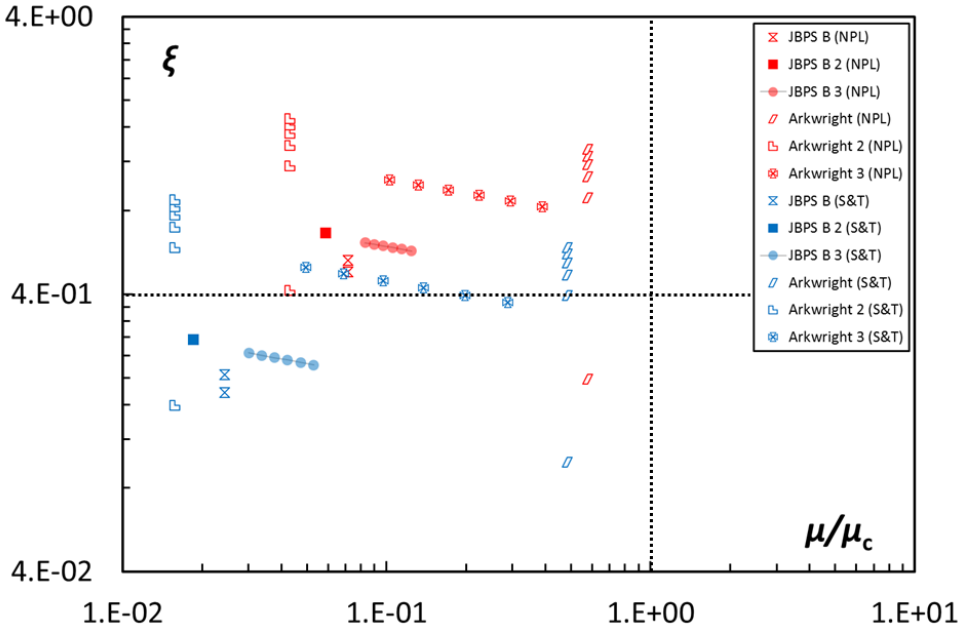

Figure 7.32: Model comparison critical viscosity/energy-based for JBPS B, 2, 3 and Arkwright, 2, 3 tests (NPL and S&T viscosity models) characterized by a different content of silica and aluminum dioxides

region but, as can be seen from Fig. 7.33a-b (Laki and Coal (bituminous) tests) the effect affects also the rebound region. Considering the data distribution according to the abscissa, the viscosity ratio values provided by the NPL model are the most squeezed to μ/μ_c =1. This behavior is related to the formulation of the viscosity-temperature relation. Taking into consideration the formulas reported for each model (see 7.8), the viscosity values are based on specific and not univocal data extrapolation. Figure 7.34 reports a sensitivity analysis of the relation viscosity-temperature provided by the seven (7) models considered in the present analysis. In order to improve the readability of the graph, a logarithmic scale is used for the ordinate axis. Each trend refers to the relationship between temperature and a normalized viscosity value (M) obtained considering the magnitude of the model's constants. As highlighted by the trends, each model is characterized by a different slope and thus, different sensitivity to the temperature. NPL and S2 models are less sensitive to a temperature variation while other models (e.g. WF and GRD) show a strong dependence to the temperature value. By increasing the temperature value of two (2) times, the normalized viscosity values increase by thirty (30) orders of magnitude.

This analysis shows the implication of particle temperature estimation or measurement as well as the interaction between viscosity and sticking models in the prediction of particle adhesion and/or rebound. Summarizing the outcomes of the analysis, Tab. 7.8 reports the model equations and, in addition, the basis on that each model is based. These two element of information, together with the sensitivity analysis reported in this work, could be useful for the proper selection of the viscosity model. Beyond the NPL model, that is based on the optical basicity, the other methods are based on specific material, that could be used as a reference for the proper application of the model. For example, the RRLG

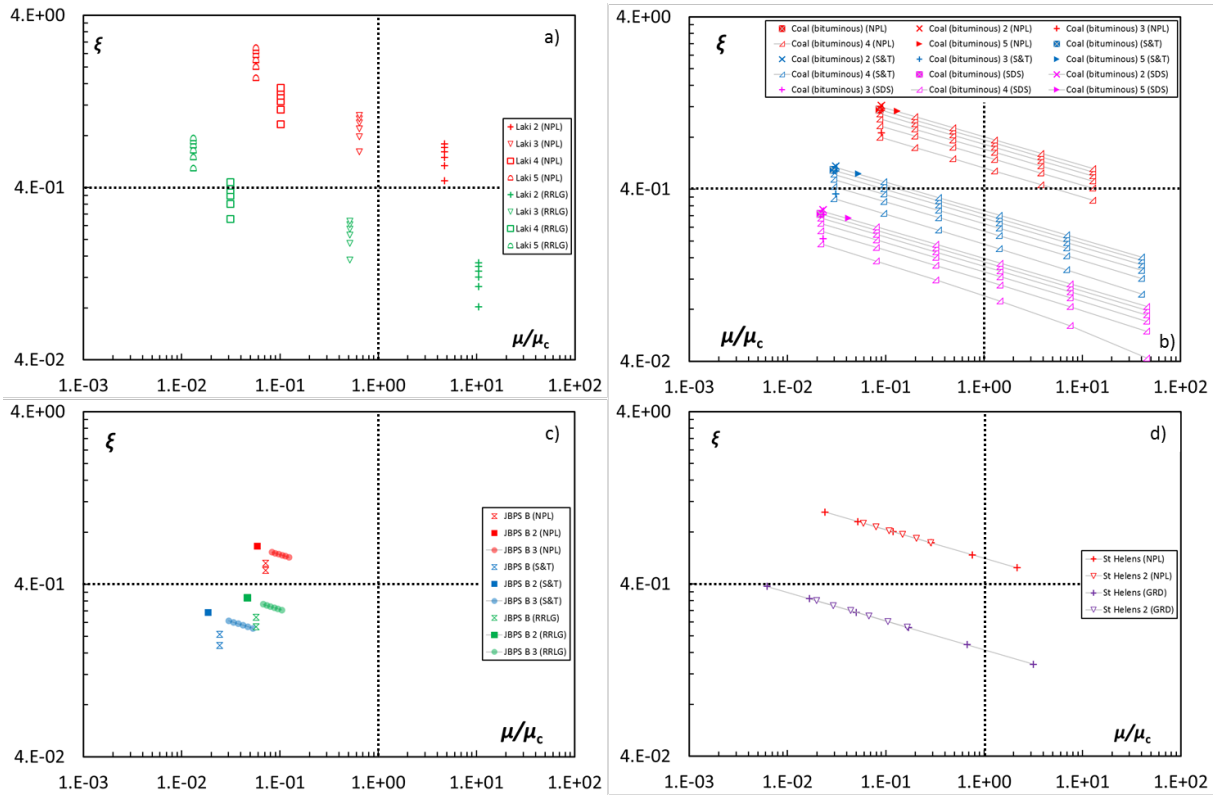

Figure 7.33: Model comparison critical viscosity/energy-based: a) Laki 2, 3, 4, 5 with NPL and RRLG models, b) Coal (bituminous), 2, 3, 4, 5 with NPL, S&T, and SDS models, c) JPBS B, 2, 3 with NPL, S&T and RRLG models and d) St. Helens, 2 with NPL and GRD models.

model is more suitable for slags instead of GRD, that is more appropriate for volcanic ashes. Other considerations can be done taking into consideration the model equation. The strong correlation between viscosity and temperature is different among the models, as reported in Fig. 7.34, and, for this reason, models characterized by steeper viscosity-to-temperature trends are more suitable for the cases in which the particle experience higher temperature gradient (such as gas turbine nozzle equipped with cooling holes). Finally, if the sticking model is based on the energy dissipation, the viscosity model prediction is fundamental in order to estimate the proper energy dissipation. In this case, a viscosity model that predicts lower viscosity values, for the same particle characteristics, is suitable for predicting the particle adhesion with a wider confidence band. Besides the dedicated experimental test that represents the greatest method used to discern the actual result, it could be useful to find a new method, based on the present evidence, able to represent the combined effects related to particle deformation and its material characteristics.

7.8 Dimensional analysis

Given the literature data related to different research fields, the analysis of non-dimensional numbers characterizing the physic of the present phenomenon, may represent

Table 7.8: Viscosity models: NPL from Mills and Sridhar (1999), S2 from Hoy et al. (1964),WF from Watt and Fereday (1969), S&T from Sreedharan and Tafti (2011),RRLG from Riboud et al. (1981), SDS from Streeter et al. (1984) and GRD from Giordano et al. (2008)

	Constitutive equations		Basis
NPL	$\ln \mu = \ln A_{NPL} + \frac{B_{NPL}}{T}$	(7.31)	Based on optical basicity values
S2	$\log \mu = 4.468 \left(\frac{\varsigma}{100}\right)^2 + 1.265\frac{10^4}{T} - 8.44$	(7.32)	Data regression based on sixty-two (62) samples of slags
WF	$\log \mu = \frac{m_{WF}\ 10^7}{(T-423)^2} + c_{WF}$	(7.33)	Data regression based on one hundred and thirteen (113) ashes samples
S&T	$log\left(\frac{\mu}{T}\right) = A_{S\&T} + \frac{10^3 B_{S\&T}}{T}$	(7.34)	Based on Non-Bridging Oxygen (NBO) values
RRLG	$log\left(\frac{\mu}{T}\right) = A_{RRLG} + \frac{10^3 B_{RRLG}}{T}$	(7.35)	Checked against twenty-two (22) industrial continuous casting slag
SDS	$\ln\left(\frac{\mu}{T}\right) = \ln A_U + \frac{10^3 B_U}{T} - \Delta$	(7.36)	Checked against seventeen (17) coal slags
GRD	$\ln \mu = \ln A_{GRD} + \frac{B_{GRD}}{T - C_{GRD}}$	(7.37)	Calibrated by means of 1774 pairs of temperature-viscosity volcanic ashes silicate melts

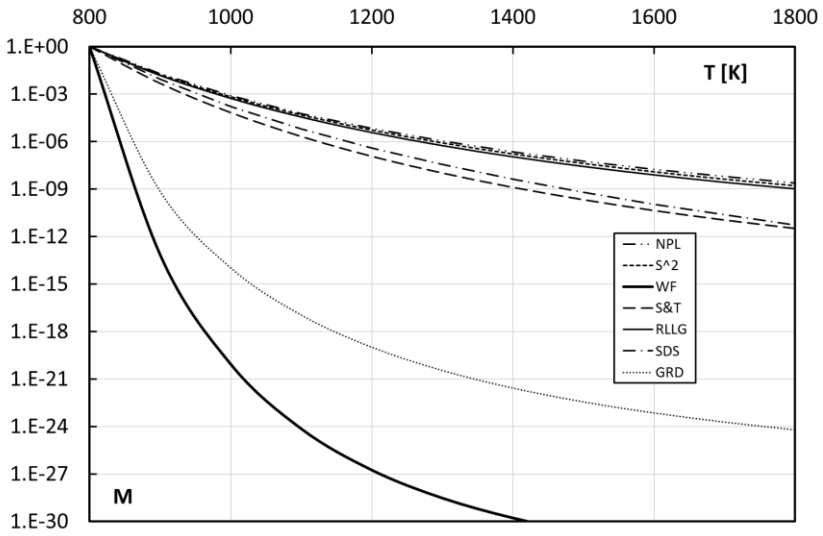

Figure 7.34: Sensitivity analysis of viscosity models

Table 7.9: Pi Theorem: set of independent variables

#	Independent variables	Symbols	{kg m s}
1	Particle density	ρ_p	$\{\text{kg m}^{-3}\}$
2	Particle diameter	d_p	{m}
3	Particle velocity	u_p	$\{\text{m s}^{-1}\}$
4	Dynamic viscosity	μ	$\{\text{kg m}^{-1}\ \text{s}^{-1}\}$
5	Surface tension	γ	$\{\text{kg s}^{-2}\}$
6	Young modulus	E	$\{\text{kg m}^{-1}\ \text{s}^{-2}\}$

a valid support for improving the comprehension of the particle impact behavior. Starting from the particle characteristics involved in the three sticking models considered in the present review, the Buckingham Pi Theorem Buckingham (1914) is applied. The relationships between the particle sticking capability and several particle characteristics by means of non-dimensional groups are reported in the first part of the present section. From the results and the literature models reported above (critical viscosity, critical velocity, and energy-based models), six (6) independent variables are identified. The set of independent variables is reported in Table 8 where they are express in terms of its fundamental dimensions.

As can be seen from Tab. 7.9 particle temperature is not included in the set of independent variables. The effect of the temperature on the particle sticking phenomenon is included in the viscosity and Young modulus variation. The first non-dimensional group neglects the surface tension (capillary forces) contribution and considers the effect of the particle temperature by particle Young modulus and particle viscosity

$$\Pi_1 = \rho_p d_p^2 \mu^{-2} E^1 = (\rho_p d_p \mu^{-2})(d_p E) \tag{7.38}$$

where the dimensional group $(d_p E)$ characterizes the critical viscosity model while the first term can be processed and expressed as a function of non-dimensional number Z (see

Eq. (7.3))

$$\Pi_1 = (d_p E)\frac{1}{(\gamma Z^2)} \tag{7.39}$$

demonstrating how the surface tension, and thus, the capillary force has to be included in the particle sticking analysis. The second group is obtained by considering particle viscosity the only structural characteristic that influences the particle sticking behavior

$$\Pi_2 = \rho_p^{-2} d_p^{-2} u_p^{-3} \mu^1 \gamma^1 = (\rho_p^{-1} d_p^{-2} u_p^{-1} \mu^1)(\rho_p^{-1} d_p^{-2} u_p^{-2} \gamma^1) \tag{7.40}$$

where the two non-dimensional groups correspond to the particle Reynolds number and particle Weber number

$$\Pi_2 = \frac{1}{(ReWe)} \tag{7.41}$$

Therefore, excluding the particle Young Modulus, particle Reynolds number and particle Weber number appear suitable for representing the particle sticking behavior. Thanks to the data related to particle dimension, density, viscosity and surface tension it is possible to calculate the particle Reynolds number and the particle Weber number, defined according to eqs. (7.1) and (7.2) supposing that the particle velocity is equal to the gas velocity. Therefore, starting from the literature data reported in Tab. 7.4, the viscosity and surface tension values reported in Fig. 7.10 and Fig. 7.21 respectively, Fig. 7.35 reports the logarithmic chart with the relationship of particle Reynolds number and particle Weber number. As mentioned, the calculation is performed using the viscosity values obtained with the NPL model. The trends related to the mono-parametric variation of particle diameter, velocity and temperature are traced. In several cases, the experimental tests are carried out using a powder sample characterized by a specific size distribution. For this reason, the data are aligned with the particle-diameter trend. The variation of the temperature determines the variation of particles properties like viscosity and surface tension. Comparing this amplitude with the particle viscosity variation proposed in Fig. 7.10, the majority of experimental tests related to particle deposition on gas turbine hot section, are located in a specific region in ten (10) orders of magnitude and four (4) orders of magnitude wide according to Reynolds and Weber number respectively. The test named ARD 5 is characterized by the lowest temperature (see Tab. 7.4) and for this reason, the particle Reynolds number assumes the lowest values. For the sake of clarity, this test is not reported in Fig. 7.35. Following the conceptual framework reported in Fig. 7.1, non-dimensional numbers allow the generalization of the present data and the comparison between the present results with those obtained in other fields of research. Comparing the We-Re regions involved in the gas turbine particle adhesion with the We-Re regions related to the analysis of printable fluids Srinivasachar et al. (1991), see Figure 7.35, some similarities can be noticed. The interactions between individual drops and the substrate as well as between adjacent drops are important in defining the resolution and accuracy of the printing process. The accuracy of the printing process is limited by the issues related to the droplet spread and/or overlap processes of adjacent drops. In particular, no-data related to gas turbine conditions belong to the region called Satellite

droplets, in which the primary drop is accompanied by a large number of satellite droplets, but almost all data belonging to the region called Too viscous. According to the literature findings Srinivasachar et al. (1991), the majority of the gas turbine fouling data have shown little tendency to create satellite droplets and splashing. This means that, for these experimental test conditions, particles are very viscous and their deformation during the impact is too low to break themselves up. In this condition and considering the chemical composition of a particle that characterizes the fouling phenomenon, the adhesion could be promoted by low-melting substances which performed a sort of glue action at the impact region Ahluwalia et al. (1986); Gupta et al. (2002); Nagarajan and Anderson (1988). Given this , particle sticking models have to consider the different interaction between particle and substrate according to the chemical composition of the particle, especially when the impact conditions imply the modification of the surface interaction. Finally, an interesting aspect is related to the limit of particle Weber number. As reported by Srinivasachar et al. (1991), for the condition We < 4, the energy is insufficient to generate suitable droplet for the printing process. This means that the sticking process does not take place and in fact, considering the We-Re plane reported in Fig. 7.35, only two test conditions, related to the smallest particle diameter, of the tests named ARD 3 and ARD 5 belong to this region. According to the literature review reported in Suman et al. (2017), these tests are carried out for studying the sticking phenomenon in cooling holes, and they are characterized by the lowest temperature values. In the light of these test conditions, the sticking phenomena detected by the Authors for these tests, are probably related to the influence of external parameter, as for example, flow structures.

Similarities with the printable fluids highlight the possibility to use non-dimensional numbers to generalized particular experimental tests (i.e. gas turbine particle deposition) findings possible original explanations of such phenomena. In this analysis, specific information obtained a priori about splashing phenomena, could be useful for settings the best experimental test avoiding inaccuracy or misinterpretation of the results. The overall analysis of the We-Re trends is reported in Fig. 7.36 where the particle Reynolds numbers are calculated according to the six (6) viscosity models considered (S2 , WF, S&T, RRLG, SDS and GRD). The regions related to the printable fluids Srinivasachar et al. (1991) are also reported.

As mentioned, the We-Re relationship seems to be strongly correlated in the particle deposition phenomena. This result is line with the literature, where it is reported how the contemporary use of Weber number and Reynolds number allows the modeling of both surface and viscous behaviors Xu et al. (1998). Starting from this consideration, non-dimensional parameters allow the definition of the type of regime involved in particle impact. It may happen that molten or quasi-molten particle impacts the blade surface, deforming itself according to Fig. 7.2. Assuming a certain degree of similarity, when a droplet (e.g. semi-molten or molten particle) impacts a wall, it may result in three different conditions: rebound, breakup or adhesion. According to the approach adopted in Xu et al.

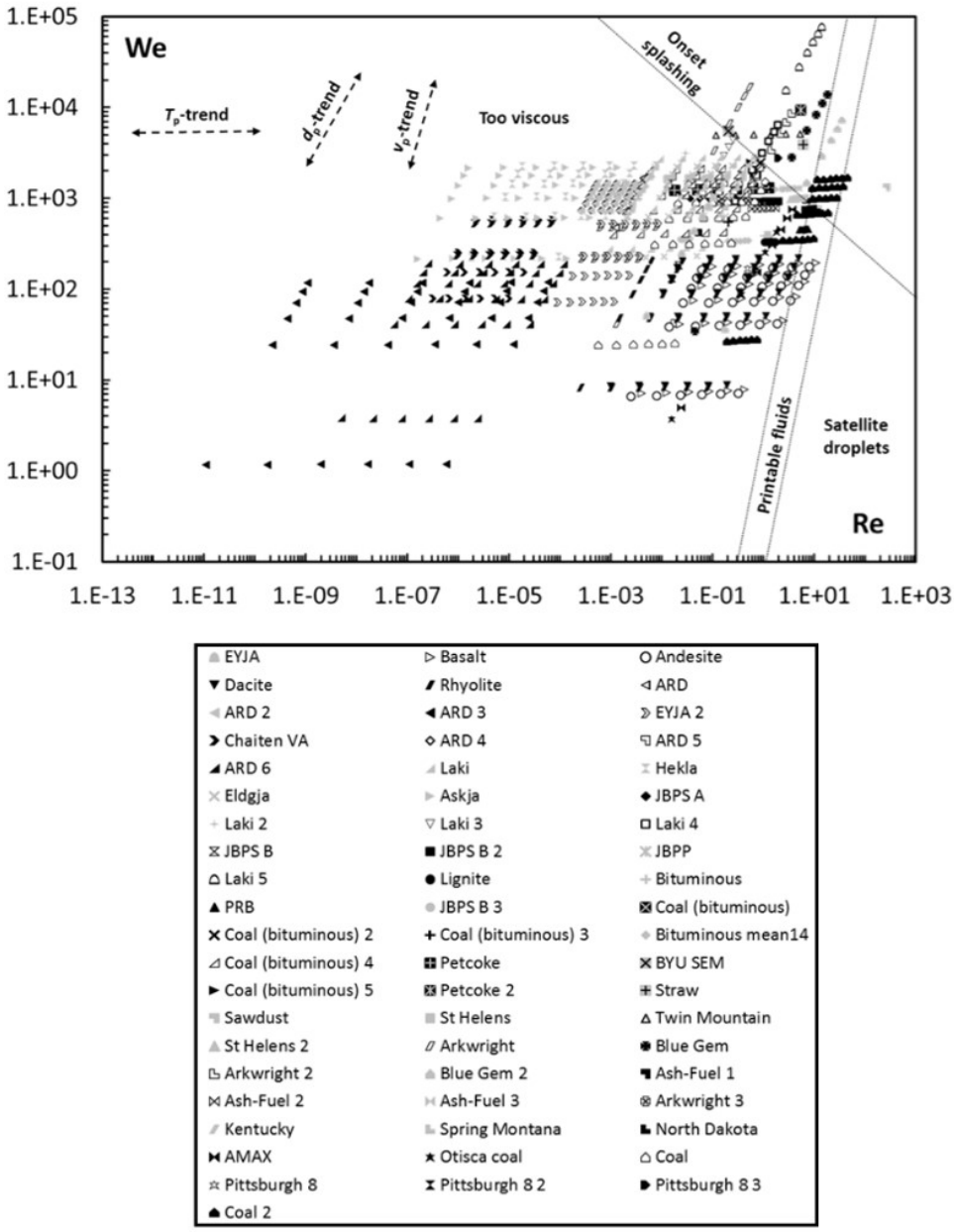

Figure 7.35: Particle Weber number as a function of the particle Reynolds number (particle viscosity values were obtained using the NPL model) where for an easier visualization of the chart, ARD 5 tests (characterized by Re = 6.8e-18 – 1.4e-16 and We = 3.5e-1 – 70) is not shown: a) traced trends refer to the variation of particle diameter, particle velocity, and particle temperature, while We-Re regions related to the analysis of printable fluids Srinivasachar et al. (1991) are superimposed

(1998) the rebound condition is promoted by the elastic forces, the breakup condition is due to the break of the interconnection forces and finally, the adhesion condition is reached when the droplet deforms itself (spreading process), generating a sort of film on the surface by a dissipative process due to its viscosity force. Thus, the comprehension of the spreading process assumes a paramount importance for particle sticking modeling Schiaffino and Sonin (1997). In order to do this, particle Ohnesorge number (see Eq. (7.3)) is used coupled with particle Weber number in order to define the particle spreading process Schiaffino and Sonin (1997). Particle Weber number is related to the force that

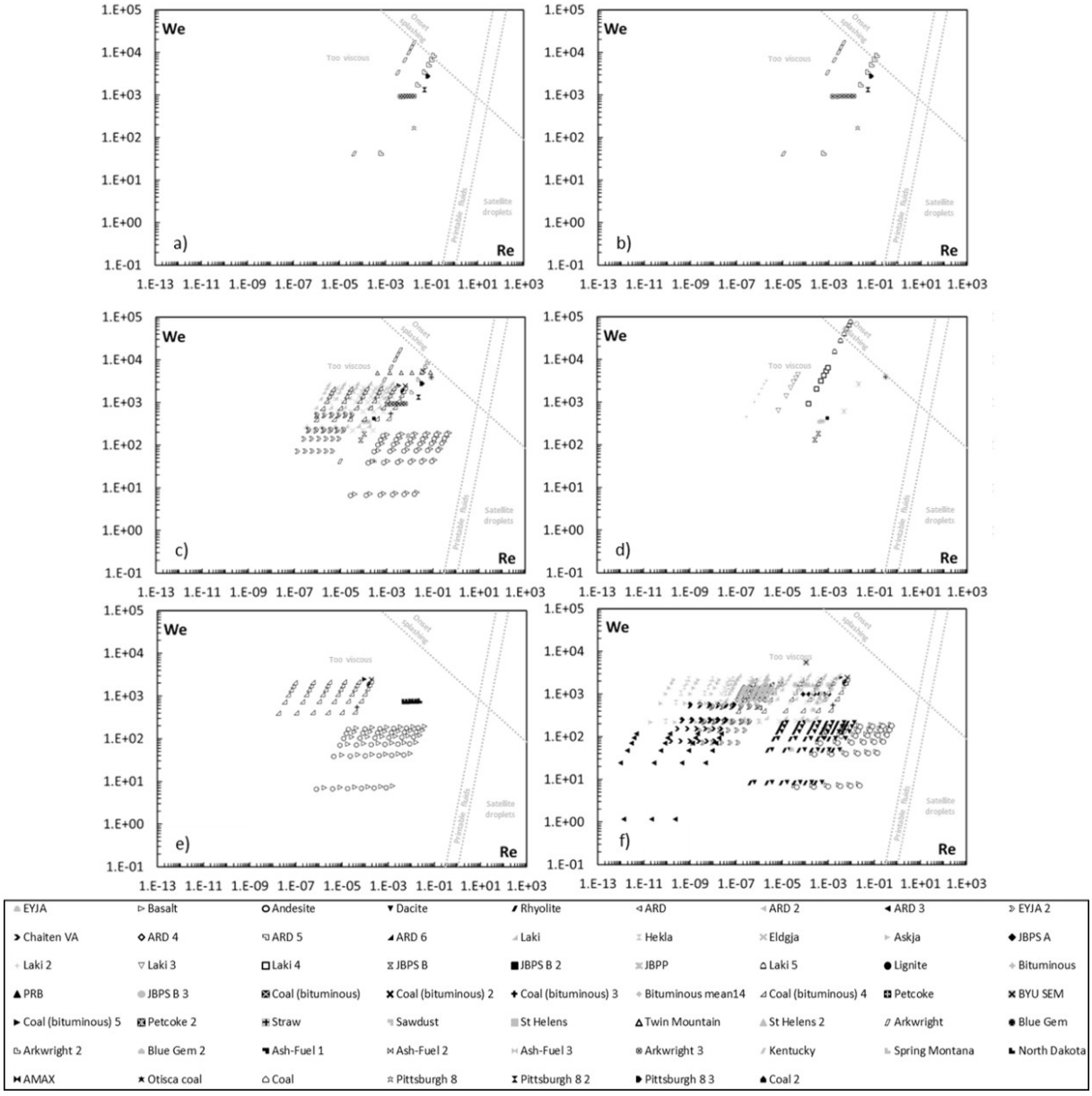

Figure 7.36: Particle Weber number as a function of the particle Reynolds number according to viscosity models: a) S2, b) WF, c) S&T, d) RRLG, e) SDS and f) GRD. Traced We-Re regions are related to the analysis of printable fluids by Srinivasachar et al. (1991) superimposed

7

generates particle spread: at higher We the force is due to particle velocity and particle diameter while at lower We the force is due to surface tension. Particle Ohnesorge number is related to the force that opposes particle spread: at higher Z the force is due to the viscosity, while at lower Z the force is due to the inertia. Figure 7.37 shows the chart We-Z defined according to the literature Schiaffino and Sonin (1997), in which the data reported in Tab. 7.4, are superimposed (the viscosity values are calculated according to the NPL model). Present data belong to the region characterized by highly viscous particle and with the impact-driven particle spread. Therefore, the particle kinetic energy works against viscous force. In this case, capillary force, and then, surface tension, does not influence the particle spread Schiaffino and Sonin (1997). At the same time, the

region called Impact driven puts the attention on phenomena such as satellite droplets and splashing which may influence the particle impact process in a gas turbine. In this case, the first particle impact generates negligible deposits but generates several smaller semi-molten particles with greater capability to stick due to their low energy content. Analogous results can be obtained using the six (6) viscosity models considered reported in Fig. 7.38 This analysis allows the comparison between the particles behavior involved in gas turbine fouling and other research fields. The non-dimensional analysis confirms the importance of particle viscosity, but at the same time, highlights the relationship with particle velocity and diameter. Viscous force act related to particle temperature but the particle spread is driven also by particle kinetic energy.

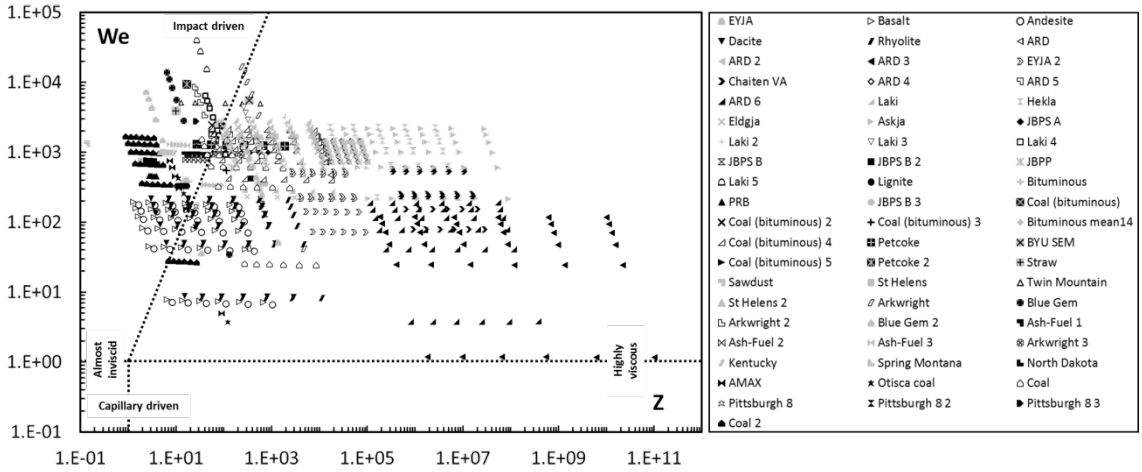

Figure 7.37: Definition of the particle spread regime using non-dimensional numbers We-Z (particle viscosity values was obtained using the NPL model

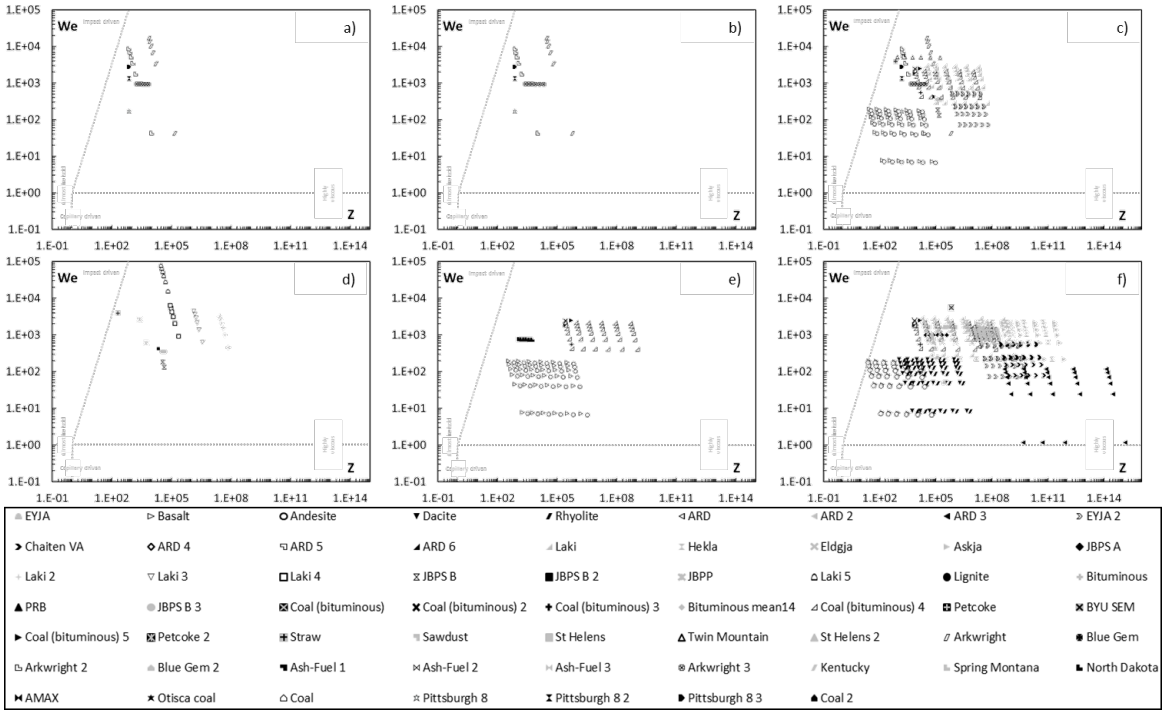

Figure 7.38: Definition of the particle spread regime using non-dimensional numbers We-Z according to viscosity models: a) S2, b) WF, c) S&T, d) RRLG e) SDS and f) GRD

7.9 Generalization of the particle impact behavior

Neither the critical viscosity/velocity nor the energy-based methods appear able to predict particle sticking for the overall particle adhesion tests adopting a general approach. The mismatch between the prediction and the actual results of the tests can be explained by two reasons. For a specific test, deposits are generated by a certain combination of particle diameter, temperature, and velocity and therefore, by considering the overall variation of these quantities during tests, some conditions may generate particle rebound. At the same time, particle characteristics such as viscosity and softening temperature are difficult-to-be-represented by a single model able to conceive a wide range of particle chemical compositions. Summing up, a particle impact test reporting adhesion can be the outcome of multiple superimposed effects in terms of particle size, temperature and impact conditions. In the last part of the present work, the generalization of particle impact behavior in a gas turbine is proposed. Non-dimensional groups listed above (Weber, Reynolds, and Ohnesorge numbers), allow for the generalization of particle impact/deposition data but describe only the effects of the impact into particle spread and no information about sticking phenomenon can be gathered. In order to give a perspective view regarding particle adhesion, the data reported in Tab. 7.4 have to be accompanied by experimental results related to the other phenomena related to particulate impact. During gas turbine operation, surface erosion, particle adhesion, and particle splashing could affect hot sections of the machinery. Erosion and fouling are generated by the same type of particles (especially rock-derived particles and coal ashes) and could take place under different or even the same conditions (such as temperature, velocity, size). Therefore, the data related to particle deposition are compared with literature data related to erosion Shinozaki et al. (2013); Tabakoff et al. (1991); Tabakoff; Kotwal and Tabakoff (1980) and splashing phenomena Dean et al. (2016). In Tab. 7.10, the data associated with erosion tests are collected in the same way of the previous ones. Particle dimensions, density, velocity, temperature, and composition are reported as well as the softening temperature calculated applying Eqs (19 – 23). These tests refer to hot erosion measurements realized using dedicated test benches. It is possible to notice how erosion tests are characterized by lower temperature with respect to those involved in particle deposition tests. In particular, Laki 6 test is very similar to the Laki 5 test (see Tab. 7.4) but it is characterized by lower particle temperature. In Tab. 7.11 data associated with splashing tests are collected. These materials are also among the ones reported in Tab. 7.4 and used for the deposition tests, but in this case, tests and particle dimensions are different. These tests consist in a spherical-pellet of volcanic ash projected at high velocities towards a substrate. Particle splashing is evaluated checking the digital images taken during the particle impact during the test Dean et al. (2016). In this case, particle splashing is the only effect known and no data related to erosion issues are reported. All materials refer to three different volcanic ashes and the particle size involved in this tests is higher with respect to the previous one. Also, in this case, the softening temperature

Table 7.10: Particle erosion data. Material composition in term of weight fraction

	Authors	Material	d [μm]	ρ [kg/m3]	v [m/s]	T [K]	Tsoft [K]	t	Na2O	K2O	CaO	MgO	SiO2	Al2O3	TiO2	Fe2O3
'13	Shinozaki et al.	Laki 6	20–100	2400	115	983	1258	T	1.2	0.1	7.8	3.1	47.2	11.6	3.7	25.2
'92	Tabakoff et al.	Coal ash	15	2900	366	800 – 1089	1288	C	0.0	0.0	0.0	0.9	48.1	21.2	0.0	20.1
'84	Tabakoff	CG&E	38.4	2900	240	422 – 922	1288	C	0.0	0.0	0.0	0.9	48.1	21.2	0.0	20.1
		CG&E 2	38.4	2900	228	756	1288	C	0.0	0.0	0.0	0.9	48.1	21.2	0.0	20.1
'80	Kotwall and Tabakoff.	Kingston	15, 28	2900	228	756	1408	C	0.2	2.1	1.3	1.0	54.4	28.6	0.5	10.1

Table 7.11: Particle splashing data. Material composition in term of weight fraction

	Authors	Material	d [μm]	ρ [kg/m3]	v [m/s]	T [K]	Tsoft [K]	t	Na2O	K2O	CaO	MgO	SiO2	Al2O3	TiO2	Fe2O3
		Laki 7	6500	2000	106	1473	1161	C	4.0	1.0	11.0	5.0	50.0	12.0	3.0	14.0
2016	Dean et al.	Hekla 2	6500	1500	106	1473	1290	C	3.0	2.0	3.0	0.0	65.0	15.0	0.5	6.0
		Eldgja 2	6500	1900	106	1473	1161	C	3.0	0.5	11.0	6.0	50.0	13.0	3.0	16.0

values are calculated applying Equations (7.17) to (7.21).

The first analysis shows the plane We-Z, Fig. 7.39, populated by the data reported in Tab. 7.4, Tab. 7.10 and Tab. 7.11 (the viscosity values are calculated according to the NPL model). Data related to particle deposition, shown in details in Fig. 7.37, are reported using grey dots in order to highlight the differences with the erosion and splashing data. As shown in Fig. 7.39, splashing data completely belong to the region called impact driven, while erosion data belong to the highly viscous region characterized by very high values of particle Ohnesorge number. This non-dimensional analysis shows quite different impact regimes involved in particle deposition and particle erosion/splashing. In the latter cases, the particle is characterized by size and/or velocity much more high with respect to the adhesion case. Higher particle Weber number implies a spread regime driven by the dynamic pressure gradient while lower values of particle Ohnesorge number implies a resistance force driven by particle inertia Schiaffino and Sonin (1997). Erosion data are collected at a lower temperature with respect to the splashing ones, and as shown in Fig. 7.39, viscous effects are much greater and the inertia force is less. Therefore, erosion phenomenon seems to be characterized by a particular combination of particle kinetic energy and viscosity able to determines particle impact with material removal from the target, without adhesion. Even if this distinction appears suitable for adequately representing the erosion occurrences, it is important to note that, especially for higher temperature, erosion issues are related also to the substrate characteristics Tabakoff. The concurrent presence of erosion and deposition has been found also in the numerical analyses proposed in 4.2. From this analysis, a quite clear pattern can be recognized: deposition, erosion and splashing data belong to different regions in the We-Z plane, with the particular characteristic that deposition and erosion regions have in common the values of particle Weber number (in this case, the most discerning parameter is the particle viscosity), while deposition and splashing regions have in common the values of particle Ohnesorge number (in this case, the most discerning parameter is the particle velocity). Therefore, the combination of particle kinetic energy and surface tension seems to well describe the deposition, erosion and splashing phenomena.

Starting from these considerations, two (2) new non-dimensional groups are proposed. Based on the Pi Theorem proposed in the previous section, by imposing a proper set of

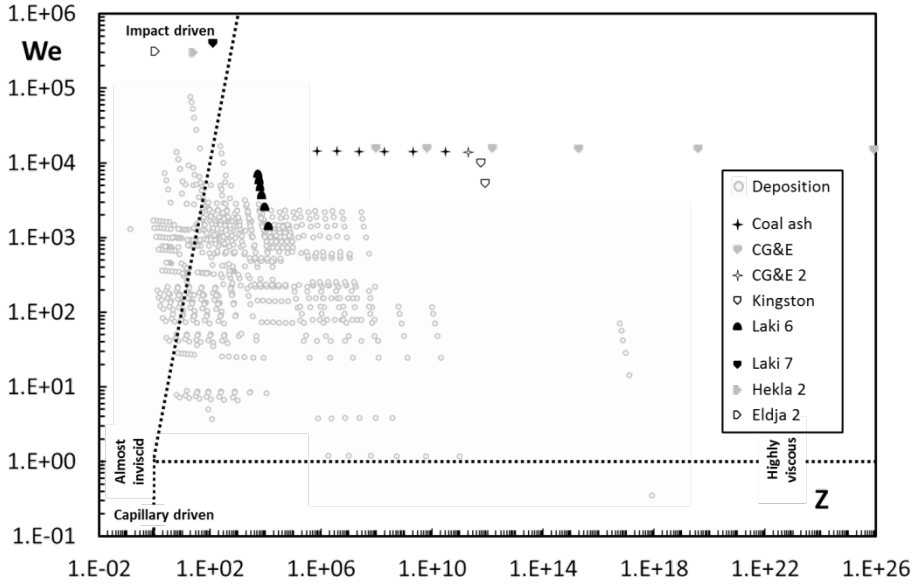

Figure 7.39: Particle spread regime using non-dimensional numbers including erosion and splashing tests (particle viscosity values was obtained using the NPL model). Particle deposition data are reported with grey dots

coefficients, the relation between kinetic energy and surface tension are

$$\Pi_3 = \rho_p d_p u_p^2 \gamma^{-1} \tag{7.42}$$

and by re-arranging the terms the third non-dimensional group can be expressed as

$$\Pi_3 = (\rho_p d_p^3 u_p^2)(d_p^{-2} \gamma^{-1}) \tag{7.43}$$

The first term represents the particle kinetic energy and the second term represents the particle surface energy. As shown above, particle kinetic energy and the surface energy work in the opposite way. If kinetic energy increases, the particle/surface interaction is driven by inertia, while if surface energy increases the particle/surface interaction is driven by surface energy (i.e. capillary forces). Defining the particle kinetic energy as

$$E_{kin} = \frac{1}{2} m u_p^2 \tag{7.44}$$

and the particle surface energy as

$$E_{surf} = \gamma A = \gamma 4 \pi r_p^2 \tag{7.45}$$

the considered non-dimensional group is defined according to the Pi Theorem as

$$K = {}^{E_{kin}}/_{E_{surf}} \tag{7.46}$$

The second parameter is related to particle softening. As highlighted above, viscous force determines how particle dissipates the kinetic energy at the impact. In order to represent this, the non-dimensional group defined as

$$\Theta = {}^{T}/_{T_{soft}} \tag{7.47}$$

is chosen. As reported, particle viscosity is directly related to particle temperature via its composition. Each material has proper characteristics and its specific value of softening temperature. This ratio represents how far the particle is from the softening state, overpassing the definition of absolute values of particle viscosity, that, as reported, is difficult-to-be-known. At the same time, the use of Θ ratio "relative" parameter allows the comparison among different conditions. As reported in Kueppers et al. (2014) working with particle temperature "pure" parameter could misalign the actual operating condition with the test operating conditions. As described in Kueppers et al. (2014), glassy volcanic ash softens at temperature values that are considerably lower than those required for crystalline silicates to start to melt and, for this reason, the use of standard materials in laboratory tests (e.g. MIL E 5007C test sand) instead of actual volcanic ash, determines no-reliable particle deposition results. Softening temperature is already used as a threshold value in the particle sticking model (such as critical viscosity model) representing the discerning values between sticky and no-sticky particles. As reported in this work, the determination of the softening temperature for a given material is well defined as a standard procedure (such as test devices, atmosphere, thermal gradient, specimen preparation, etc.) that allows the determination of the characteristic temperature (FT, HT, IT and ST) with a specific confidence band (see Fig. 7.4) Standard (2003). With the reference of the previous description, the standard method is affected by a greater inaccuracy than other ash fusion temperature tests methods (such as the TMA and DSC) but, for the aim of the present investigation, this does not represent a limitation due to the fact that the post-process is based on the particle softening temperature estimation by means of the Yin et al [86] model (see Eqs 19 – 23 for details). By contrast, the definition of a critical viscosity value and its relation with temperature are not discovered in details yet [64]. Differences in viscosity values are detected during tests with constant shear and cooling rates compared with those measured in variable shear rate and stepwise cooling experiments Hsieh et al. (2016) running with standard test conditions D 2196-15 (2015). With the present approach, the estimation of the particle behavior according to the temperature variation become easier, more accurate and reproducible rather than the particle viscosity measurement that could be affected by non-univocal test methods Seetharaman et al. (2005); Mills et al. (2014) and by rheological behavior due to the

possible non-Newtonian effects. In fact, silica melts viscosity measurements are affected by three categories of inaccuracy due to (i) device, (ii) material and (iii) fluid behavior Seetharaman et al. (2005). The first one is responsible for inadequate temperature control and geometric misalignment within the viscometer while the second determines several uncertainties related to the inhomogeneity due to evaporation, molecular degradation, improper mixing and phase separation. The latter category introduces several inaccuracies due to flow instability and transient phenomena related to non-Newtonian effects. Using the non-dimensional groups $K - \Theta$, Figure 7.40 shows the data collected for particle deposition (Tab. 7.4), erosion (7.10) and splashing 7.11. Data belonging to the three categories are clearly subdivided. Particle erosion data are divided from particle deposition data due to the different values of the ratio Θ. Also splashing data are clearly distinguished and belonging to a region characterized by higher temperature and kinetic energy. In this case, the ratio K discerns the phenomena.

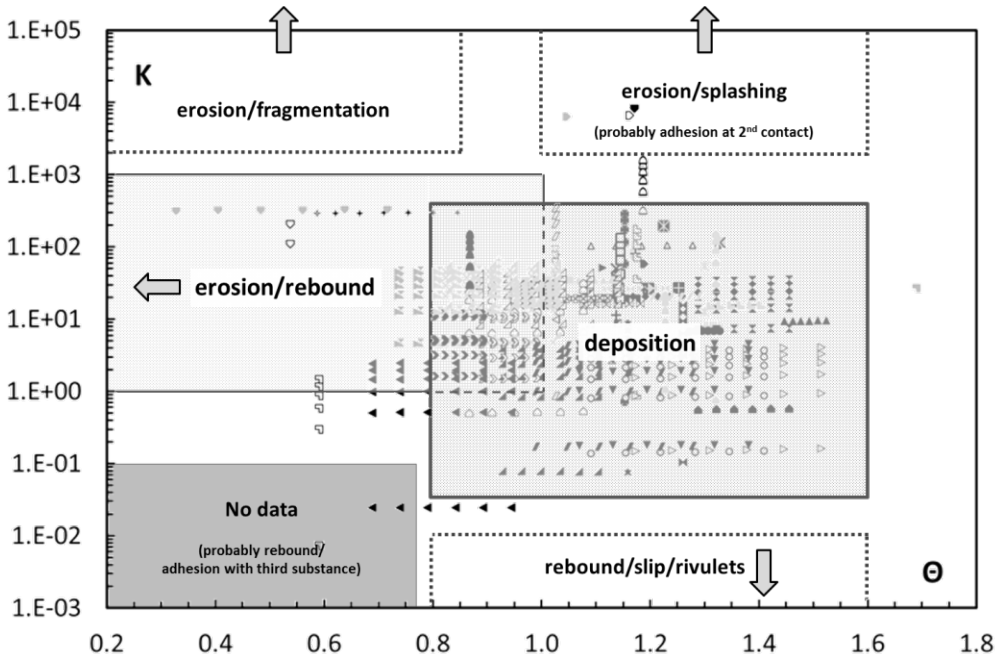

Figure 7.40: Impact behavior map using non-dimensional groups $K = E_{kin}/E_{surf}$; $\Theta = T/T_{soft}$

In the light of the present considerations, specific regions can be recognized and they are superimposed on the data collection. In the chart, different impact behaviors are identified as a function of the literature data. With the reference of Fig. 7.40, in the following description, each region will be analyzed in detail:

- *deposition*: this region comprises the data reported in Tab. 7.4 . The combination of particle temperature and softening temperature allows the dissipation of the impact energy by particle deformation determining adhesion. Particles with these characteristics are too soft to cause erosion issues and do not have enough kinetic energy to determine the splashing phenomenon. In fact, when particle temperature is higher than the softening temperature, the ratio K does not allow particle splash-

ing. The erosion phenomenon is related to the strength of the surface that strongly depends on the temperature values Singh and Sundararajan (1990); Sundararajan and Roy (1997); Wellman and Nicholls (2004) and for this reason, a certain superimposition between the deposition/erosion region has to be considered. Beyond this behavior due to the characteristics of the surface, the overlapping region is related to the definition of the temperature ratio Θ (see Eq. 49). As well reported in Gupta et al. (2002), the melting fraction at the softening temperature could be equal to 60 % depending on the composition of the ash. The correspondence of the melting fraction and the different ash fusion temperature values demonstrate that the sticking process starts in correspondence of lower value of melting fraction. Such experimental evidence confirms that the sticking process could be characterized by lower temperature values (than the softening one) and, the extension of the deposition region reported in Fig. 7.40 seems to be representative of the phenomenon. The last consideration of the present region could be related to the non-Newtonian effects during particle impact. As reported by Giehl et al. (2017), for particles characterized by a lower content of silica dioxide, the highest velocity impact does not determine the particle adhesion but, due to the high value of strain rate, particles bounce off driven by the increased stiffness;

- *erosion/rebound*: in this region, the kinetic energy is high and some particles could rebound determining the associated surface erosion. Particles are characterized by the lower capability to deform itself, and, for this reason, the dissipation of the kinetic energy that characterized the particle upon impact is dissipated through the surface generating dimples and cracks. Kinetic energy associated with the particle dimension and velocity is able to generate surface erosion as a function of the substrate resistance;

- *erosion/deposition*: in this region, particle viscosity plays a double role. It is still suitable for generating particle adhesion (the particle is sufficiently soft) but at the same time, it can determine erosion issues as well Ross et al. (1988). The particle assumes a viscoelastic property related to a semi-solid state. Experimental tests conducted in this regions should consider the double effects of particle deposition and particle erosion. The deposits obtained during this tests are affected by two phenomena and, is not suitable for generating/validate deposition or erosion models. The outcome of such tests may be the result of the simultaneous occurrence of the two effects. Thus erosion might falsify the final deposition since part of the build-up have been removed;

- *erosion and fragmentation*: this region is characterized by a higher value of particle viscosity and higher kinetic energy. Particle deposition does not take place, confirming the role of the particle softening Hamed et al. (2006) (with the reference of erosion/deposition region explanation). For example, several erosion tests at high temperature (1255 K) using alumina particles are reported. In this case, Θ is equal

to 0.54 and K is equal to 40 and no deposition is detected during tests Shin and Hamed (2016). Increasing the particle kinetic energy, the fragmentation increases as well as the erosion issues Goodwin et al. (1969); Bitter (1963). Fragmentation is due to the part of kinetic energy absorbed by the particle during the impact. This part of the energy is dissipated by the particle through its fragmentation. The amount of energy dissipated during this process is a function of particle velocity and mass, or in other words, of its kinetic energy. Therefore, starting from a certain amount of kinetic energy, erosion phenomenon is accompanied by fragmentation. This effect occurs for lower values of Θ for which the viscoelastic properties of the particle do not allow sufficient deformation able to dissipate this part of energy;

- *erosion/splashing*: this region is strongly related to the fragmentation one, but the higher values of Θ determine different particle behavior. As shown in the literature Dean et al. (2016), tests conducted with high particle temperature (1473 K), impact velocity of 100 m/s and particle diameter equal to few millimeters, generate an impact characterized by breaking up (yet during the flight) and extensive deformation on impact with the substrate. In these tests, the particle kinetic energy is equal to about 1e-2 J considerably higher than the kinetic energy involved in the particle deposition tests realized with hot gas turbine section. Therefore, even if the viscosity values are suitable for generating particle adhesion, the high values of kinetic energy determine particle break-up (splashing) and limiting particle adhesion, and then, deposits. At the same time, the particle splashing generates a large amount of smaller semi-molten droplet, re-entrained by a flowing gas Henry and Minier (2014), having lower kinetic energy. In this case, the particle behavior is very similar to the one characteristic of the deposition region;

  rebound/slip/rivulets: when the kinetic energy diminishes and/or the particle surface energy increases the particle that impacts on the surface rebounds or, in the case with very low kinetic energy particles slip on this. This phenomenon is known as a lotus effect Wenzel (1936); Cassie and Baxter (1944); Blossey (2003) particle/drop slips/rolls on the surface driven by capillary forces. Elastic phenomena could influence the particle impact or by contrast, the particle has an extremely lower energy that the rebound it is not possible;

- *no data*: in this region, no literature data are available but, in the track of the former considerations, some hints can be reported. In this region, the values of the ratio Θ imply the viscoelastic behavior of particle that could promote rebound (and the associated erosion issues), but at the same time, the lower values of the ratio K do not generate surface erosion. Therefore, if particle adhesion occurs, it is probably due to particular conditions or to the presence of a third substance or an attraction force (for example Van der Walls force) that promotes particle sticking. One of the particular condition is described well by Sacco et al. (2018). In this experimental test, the ARD particles impact the surface of the internal cooling holes with very low

velocity and significantly low temperature (¡ 728 K). In these conditions, some particles are trapped in recirculating and stagnation zones and they repeatedly impact the hot surface at low velocity Sacco et al. (2018). Regarding the presence of the third substance, experimental results Poppe et al. (2000) have shown that, in the case of dry conditions, particles are able to stick to the surface if the impact velocity (in the normal direction) is lower than a certain limit. When the values of kinetic energy are lower, due to the smaller particle diameter (0.1–1.5) μm, rather than lower velocities, and if a third substance is present, particle sticking is promoted. This condition is very to that found in the gas turbine compressor sections. Submicro-sized solid particles are a class of particles that determine compressor fouling Suman et al. (2017), or in other words, these particles stick under cold conditions. As reported in the literature, compressor fouling is promoted by the presence of third substances at the particle surface interface Zaba and Lombardi (1984); Tarabrin et al. (1998) and for these reasons, the adhesion capability that characterizes this region, could be due to the effects of particular surface conditions. Unfortunately, detailed experimental analyses are not reported in the literature. A small number of contributions (compared to those reported for hot sections) involved particle sticking analysis relate to cold conditions. On-field detections Tarabrin et al. (1998); Syverud (2007) have revealed that only the first stages are affected by deposits and are driven by the presence of liquid water at the particle surface interface. Regarding wind tunnel tests, Kurz et al. (2017) reported an experimental investigation which provides experimental data on the amount of foulants in the air that stick to a blade surface under dry and humid conditions. The tests show a higher deposition rate provided by wet surfaces compared to dry ones. Similar results are reported in Vigueras Zuniga (2007) where glue agents on the blade surface enhance the particle adhesion rate dramatically. In hot sections, glue agents are described with the name of vapor deposition Ahluwalia et al. (1986); Nagarajan and Anderson (1988); Lee et al. (2002); Shin and Gulyaeva (1998); Carpenter et al. (1985). This phenomenon, due to the presence of a condensed phase downstream the combustor sections, can increase the adhesion capabilities of nanoparticles (mass mean diameter < 0.1 μm) dragged in the vicinity of the surface by diffusion and thermophoresis forces, especially in the presence of film cooling. Vapor particles migrate through the boundary layer toward the cool wall. If the boundary layer temperature is below the dew point, condensation takes place at the wall Kaufmann (1996).

7.10 Predictive capability of K-Θ map

In this section, the impact behavior map, is checked against several different cases. The first analysis refers to the particle sticking data already used for the map identification, for which a detailed subdivision between the reported results (see Tab. 7.4) is

Table 7.12: Particle erosion data. Material composition in term of weight fraction

	Authors	Material	d_p [μm]	ρ [kg/m3]	u_p [m/s]	T [K]	Tsoft [K]	t	Na2O	K2O	CaO	MgO	SiO2	Al2O3	TiO2	Fe2O3
2015	Delimont et al..	ARD COR 1	20 – 40	2560	28	873	1366	C	3.0	3.4	3.4	1.5	72.0	12.5	0.8	3.4
		ARD COR 2	20 – 40	2560	28	1073	1366	C	3.0	3.4	3.4	1.5	72.0	12.5	0.8	3.4
		ARD COR 3	20 – 40	2560	70	1073 – 1373	1366	C	3.0	3.4	3.4	1.5	72.0	12.5	0.8	3.4
2014	Reagle et al.	ARD COR 4	20 – 40	2560	47	533	1366	C	3.0	3.4	3.4	1.5	72.0	12.5	0.8	3.4
		ARD COR 5	20 – 40	2560	77	866	1366	C	3.0	3.4	3.4	1.5	72.0	12.5	0.8	3.4
		ARD COR 6	20 – 40	2560	102	1073	1366	C	3.0	3.4	3.4	1.5	72.0	12.5	0.8	3.4

Table 7.13: Water droplet erosion characteristics data. Density is assumed equal to 1000 kg/m3, surface tension is assumed equal to 0.072 N/m and Θ= 1.1

	Authors	Material	$d_p[\mu$m]	u_p [m/s]	t	K
2009	Oka et al.	W 1	44	256	C	834
		W 2	50	226	C	739
		W 3	60	191	C	633
		W 4	72	148	C	456
		W 5	95	121	C	402
		W 6	108	105	C	345
		W 7	130	85	C	253
	Ahmad et al.	W 8	90	350 – 580	C	3190 – 8760
‘83	Hackworth	W 9	700	190 – 340	C	7312 – 23414
		W 10	1800	222 – 290	C	25669 – 43802

performed (if possible). In particular, Figure 7.41 reports the impact behavior map with the superimposition of several different tests divided according to silty (Fig. 7.41a), coal-like (Fig. 7.41b), and volcanic ash particles. Volcanic ashes are reported in both Fig. 7.41c and Fig. 7.41d for improving the readability. Each bounded region represents the covered region on the impact behavior map according to the test conditions, while the solid-colored red-region represent the test condition for which the Authors have reported the most detrimental effects related to particle sticking. The data summarized in Fig. 7.41 are all the available data which have reported the present distinction. Clear visible is the presence of contradictory results in the region named erosion/deposition (see the map description early reported) for which, tests conducted with silty and coal-like particles, do not show a high amount of deposits, while tests carried out with volcanic ashes show the greatest sticky conditions. Looking into the analysis, it is clear how the data is very dispersed, but, at the same time, it can draw two major considerations: (i) particle sticking is greater moving towards high values of Θ while (ii) the relationship between the ratio K and the sticking condition is not univocal. This means that the effects of particle inertia and the interaction between the particle and substrate is not straightforward. For example, the combination of particle size and velocity changes the heating process and may affect the deposition process Giehl et al. (2017). For the same velocity, smaller particles (lower values of K) are heated-up quicker than bigger particles (higher values of K) changing the results of the particle impact.

In the second analysis, K-Θ map presented in Fig.7.40 is checked against two different cases. The first one is related to experimental tests for measuring the coefficient of restitution (COR) at high temperature Delimont et al. (2014); Oka and Miyata (2009); Ahmad et al. (2009). Tests were performed with ARD and Tab. 7.12 reports their characteristics. The second one is related to experimental tests for evaluating the erosion due to droplets impact Oka and Miyata (2009); Ahmad et al. (2009); Hackworth (1983). Tests were performed with water and Tab. 7.13 reports their characteristics.

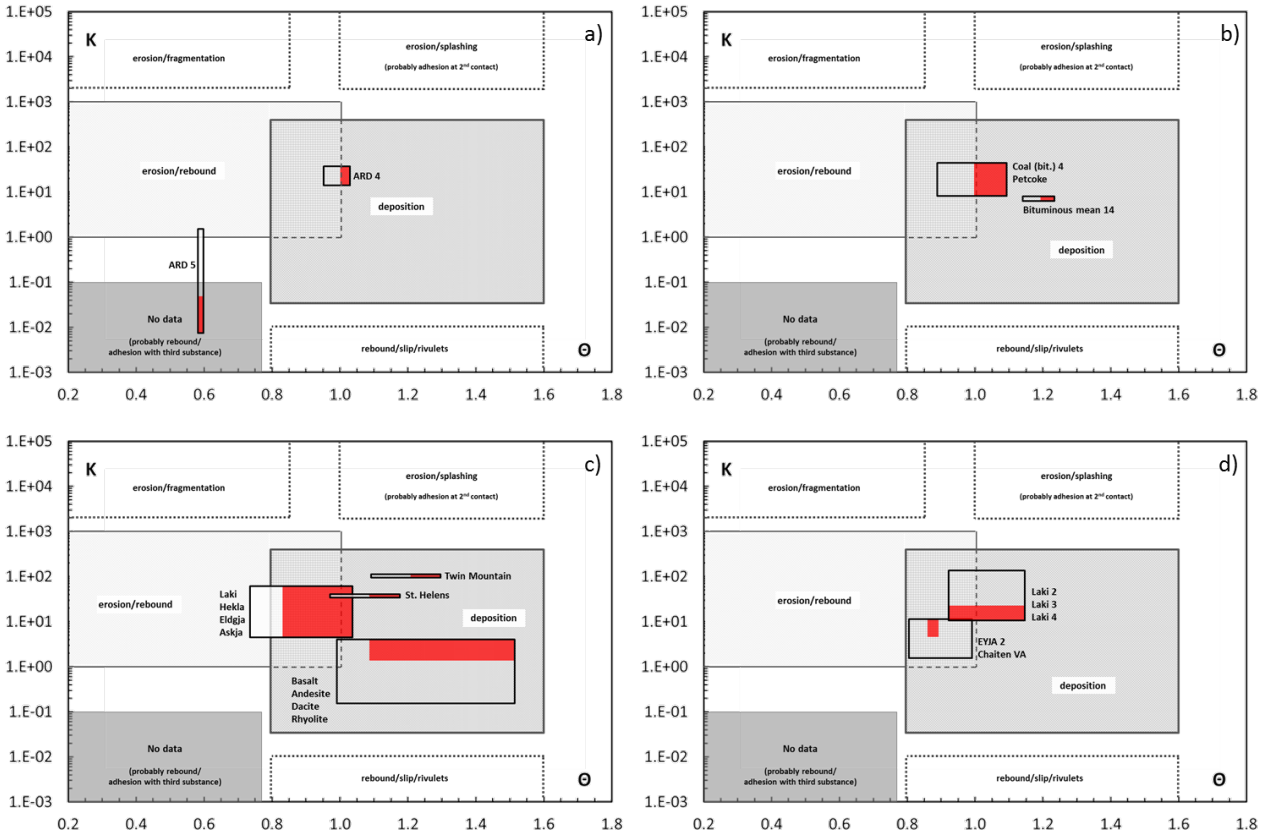

Figure 7.41: The impact behavior map with the superimposition of several different tests considering the more detrimental particle sticking regions: a) silty, b) coal-like, c) and d) volcanic ash particles

Figure 7.42 shows the superimposition of literature data reported in Tab. 7.12 and Tab. 7.13 on the K-Θ map. The tests performed with ARD are collocated in the erosion/rebound region. These tests are realized with the aim of measuring the rebound characteristics of ARD particles confirming the region highlighted in the K-Θ map. In particular, ARD COR 3 tests conducted with higher temperature (close to 1373 K) belong to the mixed region erosion/rebound-deposition. Deposition effects are recognized during the tests realized for measuring COR of ARD particles at high temperature Delimont et al. (2014). In detail, starting from about 1250 K (corresponding to $\Theta = 0.92$) to about 1370 K (corresponding to $\Theta = 1.01$) particle deposition takes place. A certain number of particles stick to the target surface as well as the remaining particles bounce on the target defining a specific value of COR. This experimental evidence, obtained with an experimental apparatus design for calculating rebound characteristics of micro-sized particles, confirms a particular region characterized by particle rebound/erosion and particle deposition. The tests performed with water droplet are located in the erosion/splashing region. These tests are realized with the aim of measuring the erosion provided by water droplets. Bigger droplets and/or higher impact velocities are collocated in the upper region, where splashing is higher. The K-Θ map provided also, in this case, a good prediction of the actual behavior even if, the comparison with water droplets over-stresses the hypotheses under which the K-Θ map exists. In fact, across the Tsoft, all materials considered for the K-Θ map identification, show a continuous trend of the relation μ-T.

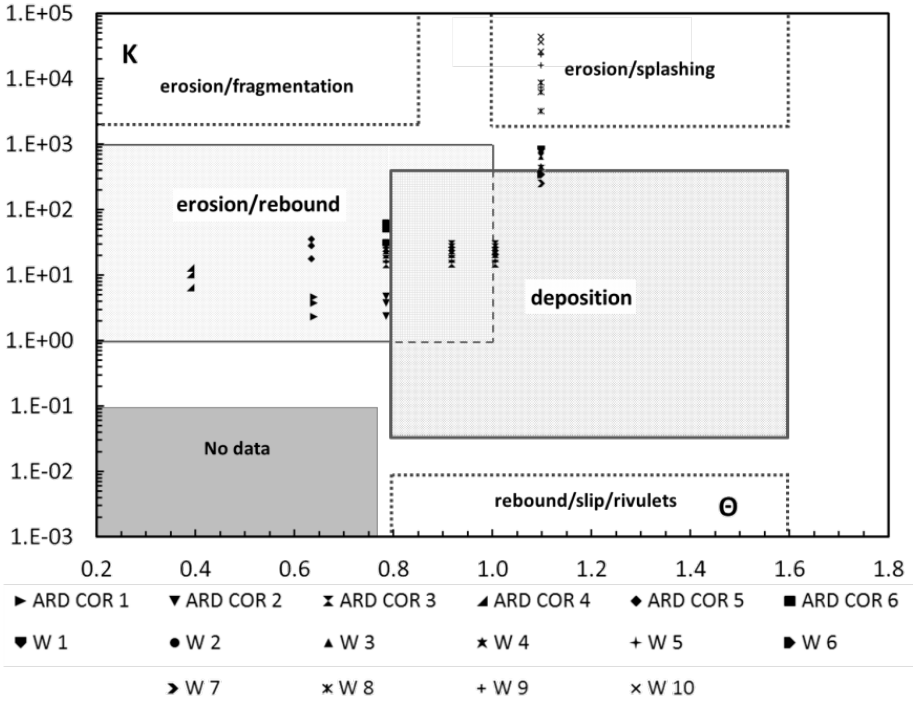

Figure 7.42: Tests of ARD rebound and water droplet erosion superimposed on the non-dimensional impact behavior map K-Θ

By contrast, water is characterized by a step function of the μ-T trend across the Tsoft (that represents ice melting).

7.11 Final Remarks

Particle sticking tests, collected in the present review, cover all materials responsible for the gas turbine fouling phenomenon (silty, volcanic ash and coal-like particles). Starting from these tests, an original data post-process based on non-dimensional groups has generated the K-Θ Map, in which several different results of a generic particle impact can be a priori determined. The identification of the K-Θ Map by means of several independent experimental results related to the evaluation of restitution coefficients and droplet erosion has confirmed that the adopted approach seems promising for using the K-Θ Map as a predictive tool. The K- Θ prediction is can be considered reliable as the impact conditions (particle chemical composition and substrate characteristics) are similar to those considered in the present literature data collection. After a detailed analysis of the literature, two main aspects have to be considered for the proper interpretation of the results: (i) the effects of the local temperature variation due to the film cooling on the blade surface and (ii) the effects of mutual interaction between particle and the substrate at a given temperature. Particle thermal characteristic (such as conductivity, specific heat, etc.) and the effects of glue agent due to the particular combination of chemical composition and temperature, could affect the result of a particle impact. These

aspects should be considered in the use of K-Θ Map and may represent the basis for further improvements in particle deposition research.

Based on over seventy (70) experimental tests related to gas turbine hot sections reported in the literature, the proposed non-dimensional particle impact behavior map summarizes all the possible effects of particle impact on surfaces. The non-dimensional parameters, used to identify the results of particle impact, are based on the assessment of particle velocity, temperature, mass, surface tension and softening temperature. On this basis, a proper characterization of particle material is required using (i) standard tests (if exist) or (ii) predictive model of particle density, surface tension and softening temperature. The generalization of the results is provided by using non-dimensional groups able to represent different particle impact behavior. All of the recognized regions (deposition, rebound/slip/rivulets, erosion/rebound, erosion and fragmentation, and erosion/splashing) are related to specific experimental evidence found in literature which highlight several effects involved in gas turbine fouling. A particular region named no data is also proposed. This region is characterized by lower particle kinetic energy, higher viscosity values, and no available literature data. Therefore, what is the reason for this lack of data for interpretation? Are these particle conditions involved in gas turbine particle deposition? Are these conditions easy to be studied by experimental tests? These questions are still open and further studies will be devoted to discover particle impact behavior and improve the knowledge about all recognized regions. Therefore, with reference to the sensitivity analysis and data post-process reported in the present section, three main outcomes can be drawn:

- the mutual correlation between the particle sticking predictive model and the model used for estimating particle characteristics (in particular particle viscosity) determine the quality of the sticking prediction. Given this, the selection of the predictive models has to be pondered according to the particle chemical composition and to the hypothesis and data which the predictive model is based on;
- the use of non-dimensional groups may represent the starting point for improving the knowledge of the gas turbine fouling and, in a wider scenario, could represent a valid support for extracting general laws useful for improving the capability of numerical tools, in the particle impact simulation;
- the predictive map can be used for estimating the particle sticking capability as well as the effects of a generic particle impact (such as erosion, splashing, etc.) characterized by specific impact conditions and particle characteristics. This approach could be useful for designing an experimental test (such as the selection of the particle chemical composition, gas temperature, etc.) or, analysis in greater detail, for characterizing a specific operating condition of the power unit.

Experimental analyses and analytical models have to take into account the effects of the

presence of third material (such as water, oily substances, etc.) at the particle/surface interface, implying several difficulties for modeling gas turbine particle deposition. All of these aspects represent the upcoming challenges, considering that both experimental and numerical analyses have to reflect the actual conditions in which the gas turbine operates.

Conclusions and Limitations

Particles dispersed in the air or in the fuel are known to be a real hazard for the gas turbine operation. This problem arises especially in case of syngas-powered turbines, due to fuel uncleanliness (e.g. tar presence). For such reasons, in this work the degradation of gas turbine due to the processing of particle laden fluids is investigated. The problem has been tackled mainly from the numerical standpoint, developing models suitable for each section under investigation. The numerical analysis has been placed side by side with experimental evidences or data available in the literature, in order to find the most suitable technique for the study of the particle effects on the flow field. Each section of the gas turbine is indeed affected by a different prevailing degradation issue that should be reliably modelled in order to have a precise estimation of its relevance and its effect on the overall performance.

Few guidelines and conclusions can be drawn from the present work:

- A number of particle deposition models has been proposed, differing both in terms of the mathematical formulation of the sticking law and in the computational technique developed for considering the effects of the deposit formation on the flow field. The differences in the techniques employed are related to the different mechanisms of sticking as well as on the different time scale of the phenomena, in each of the different situations investigated. The desire for achieving a more realistic representation of the sticking consequences has led to development of two innovative models (i.e. microscale pattern and porosity-driven approach) that might be of help in the definition of a relation between deposit and induced roughness or induced thickness consequences.

- The erosion study has proven the importance this phenomenon has in the overall evaluation of the performance degradation. This problem affects more the aero-engine applications, since bigger particles that cause material losses are blocked by filters in land-based applications. Fragmentation of particles due to impact with blades prevents high diameter particle to reach the hot section and the softening of the particles due to the passage through the combustor mitigates the erosion issue in the hot section.

- The deposit evolution over time section reports a study that investigates what happens to the deposit as time passes by. This study has the aim of investigating the conditions by which the deposit weakens and tends to be detached, in order to prolong the hardware performance/life. It has been found that the aging of the deposit in the hot section can increase the deposit toughness. The porosity-strength relation of the deposit in the hot section application is a very important parameter and experimental tests should be performed to find the appropriate relation.

- An early stage research in formalizing a blade-design technique in fouling conditions is proposed. Sticking model, mesh morphing and erosion model have been combined and a shape that minimizes the losses when the blade is exposed to particulate has been obtained. The design parameters that allow for higher performance in such conditions have been outlined. This approach for the design is thought to gain attractiveness with the growing employment of syngas for gas turbines. Such renewable fuel is always more spread and criteria for considering the HPT fouling in the design phase is sought by manufacturers.

- A generalization of the impact consequences has been proposed in order to try unify the behaviour of the particle upon impact. Starting from data available in the literature and identifying similarities with other problem studied in literature (e.g. printable fluids), a map for the detection of the particle behaviour upon impact has been realized. Such map is proposed as a candidate for the prediction of the particle impact behaviour.

This work is of course affected by some limitations, most of which have been discussed in the former sections. The most relevant will be reported here:

- The coefficients of the EBFOG sticking model proposed are tuned on experimental data for the material under analysis. A prediction of these coefficients based on the chemical composition is an ongoing project, but has not been yet formalized. Besides, data used for the formalization of the model are affected by uncertainty that, in turn, will affect the outcome of the present analysis.

- The models for deposition and detachment of the deposit on the cold section have not been tested on actual compressor geometries. Their applicability should be guaranteed, but actual test have not been performed so far.

- Although the model implemented are always based on experimental data available and the physical evidence is stressed, the outcome of the numerical simulations has never been validated. There are intrinsic difficulties in the experimental evaluation of these phenomena, related to the size and velocity of the particles, to the temperature and to the setup of the actual conditions. In this light, some simple geometries have been considered: an experimental campaign can validate more easily the results and the finding here proposed.

List of symbols

$A_{i,j}$	Area of facet
A	Hamaker constant, pre-exponential Arrhenius factor, erosion constant
B	additive constant in the log-law
C_D	drag coefficient
c	chord
C	class function
C_e	capture efficiency
$C_{in,out}$	incoming/outgoing concentration
C_K	Tabakoff constant
Cu	Cunningham factor
$C_{1,2}$	EBFOG constants
D_{ij}	Darcy matrix component
d_p	particle diameter
E	additive constant in the log-law
F^*	non dimensional detaching moment
F_{ij}	Forchheimer matrix component
F_S	particle shape factor
F_Θ	impact angle factor
HPT	High Pressure Turbine
κ	von Karman constant, mean curvature of the liquid meniscus
K	permeability, nondimensional energy
Kn	Knudsen number
k_s	equivalent sand grain
$K_{1,12,3}$	Tabakoff constant, composite Young's modulus
l_x, l_y	Face dimensions
R_a	center average line roughness
R_{dq}	root mean square roughness slope
R_q	root mean square roughness
R_{sk}	roughness skewness
Re_p	particle Reynolds number
S	Shape factor
S_a	centerline average roughness (surface parameter)
S_p	Sticking probability
T_{soft}	softening temperature
TET	Turbine Entrance Temperature
$\mathbf{u}$	flow velocity
$\mathbf{u}_p$	particle velocity
u_τ	friction velocity
V	molar volume
V_c	critical velocity
V_d^+	non dimensional deposition velocity
W_a	work of adhesion
y^+	non dimensional wall distance
Y	loss coefficient
z	profile height

Greek letters

α	operator in transfinite interpolation, pore angle
β	operator in transfinite interpolation, pore angle
β_1	impinging angle
γ	surface tension
θ	impact angle, contact angle
Θ	nondimensional temperature
ϵ	porosity
η	efficiency, computational coordinate
λ	particle aspect ratio
Λ	cost function
μ	dynamic viscosity, mean value
ν	kinematic viscosity
ξ	spread factor
ρ	density
σ	stress
τ_k	Kolmogorov time scale

τ_p	particle response time
Φ	particle volumetric fraction
Ψ	filling angle

Bibliography

Agati, G., Borello, D., Rispoli, F., and Venturini, P. (2016). An innovative approach to model temperature influence on particle deposition in gas turbines. In *ASME Turbo Expo 2016: Turbomachinery Technical Conference and Exposition*, pages V05CT12A012–V05CT12A012. American Society of Mechanical Engineers.

Ahluwalia, R., Im, K., Chuang, C., and Hajduk, J. (1986). Particle and vapor deposition in coal-fired gas turbines. In *ASME 1986 International Gas Turbine Conference and Exhibit*, pages V001T01A105–V001T01A105. American Society of Mechanical Engineers.

Ahluwalia, R., Im, K., and Wenglarz, R. (1989). Flyash adhesion in simulated coal-fired gas turbine environment. *Journal of engineering for gas turbines and power*, 111(4):672–678.

Ahmad, M., Casey, M., and Sürken, N. (2009). Experimental assessment of droplet impact erosion resistance of steam turbine blade materials. *Wear*, 267(9-10):1605–1618.

Ai, W. (2009). *Deposition of particulate from coal-derived syngas on gas turbine blades near film cooling holes*. PhD thesis, Brigham Young University-Provo.

Ai, W., Laycock, R. G., Rappleye, D. S., Fletcher, T. H., and Bons, J. P. (2009). Effect of particle size and trench configuration on deposition from fine coal flyash near film cooling holes. In *ASME Turbo Expo 2009: Power for Land, Sea, and Air*, pages 561–571. American Society of Mechanical Engineers.

Ai, W., Murray, N., Fletcher, T. H., Harding, S., and Bons, J. P. (2012a). Effect of hole spacing on deposition of fine coal flyash near film cooling holes. *Journal of Turbomachinery*, 134(4):041021.

Ai, W., Murray, N., Fletcher, T. H., Harding, S., Lewis, S., and Bons, J. P. (2012b). Deposition near film cooling holes on a high pressure turbine vane. *Journal of Turbomachinery*, 134(4):041013.

Al-Otoom, A., Bryant, G., Elliott, L., Skrifvars, B., Hupa, M., and Wall, T. (2000). Experimental options for determining the temperature for the onset of sintering of coal ash. *Energy and Fuels*, 14(1):227–233.

Aldi, N., Casari, N., Dainese, D., Morini, M., Pinelli, M., Spina, P., and Suman, A. (2018). Fouling on a multistage axial compressor in the presence of a third substance at the particle/surface interface. volume 2D-2018.

Aldi, N., Casari, N., Dainese, D., Morini, M., Pinelli, M., Spina, P. R., and Suman, A. (2017a). The effects of third substances at the particle/surface interface in compressor fouling. In *ASME Turbo Expo 2017: Turbomachinery Technical Conference and Exposition*, pages V009T27A019–V009T27A019. American Society of Mechanical Engineers.

Aldi, N., Casari, N., Dainese, D., Morini, M., Pinelli, M., Spina, P. R., and Suman, A. (2017b). Quantitative cfd analyses of particle deposition in a heavy-duty subsonic axial compressor. In *ASME Turbo Expo 2017: Turbomachinery Technical Conference and Exposition*, pages V009T27A013–V009T27A013. American Society of Mechanical Engineers.

Allaby, M. (2013). *A dictionary of geology and earth sciences*. Oxford University Press.

Anderson, R., Romanowski, C., and France, J. (1984). Adherence of ash particles from the combustion of micronized coal.[dependence on velocity, particle temperature, and target temperature]. Technical report, USDOE Morgantown Energy Technology Center, WV.

Anderson, R. J., Logan, R. G., Meyer, C. T., and Dennis, R. A. (1990). A combustion/deposition entrained reactor for high-temperature/pressure studies of coal and coal minerals. *Review of scientific instruments*, 61(4):1294–1302.

Arts, T., Lambertderouvroit, M., and Rutherford, A. (1990). Aero-thermal investigation of a highly loaded transonic linear turbine guide vane cascade: a test case for inviscid and viscous flow computations. *NASA STI/Recon Technical Report N*, 91.

Atlas, S. (1995). Verein deutscher eisenhüttenleute. *Verlag Stahleisen GmbH, Düsseldorf*, 5.

Attané, P., Girard, F., and Morin, V. (2007). An energy balance approach of the dynamics of drop impact on a solid surface. *Physics of Fluids*, 19(1):012101.

Bai, C. and Gosman, A. (1995). Development of methodology for spray impingement simulation. *SAE transactions*, pages 550–568.

Balan, C. and Tabakoff, W. (1984). Axial flow compressor performance deterioration. In *20th Joint Propulsion Conference*, page 1208.

Bammert, K. and Woelk, G. (1980). The influence of the blading surface roughness on the aerodynamic behavior and characteristic of an axial compressor. *Journal of Engineering for Power*, 102(2):283–287.

Bandyopadhyay, R., Gupta, S., Lindblom, B., Jonsson, S., French, D., and Sahajwalla, V. (2014). Assessment of ash deposition tendency in a rotary kiln using thermomechanical analysis and experimental combustion furnace. *Fuel*, 135:301–307.

Barker, B., Casaday, B., Shankara, P., Ameri, A., and Bons, J. (2013). Coal ash deposition on nozzle guide vanes—part ii: Computational modeling. *Journal of Turbomachinery*, 135(1):11015.

Barker, B., Hsu, K., Varney, B., Boulanger, A., Hutchinson, J., and Ng, W. F. (2017). An experiment-based sticking model for heated sand. In *ASME Turbo Expo 2017: Turbomachinery Technical Conference and Exposition*, pages V02DT48A014–V02DT48A014. American Society of Mechanical Engineers.

BAS, M. L., Maitre, R. L., Streckeisen, A., Zanettin, B., and on the Systematics of Igneous Rocks, I. S. (1986). A chemical classification of volcanic rocks based on the total alkali-silica diagram. *Journal of petrology*, 27(3):745–750.

Berbner, S. and Löffler, F. (1994). Influence of high temperatures on particle adhesion. *Powder Technology*, 78(3):273–280.

Bergeaud, V. and Lefebvre, V. (2010). Salome. a software integration platform for multi-physics, pre-processing and visualisation.

Bhargava, R., Meher-Homji, C., Chaker, M., Bianchi, M., Melino, F., Peretto, A., and Ingistov, S. (2007). Gas turbine fogging technology: A state-of-the-art review—part i: Inlet evaporative fogging—analytical and experimental aspects. *Journal of engineering for gas turbines and power*, 129(2):443–453.

Birello, F., Borello, D., Venturini, P., and Rispoli, F. (2013). Modelling of deposit mechanisms around the stator of a gas turbine. In *ASME Turbo Expo 2013: Turbine Technical Conference and Exposition*, pages V002T03A019–V002T03A019. American Society of Mechanical Engineers.

Bitter, J. (1963). A study of erosion phenomena part i. *wear*, 6(1):5–21.

Blossey, R. (2003). Self-cleaning surfaces—virtual realities. *Nature materials*, 2(5):301.

Bölcs, A. and Sari, O. (1988). Influence of deposit on the flow in a turbine cascade. *ASME J. Turbomach*, 110(4):512–519.

Bons, J., Prenter, R., and Whitaker, S. (2017). A simple physics-based model for particle rebound and deposition in turbomachinery. *Journal of Turbomachinery*, 139(8):081009.

Bons, J., Taylor, R., McClain, S., and Rivir, R. (2001). The many faces of turbine surface roughness. *ASME J. Turbomach*, 123(4):739–748.

Bons, J. P. (2010). A review of surface roughness effects in gas turbines. *Journal of turbomachinery*, 132(2):021004.

Bons, J. P., Crosby, J., Wammack, J. E., Bentley, B. I., and Fletcher, T. H. (2007). High-pressure turbine deposition in land-based gas turbines from various synfuels. *Journal of Engineering for Gas Turbines and Power*, 129(1):135–143.

Bons, J. P., Wammack, J. E., Crosby, J., Fletcher, D., and Fletcher, T. H. (2008). Evolution of surface deposits on a high-pressure turbine blade—part ii: Convective heat transfer. *Journal of Turbomachinery*, 130(2):021021.

Borello, D., D'Angeli, L., Salvagni, A., Venturini, P., and Rispoli, F. (2014). Study of particles deposition in gas turbine blades in presence of film cooling. In *ASME Turbo Expo 2014: Turbine Technical Conference and Exposition*, pages V05BT13A043–V05BT13A043. American Society of Mechanical Engineers.

Bottinga, Y., Weill, D., and Richet, P. (1982). Density calculations for silicate liquids. i. revised method for aluminosilicate compositions. *Geochimica et Cosmochimica Acta*, 46(6):909–919.

Boulanger, A., Patel, H., Hutchinson, J., DeShong, W., Xu, W., Ng, W., and Ekkad, S. (2016). Preliminary experimental investigation of initial onset of sand deposition in the turbine section of gas turbines. In *ASME Turbo Expo 2016: Turbomachinery Technical Conference and Exposition*, pages V001T01A003–V001T01A003. American Society of Mechanical Engineers.

Bowling, R. A. (1988). A theoretical review of particle adhesion. In *Particles on Surfaces 1*, pages 129–142. Springer.

Brach, R. M. and Dunn, P. F. (1992). A mathematical model of the impact and adhesion of microsphers. *Aerosol Science and Technology*, 16(1):51–64.

Buckingham, E. (1914). On physically similar systems; illustrations of the use of dimensional equations. *Physical review*, 4(4):345.

Burwash, W., Finlay, W., and Matida, E. (2006). Deposition of particles by a confined impinging jet onto a flat surface at re= 10 4. *Aerosol science and technology*, 40(3):147–156.

Cadorin, M., Morini, M., and Pinelli, M. (2010). Numerical analyses of high reynolds number flow of high pressure fuel gas through rough pipes. *International journal of hydrogen energy*, 35(14):7568–7579.

Carnevale, M., Wang, F., Green, J., and Mare, L. D. (2015). Lip stall suppression in powered intakes. *Journal of Propulsion and Power*, 32(1):161–170.

Carpenter, L., Crouse, F., and Halow, J. (1985). Coal-fueled turbines: Deposition research. In *ASME 1985 International Gas Turbine Conference and Exhibit*, pages V002T05A015–V002T05A015. American Society of Mechanical Engineers.

Casaday, B., Prenter, R., Bonilla, C., Lawrence, M., Clum, C., Ameri, A. A., and Bons, J. P. (2014). Deposition with hot streaks in an uncooled turbine vane passage. *ASME J. Turbomach*, 136(4):041017.

Casadevall, T. J. (1992). Volcanic hazards and aviation safety: Lessons of the past decade.

Casari, N., Pinelli, M., Suman, A., di Mare, L., and Montomoli, F. (2017a). An energy-based fouling model for gas turbines: Ebfog. *Journal of Turbomachinery*, 139(2):021002.

Casari, N., Pinelli, M., Suman, A., Di Mare, L., and Montomoli, F. (2017b). UQ lab - EBFOG deposition data http://wwwf.imperial.ac.uk/aeronautics/research/montomolilab/nicola.html.

Cassie, A. and Baxter, S. (1944). Wettability of porous surfaces. *Transactions of the Faraday society*, 40:546–551.

Ceze, M., Hayashi, M., and Volpe, E. (2009). A study of the cst parameterization characteristics. In *27th AIAA applied aerodynamics conference*, page 3767.

Chaker, M., Meher-Homji, C. B., Mee, T., and Nicolson, A. (2001). Inlet fogging of gas turbine engines: Detailed climatic analysis of gas turbine evaporative cooling potential. In *ASME Turbo Expo 2001: Power for Land, Sea, and Air*, pages V003T03A016–V003T03A016. American Society of Mechanical Engineers.

Chandra, S. and Avedisian, C. (1991). On the collision of a droplet with a solid surface. *Proc. R. Soc. Lond. A*, 432(1884):13–41.

Cheu, T.-C. (1989). Procedures for shape optimization of gas turbine disks.

Chin, J. and Lefebvre, A. (1993). Influence of flow conditions on deposits from heated hydrocarbon fuels. *Journal of Engineering for gas Turbines and Power*, 115(3):433–438.

Choi, J.-Y. and Lee, H.-G. (2002). Thermodynamic evaluation of the surface tension of molten cao–sio2–al2o3 ternary slag. *ISIJ international*, 42(3):221–228.

Ciprian, D. and Grigore, B. (2013). Classification and characterization of basalts of branisca and dobra romania, for capitalization. *Recent Adv. Ind. Manuf. Technol.*, pages 64–65.

Clarkson, R. J., Majewicz, E. J., and Mack, P. (2016). A re-evaluation of the 2010 quantitative understanding of the effects volcanic ash has on gas turbine engines. *Proceedings of the Institution of Mechanical Engineers, Part G: Journal of Aerospace Engineering*, 230(12):2274–2291.

Clift, R., Grace, J. R., and Weber, M. E. (2005). *Bubbles, drops, and particles*. Courier Corporation.

Cohn, A. (1982). Effect of gas and metal temperatures on gas turbine deposition. In *1982 Joint Power Generation Conference: GT Papers*, pages V001T01A004–V001T01A004. American Society of Mechanical Engineers.

Coleman, H. W. and Steele, W. G. (2018). *Experimentation, validation, and uncertainty analysis for engineers*. John Wiley & Sons.

Corsini, A., Rispoli, F., Sheard, A., Takizawa, K., Tezduyar, T., and Venturini, P. (2014). A variational multiscale method for particle-cloud tracking in turbomachinery flows. *Computational Mechanics*, 54(5):1191–1202.

Courtial, P. and Dingwell, D. B. (1995). Nonlinear composition dependence of molar volume of melts in the cao-al2o3-sio2 system. *Geochimica et Cosmochimica Acta*, 59(18):3685–3695.

Crosby, J. M., Lewis, S., Bons, J. P., Ai, W., and Fletcher, T. H. (2007). Effects of particle size, gas temperature and metal temperature on high pressure turbine deposition in land based gas turbines from various synfuels. In *ASME Turbo Expo 2007: Power for Land, Sea, and Air*, pages 1365–1376. American Society of Mechanical Engineers.

D 2196-15, A. (2015). Standard test methods for rheological properties of non-newtonian materials by rotational viscometer. *Astm International*.

D388, A. (2013). Standard classification of coals by rank. *Annual Book of Standards*, 5.

Daphalapurkar, N., Wang, F., Fu, B., Lu, H., and Komanduri, R. (2011). Determination of mechanical properties of sand grains by nanoindentation. *Experimental Mechanics*, 51(5):719–728.

Das, S. K., Godiwalla, K., Mehrotra, S., Sastry, K., and Dey, P. (2006). Analytical model for erosion behaviour of impacted fly-ash particles on coal-fired boiler components. *Sadhana*, 31(5):583–595.

Das, S. K., Sharma, M. M., and Schechter, R. S. (1995). Adhesion and hydrodynamic removal of colloidal particles from sufaces. *Particulate science and technology*, 13(3-4):227–247.

Davis, D. Y. and Stearns, E. M. (1985). Energy efficient engine: Flight propulsion system final design and analysis.

de Jong, W., Ünal, Ö., Andries, J., Hein, K. R., and Spliethoff, H. (2003). Biomass and fossil fuel conversion by pressurised fluidised bed gasification using hot gas ceramic filters as gas cleaning. *Biomass and Bioenergy*, 25(1):59–83.

Dean, J., Taltavull, C., and Clyne, T. W. (2016). Influence of the composition and viscosity of volcanic ashes on their adhesion within gas turbine aeroengines. *Acta Materialia*, 109:8–16.

Degereji, M., Ingham, D., Ma, L., Pourkashanian, M., and Williams, A. (2012). Numerical assessment of coals/blends slagging potential in pulverized coal boilers. *Fuel*, 102:345–353.

Dehbi, A. (2008). Turbulent particle dispersion in arbitrary wall-bounded geometries: A coupled cfd-langevin-equation based approach. *International Journal of Multiphase Flow*, 34(9):819–828.

Delaney, G., Weaire, D., Hutzler*, S., and Murphy, S. (2005). Random packing of elliptical disks. *Philosophical Magazine Letters*, 85(2):89–96.

Delimont, J., Murdock, M., Ng, W., and Ekkad, S. (2014). Effect of near melting temperatures on microparticle sand rebound characteristics at constant impact velocity. *ASME Turbo Expo 2014: Turbine Technical Conference and Exposition*.

Derby, B. (2010). Inkjet printing of functional and structural materials: fluid property requirements, feature stability, and resolution. *Annual Review of Materials Research*, 40:395–414.

Diakunchak, I. S. (1992). Performance deterioration in industrial gas turbines. *Journal of Engineering for Gas Turbines and Power*, 114(2):161–168.

Donev, A., Cisse, I., Sachs, D., Variano, E. A., Stillinger, F. H., Connelly, R., Torquato, S., and Chaikin, P. M. (2004). Improving the density of jammed disordered packings using ellipsoids. *Science*, 303(5660):990–993.

Dong, M., Li, X., Mei, Y., and Li, S. (2018). Experimental and theoretical analyses on the effect of physical properties and humidity of fly ash impacting on a flat surface. *Journal of Aerosol Science*, 117:85–99.

Dunn, M., Padova, C., Moller, J., and Adams, R. (1987). Performance deterioration of a turbofan and a turbojet engine upon exposure to a dust environment. *Journal of engineering for gas turbines and power*, 109(3):336–343.

Dunn, M. G. (2012). Operation of gas turbine engines in an environment contaminated with volcanic ash. *Journal of Turbomachinery*, 134(5):051001.

Dunn, M. G., Baran, A. J., and Miatech, J. (1994). Operation of gas turbine engines in volcanic ash clouds. In *ASME 1994 International Gas Turbine and Aeroengine Congress and Exposition*, pages V003T05A001–V003T05A001. American Society of Mechanical Engineers.

Dykhuizen, R. and Smith, M. (1998). Gas dynamic principles of cold spray. *Journal of Thermal Spray Technology*, 7(2):205–212.

ECN. Phyllis2. Accessed: 2018-11-19.

Edwards, J., McLaury, B., and Shirazi, S. (2000). Evaluation of alternative pipe bend fittings in erosive service. In *Proceedings of ASME Fluids Engineering Summer Meeting, Boston, MA, ASME Paper No. FEDSM2000-11245*.

El-Batsh, H. and Haselbacher, H. (2000). Effect of turbulence modeling on particle dispersion and deposition on compressor and turbine blade surfaces. In *ASME Turbo Expo 2000: Power for Land, Sea, and Air*, pages V001T03A084–V001T03A084. American Society of Mechanical Engineers.

El-Batsh, H. and Haselbacher, H. (2002). Numerical investigation of the effect of ash particle deposition on the flow field through turbine cascades. In *ASME Turbo Expo 2002: Power for Land, Sea, and Air*, pages 1035–1043. American Society of Mechanical Engineers.

El-Batsh, M. H. (2001). *Modeling particle deposition on compressor and turbine blade surfaces*. PhD thesis, Vienna University of Technology.

Eldred, M. S. (1998). Optimization strategies for complex engineering applications. Technical report, Sandia National Labs., Albuquerque, NM (United States).

Elghobashi, S. (1991). Particle-laden turbulent flows: direct simulation and closure models. In *Computational fluid Dynamics for the Petrochemical Process Industry*, pages 91–104. Springer.

Elghobashi, S. (1994). On predicting particle-laden turbulent flows. *Applied Scientific Research*, 52(4):309–329.

Endo, Y., Hasebe, S., and Kousaka, Y. (1997). Dispersion of aggregates of fine powder by acceleration in an air stream and its application to the evaluation of adhesion between particles. *Powder technology*, 91(1):25–30.

Fackrell, J. E., Brown, K., and Young, J. B. (1994a). Modelling particle deposition in gas turbines employed in advanced coal-fired systems. In *ASME 1994 International Gas Turbine and Aeroengine Congress and Exposition*, pages V003T05A012–V003T05A012. American Society of Mechanical Engineers.

Fackrell, J. E., Tabberer, R. J., Young, J. B., and Fantom, I. R. (1994b). Modelling alkali salt vapour deposition in the british coal topping cycle system. In *ASME 1994 International Gas Turbine and Aeroengine Congress and Exposition*, pages V003T05A003–V003T05A003. American Society of Mechanical Engineers.

Finnie, I. (1972). Some observations on the erosion of ductile metals. *wear*, 19(1):81–90.

Forsyth, P., Gillespie, D. R., McGilvray, M., and Galoul, V. (2016). Validation and assessment of the continuous random walk model for particle deposition in gas turbine engines. In *ASME Turbo Expo 2016: Turbomachinery Technical Conference and Exposition*, pages V001T01A026–V001T01A026. American Society of Mechanical Engineers.

Forsyth, P. R., Gillespie, D. R., and McGilvray, M. (2018). Development and applications of a coupled particle deposition—dynamic mesh morphing approach for the numerical simulation of gas turbine flows. *Journal of Engineering for Gas Turbines and Power*, 140(2):022603.

Frenkel, J. (1945). Viscous flow of crystalline bodied under the action of surface tension. *J. Phys.(USSR)*, 9:385–391.

Fuks, N. A. (1989). *The mechanics of aerosols*. Dover Publications.

Fulcher, G. S. (1925). Analysis of recent measurements of the viscosity of glasses. *Journal of the American Ceramic Society*, 8(6):339–355.

Gbadebo, S. A., Hynes, T. P., and Cumpsty, N. A. (2004). Influence of surface roughness on three-dimensional separation in axial compressors. In *ASME Turbo Expo 2004: Power for Land, Sea, and Air*, pages 471–481. American Society of Mechanical Engineers.

Ghenaiet, A. (2012). Study of sand particle trajectories and erosion into the first compression stage of a turbofan. *Journal of turbomachinery*, 134(5):051025.

Ghidossi, R., Bonnet, J.-P., Rebollar-Perez, G., Carretier, E., Ferrasse, J.-H., Vicente, J., Topin, F., and Moulin, P. (2009). Separation of particles from hot gases using metallic foams. *journal of materials processing technology*, 209(8):3859–3868.

Gidaspow, D. (1994). *Multiphase flow and fluidization: continuum and kinetic theory descriptions*. Academic press.

Giehl, C., Brooker, R. A., Marxer, H., and Nowak, M. (2017). An experimental simulation of volcanic ash deposition in gas turbines and implications for jet engine safety. *Chemical Geology*, 461:160–170.

Giordano, D., Russell, J. K., and Dingwell, D. B. (2008). Viscosity of magmatic liquids: a model. *Earth and Planetary Science Letters*, 271(1-4):123–134.

Gislason, S. R., Hassenkam, T., Nedel, S., Bovet, N., Eiriksdottir, E. S., Alfredsson, H. A., Hem, C. P., Balogh, Z. I., Dideriksen, K., Oskarsson, N., Sigfusson, B., Larsen, G., and Stipp, S. L. S. (2011). Characterization of eyjafjallajökull volcanic ash particles and a protocol for rapid risk assessment. *Proceedings of the National Academy of Sciences*, 108(18):7307–7312.

Gökoğlu, S. A. and Rosner, D. E. (1984). Comparisons of rational engineering correlations of thermophoretically-augmented particle mass transfer with stan5-predictions for developing boundary layers. In *ASME 1984 International Gas Turbine Conference and Exhibit*, pages V003T05A006–V003T05A006. American Society of Mechanical Engineers.

Goodhand, M. N., Walton, K., Blunt, L., Lung, H. W., Miller, R. J., and Marsden, R. (2016). The limitations of using "ra" to describe surface roughness. *Journal of Turbomachinery*, 138(10):101003.

Goodwin, J., Sage, W., and Tilly, G. (1969). Study of erosion by solid particles. *Proceedings of the Institution of Mechanical Engineers*, 184(1):279–292.

Gosman, A. and Ioannides, E. (1983). Aspects of computer simulation of liquid-fueled combustors. *Journal of energy*, 7(6):482–490.

Grant, G. and Tabakoff, W. (1975). Erosion prediction in turbomachinery resulting from environmental solid particles. *Journal of Aircraft*, 12(5):471–478.

Grau, A. and Masson, C. (1976). Densities and molar volumes of silicate melts. *Canadian Metallurgical Quarterly*, 15(4):367–374.

Guffanti, M., Mayberry, G. C., Casadevall, T. J., and Wunderman, R. (2009). Volcanic hazards to airports. *Natural hazards*, 51(2):287–302.

Gupta, S., Gupta, R., Bryant, G., Juniper, L., and Wall, T. (2002). Thermomechanical analysis and alternative ash fusibility temperatures. In *Impact of Mineral Impurities in Solid Fuel Combustion*, pages 155–169. Springer.

Gupta, S., Wall, T., Creelman, R., and Gupta, R. (1998). Ash fusion temperatures and the transformations of coal ash particles to slag. *Fuel processing technology*, 56(1-2):33–43.

Hackworth, J. (1983). Damage of infrared-transparent materials exposed to rain environments at high velocities. In *Scattering in Optical Materials II*, volume 362, pages 123–137. International Society for Optics and Photonics.

Hamed, A. and Kuhn, T. P. (1995). Effects of variational particle restitution characteristics on turbomachinery erosion. *Journal of Engineering for Gas Turbines and Power*, 117(3):432–440.

Hamed, A., Tabakoff, W., and Wenglarz, R. (2006). Erosion and deposition in turbomachinery. *Journal of propulsion and power*, 22(2):350–360.

Hanao, M., Tanaka, T., Kawamoto, M., and Takatani, K. (2007). Evaluation of surface tension of molten slag in multi-component systems. *ISIJ international*, 47(7):935–939.

Hansen, L. A., Frandsen, F. J., and Dam-Johansen, K. (2002). Ash fusion quantification by means of thermal analysis. In *Impact of Mineral Impurities in Solid Fuel Combustion*, pages 181–193. Springer.

Helton, J. C., Johnson, J. D., Sallaberry, C. J., and Storlie, C. B. (2006). Survey of sampling-based methods for uncertainty and sensitivity analysis. *Reliability Engineering & System Safety*, 91(10-11):1175–1209.

Henry, C. and Minier, J.-P. (2014). Progress in particle resuspension from rough surfaces by turbulent flows. *Progress in Energy and Combustion Science*, 45:1–53.

Hertz, H. (1986). Translated and reprinted in english in hertzõs miscellaneous paper.

Heutling, F., Uihlein, T., Brendel, T., Eichmann, W., and Ucker, M. (2009). Erosionsschutz für titan-und superlegierungen. *Galvanotechnik*, 100(5).

Hofmann, P., Panopoulos, K., Fryda, L., Schweiger, A., Ouweltjes, J., and Karl, J. (2008). Integrating biomass gasification with solid oxide fuel cells: effect of real product gas tars, fluctuations and particulates on ni-gdc anode. *International journal of hydrogen energy*, 33(11):2834–2844.

Holt, N. A. and Alpert, S. B. (2001). Integrated gasification combined-cycle power plants.

Hoy, H., Roberts, A., and Wilkins, D. (1964). *Behaviour of Mineral Matter in Slagging Gasification Process*. Institution of Gas Engieners.

Hsieh, P. Y., Kwong, K.-S., and Bennett, J. (2016). Correlation between the critical viscosity and ash fusion temperatures of coal gasifier ashes. *Fuel Processing Technology*, 142:13–26.

Igie, U. (2017). Gas turbine compressor fouling and washing in power and aerospace propulsion. *Journal of Engineering for Gas Turbines and Power*, 139(12):122602.

Ingram, D. M., Causon, D. M., and Mingham, C. G. (2003). Developments in cartesian cut cell methods. *Mathematics and Computers in Simulation*, 61(3):561–572.

ISO 12103-1:2016 (2016). Road vehicles – Test contaminants for filter evaluation – Part 1: Arizona test dust. Standard, International Organization for Standardization, Geneva, CH.

Israelachvili, J. N. (2011). *Intermolecular and surface forces*. Academic press.

Issa, R. I. (1986). Solution of the implicitly discretised fluid flow equations by operator-splitting. *Journal of computational physics*, 62(1):40–65.

Jackson, R. L. and Green, I. (2005). A finite element study of elasto-plastic hemispherical contact against a rigid flat. *Journal of tribology*, 127(2):343–354.

Jasak, H. (2009). Dynamic mesh handling in openfoam. In *47th AIAA Aerospace Sciences Meeting Including the New Horizons Forum and Aerospace Exposition*, page 341.

Jensen, J. W., Squire, S. W., Bons, J. P., and Fletcher, T. H. (2005). Simulated land-based turbine deposits generated in an accelerated deposition facility. *Journal of turbomachinery*, 127(3):462–470.

Jiang, L.-Y., Han, Y., and Patnaik, P. (2018). Characteristics of volcanic ash in a gas turbine combustor and nozzle guide vanes. *Journal of Engineering for Gas Turbines and Power*, 140(7):071502.

Johnson, K., Kendall, K., and Roberts, A. (1971). Surface energy and the contact of elastic solids. *Proceedings of the Royal Society of London A: Mathematical, Physical and Engineering Sciences*, 324(1558):301–313.

Jones, H. (1971). Cooling, freezing and substrate impact of droplets formed by rotary atomization. *Journal of Physics D: Applied Physics*, 4(11):1657.

Kaliazine, A. L., Piroozmand, F., Cormack, D. E., and Tran, H. N. (1997). Sootblower optimization ii: Deposit and sootblower interaction. *Tappi journal*, 80(11):201–207.

Kaufmann, E. (1996). Considerations when burning ash-bearing fuels in heavy duty gas turbines. *GE Power Generation, Schenectady, NY, Technical Report No. GER-3764A*.

Kim, J., Dunn, M., Baran, A., Wade, D., and Tremba, E. (1992). Deposition of volcanic materials in the hot sections of two gas turbine engines. In *ASME 1992 International Gas Turbine and Aeroengine Congress and Exposition*, pages V003T05A001–V003T05A001. American Society of Mechanical Engineers.

Kim, T. W. and Bhushan, B. (2008). The adhesion model considering capillarity for gecko attachment system. *Journal of The Royal Society Interface*, 5(20):319–327.

Kimura, S., Spiro, C., and Chen, C. (1987). Combustion and deposition in coal-fired turbines. *Journal of engineering for gas turbines and power*, 109(3):319–324.

Kleinhans, U., Wieland, C., Babat, S., Scheffknecht, G., and Spliethoff, H. (2016). Ash particle sticking and rebound behavior: A mechanistic explanation and modeling approach. *Proceedings of the Combustion Institute*.

Kleinhans, U., Wieland, C., Frandsen, F. J., and Spliethoff, H. (2018). Ash formation and deposition in coal and biomass fired combustion systems: Progress and challenges in the field of ash particle sticking and rebound behavior. *Progress in Energy and Combustion Science*, 68:65–168.

Kline, S. and McClintock, F. (1953). Describing uncertainties in single-sample experiments,'a sme mechanical engineering, vol. 75.

Klinkov, S. V., Kosarev, V. F., and Rein, M. (2005). Cold spray deposition: significance of particle impact phenomena. *Aerospace Science and Technology*, 9(7):582–591.

Kotwal, R. and Tabakoff, W. (1980). A new approach for erosion prediction due to fly ash. In *ASME 1980 International Gas Turbine Conference and Products Show*, pages V01BT02A002–V01BT02A002. American Society of Mechanical Engineers.

Kueppers, U., Cimarelli, C., Hess, K.-U., Taddeucci, J., Wadsworth, F. B., and Dingwell, D. B. (2014). The thermal stability of eyjafjallajökull ash versus turbine ingestion test sands. *Journal of Applied Volcanology*, 3(1):4.

Kulfan, B. and Bussoletti, J. (2006). " fundamental" parameteric geometry representations for aircraft component shapes. In *11th AIAA/ISSMO multidisciplinary analysis and optimization conference*, page 6948.

Kurz, R. and Brun, K. (2001). Degradation in gas turbine systems. *Journal of Engineering for Gas Turbines and Power*, 123(1):70–77.

Kurz, R. and Brun, K. (2012). Fouling mechanisms in axial compressors. *Journal of engineering for gas turbines and power*, 134(3):032401.

Kurz, R., Musgrove, G., and Brun, K. (2017). Experimental evaluation of compressor blade fouling. *Journal of Engineering for Gas Turbines and Power*, 139(3):032601.

Kyprianidis, K. G. (2011). Future aero engine designs: an evolving vision. In *Advances in gas turbine technology*. InTech.

Lau, H. and Windand, M. (2014). Thermal protection layer destroyed, sensors blocked.

Lawson, S. and Thole, K. (2009). The effects of simulated particle deposition on film cooling. In *ASME Turbo Expo 2009: Power for Land, Sea, and Air*, pages 41–51. American Society of Mechanical Engineers.

Lawson, S. A. and Thole, K. A. (2010). Simulations of multi-phase particle deposition on endwall film-cooling. In *ASME Turbo Expo 2010: Power for Land, Sea, and Air*, pages 151–162. American Society of Mechanical Engineers.

Laycock, R. and Fletcher, T. H. (2016). Independent effects of surface and gas temperature on coal fly ash deposition in gas turbines at temperatures up to 1400 c. *Journal of Engineering for Gas Turbines and Power*, 138(2):021402.

Laycock, R. G. and Fletcher, T. H. (2013). Time-dependent deposition characteristics of fine coal fly ash in a laboratory gas turbine environment. *Journal of Turbomachinery*, 135(2):021003.

Laycock, R. G. and Fletcher, T. H. (2017). Erratum:"time-dependent deposition characteristics of fine coal fly ash in a laboratory gas turbine environment"[asme j. turbomach., 2012, 135 (2), p. 021003. *Journal of Turbomachinery*, 139(12):127001.

Laycock, R. G. and Fletcher, T. H. (2018). Formation of deposits from heavy fuel oil ash in an accelerated deposition facility at temperatures up to 1219 c. *Fuel Processing Technology*, 175:35–43.

Lee, B. E., Fletcher, C. A., Shin, S. H., and Kwon, S. B. (2002). Computational study of fouling deposit due to surface-coated particles in coal-fired power utility boilers. *Fuel*, 81(15):2001–2008.

Legoux, J.-G., Irissou, E., and Moreau, C. (2007). Effect of substrate temperature on the formation mechanism of cold-sprayed aluminum, zinc and tin coatings. *Journal of Thermal Spray Technology*, 16(5-6):619–626.

Levy, A., Aghazadeh, M., and Hickey, G. (1986). The effect of test variables on the platelet mechanism of erosion. *Wear*, 108(1):23–41.

Linden, D. H. et al. (2001). Corrosion control in industrial axial flow compressors. In *Proceedings of the 30th Turbomachinery Symposium*. Texas A&M University. Turbomachinery Laboratories.

Liu, B. Y. and Agarwal, J. K. (1974). Experimental observation of aerosol deposition in turbulent flow. *Journal of Aerosol Science*, 5(2):145–155.

López, A., Nicholls, W., Stickland, M. T., and Dempster, W. M. (2015). CFD study of jet impingement test erosion using ansys fluent® and openfoam®. *Computer Physics Communications*, 197:88–95.

Lü, S., Zhang, R., Yao, Z., Yi, F., Ren, J., Wu, M., Feng, M., and Wang, Q. (2012). Size distribution of chemical elements and their source apportionment in ambient coarse, fine, and ultrafine particles in shanghai urban summer atmosphere. *Journal of Environmental Sciences*, 24(5):882–890.

Lundgreen, R., Sacco, C., Prenter, R., and Bons, J. P. (2016). Temperature effects on nozzle guide vane deposition in a new turbine cascade rig. In *ASME Turbo Expo 2016: Turbomachinery Technical Conference and Exposition*, pages V05AT13A021–V05AT13A021. American Society of Mechanical Engineers.

Lyons, W. A. and Pease, S. R. (1973). Detection of particulate air pollution plumes from major point sources using erts-1 imagery. *Bulletin of the American Meteorological Society*, 54(11):1163–1170.

Macpherson, G. B., Nordin, N., and Weller, H. G. (2009). Particle tracking in unstructured, arbitrary polyhedral meshes for use in CFD and molecular dynamics. *Communications in Numerical Methods in Engineering*, 25(3):263–273.

Madejski, J. (1976). Solidification of droplets on a cold surface. *International Journal of Heat and Mass Transfer*, 19(9):1009–1013.

Mainsah, E., Chetwynd, D., et al. (2013). *Metrology and properties of engineering surfaces*. Springer Science & Business Media.

Mao, T., Kuhn, D. C., and Tran, H. (1997). Spread and rebound of liquid droplets upon impact on flat surfaces. *AIChE Journal*, 43(9):2169–2179.

Marcantoni, L., Tamagno, J., and Elaskar, S. (2012). High speed flow simulation using openfoam. *Mecánica Computacional*, 31:2939–2959.

Marti, A., Folch, A., Jorba, O., and Janjic, Z. (2017). Volcanic ash modeling with the online nmmb-monarch-ash v1. 0 model: model description, case simulation, and evaluation. *Atmospheric Chemistry and Physics*, 17:4005–4030.

McCabe, W. L., Smith, J. C., and Harriott, P. (1985). *Unit operations of chemical engineering*. McGraw-Hill New York.

Melchior, T., Putz, G., and Muller, M. (2009). Surface tension measurements of coal ash slags under reducing conditions at atmospheric pressure. *Energy & Fuels*, 23(9):4540–4546.

Menter, F. R., Kuntz, M., and Langtry, R. (2003). Ten years of industrial experience with the sst turbulence model. *Turbulence, heat and mass transfer*, 4(1):625–632.

Mezheritsky, A. and Sudarev, A. V. (1990). The mechanism of fouling and the cleaning technique in application to flow parts of the power generation plant compressors. In *ASME 1990 International Gas Turbine and Aeroengine Congress and Exposition*, pages V004T11A003–V004T11A003. American Society of Mechanical Engineers.

Mills, K. and Keene, B. (1987). Physical properties of bos slags. *International Materials Reviews*, 32(1):1–120.

Mills, K. and Sridhar, S. (1999). Viscosities of ironmak and steelmaking slags. *Ironmaking & Steelmaking*, 26(4):262–268.

Mills, K. C., Hayashi, M., Wang, L., and Watanabe, T. (2014). The structure and properties of silicate slags. In *Treatise on Process Metallurgy: Process Fundamentals*, pages 149–286. Elsevier.

Morini, M., Pinelli, M., Spina, P. R., and Venturini, M. (2010). Influence of blade deterioration on compressor and turbine performance. *Journal of engineering for gas turbines and power*, 132(3):032401.

Morini, M. and Venturini, M. (2012). An innovative inlet air cooling system for igcc power augmentation: Part i—analysis of igcc plant components. In *ASME Turbo Expo 2012: Turbine Technical Conference and Exposition*, pages 859–869. American Society of Mechanical Engineers.

Morsi, S. and Alexander, A. (1972). An investigation of particle trajectories in two-phase flow systems. *Journal of Fluid mechanics*, 55(2):193–208.

Mücke, E. P., Saias, I., and Zhu, B. (1996). Fast randomized point location without preprocessing in two- and three-dimensional delaunay triangulations. *Proceedings of the Twelfth Annual Symposium on Computational Geometry*, pages 274–283.

Mukherjee, P. P., Das, M. K., and Muralidhar, K. (2018). *Modeling Transport Phenomena in Porous Media with Applications*. Springer.

Mund, F. C. and Pilidis, P. (2006). Gas turbine compressor washing: historical developments, trends and main design parameters for online systems. *Journal of engineering for gas turbines and power*, 128(2):344–353.

Mustafa, Z., Pilidis, P., Teixeira, J. A. A., and Ahmad, K. A. (2006). Cfd aerodynamic investigation of air-water trajectories on rotor-stator blade of an axial compressor for online washing. In *ASME Turbo Expo 2006: Power for Land, Sea, and Air*, pages 1385–1394. American Society of Mechanical Engineers.

Myhre, G., Shindell, D., Bréon, F.-M., Collins, W., Fuglestvedt, J., Huang, J., Koch, D., Lamarque, J.-F., Lee, D., Mendoza, B., et al. (2013). Anthropogenic and natural radiative forcing. *Climate change*, 423:658–740.

Mysen, B. O. (1988). *Structure and properties of silicate melts*. Number 549.6 MYS.

Nagarajan, R. and Anderson, R. (1988). Effect of coal constituents on the liquid-assisted capture of impacting ash particles in direct coal-fired gas turbines. In *ASME 1988 International Gas Turbine and Aeroengine Congress and Exposition*, pages V003T05A010–V003T05A010. American Society of Mechanical Engineers.

Nair, S., Pemen, A., Yan, K., Van Gompel, F., Van Leuken, H., Van Heesch, E., Ptasinski, K., and Drinkenburg, A. (2003). Tar removal from biomass-derived fuel gas by pulsed corona discharges. *Fuel Processing Technology*, 84(1-3):161–173.

Nakamoto, M., Kiyose, A., Tanaka, T., Holappa, L., and Hämäläinen, M. (2007). Evaluation of the surface tension of ternary silicate melts containing al2o3, cao, feo, mgo or mno. *ISIJ international*, 47(1):38–43.

Namkung, H., Hu, X., Kim, H.-T., Wang, F., and Yu, G. (2016). Evaluation of sintering behavior of ash particles from coal and rice straw using optical heating stage microscope at high temperature fouling conditions. *Fuel Processing Technology*, 149:195–208.

Naraparaju, R., Lau, H., Lange, M., Fischer, C., Kramer, D., Schulz, U., and Weber, K. (2018). Integrated testing approach using a customized micro turbine for a volcanic ash and cmas related degradation study of thermal barrier coatings. *Surface and Coatings Technology*, 337:198–208.

Nemec, D. and Levec, J. (2005). Flow through packed bed reactors: 1. single-phase flow. *Chemical Engineering Science*, 60(24):6947–6957.

Ni, J., Yu, G., Guo, Q., Zhou, Z., and Wang, F. (2011). Submodel for predicting slag deposition formation in slagging gasification systems. *Energy & Fuels*, 25(3):1004–1009.

Nicholson, G. (1990). Gas turbine cleaning at the utrecht site of dutch utility company. *Turbomachinery International*.

Nield, D. A., Bejan, A., et al. (2006). *Convection in porous media*, volume 3. Springer.

Nikuradse, J. (1933). Laws of flow in rough pipes. In *VDI Forschungsheft*. Citeseer.

Nowok, J. (1996). Densification, shrinkage and strength development in selected coal ashes. *Journal of the Institute of Energy*, 69(478):9–11.

Ogiriki, E. A., Li, Y. G., Nikolaidis, T., Isaiah, T. E., and Sule, G. (2015). Effect of fouling, thermal barrier coating degradation and film cooling holes blockage on gas turbine engine creep life. *Procedia CIRP*, 38:228–233.

Oka, Y. and Miyata, H. (2009). Erosion behaviour of ceramic bulk and coating materials caused by water droplet impingement. *Wear*, 267(11):1804–1810.

O'Neill, M. (1968). A sphere in contact with a plane wall in a slow linear shear flow. *Chemical Engineering Science*, 23(11):1293–1298.

Ontiveros-Ortega, A., Moleon, J., Plaza, I., and Guillén, C. (2016). Effect of interfacial properties on mechanical stability of ash deposit. *Journal of Rock Mechanics and Geotechnical Engineering*, 8(2):187–197.

Orr, F., Scriven, L., and Rivas, A. P. (1975). Pendular rings between solids: meniscus properties and capillary force. *Journal of Fluid Mechanics*, 67(04):723–742.

Ouellette, N. T., Xu, H., and Bodenschatz, E. (2006). A quantitative study of three-dimensional lagrangian particle tracking algorithms. *Experiments in Fluids*, 40(2):301–313.

Parker, G. and Lee, P. (1972). Studies of the deposition of sub-micron particles on turbine blades. *Proceedings of the Institution of Mechanical Engineers*, 186(1):519–526.

Pasandideh-Fard, M., Qiao, Y., Chandra, S., and Mostaghimi, J. (1996). Capillary effects during droplet impact on a solid surface. *Physics of fluids*, 8(3):650–659.

Patankar, S. (1980). *Numerical heat transfer and fluid flow*. CRC press.

Persson, M., Zhang, J., and Seetharaman, S. (2007). A thermodynamic approach to a density model for oxide melts. *steel research international*, 78(4):290–298.

Perullo, C. A., Barron, J., Grace, D., Angello, L., and Lieuwen, T. (2015). Evaluation of air filtration options for an industrial gas turbine. In *ASME Turbo Expo 2015: Turbine Technical Conference and Exposition*, pages V003T08A011–V003T08A011. American Society of Mechanical Engineers.

Poppe, T., Blum, J., and Henning, T. (2000). Analogous experiments on the stickiness of micron-sized preplanetary dust. *The Astrophysical Journal*, 533(1):454.

Portnikov, D. and Kalman, H. (2014). Determination of elastic properties of particles using single particle compression test. *Powder Technology*, 268:244–252.

Prenter, R., Ameri, A., and Bons, J. P. (2016). Deposition on a cooled nozzle guide vane with nonuniform inlet temperatures. *J. Turbomach*, 138(10):101005.

Prenter, R., Ameri, A., and Bons, J. P. (2017). Computational simulation of deposition in a cooled high-pressure turbine stage with hot streaks. *Journal of Turbomachinery*, 139(9):091005.

Prenter, R., Whitaker, S. M., Ameri, A., and Bons, J. P. (2014). The effects of slot film cooling on deposition on a nozzle guide vane. In *ASME Turbo Expo 2014: Turbine Technical Conference and Exposition*, pages V03AT03A017–V03AT03A017. American Society of Mechanical Engineers.

Raj, R. (1983). Deposition results of a transpiration air-cooled turbine vane cascade in a contaminated gas stream. *Journal of engineering for power*, 105(4):826–833.

Raj, R. and Moskowitz, S. (1984). Experimental studies of deposition by electrostatic charge on turbine blades. In *ASME 1984 International Gas Turbine Conference and Exhibit*, pages V003T05A007–V003T05A007. American Society of Mechanical Engineers.

Ravi, V., Jog, M., and Manglik, R. (2010). Effects of interfacial and viscous properties of liquids on drop spread dynamics. In *Proceedings of the 22nd Annual Meeting of the Institute of Liquid Atomization and Spray Systems, Paper Number ILASS2010-0142. Cincinnati, OH*, pages 16–19.

Reeks, M., Reed, J., and Hall, D. (1988). On the resuspension of small particles by a turbulent flow. *Journal of Physics D: Applied Physics*, 21(4):574.

Reid, L. and Moore, R. D. (1978). Design and overall performance of four highly loaded, high speed inlet stages for an advanced high-pressure-ratio core compressor.

Reitzer, B. (1964). Rate of scale formation in tubular heat exchangers. mathematical analysis of factors influencing rate of decline of over-all heat transfer coefficients. *Industrial & Engineering Chemistry Process Design and Development*, 3(4):345–348.

Rezaei, H. R., Gupta, R. P., Wall, T. F., Miyamae, S., and Makino, K. (2002). Modelling the initial structure of ash deposits and structure changes due to sintering. In *Impact of Mineral Impurities in Solid Fuel Combustion*, pages 753–766. Springer.

Riboud, P., Roux, Y., Lucas, L., and Gaye, H. (1981). Improvement of continuous casting powders. *Fachberichte Huttenpraxis Metallweiterverarbeitung*, 19(8):859–869.

Richards, G., Logan, R., Meyer, C., and Anderson, R. (1992). Ash deposition at coal-fired gas turbine conditions: surface and combustion temperature effects. *Journal of engineering for gas turbines and power*, 114(1):132–138.

Rinard, G., Rugg, D. E., and Yamamoto, T. (1987). High-temperature high-pressure electrostatic precipitator electrical characterization and collection efficiency. *IEEE transactions on industry applications*, (1):114–119.

Rispoli, F., Delibra, G., Venturini, P., Corsini, A., Saavedra, R., and Tezduyar, T. E. (2015). Particle tracking and particle–shock interaction in compressible-flow computations with the v-sgs stabilization and $YZ\beta$ shock-capturing. *Computational Mechanics*, 55(6):1201–1209.

Ross, J. S., Anderson, R. J., and Nagarajan, R. (1988). Effect of sodium on deposition in a simulated combustion gas turbine environment. *Energy & fuels*, 2(3):282–289.

Rosti, M. E., Cortelezzi, L., and Quadrio, M. (2015). Direct numerical simulation of turbulent channel flow over porous walls. *Journal of Fluid Mechanics*, 784:396–442.

Sacco, C., Bowen, C., Lundgreen, R., Bons, J., Ruggiero, E., Allen, J., and Bailey, J. (2018). Dynamic similarity in turbine deposition testing and the role of pressure. *Journal of Engineering for Gas Turbines and Power*, 140(10):102605.

Scheller, B. L. and Bousfield, D. W. (1995). Newtonian drop impact with a solid surface. *AIChE Journal*, 41(6):1357–1367.

Schiaffino, S. and Sonin, A. A. (1997). Molten droplet deposition and solidification at low weber numbers. *Physics of Fluids*, 9(11):3172–3187.

Schurovsky, V. and Levikin, A. (1986). Fouling and cleaning of gas turbine axial compressor flow path. *Moscow, series Transport and Gas Conservation*, 11.

Seetharaman, S., Mukai, K., and Sichen, D. (2005). Viscosities of slags-an overview. *steel research international*, 76(4):267–278.

Senior, C. and Srinivasachar, S. (1995). Viscosity of ash particles in combustion systems for prediction of particle sticking. *Energy & Fuels*, 9(2):277–283.

Sethi, V. and John, W. (1993). Particle impaction patterns from a circular jet. *Aerosol science and technology*, 18(1):1–10.

Sharma, S., Dolan, M., Park, D., Morpeth, L., Ilyushechkin, A., McLennan, K., Harris, D., and Thambimuthu, K. (2008). A critical review of syngas cleaning technologies—fundamental limitations and practical problems. *Powder Technology*, 180(1-2):115–121.

Shin, D. and Hamed, A. (2016). Advanced high temperature erosion tunnel for testing tbc and new turbine blade materials. In *ASME Turbo Expo 2016: Turbomachinery Technical Conference and Exposition*, pages V006T21A011–V006T21A011. American Society of Mechanical Engineers.

Shin, S. and Gulyaeva, R. (1998). Density and surface tension of melts of the feo x-al 2 o 3-cao-sio 2 systems. *Rasplavy*, (4):33–39.

Shinozaki, M., Roberts, K. A., van de Goor, B., and Clyne, T. W. (2013). Deposition of ingested volcanic ash on surfaces in the turbine of a small jet engine. *Advanced Engineering Materials*, 15(10):986–994.

SID, S. I. D. (2009). Aeronautical information manual.

Sidhu, T., Prakash, S., and Agrawal, R. (2006). Hot corrosion and performance of nickel-based coatings. *Current Science*, pages 41–47.

Singh, S. and Tafti, D. (2013). Predicting the coefficient of restitution for particle wall collisions in gas turbine components. In *ASME Turbo Expo 2013: Turbine Technical Conference and Exposition*, pages V06BT37A041–V06BT37A041. American Society of Mechanical Engineers.

Singh, S. and Tafti, D. (2015). Particle deposition model for particulate flows at high temperatures in gas turbine components. *International Journal of Heat and Fluid Flow*, 52:72–83.

Singh, S. and Tafti, D. K. (2016). Prediction of sand transport and deposition in a two-pass internal cooling duct. *Journal of Engineering for Gas Turbines and Power*, 138(7):072606.

Singh, T. and Sundararajan, G. (1990). The erosion behavior of 304 stainless steel at elevated temperatures. *Metallurgical Transactions A*, 21(12):3187.

Skinner, S. N. and Zare-Behtash, H. (2018). State-of-the-art in aerodynamic shape optimisation methods. *Applied Soft Computing*, 62:933–962.

Smith, C., Barker, B., Clum, C., and Bons, J. (2010). Deposition in a turbine cascade with combusting flow. In *ASME Turbo Expo 2010: Power for Land, Sea, and Air*, pages 743–751. American Society of Mechanical Engineers.

Smith, W. H. (2012). *Air pollution and forests: interactions between air contaminants and forest ecosystems*. Springer Science & Business Media.

Soltani, M. and Ahmadi, G. (1994). On particle adhesion and removal mechanisms in turbulent flows. *Journal of Adhesion Science and Technology*, 8(7):763–785.

Song, W., Hess, K.-U., Damby, D. E., Wadsworth, F. B., Lavallée, Y., Cimarelli, C., and Dingwell, D. B. (2014). Fusion characteristics of volcanic ash relevant to aviation hazards. *Geophysical Research Letters*, 41(7):2326–2333.

Song, W., Lavallée, Y., Hess, K.-U., Kueppers, U., Cimarelli, C., and Dingwell, D. B. (2016). Volcanic ash melting under conditions relevant to ash turbine interactions. *Nature communications*, 7:10795.

Song, W., Lavallee, Y., Wadsworth, F. B., Hess, K.-U., and Dingwell, D. B. (2017). Wetting and spreading of molten volcanic ash in jet engines. *The Journal of Physical Chemistry Letters*, 8(8):1878–1884.

Spalding, D. (1961). A single formula for the "law of the wall". *Journal of Applied Mechanics*, 28(3):455–458.

Sparks, R. S. J., Bursik, M., Carey, S., Gilbert, J., Glaze, L., Sigurdsson, H., and Woods, A. (1997). *Volcanic plumes*. Wiley.

Speight, J. G. (2015). *Handbook of coal analysis*. John Wiley & Sons.

Spiro, C., Kimura, S., and Chen, C. (1987). Ash behavior during combustion and deposition in coal-fueled gas turbines. *Journal of engineering for gas turbines and power*, 109(3):325–330.

Sreedharan, S. S. and Tafti, D. K. (2010). Composition dependent model for the prediction of syngas ash deposition with application to a leading edge turbine vane. In *ASME Turbo Expo 2010: Power for Land, Sea, and Air*, pages 615–626. American Society of Mechanical Engineers.

Sreedharan, S. S. and Tafti, D. K. (2011). Composition dependent model for the prediction of syngas ash deposition in turbine gas hotpath. *International journal of heat and fluid flow*, 32(1):201–211.

Srinivasachar, S., Helble, J. J., and Boni, A. A. (1991). An experimental study of the inertial deposition of ash under coal combustion conditions. In *Symposium (International) on Combustion*, volume 23, pages 1305–1312. Elsevier.

Sripawadkul, V., Padulo, M., and Guenov, M. (2010). A comparison of airfoil shape parameterization techniques for early design optimization. In *13th AIAA/ISSMO multidisciplinary analysis optimization conference*, page 9050.

Standard, A. (2003). Standard test method for fusibility of coal and coke ash. *Astm International*.

Stow, C. and Hadfield, M. (1981). An experimental investigation of fluid flow resulting from the impact of a water drop with an unyielding dry surface. *Proc. R. Soc. Lond. A*, 373(1755):419–441.

Streeter, R. C., Diehl, E. K., and Schobert, H. H. (1984). Measurement and prediction of low-rank coal slag viscosity. In *Schobert, HH: The Chemistry of Low-Rank Coals. ACS Symposium series*, volume 264, page 195.

Stronge, W. J. (2018). *Impact mechanics*. Cambridge university press.

Suder, K. L., Chima, R. V., Strazisar, A. J., and Roberts, W. B. (1995). The effect of adding roughness and thickness to a transonic axial compressor rotor. *Journal of Turbomachinery*, 117(4):491–505.

Sukenaga, S., Haruki, S., Nomoto, Y., Saito, N., and Nakashima, K. (2011). Density and surface tension of cao–sio2–al2o3–r2o (r= li, na, k) melts. *ISIJ international*, 51(8):1285–1289.

Suman, A. (2015). *An innovative methodology for the analysis of microparticle deposits in transonic and subsonic blades for the assessment of compressor degradation*. PhD thesis, Università degli Studi di Ferrara.

Suman, A., Casari, N., Fabbri, E., Pinelli, M., di Mare, L., and Montomoli, F. (2018). Gas turbine fouling tests: Review, critical analysis and particle impact behavior map. *Journal of engineering for gas turbines and power*, Art in press.

Suman, A., Morini, M., Aldi, N., Casari, N., Pinelli, M., and Spina, P. R. (2017). A compressor fouling review based on an historical survey of asme turbo expo papers. *Journal of Turbomachinery*, 139(4):041005.

Suman, A., Morini, M., Kurz, R., Aldi, N., Brun, K., Pinelli, M., and Spina, P. (2015). Quantitative computational fluid dynamic analyses of particle deposition on a transonic axial compressor blade-part ii: Impact kinematics and particle sticking analysis. *Journal of Turbomachinery*, 137(2).

Sundararajan, G. and Roy, M. (1997). Solid particle erosion behaviour of metallic materials at room and elevated temperatures. *Tribology International*, 30(5):339–359.

Syverud, E. (2007). *Axial compressor performance deterioration and recovery through online washing*. PhD thesis, Fakultet for ingeniørvitenskap og teknologi.

Syverud, E., Brekke, O., and Bakken, L. E. (2005). Axial compressor deterioration caused by saltwater ingestion. In *ASME Turbo Expo 2005: Power for Land, Sea, and Air*, pages 327–337. American Society of Mechanical Engineers.

Tabakoff, W. Review-turbomachinery performance deterioration exposed to solid particulates environment (1984) journal of fluids engineering. *Transactions of the ASME*, 106(2):125–134.

Tabakoff, W. (1987). Compressor erosion and performance deterioration. *Journal of fluids engineering*, 109(3):297–306.

Tabakoff, W., Hamed, A., and Metwally, M. (1990). Effect of particle size distribution on particle dynamics and blade erosion in axial flow turbines. In *ASME 1990 International Gas Turbine and Aeroengine Congress and Exposition*. American Society of Mechanical Engineers.

Tabakoff, W., Hamed, A., Metwally, M., and Pasin, M. (1991). High temperature erosion resistance of coatings for gas turbine. In *ASME 1991 International Gas Turbine and Aeroengine Congress and Exposition*, pages V003T05A007–V003T05A007. American Society of Mechanical Engineers.

Tabakoff, W. and Malak, M. F. (1985). Laser measurements of fly ash rebound parameters for use in trajectory calculations. In *ASME 1985 International Gas Turbine Conference and Exhibit*. American Society of Mechanical Engineers.

Taiwo, A. M., Beddows, D. C., Shi, Z., and Harrison, R. M. (2014). Mass and number size distributions of particulate matter components: Comparison of an industrial site and an urban background site. *Science of the Total Environment*, 475:29–38.

Talbot, L., Cheng, R., Schefer, R., and Willis, D. (1980). Thermophoresis of particles in a heated boundary layer. *Journal of fluid mechanics*, 101(04):737–758.

Taleb, N. N. (2007). Black swans and the domains of statistics. *The American Statistician*, 61(3):198–200.

Taltavull, C., Dean, J., and Clyne, T. W. (2015). Adhesion of volcanic ash particles under controlled conditions and implications for their deposition in gas turbines. *Advanced Engineering Materials*.

Tammann, G. and Hesse, W. (1926). The dependence of viscosity upon the temperature of supercooled liquids. *Z. Anorg. Allg. Chem*, 156:245–257.

Tamon, H., Imanaka, H., Sano, N., Okazaki, M., and Tanthapanichakoon, W. (1998). Removal of aromatic compounds in gas by electron attachment. *Industrial & engineering chemistry research*, 37(7):2770–2774.

Tarabrin, A., Schurovsky, V., Bodrov, A., and Stalder, J.-P. (1998). Influence of axial compressor fouling on gas turbine unit perfomance based on different schemes and with different initial parameters. In *ASME 1998 International Gas Turbine and Aeroengine Congress and Exhibition*, pages V004T11A006–V004T11A006. American Society of Mechanical Engineers.

Tassicker, O. (1986). High temperature-pressure electrostatic precipitator for electric power generation technologies: an overview of the status. In *IChE Symp. Ser*, volume 99, pages 331–339.

Taylor, H. and Lichte, F. (1980). Chemical composition of mount st. helens volcanic ash. *Geophysical Research Letters*, 7(11):949–952.

Temime, B. Atmospheric aerosols: physical properties; chemical composition; health & environmental effects. *Department of Chemistry, University College Cork, Cork, Ireland*.

Thévenin, D. and Janiga, G. (2008). *Optimization and computational fluid dynamics*. Springer Science & Business Media.

Thompson, J. F., Soni, B. K., and Weatherill, N. P. (1998). *Handbook of grid generation*. CRC press.

Thulin, R. D., Howe, D. C., and Singer, I. D. (1982). Energy efficient engine high-pressure turbine detailed design report. Technical report, NASA CR-165608.

Tippayawong, N. and Preechawuttipong, I. (2011). Analytical prediction of particle detachment from a flat surface by turbulent air flows. *Chiang Mai Journal of Science*, 38(3):503–507.

Tomas, J. (2007). Adhesion of ultrafine particles—a micromechanical approach. *Chemical Engineering Science*, 62(7):1997–2010.

Ukiwe, C. and Kwok, D. Y. (2005). On the maximum spreading diameter of impacting droplets on well-prepared solid surfaces. *Langmuir*, 21(2):666–673.

Vadasz, P. and Havlik, M. (1995). Density and surface tension of slag melts of the system fe 2 o 3-feo-cao-sio 2. *Ceramics- Silikaty*, 39(3):92–98.

Vanderplaats, G. N. (1973). Conmin: a fortran program for constrained function minimization: user's manual.

Vargas, S., Frandsen, F., and Dam-Johansen, K. (2001). Rheological properties of high-temperature melts of coal ashes and other silicates. *Progress in Energy and Combustion Science*, 27(3):237–429.

Vigueras Zuniga, M. O. (2007). *Analysis of gas turbine compressor fouling and washing on line*. PhD thesis, Cranfield University.

Villot, A., Gonthier, Y., Gonze, E., Bernis, A., Ravel, S., Grateau, M., and Guillaudeau, J. (2012). Separation of particles from syngas at high-temperatures with an electrostatic precipitator. *Separation and purification technology*, 92:181–190.

Visser, J. (1972). On hamaker constants: A comparison between hamaker constants and lifshitz-van der waals constants. *Advances in colloid and interface science*, 3(4):331–363.

Vogel, H. (1921). The law of the relation between the viscosity of liquids and the temperature. *Phys. Z*, 22:645–646.

Wadsworth, F., Vasseur, J., Llewellin, E., Schauroth, J., Dobson, K., Scheu, B., and Dingwell, D. (2016). Sintering of viscous droplets under surface tension. *Proceedings of the Royal Society A: Mathematical, Physical and Engineering Sciences*, 472(2188).

Wall, S., John, W., Wang, H.-C., and Goren, S. L. (1990). Measurements of kinetic energy loss for particles impacting surfaces. *Aerosol Science and Technology*, 12(4):926–946.

Walsh, P. M., Sayre, A. N., Loehden, D. O., Monroe, L. S., Beér, J. M., and Sarofim, A. F. (1990). Deposition of bituminous coal ash on an isolated heat exchanger tube: effects of coal properties on deposit growth. *Progress in Energy and Combustion Science*, 16(4):327–345.

Wammack, J. E., Crosby, J., Fletcher, D., Bons, J. P., and Fletcher, T. H. (2008). Evolution of surface deposits on a high-pressure turbine blade—part i: Physical characteristics. *Journal of Turbomachinery*, 130(2):021020.

Wang, J., Vujanovic, M., and Sunden, B. (2018). A review of multiphase flow and deposition effects in film-cooled gas turbines. *THERMAL SCIENCE*, 22(5):1905–1921.

Wang, X.-y., Pu, J., Yuan, R.-m., and Wang, J.-h. (2016). Combined influence of surface deposition and hole-blockage on film-cooling performances. In *ASME Turbo Expo 2016: Turbomachinery Technical Conference and Exposition*, pages V05CT19A019–V05CT19A019. American Society of Mechanical Engineers.

Watt, J. and Fereday, F. (1969). The flow properties of slag formed from the ashes of british coals. *J. Ind. Fuel*, 42.

Weaver, M. M., Dunn, M. G., and Heffernan, T. (1996). Experimental determination of the influence of foreign particle ingestion on the behavior of hot-section components including lamilloy®. In *ASME 1996 International Gas Turbine and Aeroengine Congress and Exhibition*, pages V003T05A014–V003T05A014. American Society of Mechanical Engineers.

Webb, J., Casaday, B., Barker, B., Bons, J., Gledhill, A., and Padture, N. (2012). Coal ash deposition on nozzle guide vanes-part i experimental characteristics of four coal ash types. *ASME J. of Turbomach*, 135(2).

Webb, J., Casaday, B., Barker, B., Bons, J., Gledhill, A., and Padture, N. (2013). Coal ash deposition on nozzle guide vanes—part i: Experimental characteristics of four coal ash types. *Journal of Turbomachinery*, 135(2):021033.

Webb, J. J. (2011). The effect of particle size and film cooling on nozzle guide vane deposition. Master's thesis, The Ohio State University.

Weller, H. G., Tabor, G., Jasak, H., and Fureby, C. (1998). A tensorial approach to computational continuum mechanics using object-oriented techniques. *Computers in physics*, 12(6):620–631.

Wellman, R. and Nicholls, J. (2004). High temperature erosion–oxidation mechanisms, maps and models. *Wear*, 256(9-10):907–917.

Wenglarz, R. and Cohn, A. (1983). Turbine deposition evaluations using simplified tests. In *ASME 1983 International Gas Turbine Conference and Exhibit*. American Society of Mechanical Engineers.

Wenglarz, R. and Fox, R. (1990). Physical aspects of deposition from coal-water fuels under gas turbine conditions. *Journal of Engineering for Gas Turbines and Power*, 112(1):9–14.

Wenglarz, R. A. (1987). Direct coal-fueled combustion turbines. In *ASME 1987 International Gas Turbine Conference and Exhibition*, pages V003T05A008–V003T05A008. American Society of Mechanical Engineers.

Wenglarz, R. A. (1991). An approach for evaluation of gas turbine deposition. In *ASME 1991 International Gas Turbine and Aeroengine Congress and Exposition*, pages V003T05A008–V003T05A008. American Society of Mechanical Engineers.

Wenzel, R. N. (1936). Resistance of solid surfaces to wetting by water. *Industrial & Engineering Chemistry*, 28(8):988–994.

Weymann, H. (1962). On the hole theory of viscosity, compressibility, and expansivity of liquids. *Kolloid-Zeitschrift und Zeitschrift für Polymere*, 181(2):131–137.

Whitaker, S. M., Lundgreen, R. K., and Bons, J. P. (2017). Effects of metal surface temperature on deposition-induced flow blockage in a vane leading edge cooling geometry. In *ASME Turbo Expo 2017: Turbomachinery Technical Conference and Exposition*, pages V02DT48A020–V02DT48A020. American Society of Mechanical Engineers.

Whitaker, S. M., Peterson, B., Miller, A. F., and Bons, J. P. (2016). The effect of particle loading, size, and temperature on deposition in a vane leading edge impingement cooling geometry. *ASME Paper No. GT2016-57413*.

Whitaker, S. M., Prenter, R., and Bons, J. P. (2015). The effect of freestream turbulence on deposition for nozzle guide vanes. *Journal of Turbomachinery*, 137(12):121001.

Whitlow, G., Lee, S., Mulik, P., Wenglarz, R., Sherlock, T., and Cohn, A. (1983). Combustion turbine deposition observations from residual and simulated residual oil studies. *Journal of Engineering for Power*, 105(1):88–96.

Wilcox, M., Baldwin, R., Garcia-Hernandez, A., and Brun, K. (2010). Guideline for gas turbine inlet air filtration systems. *Gas Machinery Research Council, Dallas, TX*.

Wilcox, M., Kurz, R., Brun, K., et al. (2011). Successful selection and operation of gas turbine inlet filtration systems. In *Proceedings of the 40th Turbomachinery Symposium*. Texas A&M University. Turbomachinery Laboratories.

Wing, R. and McGill, I. (1981). The protection of gas turbine blades: a platinum aluminide diffusion coating. *Aircraft Engineering and Aerospace Technology*, 53(10):15–21.

Wood, E. J., Ng, W. F., Vandsburger, U., and LePera, S. (2010). Simulated syngas ash deposits on a flat plate using teflon and pvc particles. In *ASME Turbo Expo 2010: Power for Land, Sea, and Air*, pages 563–569. American Society of Mechanical Engineers.

Wu, C., Cheng, G., and Ma, Q. (2014). Calculating models on the surface tension of cao-feo-sio2 molten slags. *Research of Materials Science*, 3(1).

Wylie, S., Bucknell, A., Forsyth, P., McGilvray, M., and Gillespie, D. R. (2017). Reduction in flow parameter resulting from volcanic ash deposition in engine representative cooling passages. *Journal of Turbomachinery*, 139(3):031008.

Xu, H., Liu, Y., He, P., and Wang, H. (1998). The tar model for calculation of droplet/wall impingement. *Journal of fluids engineering*, 120(3):593–597.

Yin, C., Luo, Z., Ni, M., and Cen, K. (1998). Predicting coal ash fusion temperature with a back-propagation neural network model. *Fuel*, 77(15):1777–1782.

Yu, K. and Tafti, D. (2016). Impact model for micrometer-sized sand particles. *Powder Technology*, 294:11–21.

Yu, K. and Tafti, D. (2017). Size and temperature dependent deposition model of micro-sized sand particles. In *ASME Turbo Expo 2017: Turbomachinery Technical Conference and Exposition*, pages V02DT48A008–V02DT48A008. American Society of Mechanical Engineers.

Zaba, T. (1980). Losses in gas-turbines due to deposits on the blading. *Brown Boveri Review*, 67(12):715–722.

Zaba, T. and Lombardi, P. (1984). Experience in the operation of air filters in gas turbine installations. In *ASME 1984 International Gas Turbine Conference and Exhibit*, pages V004T10A009–V004T10A009. American Society of Mechanical Engineers.

Zagnoli, D., Prenter, R., Ameri, A., and Bons, J. P. (2015). Numerical study of deposition in a full turbine stage using steady and unsteady methods. In *ASME Turbo Expo 2015: Turbine Technical Conference and Exposition*, pages V02CT44A026–V02CT44A026. American Society of Mechanical Engineers.

Zbogar, A., Frandsen, F., Jensen, P. A., and Glarborg, P. (2009). Shedding of ash deposits. *Progress in energy and combustion science*, 35(1):31–56.

Zender, C. S., Bian, H., and Newman, D. (2003). Mineral dust entrainment and deposition (DEAD) model: Description and 1990s dust climatology. *Journal of Geophysical Research: Atmospheres*, 108(D14).

Zhang, Z. and Chen, Q. (2007). Comparison of the eulerian and lagrangian methods for predicting particle transport in enclosed spaces. *Atmospheric environment*, 41(25):5236–5248.

List of publications

Some of the research leading to this thesis has appeared previously in the following publications.

1. Casari, N., Pinelli, M., Suman, A., di Mare, L., & Montomoli, F. (2017). An energy-based fouling model for gas turbines: EBFOG. *Journal of Turbomachinery*, **139**(2), 021002.

    - Presented a ASME Turbo Expo 2016: Turbomachinery Technical Conference and Exposition GT2016-58044, June 13-17, 2016,Seoul, South Korea

2. Casari, N., Pinelli, M., Suman, A., di Mare, L., & Montomoli, F. (2017). Gas turbine blade geometry variation due to fouling. Proceedings of European Turbomachinery Conference, 3-7 April 2017, Stockholm, Sweden

3. Casari, N., Pinelli, M., Suman, A., di Mare, L., & Montomoli, F. (2018). EBFOG: Deposition, Erosion, and Detachment on High-Pressure Turbine Vanes. *Journal of Turbomachinery*, **140**(6), 061001.

    - Presented a ASME Turbo Expo 2017: Turbomachinery Technical Conference and Exposition GT2017-64526,June 26-30, 2017, Charlotte, NC USA

4. Aldi, N., Casari, N., Dainese, D., Morini, M., Pinelli, M., Spina, P. R., & Suman, A. (2018). Quantitative Computational Fluid Dynamics Analyses of Particle Deposition in a Heavy-Duty Subsonic Axial Compressor. *Journal of Engineering for Gas Turbines and Power*, **140**(8), 082601.

    - Presented a ASME Turbo Expo 2017: Turbomachinery Technical Conference and Exposition GT2017-63563,June 26-30, 2017, Charlotte, NC USA

5. Aldi, N., Casari, N., Morini, M., Pinelli, M., Spina, P. R., & Suman, A. (2019). Gas Turbine Fouling: A Comparison Among 100 Heavy-Duty Frames. *Journal of Engineering for Gas Turbines and Power*, **141**(3), 032401.

    - Presented a ASME Turbo Expo 2018: Turbomachinery Technical Conference and Exposition GT2018-76947,June 11 – 15 ,2018, Oslo, Norway

6. Suman A, Casari N, Fabbri E, Pinelli M, di Mare L, & Montomoli F. Gas Turbine Fouling Tests: Review, Critical Analysis and Particle Impact Behavior Map. (2018) *Journal of Engineering for Gas Turbines and Power, Art. in press.*

    - Presented a ASME Turbo Expo 2018: Turbomachinery Technical Conference and Exposition GT2018-76947,June 11 – 15 ,2018, Oslo, Norway

7. Aldi, N., Casari, N., Dainese, D., Morini, M., Pinelli, M., Spina, P. R., & Suman, A.. The Effects of Third Substances at the Particle/Surface Interface in Compressor Fouling. Presented at ASME Turbo Expo 2017: Turbomachinery Technical Conference and Exposition GT2017-6 4425, June 26-30, 2017, Charlotte, NC USA

8. Casari, N., Pinelli, M., & Suman, A.. On Deposition and Build-Up Detachment in Compressor Fouling. In ASME Turbo Expo 2018: Turbomachinery Technical Conference and Exposition GT2018-76776, June 11-15, 2018, Oslo, Norway

9. Casari, N., Pinelli, M., & Suman, A.. An innovative approach towards fouling modeling: Microscale deposition pattern and its effect on the flow field. In ASME Turbo Expo 2018: Turbomachinery Technical Conference and Exposition GT2018-76882, June 11-15, 2018, Oslo, Norway

Appendix 1

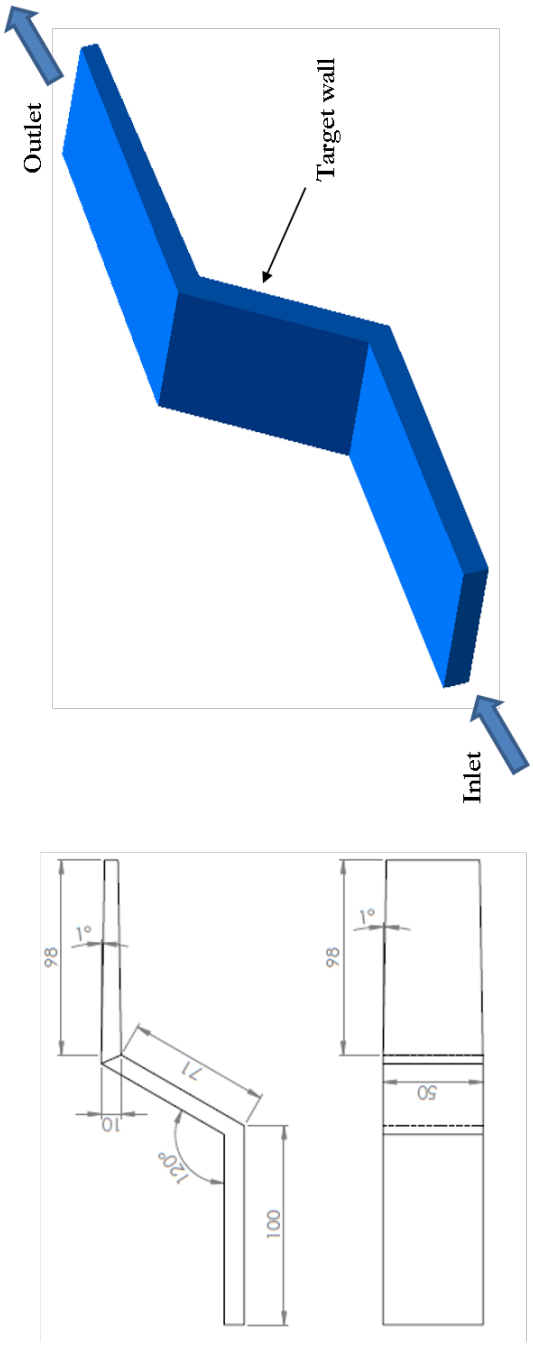

Figure A1.1: Technical design for the bended duct test case

This page was intentionally left blank.

Appendix 2

Compressor fouling due to particle adhesion is characterized by three main peculiarities Kurz and Brun (2012); Suman et al. (2017):

- particles impact velocity could vary from 0 m/s to over 400 m/s in the case of transonic stages;
- contaminants are particles with a diameter in the range from 0.1 μm to 2.0 μm (smaller particles are usually not so relevant in terms of mass while larger particles are usually separated from the airflow by filtration systems, in the case of land-based units or by the action of the fan in the case of aero-engines);
- the particle characteristics (such as shape, dimension, etc.) do not change during the impact thanks to its mechanical strength (such as particle Young modulus that varies only at higher temperature values El-Batsh (2001); Ai (2009)

These points represent the guidelines on which the experimental test bench and the data analysis reported in the present work are carried out. The impact and the adhesion of micro-metric particles have been experimentally studied in the aerosol technology field, in which the test benches allow the proper control of the particle impact behavior. For this reason, the layout and the operation features of the present test bench, are based on this type of applications which are characterized by simplified targets, as flat surfaces located in front of the particle injector Poppe et al. (2000) and Wall et al. (1990); Sethi and John (1993). The proper positions of nozzle and target, as well as the combination of the Reynolds number of the injector, given the opportunity to study different particle impact behavior Burwash et al. (2006).

The test bench layout equipped with all devices is reported in Fig. A2.1. The particle preparation is demanded to the aerosol generator TOPAS SAG-410/U. This device is able to reproduce a constant feeding rate of solid sub-microsized particles. The preparation process is based on a calibrated ring with a controlled rotational speed. The particles are carried on the rotating ring by means of a hopper feeder that guarantees the continuity and the reproducibility of the preparation process. The rotating ring carries the particles from the hopper feeder to the suction port in which a constant pressure is imposed. Finally, the

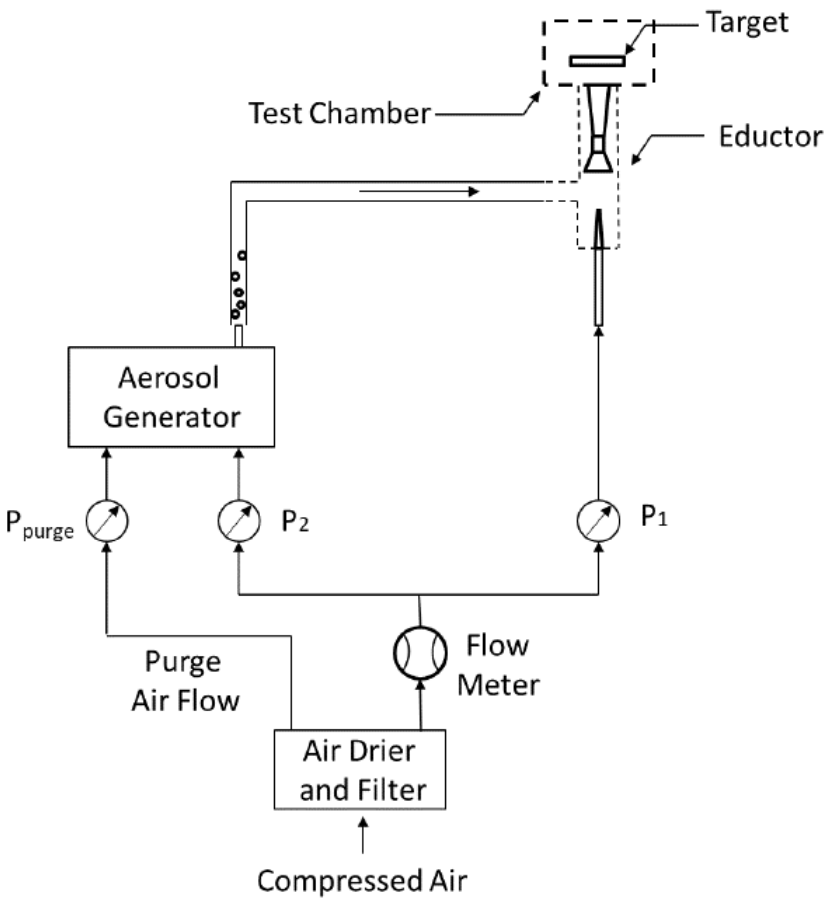

Figure A2.1: Test-bench layout

particles are sucked up from the rotating ring and accelerated by means of a specifically-designed eductor system, able to increase the airflow velocity up to 50 m/s. According to this procedure, the contaminated air at the eductor exhaust is characterized by a certain velocity and a controlled number of particles. The operation of the aerosol generator and the eductor system is realized by means of shop air. Both of primary air (used for the operation of the feeding system) and the dilution air (used for increasing the particle velocity) are controlled and measured (in terms of pressure, temperature and mass flow rate) during each test. The impact plate is placed 8 mm-far from the eductor exhaust port in order to reduce the influence of the back-pressure on the eductor operation. The impact plate is designed in order to reproduce the quasi-ideal stagnation condition in front of the eductor exhaust port. The impact plate is an assembly of two parts: the target holder and the metallic target. With this design, it is possible to test several metallic targets with the same experimental set-up. The metallic target has a square frontal area (20 mm x 20 mm) and it is obtained by means of a milling process. The surface roughness of the target is accounted for one of the sensitivity analyses presented in this paper. In a different way of literature findings Dong et al. (2018), in the present research, the particle diameter and surface roughness level are comparable playing an important role in the particle adhesion. Finally, the eductor system is closed in a protective case equipped with a hygrometer. Therefore, in line with Dong et al. (2018), the humidity of the outlet gas is continuously monitored in order to give a reference value of the test conditions. It is well known the

effects of air humidity on the microsized particle agglomeration Endo et al. (1997). and, due to this, the present results of adhesion/detachment process refers to the following humidity condition. In the present work, the humidity value is not considered for the sensitivity analysis of the particle sticking behavior but it is recorded for giving the actual impact conditions for each test. Each impact test was carried out with a humidity level of the outlet gas of 51 $\pm$ 1 % together with a room humidity value of 48 % $\pm$ 1 %. With reference to Burwash et al. (2006), the fluid dynamic and geometric features of the eductor are also reported. According to Burwash et al. (2006), the dimensionless distances from the nozzle exit to the impaction surface L/D (where L represents the distance between the eductor outlet section and the target, while D represents the eductor diameter) is equal to 1.3 for all the test conditions. As reported in Burwash et al. (2006), this short distance leads with a deposition phenomenon dominated by the turbulent dispersion instead of inertia. Regarding the eductor Reynolds number, according to the tests conditions, it is comprised in the range from 7500 to 12'500, very similar to that used in Burwash et al. (2006).

This page was intentionally left blank.

Sezioni

Università degli Studi di Ferrara

Dottorati di ricerca

Il tuo indirizzo e-mail

nicola.casari@unife.it

Oggetto:

Dichiarazione di conformità della tesi di Dottorato

Io sottoscritto Dott. (Cognome e Nome)

Casari Nicola

Nato a:

Legnago

Provincia:

Verona

Il giorno:

13/12/1991

Avendo frequentato il Dottorato di Ricerca in:

Scienze dell'Ingegneria

Ciclo di Dottorato

31

Titolo della tesi:

Modeling approaches for gas turbine deterioration analysis

Titolo della tesi (traduzione):

Approcci per la modellazione dell'analisi del deterioramento di turbine a gas

Tutore: Prof. (Cognome e Nome)

Pinelli Michele

Settore Scientifico Disciplinare (S.S.D.)

ING-IND/08

Parole chiave della tesi (max 10):

Gas Turbines, Fouling, Erosion, Performance Degradation, CFD

Consapevole, dichiara

CONSAPEVOLE: (1) del fatto che in caso di dichiarazioni mendaci, oltre alle sanzioni previste dal codice penale e dalle Leggi speciali per l'ipotesi di falsità in atti ed uso di atti falsi, decade fin dall'inizio e senza necessità di alcuna formalità dai benefici conseguenti al provvedimento emanato sulla base di tali dichiarazioni; (2) dell'obbligo per l'Università di provvedere al deposito di legge delle tesi di dottorato al fine di assicurarne la conservazione e la consultabilità da parte di terzi; (3) della procedura adottata dall'Università di Ferrara ove si richiede che la tesi sia consegnata dal dottorando in 2 copie di cui una in formato cartaceo e una in formato pdf non modificabile su idonei supporti (CD-ROM, DVD) secondo le istruzioni pubblicate sul sito: http://www.unife.it/studenti/dottorato alla voce ESAME FINALE – disposizioni e modulistica; (4) del fatto che

l'Università, sulla base dei dati forniti, archivierà e renderà consultabile in rete il testo completo della tesi di dottorato di cui alla presente dichiarazione attraverso l'Archivio istituzionale ad accesso aperto "EPRINTS.unife.it" oltre che attraverso i Cataloghi delle Biblioteche Nazionali Centrali di Roma e Firenze; DICHIARO SOTTO LA MIA RESPONSABILITA': (1) che la copia della tesi depositata presso l'Università di Ferrara in formato cartaceo è del tutto identica a quella presentata in formato elettronico (CD-ROM, DVD), a quelle da inviare ai Commissari di esame finale e alla copia che produrrò in seduta d'esame finale. Di conseguenza va esclusa qualsiasi responsabilità dell'Ateneo stesso per quanto riguarda eventuali errori, imprecisioni o omissioni nei contenuti della tesi; (2) di prendere atto che la tesi in formato cartaceo è l'unica alla quale farà riferimento l'Università per rilasciare, a mia richiesta, la dichiarazione di conformità di eventuali copie; (3) che il contenuto e l'organizzazione della tesi è opera originale da me realizzata e non compromette in alcun modo i diritti di terzi, ivi compresi quelli relativi alla sicurezza dei dati personali; che pertanto l'Università è in ogni caso esente da responsabilità di qualsivoglia natura civile, amministrativa o penale e sarà da me tenuta indenne da qualsiasi richiesta o rivendicazione da parte di terzi; (4) che la tesi di dottorato non è il risultato di attività rientranti nella normativa sulla proprietà industriale, non è stata prodotta nell'ambito di progetti finanziati da soggetti pubblici o privati con vincoli alla divulgazione dei risultati, non è oggetto di eventuali registrazioni di tipo brevettale o di tutela. PER ACCETTAZIONE DI QUANTO SOPRA RIPORTATO

Firma del dottorando

Ferrara, li 12/03/2019 (data) Firma del Dottorando _____

Firma del Tutore

Visto: Il Tutore Si approva Firma del Tutore _____